CFD Modeling of Fluid-Morphology-Soil Interaction for Marine Structures

by

Yuzhu Li

Thesis submitted in fulfilment of
the requirements for the degree of
PHILOSOPHIAE DOCTOR
(PhD)

Faculty of Science and Technology
Department of Mechanical and Structural Engineering and Materials Science
2019

University of Stavanger
N-4036 Stavanger
NORWAY
www.uis.no

ISBN: 978-82-7644-867-2
ISSN: 1890-1387
PhD Thesis UiS No. 473

Preface

This thesis is submitted in partial fulfillment of the requirements for the degree of Doctor of Philosophy (PhD) at the University of Stavanger (UiS), Norway. The research work has been carried out at the Faculty of Science and Technology, Department of Mechanical and Structural Engineering and Material Science, in the period from April 2016 to May 2019. The PhD project was financed by the Statoil Akademia program at the University of Stavanger.

Yuzhu Li
2019

A Duet of Water and Soil - Spring of Life. Acrylic on canvas / painted for the theme of my PhD thesis / Yuzhu Li / 2019.

Abstract

In the offshore and subsea environment, scour and liquefaction are two main risks faced by the offshore foundations and subsea structures. Based on the integrated study of flow physics, scour/erosion processes and soil mechanics, the present PhD project aims to develop and improve the numerical models for predicting the soil liquefaction and scour/erosion around offshore foundations and subsea structures.

For liquefaction analysis, an integrated model of wave-induced soil response around offshore foundations and coastal structures is developed within the finite volume method (FVM) based OpenFOAM®* framework. The model consists of a consolidation analysis solver, an anisotropic poro-elastic soil response solver, and a momentary liquefaction analysis module. First, the poro-elastic soil model in the quasi-static form developed in the previous work is incorporated in the integrated wave-structure-seabed interaction (WSSI) model. It is validated in the present work and applied to investigate the liquefaction risk around gravity-based offshore foundations and rubble mound breakwaters with submerged berms. Then, the partial-dynamic form of the poro-elastic soil model ($u-p$ model) with considering the acceleration of the soil is implemented. It is found that the $u-p$ model provides a better prediction of excess pore pressure than the quasi-static model when reproducing the experiment of standing wave-induced pore pressure below a vertical wall. Two liquefaction criteria based on the vertical effective stress and based on the excess pore pressure, respectively, are implemented. It appears that

*OpenFOAM® is a registered trademark of OpenCFD Ltd.

the criteria based on the excess pore pressure provides more conservative solutions than that based on the vertical effective stress for evaluating the liquefaction risk around gravity-based offshore foundations.

Scour beneath marine structures is simulated by using a fully-coupled hydrodynamic and morphologic model developed in the previous work. In the hydrodynamic model, the unsteady Reynolds-averaged Navier-Stokes (URANS) equations are solved together with the $k-\omega$ turbulence closure. The morphological model is based on the sediment continuity (Exner) equation. In the present PhD work, the fully-coupled hydrodynamic and morphologic model is validated against existing experiments. The model is then employed to simulate scour beneath two tandem pipelines under wave-plus-current conditions for a variety of Keulegan-Carpenter (KC) numbers, relative current strengths and horizontal gap distances between the two pipelines.

Considering both the seepage in the seabed and the sediment transport at the bed surface, a numerical model to couple the scouring process with continuous upward seepage in the seabed is proposed. A small seepage can cause significant changes to the hydrodynamic force on the bed surface and stability of bed particles, which can further affect sediment transport processes and scour patterns around subsea structures. The coupled scour and seepage model is developed based on the aforementioned fully-coupled hydrodynamic and morphologic model and is validated against existing experiments. The validated model is then applied to investigate the scour development beneath a submarine pipeline subjected to different upward seepage flows. A general finding is that with different upward seepage flows, the scour depth beneath the subsea pipeline may either increase or decrease, or remain similar in value, while the scour width is generally increased with the existence of large upward hydraulic gradients.

Acknowledgements

I would like to first say a very big thank you to my supervisor Professor Muk Chen Ong for all the support and contributions of time, ideas, and funding to make my PhD experience productive and stimulating. Many thanks also to my co-supervisors, Professor Ove Tobias Gudmestad and Professor Bjørn Helge Hjertager for the good advice during my PhD studies. Without the guidance and constant feedback from my supervisors, this PhD would not have been achievable within three years.

I would like to thank Dr. Tian Tang who helped me during the beginning of my PhD. Thanks to her good previous work so that I could have a basis to start with. I would like to thank Dr. Wen-Gang Qi from the Chinese Academy of Sciences for providing me the experimental data to validate the wave-structure-soil interaction model in this thesis. Thanks also to his friendship and generous help.

During this PhD, I had a three-month visit at DTU, where I had a good time and a happy memory. I would like to express my sincere thanks to Associate Professor David R. Fuhrman and Dr. Bjarke Eltard Larsen for the pleasant and fruitful collaboration.

I am also grateful to my colleagues in UiS, for sharing the good lunchtime and waffle Fridays. I specially thanks to Associate Professor Lin Li for time together at the same office and Associate Professor Fenfang Zhao for the accompany in the evenings during my last period of PhD work. I want to express my earnest thanks to Professor Dimitrios Pavlou for the great

friendship and the common art hobbies: painting and photography, which relieved my stress and filled me with curiosity and creativity.

I would also like to say a heartfelt thank you to my mother and my life coach - my father for always loving me and encouraging me to embrace life and face challenges with a positive attitude.

And finally, thank you, Dominic Wong, for the ultimate love and freedom you have given me. Thank you for being by my side throughout this PhD, and thank you for helping me to become a better version of myself. Without you, I would not have had so much persistence and perseverance during this journey.

List of Appended Papers

Paper I Li Y., Ong M. C., and Tang T. (2018). "Numerical analysis of wave-induced poro-elastic seabed response around a hexagonal gravity-based offshore foundation". Coastal Engineering, 136, 81-95.

Paper II Li Y., Ong M. C., Gudmestad O. T., and Hjertager, B. H. (2019), "The effects of slab geometry and wave direction on the soil liquefaction around offshore foundations". Accepted by Ships and Offshore Structures.

Paper III Celli D., Li Y., Ong M. C., and Risio M.D. (2019). "The role of submerged berms on the momentary liquefaction around conventional rubble mound breakwaters". Applied Ocean Research, 0141-1187.

Paper IV Li Y., Ong M. C., and Tang T. (2019). "A numerical toolbox for seabed response analysis around marine structures". Submitted to Ocean Engineering.

Paper V Li Y., Ong M. C., Fuhrman, D. R., and Larsen B.E., (2019). "Numerical investigation of wave-plus-current induced scour beneath two submarine pipelines in tandem". Submitted to Coastal Engineering.

Paper VI Li Y., Ong M. C., and Fuhrman, D. R. (2019). "CFD investigations of scour beneath a submarine pipeline with the effect of upward seepage". Submitted to Coastal Engineering.

Declaration of Authorship

All the six papers that serve as the core content of this thesis are co-authored.

- For Paper I and Paper IV, I was the first author and contributed to the main idea of the paper. I did numerical solver implementations based on the third author Dr. Tian Tang's previous work. I also carried out numerical simulations and wrote the paper. The second author Professor Muk Chen Ong participated in the discussions of the idea and the numerical simulations, and contributed to the paper writing. The third author Dr. Tian Tang provided advice and help to the numerical set-up of the simulations.

- Paper II was a course project paper for the PhD course 'Environmental Loads on Structures' taught by the third author Professor Ove Tobias Gudmestad. I was the first author and contributed to the main idea of the paper. I carried out numerical simulations and wrote the paper. The co-authors Professor Muk Chen Ong, Professor Ove Tobias Gudmestad and Professor Bjørn Helge Hjertager participated in the discussion of the idea and gave comments to the paper writing.

- Paper III was based on the numerical solvers implemented in Paper I. I was the second author and contributed to the idea of paper and the discussion of how to conduct the numerical simulations. I also checked the numerical results and revised the paper draft. The first author Dr. Daniele Celli generated the main idea of this paper, performed main simulations and wrote the paper. The third and fourth authors Professor Muk Chen Ong and Dr. Marcello Di Risio participated in the discussion of the idea and provided comments to the paper writing.

- Paper V was conducted during my visit at Technical University of Denmark (DTU). I was the first author and contributed to the main idea of the paper. I carried out numerical simulations and wrote the

paper. The second author Professor Muk Chen Ong participated in the discussions of the idea and gave comments to the paper writing. The third author Associate Professor David R. Fuhrman helped on the numerical set-up and simulations and gave advice and revisions to the draft. The fourth author Dr. Bjarke Eltard Larsen contributed in conducting the numerical simulations and gave comments to the draft.

- For Paper VI, I was the first author and came up with the idea of the paper. I did numerical solver implementations, carried out numerical simulations and wrote the paper. The second author Professor Muk Chen Ong participated in the discussions of the idea and the numerical solver implementations, and contributed to the paper writing. The third author Associate Professor David R. Fuhrman participated in the discussion and provided comments to the draft.

List of Additional Papers Not Included in the Thesis

Paper I Pavlou, D. G., and Li, Y. (2018). "Seabed Dynamic Response of Offshore Wind Turbine Foundation under Vertical Harmonic Loading: An Analytic Solution". Mathematical Problems in Engineering, 2018.

Paper II Li, Y., Ong, M. C., Gudmestad, O. T., and Hjertager, B. H. (2018, June). Numerical Analysis of Steep Wave-Induced Seabed Response and Liquefaction Around Gravity-Based Offshore Foundations. In ASME 2018 37th International Conference on Ocean, Offshore and Arctic Engineering (pp. V009T10A025-V009T10A025). American Society of Mechanical Engineers.

Paper III Li, Y., Tang, T., and Ong, M. C. (2017, June). A 3D Wave-Structure-Seabed Interaction Analysis of a Gravity-Based Wind Turbine Foundation. In ASME 2017 36th International Conference on Ocean, Offshore and Arctic Engineering (pp. V009T10A009-V009T10A009). American Society of Mechanical Engineers.

Paper IV Li Y., (2016), "Implementation of multiple time steps for the multi-physics solver based on ChtMultiRegionFoam". In Proceedings of CFD with OpenSource Software, 2016, Edited by Nilsson. H., http://www.tfd.chalmers.se/ hani/kurser/OS_CFD_2016

Table of contents

Chapter 1

Introduction

1.1 Background and motivation

The rapid development of offshore oil and gas industry and offshore wind industry has drawn substantial attention to the technology of subsea structure and offshore foundation designs among industrial and academic communities. In order to achieve good operational conditions and to alleviate potential risks, it is essential to assess hydrodynamic loads acting on the offshore foundations and the subsea structures (such as monopile foundations, gravity-based foundations, suction-bucket foundations, subsea caissons, subsea protection covers and marine pipelines) precisely. Moreover, in areas with soil that is prone to scour or liquefaction in waves and current, the stability of the structure will be affected. In order to reduce the potential risks, uncertainties and ultimately the cost of the design and construction, a good physical understanding and comprehensive modelling of fluid interacting with the morphological soil bed around marine structures is requisite.

When designing offshore foundations and subsea structures, one of the essential work is to assess their geotechnical stability. This involves evaluation of wave-induced pore pressure distribution, seepage flows in the porous seabed and the potential liquefaction risk around the structure. In geotechnical

engineering terminology, liquefaction stands for the condition that the effective stresses between individual soil particles vanish so that the fluid-sediment mixture together acts like a fluid (Sumer, 2014a). When the soil is liquefied, gravity structures may fail. Figure 1.1 shows the collapse of a quay wall after the soil foundation is liquefied due to earthquake. In the presence of waves, liquefaction is generated mainly by two different mechanisms. The first one is residual liquefaction due to the build-up of pore pressure which may occur when a loose sand bed is exposed to waves. The second one is momentary liquefaction due to an upward-directed vertical pressure gradient in the soil during the passage of a wave trough (Jeng, 2012; Sumer, 2014a), which can occur to the soil in a dense status. The natural seabed sand experiences the 'wave-induced compaction' (Sumer, 2014a) for a long history. Under cyclic loading, the loose soil will experience the built up and then dissipation of the pore pressure. The loose soil particles will rearrange the relative positions to a more dense status. When the compaction process is fully completed, residual liquefaction should not occur a second time with the same environmental load strength and duration (Fredsøe, 2016). For the natural seabed in a dense status due to the long history of 'wave-induced compaction' process, the poro-elastic theory and momentary (instantaneous) liquefaction analysis can provide satisfactory results (Ye et al., 2015b). The present study focuses on the investigation of momentary liquefaction in the poro-elastic seabed. However, in some offshore areas, there might exist newly deposited loose sand soil which is typical elastoplastic soil so that a poro-elastoplastic soil model should be utilized. This kind of sand soil has a weak bearing capability and is easy to liquefy under cyclic loading. Therefore, it can be risky to build the marine structures upon it (Ye and Wang, 2016). Also, in some fields, when the seabed is active due to continuous sediment transport with sand waves so that the soil is constantly being reworked, residual liquefaction can be encountered.

Figure 1.1 Damage to a quay wall at Akita Port. The seabed is liquefied after the 1983 Nihonkai–chubu earthquake (Sumer, 2014a).

Typically, in conventional geotechnical soil modelling, simplified wave pressure fields derived from analytical wave theories are applied on top of the seabed. When structures with complicated geometry are present in the water such analytical expressions are not available. Better prediction can be achieved by using multi-physic numerical models, where the interaction between nonlinear waves and soil in the presence of the structure can be better solved by CFD simulations yielding accurate pressure distributions in the vicinity of the structure. Liu et al. (2007) made the first effort on investigating seabed response in waves using an integrated CFD approach. They applied a solver in the OpenFOAM® framework for two immiscible incompressible fluids (water and air) to produce a wave field with free surface. They also implemented a poro-elastic soil solver by discretizing the Biot's equations (Biot, 1941) in an finite-volume-method (FVM) manner for analyzing the seabed response. Tang et al. (2014) extended their work into an anisotropic model in the quasi-static form. However, these solvers in the quasi-static form did not consider the inertial force associated with the motion of the soil sediments. Meanwhile, more validation work is needed to fully validate these solvers in order to practically solve engineering problems. The present PhD

project aims to take a step forward in modeling the interaction between waves and soil around marine structures in order to predict the potential liquefaction risk. A more systematic toolbox is built including a consolidation analysis solver, anisotropic soil solvers in the quasi-static form and partial-dynamic forms, and a liquefaction module consisting of different liquefaction criteria. Applications of the toolbox in solving the wave-induced response around gravity-based offshore foundations and the rubble mound breakwater with submerged berms are also conducted in the present PhD work.

Another important fact that happens to the marine structures is scour. Scour is the removal of granular bed material due to hydrodynamic forces in the vicinity of marine structures (Sumer and Fredsøe, 2002). Marine structures such as offshore foundations and subsea pipelines are often located at a seabed consisting of mobile sediments. Due to the erosive action of waves and currents, local scour around foundations or below pipelines commonly occurs. Figure 1.2 shows that after the onset of scour, the scour hole is expanding along the length of the pipeline and causes pipeline suspension. The free hanging section sags into the scour hole and may also be subject to vortex induced vibration which causes fatigue of the free span and ultimately leads to pipeline failure. The present PhD study on scour prediction below marine pipelines utilizes a fully-coupled hydrodynamic and morphologic scour model (Jacobsen, 2011; Jacobsen and Fredsoe, 2014) based on RANS equations coupled with the $k-\omega$ turbulence closure .

Extensive studies have been performed to predict the scour around a single submarine pipeline in the open literature, though pipelines may also be laid in tandem. In such tandem arrangements, in addition to the usual environmental loads, the spacing between multiple pipelines can also affect the resulting flow and scour patterns. The present PhD study utilizes the aforementioned scour model (Jacobsen, 2011; Jacobsen and Fredsoe, 2014) to investigate the wave-plus-current induced scour beneath two submarine pipelines in tandem. Environmental conditions involving the pure-wave condition, the waves plus

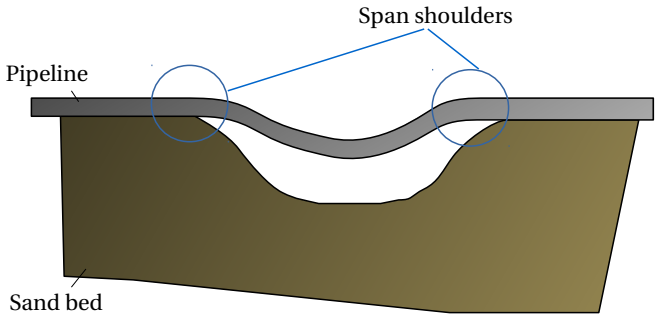

Figure 1.2 Sketch of pipeline suspension due to scour.

a low-strength current condition, and the condition of waves plus a current with equal strength to the wave-induced flow are simulated. Also, the effects of KC number, relative current strength and horizontal gap ratio on scour beneath two submarine pipelines are investigated.

In fact, previous studies have been focused on understanding scour and liquefaction in a separate manner. However, evidence shows that the processes of scour and liquefaction can be closely related. In the experiment of Sumer et al. (2007), they observed the occurrence of liquefaction, compaction and scour around a monopile in sequence in the same experiment. Sumer et al. (2006) conducted experiments to understand the sequence of sediment behaviour during wave-induced liquefaction in the soil. They found that the sand ripples started to emerge after the liquefaction and compaction process. This implies that scour does not occur during the liquefaction process since the liquefied fluid-sediment mixture does not have a repose angle. Therefore, it is not feasible to model the scour process of liquefying sand bed. However, scour can happen in the condition with seepage flows induced by high upward hydraulic gradients in the seabed without reaching the liquefaction threshold. In the present PhD study, a numerical model of scour beneath subsea structures with considering the effect of upward seepage in the seabed is proposed. The seepage velocity inside the porous seabed is usually small

compared to the free-stream velocity (Lu et al., 2008), so that it can have a minor effect to the free-stream velocity field. However, a small seepage can have a significant change to the hydrodynamic force on the bed surface and the stability of bed particles, which can further affect sediment transport processes and scour patterns around subsea structures. New scour profiles due to the incoming flow and the effect of the upward seepage will emerge. The equilibrium scour depth and scour width with upward seepage can be different from that without upward seepage.

1.2 Thesis overview

The present PhD project consists of three main parts:

- The modeling of wave-induced seabed response and liquefaction around offshore and coastal structures, in which the structures are mainly the gravity-based foundations and the breakwater.
- The modeling of scour beneath marine structures, in which the structures are mainly the submarine pipelines.
- The coupling of scour beneath marine structures with upward seepage in the seabed, in which this new model is applied to submarine pipelines.

The structure of the thesis is presented in Figure 1.3 and described as follows.

Chapter 2: The second chapter provides a review of previous work, in terms of the study of wave-induced seabed response and liquefaction analysis around marine structures and the study of scour beneath submarine pipelines. The investigation approaches of wave-induced seabed response are mainly in three forms: experimental study, theoretical modeling and numerical modeling. The study of scour are mainly in the forms of empirical modeling based on experimental data and numerical modeling based on potential flow theory or

turbulent models. The review of scour beneath marine pipelines includes both two-dimensional (2D) studies and three-dimensional (3D) studies, from the onset of scour, tunnel and lee-wake erosion to the 3D development of scour hole along the pipeline. Based on the review of previous studies, research questions, in alignment with the research objectives, are raised.

Chapter 3: The third chapter presents the modeling of wave-structure-seabed interaction and the prediction of momentary liquefaction around gravity-based offshore foundations. In this chapter, the first section presents the validation and applications of the anisotropic quasi-static Biot's consolidation model developed in FVM-based OpenFOAM framework by Tang (2014). The second section presents an extended study using the same model to investigate the effects of slab geometry and wave direction on liquefaction around gravity-based foundations. The third section presents an application of the investigation on the role of submerged berms on the momentary liquefaction around conventional rubble mound breakwaters.

Chapter 4: Apart from the quasi-static Biot's consolidation model, the partial-dynamic form (u-p approximation form) of the poro-elastic soil model is also developed in this PhD work. The fourth chapter presents the model development, validation and application of the anisotropic partial-dynamic soil model. An open-source wave-structure-seabed interaction (WSSI) toolbox is described. A systematic study of wave-induced seabed response around offshore structures including the consolidation analysis, wave-structure-seabed interaction analysis and liquefaction analysis is presented in this chapter.

Chapter 5: The fifth chapter presents a study of scour beneath marine pipelines. 2D local scour beneath two submarine pipelines in tandem under wave-plus-current conditions is investigated. Effects of horizontal gap ratios (the horizontal gap distance between two pipelines divided by the pipeline diameter) ranging from 1 to 4 are investigated. In this chapter, the scour is

modelled by using the fully-coupled hydrodynamic and morphologic model developed in Jacobsen (2011) and Jacobsen and Fredsoe (2014).

Chapter 6: The sixth chapter presents the modeling of scour beneath the marine structures considering the effect of upward seepage. The mathematical derivation of the model is presented. The numerical model is implemented based on the fully-coupled hydrodynamic and morphologic model described in Chapter 5. The model is validated against existing experiments and applied to investigate the scour development beneath a submarine pipeline subjected to different upward hydraulic gradients.

Chapter 7: In the last chapter, conclusions, original contributions to the PhD project and the recommendations for future work are presented.

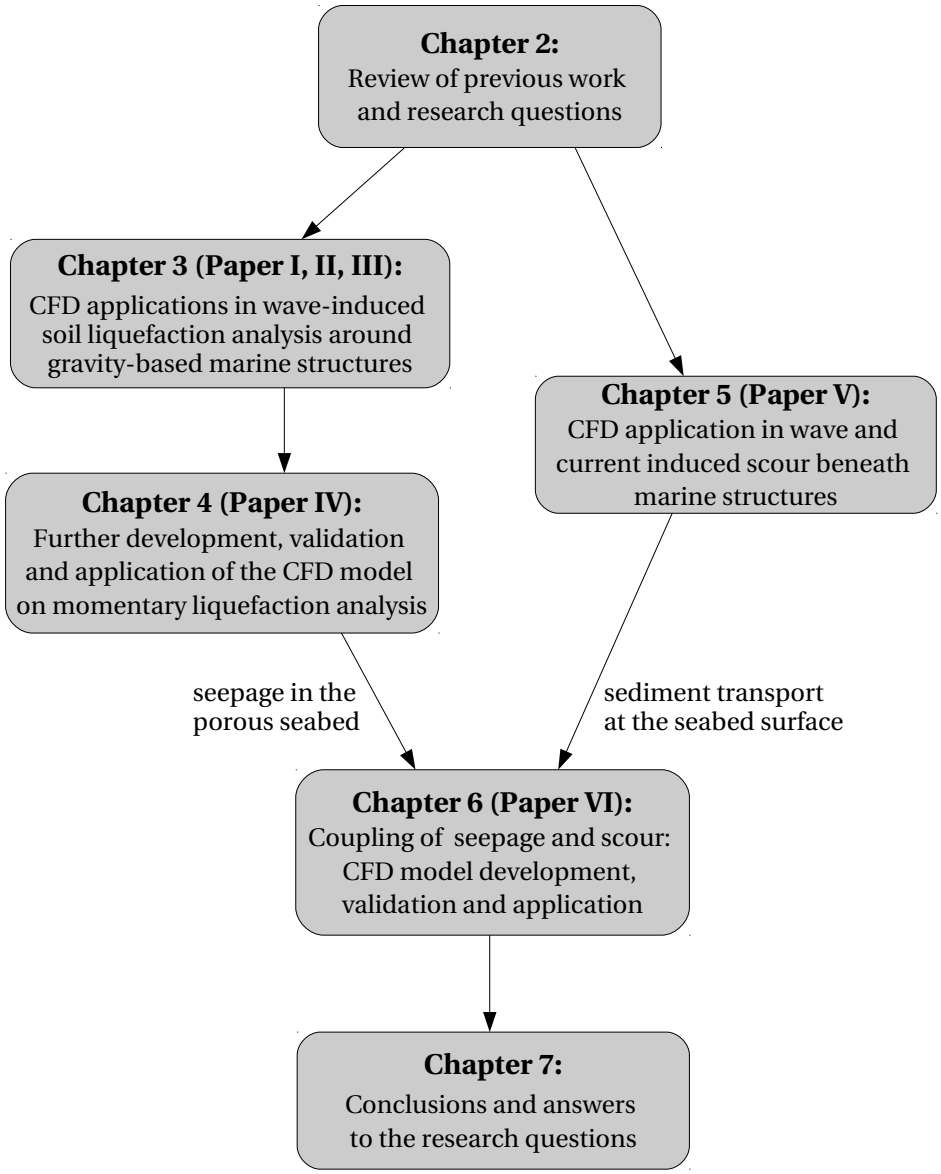

Figure 1.3 Structure of the present thesis.

Chapter 2

Review of previous work

2.1 Wave-induced seabed response and liquefaction

During the past several decades, investigations on the wave-induced seabed response are mainly in three forms: experimental study, theoretical modeling and numerical modeling.

2.1.1 Experimental study

The experimental study of the wave-induced soil response including wave tank tests and centrifuge tests. The wave tank tests have been widely conducted by coastal engineers. For example, Tsai and Lee (1995) conducted experiments in a wave flume of standing waves induced pore pressure in the sand bed in the vicinity of a vertical wall. The sand was in medium firmness and showed a poro-elastic behavior. Sumer et al. (1999) conducted experimental study on the process of sinking and floatation of a pipeline in a silt bed in progressive waves. The pore pressure build-up in the soil beneath the pipeline was measured. Teh et al. (2003) studied the behavior of submarine pipelines on a liquefied seabed. They observed that the build-up pore pressure

rate was not affected by the soil depth before liquefaction. However, as the liquefaction occurred, the pore pressure build-up rate near to the bottom of the soil layers was reduced. Chowdhury et al. (2006) preformed momentary liquefaction tests of the sand bed in waves. They found that the degree of saturation is an important factor for the pore pressure attenuation and the phase lag. Kudella et al. (2006a) performed large-scale model tests in a wave flume on the pore pressure build-up beneath a breakwater. They observed significant residual pore pressure in the soil which was induced by the caisson motions under breaking wave loads. Sumer et al. (2012) validated an analytical model for predicting the seabed liquefaction under waves based on experimental tests. The process of pore pressure build-up and resulting soil liquefaction under progressive waves were discussed. Kirca et al. (2013) performed laboratory tests on seabed liquefaction beneath standing waves. Their experimental results implied that the seabed liquefaction under standing waves had different features from that caused by progressive waves. The pore pressure were built up in the areas around the standing wave nodes and subsequently spread out towards the antinodes.

The centrifuge test is an alternative approach for physical modeling of the soil response in waves. However, it is more difficult to conduct than the wave tank test. The usage of centrifuge test was first proposed by Phillips (1869). An increased gravitational acceleration was applied in the centrifuge to produce identical self-weight stresses to that in real scales (Sekiguchi and Phillips, 1991). An important work on applying the centrifuge technique to investigate the wave-induced seabed liquefaction was Sassa and Sekiguchi (1999). Nevertheless, the challenges such as sample preparation and well-controlled wave generation still remain to be tackled for using the centrifuge facilities. Sumer (2014a) has conducted a non-dimensional comparison between the centrifuge wave tank test (Sassa and Sekiguchi, 1999) and the standard wave flume test (Sumer et al., 2006) to investigate the residual liquefaction. The results showed a reasonably good agreement. The comparison

study implied that standard wave flume tests are feasible for investigating the buildup of pore pressure and residual liquefaction if the results are analyzed in a non-dimensional manner.

2.1.2 Theoretical modeling

During the past several decades, various theoretical models for predicting the wave-induced seabed response have been proposed using different assumptions. For the seabed soil, the interaction between the pore fluid phase and the solid phase makes it difficult to evaluate the seabed response using classical single-phase models. Biot (1941) first proposed the poro-elasticity theory (Biot's consolidation model) for wave-induced seabed response modeling. The model has been commonly used until today as it describes porous seabed including coupling between the pore fluid motion and the soil motion. Yamamoto et al. (1978) derived an analytical solution to Biot's consolidation model in the infinite seabed. The solution was further extended to layered inhomogeneous seabed later (Yamamoto, 1981). Madsen (1978) also obtained analytical solutions to the poro-elasticity equations established by Biot (1941). They applied Biot's consolidation model to a hydraulically anisotropic and partially saturated seabed. Later, Jeng and Seymour (1997) extended Biot's consolidation model to investigate the soil with finite depth. Hsu and Jeng (1994a) extended the model to investigate the anisotropic soil with finite depth in a homogeneously unsaturated condition.

However, Biot's consolidation model does not consider the accelerations due to pore fluid and soil motions. Therefore, this model is also known as the quasi-static model. Zienkiewicz et al. (1980) first extended Biot's consolidation model (Biot, 1956) to a 1D partial-dynamic form with the consideration of the acceleration of the soil skeleton. The 1D form of Zienkiewicz et al. (1980) was further extended to 2D by Jeng and Rahman (2000). In the work of Ulker et al. (2009b) and Ulker et al. (2010), three forms of the Biot's poro-elastic soil model were discussed, in terms of the quasi-static form, the

partial-dynamic form (i.e., the $u-p$ formulation), and the fully-dynamic form. The difference between the forms is based on the consideration of including inertial terms associated with the motion of fluids and solids. The fully-dynamic Biot's model contains the terms associated with the acceleration of the soil and relative acceleration of the fluid compared to the soil. However, it was reported that the fully-dynamic solution could provide a good prediction but the solutions were lengthy and difficult to be applied in engineering practice, as discussed in the work of Jeng and Rahman (2001) and Jeng and Cha (2003).

Besides linear poro-elastic models, advanced soil models such as the poro-elastoplastic model have also been developed, such as in Sassa and Sekiguchi (1999), Sassa and Sekiguchi (2001) and Sekiguchi et al. (1995). The poro-elastoplastic models can provide a better prediction on the soil with large deformation. However, these exact analytic solutions of wave-induced seabed response had very limited applications to offshore engineering problems. In the theoretical models, the presence of the structure was usually not considered and the wave models were usually over-simplified. Therefore, they cannot deal with the situation of the interaction between nonlinear waves and the seabed in the presence of offshore structures in the real offshore environment.

2.1.3 Numerical modeling

In recent years, with the rapid development of computer capabilities, numerical modeling approach has been applied in a large number of studies on wave-induced seabed response problems. With numerical modeling, a complete Navior-Stokes hydrodynamic model can be solved in order to provide a realistic picture of the dynamic waves interacting with the structure and the soil. The advantage of using numerical modeling approach on wave-induced seabed response problems is also attributed to its multi-physic modeling capability. Integrated models of such problems should incorporate multiple

physical domains including the fluid domain of waves and the solid domain(s) of the seabed (and the structure). To date, most of the numerical studies in the open literature followed the manner of using the volume of fluid (VOF) method or boundary element method (BEM) to solve the wave domain and a separate code or software based on the finite element method (FEM) or finite difference method (FDM) to solve the soil domain (Jeng et al., 2013a; Sui et al., 2016; Ye, 2012b; Zhang et al., 2015). For example, Jeng et al. (2013a) proposed a model for the wave-induced seabed response around marine structures. In their work, the VOF method is applied to model the waves and the FEM is applied for the soil analysis. Jeng (2012) reviewed the numerical methods for wave-seabed interaction in terms of FDM (Zen and Yamazaki, 1990a,b), FEM (Gatmiri, 1990; Jeng and Hsu, 1996; Jeng and Lin, 2000; Okusa, 1985) and BEM (Raman-Nair et al., 1991), respectively. Among them, the FEM method has been most commonly used.

In recent years, with the development of open-source software, the finite-volume-method (FVM) -based OpenFOAM becomes a platform for multi-physic solver development. Using the same numerical method within the same framework, the time and computational memory required by the data exchange between different physical domains can be reduced. Liu et al. (2007) first discretized the Biot's equations in an FVM manner by using the framework of OpenFOAM. Tang et al. (2014) implemented a three-dimensional FVM-based anisotropic poro-elastic Biot's model in the quasi-static form.The quasi-static anisotropic poro-elastic solver by Tang et al. (2014) was validated and applied in the work of Li et al. (2018) in which the anisotropic consideration was proved to be practical for modeling the seabed of medium and coarse sand. Plasticity modeling of the soil in OpenFOAM is also seen in the literature. Tang et al. (2015) implemented an FVM-based code of poro-elasto-plasticity soil model. The model was built based on the Biot's consolidation theory and combined with a perfect plasticity Mohr-Coulomb

constitutive relation. Elsafti and Oumeraci (2016a) implemented a multi-yield surface plasticity model to simulate plastic soil response under cyclic loads.

The numerical modeling approach has been widely taken in the study of wave-induced seabed response, still, careful validations and verifications of the numerical models are always essential. For a long time, the wave-structure-seabed interaction models developed in the previous work can only be validated against the experiments of wave-soil interaction experiments excluding the structure. Recently, Qi and Gao (2014) performed a series of experiments to investigate the local scour and pore pressure in the seabed around a large-diameter monopile in the conditions of pure wave, pure current and combined waves and current. However, in the paper of Qi and Gao (2014), the experimental data of the pore pressure around the monopile under wave-only condition were not presented. Through personal contact with Qi (2018), the unpublished data of pore pressure around the monopile under wave-only conditions were allowed to be processed and presented in the present PhD work to validate the model of wave-induced seabed response around offshore structures developed in the FVM-based OpenFOAM framework.

2.2 Scour beneath submarine pipelines

The scour processes beneath a pipeline can be divided into a series of mechanisms including the onset of scour, the tunnel and lee-wake erosion, and scour development along the pipeline (Fredsøe, 2016; Sumer and Fredsøe, 2002). The onset of scour and the tunnel and lee-wake erosion are commonly studied in a 2D manner, while the scour development along the pipeline is usually modeled in a 3D manner. The study approaches of scour beneath submarine pipelines are mainly in the forms of empirical modeling based on experimental data and numerical modeling based on potential flow theory or turbulent models. The following review will cover these forms of approaches in each scour process.

2.2.1 Onset of scour

2D studies on scour considered the situation that a steady flow meets the pipeline perpendicularly. The pipeline laid on the sediment bed subjected to incoming flows causes a pressure difference between the upstream stagnation pressure and the lower pressure in the lee-side wake. Therefore, a seepage flow in the sand bed can be induced underneath the pipeline and piping may occur. Chiew (1990) did experimental study on the scour process initiated by piping. He measured the pressure gradient around the pipe and confirmed that the threshold of onset of scour below the pipe is when the hydraulic gradient in the sediment exceeds the critical value of $i_c = (1-n)(s-1)$, where n is the porosity and s is the relative density of the sediment to the fluid. Sumer et al. (2001) did similar experimental tests and confirmed that the excessive seepage flow induced piping is the reason to cause the onset of scour below the pipeline. In terms of numerical modeling, Zang et al. (2009) performed numerical investigations on the onset of scour considering different initial embeded depth of the pipeline using a $k-\omega$ turbulence closure. They proposed a onset condition for waves and steady currents. The effects of Reynolds number (Re) and Keuleagan–Carpenter number (KC) on the pressure drop between the upstream and downstream of the pipeline were evaluated. Similarly, Gao and Luo (2010) conducted numerical studies with a finite-element method (FEM) model on the initiation of scour for pipeline partially-embedded in a sandy seabed. They found that the critical flow velocity for the initiation of scour has an approximately linear relationship with the soil internal friction angle.

2.2.2 Tunnel and lee-wake erosion

The onset of scour is followed by the process of tunnel erosion where the flow velocity beneath the pipe is higher than the undisturbed flow due to flow contraction (Hansen et al., 1986; Sumer and Fredsøe, 2002). The amplified

bed stress causes tremendous sediment transport and the gap between the pipe and the sand bed increases. The stage of tunnel erosion is followed by the so-called lee-wake erosion. When the gap between the pipeline and the bed reaches approximately 5–10% of the pipe diameter (Sumer et al., 1988), the vortex shedding will begin to occur. Finally, the scour will reach a steady equilibrium stage where the bed shear stress underneath the pipe becomes constant and equal to its undisturbed value. Extensive studies have been performed to investigate the process of tunnel and lee-wake erosion below pipelines and the equilibrium scour depth and profiles in steady currents, waves and combined waves and current, respectively.

2.2.2.1 Scour in steady currents

For scour in steady currents, Mao (1986) performed a series of experiments involving scour beneath pipelines under a variety of current velocities. It was found that the equilibrium scour depth divided by the pipeline diameter S_e/D is a weakly varying function of the Shields parameters θ for the live bed scour. An empirical formula for the equilibrium scour depth based on Mao (1986)'s experimental measurement was established by Sumer and Fredsøe (2002). In the clear-water regime, the variation in scour depth with θ was large, and therefore no simple formula exists. In the live-bed regime, the empirical relation is expressed as

$$S_e/D = 0.6 \pm \sigma \tag{2.1}$$

where D is the pipeline diameter and $\sigma = 0.2$ is the standard deviation (Sumer and Fredsøe, 2002). Zhang et al. (2017) carried out a series of experiments involving scour beneath two tandem pipelines in steady currents with horizontal gap distance between the two pipelines ranging from 0 to $5.9D$. They found that for horizontal gap distance between 0 and $3D$, the equilibrium scour depth beneath the downstream pipeline was slightly larger than that

upstream. However, for larger horizontal gap distance between $3D$ to $5.9D$, the equilibrium scour depth beneath the downstream pipeline was slightly smaller than that upstream. Their results also showed that the time scale of scour beneath the downstream pipeline was generally larger (by up to a factor 4) than that for the upstream pipeline.

In addition to experimental studies, early attempts on numerically modelling the scour beneath pipelines were based on potential flow theory. Hansen et al. (1986) and Fredsøe and Hansen (1987) modified the potential flow theory by adding a vortex tube to ensure a more correct description of the flow beneath the pipe. The modified potential flow theory can well predict the final scour hole depth beneath the pipe. The studies of Chao and Hennessy (1972), Chiew (1991) and Li and Cheng (1999) can also predict the final scour depth and the upstream slope. However, the potential flow theory cannot capture the flow separation and formation of lee-wake vortices. Therefore, the downstream slope cannot be predicted (Sumer and Fredsøe, 2002). More recent attempts at the numerical modelling of scour beneath submarine pipelines have been based on the complete Navier-Stokes equations, with turbulence modelling in the form of either Reynolds-averaged formulations or Large Eddy Simulations (LES). Li and Cheng (2000, 2001) have used LES to model the local scour beneath a pipeline. Their studies modeled the scour development using local amplification of the bed shear stress. Such models do not require any empirical equations for the bed load sediment transport or suspended load transport, but they did not model the sediment transport process. Brørs (1999) used a $k-\varepsilon$ turbulence model to solve the Reynolds-averaged Navier-Stokes (RANS) equations and established a numerical model to describe the flow, sediment transport and morphology in steady currents. Liang et al. (2005) compared a $k-\varepsilon$ turbulence model with LES. They found that both turbulence models provided good results, while the $k-\varepsilon$ turbulence model performed better. Lee et al. (2016) developed a two-phase model for simulating sediment transport in the sheet flow condition.

The $k-\varepsilon$ turbulence model was adopted in their work for computing the Reynolds stresses. They found that for pipeline scour, the predicted scour rate beneath the pipeline agreed well with the experiment. However, they reported that the model could not capture the vortex shedding so that the sediment deposition behind the pipeline was overestimated. Mathieu et al. (2018) compared the $k-\varepsilon$ turbulence model and the $k-\omega$ model proposed by Wilcox (2006, 2008) for predicting scour beneath a pipeline using a two-phase flow sediment transport model, they concluded that using the $k-\omega$ turbulence model can provide more accurate numerical predictions of the lee-wake erosion than using the $k-\varepsilon$ turbulence model. The $k-\omega$ SST (shear–stress transport) model by Menter (1994) has also been employed to close the RANS in some recent works. Menter (1994) found that $k-\omega$ SST provided better results in flows with strong adverse pressure gradients. Zhao et al. (2015) performed numerical studies of local scour around two pipelines in tandem in steady currents using an FEM numerical model with the $k-\omega$ SST turbulence closure. They also studied the local scour below pipeline with piggyback in steady currents in Zhao and Cheng (2008) using the same turbulence model.

2.2.2.2 Scour in oscillatory Flow

For scour in waves, Sumer and Fredsøe (1990) investigated the variation of the scour depth with the Keulegan–Carpenter number (KC). In the live-bed regime, experimental results were fitted with the empirical equation expressed as

$$S_e/D = 0.1\sqrt{KC} \tag{2.2}$$

Liang and Cheng (2005) carried out a numerical study of scour in waves and used a $k-\omega$ turbulence model for closure. Fuhrman et al. (2014) likewise used a $k-\omega$ turbulence model (Wilcox, 2006, 2008) to solve the unsteady RANS equations and simulated both the scour development, as well as back-filling, that occurs for various KC. Kazeminezhad et al. (2011) used an

Eulerian two-phase flow model to investigate the wave-induced tunnel scour beneath pipelines. The model was based on the Euler-Euler coupled governing equations for both the fluid and the sediment phases. A modified $k-\varepsilon$ turbulence closure was utilized for solving the fluid phase.

2.2.2.3 Scour in waves plus current

In the case of combined waves and current, Sumer and Fredsøe (1996) conducted experiments covering a wide range of KC and the relative current strength m. m is defined by

$$m = \frac{U_c}{U_c + U_m} \tag{2.3}$$

where U_m is the near-bed orbital velocity amplitude of the oscillating flow and U_c is the current velocity at the center of the pipeline. With this definition $m = 0$ corresponds to a pure-wave condition and $m = 1$ corresponds to a pure-current condition. It was found that the scour depth may increase or decrease in wave-plus-current conditions relative to pure-wave conditions, depending on both KC and m. They also found that when $m > 0.7$ (i.e. strong currents), the equilibrium scour depth S_e/D is the same as in the current-alone case. An empirical relation for the equilibrium scour depth in combined waves and current was proposed in Sumer and Fredsøe (1996) which fitted well with the experimental data:

$$S_e = S_c F \tag{2.4}$$

where S_c is the equilibrium scour depth in the pure current ($S_c/D = 0.6 \pm 0.2$). F is calculated by

$$F = \begin{cases} \frac{5}{3}(KC)^{a_m}\exp(2.3b_m), & 0 \le m \le 0.7 \\ 1, & m \ge 0.7 \end{cases} \tag{2.5}$$

where

$$a_m = \begin{cases} 0.557 - 0.912(m-0.25)^2, & 0 \leq m \leq 0.4 \\ -2.14m + 1.46, & 0.4 \leq m \leq 0.7 \end{cases} \tag{2.6}$$

$$b_m = \begin{cases} -1.14 + 2.24(m-0.25)^2, & 0 \leq m \leq 0.4 \\ 3.3m - 2.5, & 0.4 \leq m \leq 0.7 \end{cases} \tag{2.7}$$

Larsen et al. (2016) simulated the scour below a pipeline in wave-plus-current conditions with the same model as in Fuhrman et al. (2014). In their work, similar trends as seen in Sumer and Fredsøe (1996) were obtained for the variation of the equilibrium scour depth with the relative current strength m. Based on the numerical results, they also suggested an expression for the timescale in the wave-plus-current conditions:

$$T^* = \Gamma(m)\theta_{cw}^{-\frac{5}{3}} \tag{2.8}$$

$$\Gamma(m) = \frac{1}{50} + 0.015\left(e^{-350(m-0.5)^2} + e^{-25(m-0.53)^2}\right) \tag{2.9}$$

where θ_{cw} is the Shields parameter in the combined waves and current condition.

2.2.3 3D development of scour hole along the pipeline

After the onset of scour, the scour hole occurs occasionally along the pipeline in the spanwise direction and propagates along the pipeline. As the scour hole length along the pipeline becomes sufficiently long, the pipeline starts to sag down into the scour hole, as shown previously in Figure 1.2. The sinking velocity of the pipeline into the scour hole is affected by the spreading speed of the scour hole (Fredsøe, 2016). Researchers have made efforts on investigating the spreading rate of scour along the pipe. However, to date, there is no definitive answers to the problem. Gravesen and Fredsøe (1983) discussed the time scale for the spread of scour hole. They claimed that when the pipeline touched the bottom of the scour hole, it blocked the flow

and led to the backfilling and self-burying process. Fredsoe et al. (1988) did a further investigation on the 3D scour below pipelines. They found that when the sinking pipe touched the bottom of the scour hole, it will prevent the scour hole from further development and the long span will transform into two small free spans at each side between the touched down points and the span shoulders. Their model suggested a maximum length for the free span development. Hansen et al. (1991) studied the spanwise development of scour hole with various initial embedment depths. They observed that as the embedment of the pipeline at the shoulders increased, the rate of free-span development decreased. They also proposed a semi-empirical model for predicting the spreading rate of the scour along the pipeline in the steady current:

$$c = \frac{1}{-eD}\frac{dV}{dt} \tag{2.10}$$

where c is the erosion rate along the pipeline, e is the embedment depth of pipeline, D is the pipeline diameter, dV/dt is the volumetric rate of sediment transport. In addition, Sumer and Fredsøe (1993) did experiments on the span development below a pipeline. They observed that the pipeline stopped sinking into the scour hole when it sank to a level where is was protected against the flow. After the pipeline stopped sinking, backfilling process started. A more detailed 3D study of scour below the pipeline in steady currents was performed by Cheng et al. (2009). They measured the scour spreading velocity along the pipeline after the initiation of the scour. Two phases of scour rates was observed. At the beginning stage, the strong 3D flows amplified the bed shear stress and the initial scour propagating rate was high. At a later stage, both the scour length and the scour width increased, the scour propagating rate slowed down and the flow structure beneath the pipeline became more 2D. Cheng et al. (2014) extended their experimental studies in wave-only and combined wave and current conditions. They found that the scour propagation rate c increases with KC in a way similar to the 2D scour cases. Wu and Chiew (2012, 2013, 2014) conducted a series of

experiments to study the mechanics of three-dimensional pipeline scour. Wu and Chiew (2012, 2013) studied the scour spreading rate in the clear-water condition. Similar to the finding of Cheng et al. (2009), they observed the spreading rate decreased with an increasing embedment. They also found that the spreading rate increased with a decreasing water depth. In the study of Wu and Chiew (2014), they performed a further investigation on how the pressure difference between the upstream and downstream parts of the pipeline affected the scour propagation rate in the spanwise direction. They concluded that both the two factors, i.e., the differential pressure and the local bed shear stress affected the propagation rate of the scour hole along the pipeline in the spanwise direction.

As for 3D modeling of the scour along the pipeline, Bernetti et al. (1990) is considered as the first to propose a simple theoretical model for the scour spreading along the pipeline. Their assumption of a constant slope which was equal to the repose angle of the sediment has been confirmed by the experiment of Cheng et al. (2009). However, their model did not consider the self-burial process which can slow down the spreading rate. Hansen et al. (1995, 1991) made further effort on the simple computational model for lateral spreading of scour. They found that the downstream side of the pipeline had a faster scour spreading rate than the upstream side, which was also observed in Cheng et al. (2009) later on. Chen and Cheng (2001) performed 3D modeling of laminar flow around free span shoulders of the pipeline. A spiral type of vortex tube was found around the span shoulders. However, the scour profile in the perpendicular direction of the pipe was simplified as a horizontal bed. Chen and Cheng (2004) extended their study to turbulent flow cases. They solved the 3D Navier-Stokes equations using a Smagorinsky SGS (subgrid-scale) turbulence closure. The model was able to simulate the complicated near-shoulder flow pattern. However, it remained to be validated by experiments. Cheng and Zhao (2010) established a 3D numerical model for simulating scour below a pipeline. The 3D flow was

simulated by using the finite element model developed by Zhao et al. (2009). They found that in the middle section of the free span, the scour pattern is similar to that observed in the 2D experiments and numerical simulations in previous studies. The predicted spreading rate of scour hole along the pipeline was lower than that measured in the laboratory tests.

In fact, even though scour below submarine pipelines contains 3D features, much can be learned from empirical equations and numerical models in 2D studies (Fredsøe, 2016; Sumer, 2007).

2.3 Research questions

Based on discussions in the previous studies, the research questions, in alignment with the research objectives, are raised as follows.

Q1 How to validate the integrated finite-volume (FV) wave-structure-seabed interaction (WSSI) model based on existing experimental data before applying the model to engineering practice?

Q2 Wave-induced soil response around monopile foundations has been extensively investigated in the previous studies. However, the wave-induced soil response around gravity-based offshore foundations of more complex geometries has not been investigated. What is the procedure of investigating the wave-induced soil response around gravity-based offshore foundations?

Q3 How will the geometry of the gravity-based foundations and the incoming wave directions affect the wave field, soil response and liquefaction risk in the vicinity of the foundation?

Q4 Apart from the offshore foundations, previous research studies of wave-structure-seabed interaction have also been focused on coastal structures such as rubble mound breakwaters. The deployment of submerged

berms at the toe of conventional rubble mound breakwaters can be effective in improving the stability of the armor layer and reducing the probability of scour occurrences. Can the berms also reduce the liquefaction risk around breakwaters under dynamic wave loading?

Q5 There are different forms of poro-elastic soil models and also various liquefaction criteria proposed in the open literature. Which form of the soil model and which liquefaction criteria should we choose for better predicting the soil response and momentary liquefaction risk around gravity-based structures?

Q6 Extensive studies have been performed to predict the scour around a single submarine pipeline, though pipelines may also be laid in tandem. In such tandem arrangements, how will the environmental loads and the spacing between two pipelines affect the resulting flow and scour patterns?

Q7 When modeling scour beneath subsea structures, previous studies commonly regarded the seabed as an impermeable wall and the effect of seepage flow in the seabed on the mobility of bed particles was ignored. In fact, the seabed soil is a porous medium and the seepage flows can exist in the porous seabed. Therefore, how to model the interaction between sediment transport and upward seepage in the seabed?

Q8 How will upward seepage inside the seabed affect scour patterns around marine pipelines?

The research questions raised above will be addressed in this thesis. In the following chapters,

- Question 1 will be addressed in Chapter 3 – Paper I and Chapter 4 – Paper IV;
- Question 2 will be addressed in Chapter 3 – Paper I and Chapter 4 – Paper IV;

- Question 3 will be addressed in Chapter 3 – Paper II;
- Question 4 will be addressed in Chapter 3 – Paper III;
- Question 5 will be addressed in Chapter 4 – Paper IV;
- Question 6 will be addressed in Chapter 5 – Paper V;
- Questions 7 and 8 will be addressed in Chapter 6 – Paper VI.

The answers to these research questions will be summarized again in the conclusion part in Chapter 7.

Chapter 3

Momentary liquefaction around gravity-based structures

This chapter presents three papers on the applications of the wave-structure-seabed interaction model in the prediction of seabed response and momentary liquefaction around gravity-based structures. For each paper, consolidation analysis in the presence of the structures are performed. The first section is a published paper on the modeling of wave-structure-seabed interaction and the prediction of momentary liquefaction around a hexagonal gravity-based offshore foundation. The anisotropic quasi-static Biot's consolidation model developed in FVM-based OpenFOAM® framework is validated. A parametric study with different wave heights and a sensitivity study with isotropic and anisotropic soil properties are presented. The second section and the third section present two papers using the same model on the investigations of seabed response and momentary liquefaction around gravity-based offshore foundations and rubble mound breakwaters. The paper in the second section investigates the effects of slab geometries and wave directions on liquefaction patterns around the foundation. The paper in the third section investigates the effects of submerged berms on liquefaction patterns around the rubble mound breakwaters.

3.1 Paper I: Numerical analysis of wave-induced poro-elastic seabed response around a hexagonal gravity-based offshore foundation

Yuzhu Li[a], Muk Chen Ong[a], Tian Tang[b]
[a] Department of Mechanical and Structural Engineering and Materials Science, University of Stavanger, N-4036 Stavanger, Norway
[b] Bekaert Technology Center, Deerlijk, 8540, Belgium

Abstract*: In order to prevent the future risk of soil and structural failures for the offshore foundations, it is essential to evaluate the seabed soil behaviors in the vicinity of the foundation under dynamic wave loadings. The objective of this paper is to investigate the wave-induced soil response and liquefaction risk around a hexagonal gravity-based offshore foundation. Three-dimensional (3D) numerical analysis is performed by applying an integrated multi-physic model developed in the finite volume method (FVM) based OpenFOAM framework. The integrated model incorporates solvers of the nonlinear waves, the linear elastic structure and the anisotropic poro-elastic seabed soil. The free surface model and soil model are verified by grid convergence studies. The wave-induced soil response model is validated by reproducing a laboratory experiment and a good agreement is obtained.

Distributions of wave-induced shear stress, pore pressure, vertical displacement and seepage flow structure in the seabed are investigated. It is found that the presence of the foundation significantly amplifies the wave-induced shearing effect and vertical displacement in the underlying seabed soil. Seabed consolidation state in the presence of the structure is evaluated. Since the foundation is embedded in the seabed at a depth, the vertices of the hexagonal foundation cause the stress concentration in the nearby soil during the consolidation process. Therefore, the momentary liquefaction at

*This is a journal paper published in Coastal Engineering 136 (2018): 81-95.

the vertices is not as significant as that at the edges due to the high initial effective stress. A parametric study with different wave heights is conducted to examine the changes of soil response and momentary liquefaction depth around the hexagonal foundation. Effects of isotropic and anisotropic soil permeability on the pore pressure distribution are investigated. It shows that the effect of anisotropic permeability should be considered for the medium sand that is modelled in the present study.

keywords: wave-structure-seabed interaction; gravity-based offshore foundation; hexagonal foundation; momentary liquefaction

3.1.1 Introduction

The last two decades have seen tremendous increase of offshore structures, which brings great attention to the engineers and researchers to assess the structure foundation stability in the seabed under dynamic wave loadings. The interaction between waves, structure and soil has become a critical topic for preventing future offshore structure failures due to geotechnical nature. Nevertheless, accurate assessment of the wave-induced pore pressure and soil displacements has been a challenging task, mainly due to the complexity of the external dynamic wave loadings and the seabed material itself.

In the previous research, efforts have been made to model wave-structure-seabed interaction numerically. Some of the works concentrate on modeling the wave effect accurately but oversimplified the soil model of the seabed. For example, Chen et al. (2014) built a numerical model of wave-structure interaction with simplifying the seabed as solid wall conditions. Ong et al. (2013) performed the dynamic analysis of an offshore monopile wind turbine by simplifying the soil model as nonlinear springs with stiffness properties. Other works employed more accurate soil models with simplified wave models. For example, Sassa and Sekiguchi (2001) conducted finite element analyses of wave-induced liquefaction of sand beds, Geremew (2011) analyzed the

development of pore pressure in isotropic porous formation caused by wave-induced cyclic loading. In their works, the waves were simulated based on the linear wave assumption.

To date, the majority of numerical models on wave-structure-seabed interaction were limited to 2D studies, such as the model of wave-seabed-pipelines interaction (Luan et al., 2008) and wave-seabed-breakwater interaction (Ulker et al., 2010; Ye, 2012b). Few 3D numerical models for the wave-seabed-pipeline interactions have been conducted to investigate the influence of wave obliquity, while most of the studies were limited to linear wave loadings (Shabani et al., 2008; Zhang et al., 2011). In recent years, some 3D numerical studies have focused on wave-induced seabed response around monopile foundations (Chang and Jeng, 2014; Li et al., 2011; Sui et al., 2016; Zhang et al., 2015), but very limited literatures studied the wave-structure-seabed interaction of the hexagonal gravity-based foundation or other offshore foundations with more complex geometries.

Ye et al. (2013) proposed a 3D one-way coupled model for wave-seabed-breakwater interaction by employing finite volume method (FVM) for the wave model and finite element method (FEM) for the solid domains (i.e., soil and structure). To date, most of the 3D studies follow the traditional manner of using the FVM or boundary element method (BEM) to solve the waves and a separate code or software based on the FEM or finite difference method (FDM) to solve the soil domain. An external port was normally required for data exchange and time step update between two different numerical tools, which may incur a high usage of computational memory and low efficiency. Recently, Tang et al. (2015) developed a set of soil solvers based on FVM and established an integrated system for modeling the 3D wave-structure-seabed interaction incorporating all subdomains in the FVM-based OpenFOAM framework. Consequently, the usage of additional software or portal for data transfer between different numerical methods can be avoided. Lin et al. (2017) applied the integrated FVM-based wave-structure-seabed interaction model to

analyze the wave-induced dynamic seabed response surrounding the monopile foundation. A nonlinear wave model and a Biot's poro-elastic soil model were used in their work. However, the monopile foundation was assumed to be rigid and its response was not solved. Thus, the effect of wave-induced structure stress on the local seabed was not examined. Recently, Sui et al. (2017) and Zhao et al. (2017a) studied the wave-seabed-monopile interaction with considering the consolidation state. It shows that the assessment of soil consolidation behavior in the presence of marine structures is essential for the liquefaction analysis.

It should be noted that soil permeability has a significant effect on the pore pressure generation and liquefaction. Zhang et al. (2011) studied the anisotropic seabed response around a submarine pipeline in waves and current. Their numerical results presented significant effects of anisotropic soil behavior on the seabed liquefaction.

Considering all the factors mentioned above, the objective of the present work is to investigate the wave-induced soil response and liquefaction risk around a hexagonal gravity-based offshore foundation. The features in the present work are:

1) Proper wave theories of Stokes second-order and fifth-order waves are adopted to model the waves in a better accuracy based on the water depth and wave conditions.

2) A poro-elastic soil model is incorporated for the first approximation. The poro-elastic soil model adopted is to account for anisotropy, since most of the nature soils display some degree of anisotropy, i.e., having different elastic and hydraulic properties in different directions, according to Hsu and Jeng (1994a).

3) The foundation is considered as linear elastic and the effect of the wave-induced structural stress on the seabed is examined.

4) A parametric study with a series of wave heights is carried out to investigate the changes of soil response and the occurrence of the momentary liquefaction around the hexagonal foundation.

5) The interaction between the multiple physical domains is implemented by interface coupling and dynamic boundary data updating in an integrated FVM-based framework.

3.1.2 Mathematical models and the coupling algorithm

3.1.2.1 Free Surface Navier-Stokes Wave Model

The wave domain is governed by incompressible Navier-Stokes equations including the continuity equation and the momentum equations.

$$\nabla \cdot \mathbf{u} = 0 \tag{3.1}$$

$$\frac{\partial \mathbf{u}}{\partial t} + (\mathbf{u} \cdot \nabla)\mathbf{u} = -\frac{1}{\rho}\nabla p + \mathbf{g} + \frac{1}{\rho}\nabla \cdot \boldsymbol{\tau} \tag{3.2}$$

where $\mathbf{u}$ denotes the velocity vector with three components in x,y,and z direction respectively; $\mathbf{g}$ denotes the gravitational acceleration; ρ is the fluid density regarded as a constant for incompressible fluid; p is the pressure and $\boldsymbol{\tau}$ is the viscous stress tensor with Einstein notation of τ_{ij}. For Newtonian fluid,

$$\tau_{ij} = 2\mu\sigma_{ij} \tag{3.3}$$

where μ is the dynamic viscosity of fluid. σ_{ij} is defined by

$$\sigma_{ij} = \frac{1}{2}\left(\frac{\partial u_i}{\partial x_j} + \frac{\partial u_j}{\partial x_i}\right) \tag{3.4}$$

where $i, j \in$ [1,2,3]. u_i and u_j denote the velocity components in x, y and z direction respectively.

3.1.2.2 Keulegan-Carpenter Number

The Keulegan-Carpenter number (KC number) is relatively small for the present simulated condition, with a maximum KC number of 0.966. A small value of KC number indicates that the drag force which comes from the viscosity becomes negligible compared to inertial forces. The definition of the KC number is given in the equation below (Journée and Massie, 2000):

$$KC = \frac{u_a \cdot T}{D} \tag{3.5}$$

where T is the wave period and D is the diameter of the structure along the wave propagation direction. In sinusoidal waves, $u_a = \omega \cdot x_a$, in which x_a is the (horizontal) water displacement amplitude. In this work, the inertial force is dominant and the viscous effect is negligible due to the small KC number. Hence, turbulence modeling is not considered.

3.1.2.3 Linear Elastic Structure Model

The elastic structure domain is governed by a linear momentum balance equation and isotropic linear elastic strain-displacement relations:

$$\nabla \cdot \boldsymbol{\sigma} = \nabla \cdot [2\mu\boldsymbol{\varepsilon} + \lambda \mathrm{tr}(\boldsymbol{\varepsilon})\mathbf{I}] = 0 \tag{3.6}$$

$$\boldsymbol{\varepsilon} = 1/2(\nabla\mathbf{U} + \nabla\mathbf{U}^T) \tag{3.7}$$

where $\boldsymbol{\sigma}$ is the stress tensor; $\boldsymbol{\varepsilon}$ is the small strain tensor; $\mathbf{U}$ is the structural displacement vector consisting of three coupled components. μ and λ are the Lamé's coefficients of elastic material properties, relating to more commonly used Young's modulus E and Poisson's ratio ν.

In the FVM analysis, the coupling of the three displacement components U_x, U_y, U_z are handled by using the segregated strategy (Demirdžić and Martinović, 1993; Demirdžić and Muzaferija, 1994). Substitute Eqn. 3.7 into Eqn. 3.6 and the combined equation can be split into an implicit part and an

explicit part, shown in Eqn. 3.8.

$$\nabla \cdot [(2\mu + \lambda)\nabla \mathbf{U}] = -\nabla \cdot [\mu(\nabla \mathbf{U})^T + \lambda \mathbf{I} \mathrm{tr}(\nabla \mathbf{U}) - (\mu + \lambda)\nabla \mathbf{U}] \qquad (3.8)$$

The left hand side of the equation is the implicit part and the right hand side of the equation is the explicit part. Equation 3.8 is solved iteratively until the explicit terms essentially become implicit based on a fixed-point interaction algorithm (Jasak and Weller, 2000).

3.1.2.4 Anisotropic Biot's Porous Soil Model

The seabed soil is modelled based on the following assumptions:

1) The seabed is horizontally flat, close to fully saturated, with anisotropic permeabilities in vertical and horizontal directions.

2) The soil skeleton generally obeys Hooke's law with elastic properties.

The classical Biot's consolidation equations (Biot, 1941) are adopted to model the coupled soil behavior with the interaction between solid skeleton and the pore fluids, considering the anisotropic soil characteristics. The soil domain is governed by a quasi-static momentum balance equation for soil mixture and a mass balance equation of the pore fluid based on Darcy's law.

Quasi-static momentum balance equation is presented in Eqn. 3.9.

$$\nabla \cdot [\mathbf{C} : \frac{1}{2}(\nabla \mathbf{U} + (\nabla \mathbf{U})^T)] - \nabla p = 0 \qquad (3.9)$$

where $\mathbf{U}$ is the soil (skeleton) displacement, p is the pore fluid pressure and $\mathbf{C}$ is the fourth-order elastic stiffness tensor. For anisotropic soil materials, the orthotropic elastic stress-strain relation can be expressed in a 6×6 matrix

notation:

$$\boldsymbol{\sigma}' = \begin{pmatrix} \sigma'_{xx} \\ \sigma'_{yy} \\ \sigma'_{zz} \\ \sigma_{xy} \\ \sigma_{yz} \\ \sigma_{xz} \end{pmatrix} = \begin{bmatrix} A_{11} & A_{12} & A_{31} & 0 & 0 & 0 \\ A_{12} & A_{22} & A_{23} & 0 & 0 & 0 \\ A_{31} & A_{23} & A_{33} & 0 & 0 & 0 \\ 0 & 0 & 0 & A_{44} & 0 & 0 \\ 0 & 0 & 0 & 0 & A_{55} & 0 \\ 0 & 0 & 0 & 0 & 0 & A_{66} \end{bmatrix} \begin{pmatrix} \varepsilon_{xx} \\ \varepsilon_{yy} \\ \varepsilon_{zz} \\ \varepsilon_{xy} \\ \varepsilon_{yz} \\ \varepsilon_{xz} \end{pmatrix} = \mathbf{C} : \boldsymbol{\varepsilon} \tag{3.10}$$

where $\boldsymbol{\sigma}'$ is the effective stress tensor. According to the work of Demirdžić et al. (2000), the 9 independent coefficients A_{ij} are calculated from Young's modulus E_i and Poisson's ratio ν_{ij} and shear modulus G_{ij} as follows:

$$\begin{aligned} A_{11} &= \frac{1-\nu_{yz}\nu_{zy}}{JE_yE_z}, & A_{22} &= \frac{1-\nu_{xz}\nu_{zx}}{JE_xE_z}, & A_{33} &= \frac{1-\nu_{yx}\nu_{xy}}{JE_yE_x}, \\ A_{12} &= \frac{\nu_{xy}+\nu_{zy}\nu_{xz}}{JE_xE_z}, & A_{23} &= \frac{\nu_{yz}+\nu_{yx}\nu_{xz}}{JE_xE_y}, & A_{31} &= \frac{\nu_{zx}+\nu_{yx}\nu_{zy}}{JE_yE_z}, \\ A_{44} &= 2G_{xy}, & A_{55} &= 2G_{yz}, & A_{66} &= 2G_{zx} \end{aligned} \tag{3.11}$$

where

$$J = \frac{1-\nu_{xy}\nu_{yx}-\nu_{yz}\nu_{zy}-\nu_{xz}\nu_{zx}-2\nu_{yx}\nu_{zy}\nu_{xz}}{E_xE_yE_z} \tag{3.12}$$

The mass balance equation of the pore fluid is shown in Eqn. 3.13:

$$\frac{n}{K'}\frac{\partial p}{\partial t} - \frac{1}{\gamma_w}\nabla\cdot(\mathbf{k}\cdot\nabla p) + \frac{\partial}{\partial t}(\nabla\cdot\mathbf{U}) = 0 \tag{3.13}$$

where n denotes the soil porosity, γ_w denotes the specific weight of water in soil, and $\mathbf{k}$ denotes the diagonal permeability tensor with values of k_x, k_y and k_z. The bulk modulus of the compressible pore flow K' is approximately computed by the formulation (Vafai and Tien, 1981):

$$\frac{1}{K'} = \frac{1}{K_w} + \frac{1-S_r}{p_a} \tag{3.14}$$

where S_r denotes the degree of soil saturation, K_w denotes the bulk modulus of pure water ($\approx$ 2GPa), and p_a denotes the absolute pore water pressure.

In the context of FVM, the previously mentioned segregated manner is applied to solve the strong pressure-displacement coupling and the coupling between the displacement components U_x, U_y and U_z.

3.1.2.5 Boundary Coupling Algorithm

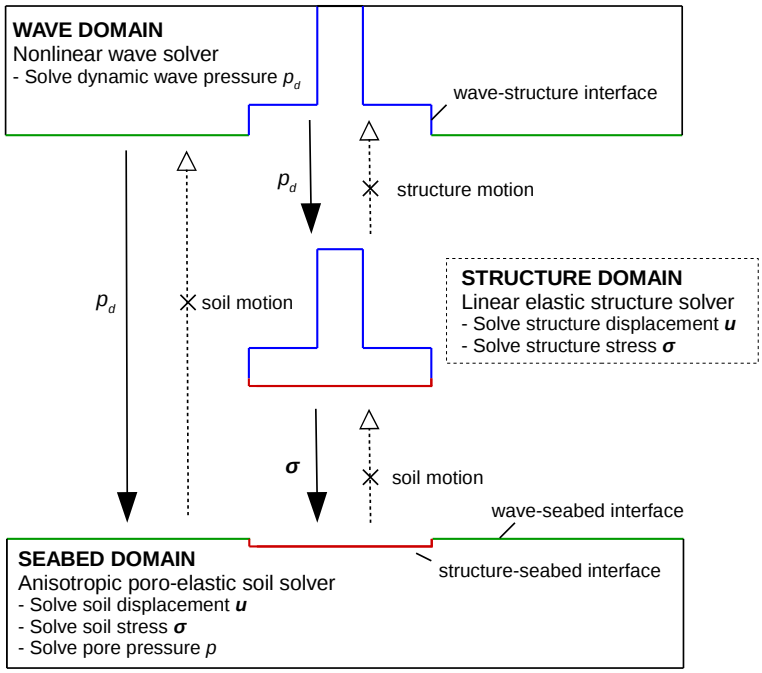

Figure 3.1 One-way boundary coupling algorithm of wave-structure-seabed interaction.

In the coupling procedures, data (i.e. dynamic wave pressure and wave-induced structural stress) exchange between three domains via the common boundaries. Due to the small magnitude of wave-induced structure vibration and minor elastic solid deformation compared to the wave length, an one-way coupling algorithm is adopted, i.e. the time-varying data transfer in the

single direction, which is from the waves to the structure, from the waves to the seabed and from the structure to the seabed. The structure and seabed responses will not alter the wave domain. The schematic coupling procedures are presented in Figure 3.1: the dynamic wave pressure p_d transfers from waves to the structure and the seabed; wave pressure induces the displacement and stress on the structure and then indirectly transfer to the seabed.

For multi-physic solvers, it is worthwhile to consider that different physics may have various demands on the convergence and stability requisitions. In the engineering practice, the time step and the grid size needed for solving the linear elastic solid regions can be relatively larger than what are needed for solving the nonlinear fluid region containing a free surface, referring to the work of Li (2016). Calculating multiple domains with the same grid size and looping at the same time step are not efficient. In the present model, time-varying boundary conditions are implemented at the interfaces, interpolating the values from the supplied domain in space and time. At start up, this boundary condition generates the triangulation in three vertices and performs a linear interpolation for every face center. Then, the values are interpolated linearly between the time instants. Therefore, the grid sizes and the time steps for the three domains are allowed to be various, which increases the efficiency of the integrated model and reduces the computational power.

3.1.3 Model Validation

The nonlinear waves are modelled by using a wave generation toolbox `waves2Foam` (Jacobsen et al., 2012) for the OpenFOAM CFD library. The wave-structure interaction model by `waves2Foam` has been validated in previous works (Chen et al., 2014; Jacobsen et al., 2012; Paulsen et al., 2014). In the present work, the wave-induced seabed response model is validated by comparing the numerical results to the experimental data by Tsai and Lee (1995). Their experiment investigated the standing waves induced pore pressure in the sand bed in the vicinity of a vertical wall. The laboratory

Table 3.1 Physical properties of the wave and soil for model validation (experiment conducted by Tsai and Lee (1995)).

Wave parameters		Soil parameters			
Wave height H (cm)	5.1	Permeability k (m/s)	1.2×10^{-4}	Young's modules E (N/m^2)	6.86×10^{7}
Wave period T (s)	1.5	Porosity n	0.38	Shear modulus G (N/m^2)	2.64×10^{7}
Wave type	second-order	Poisson's ratios ν	0.3	Saturation degree S_r	0.98

experiment was carried out in a 100m wave flume. Waves propagated to the sand bed region and reflected at a vertical smooth wall at the end of the wave flume. Soil response of sand in medium firmness under and close to the vertical wall in the action of standing waves were examined. Nine pore pressure transducers were installed in the sand bed. Among the transducers, four were placed right below the wall from the mudline with 10cm vertical distance in between. Another five transducers were placed parallel to the mudline at a depth of 10cm in the sand bed with distances of $kx = 1/10\pi$, $2/10\pi$, $3/10\pi$, $4/10\pi$ and $5/10\pi$ to the wall, where k is the wave number, $k = 2\pi/L$, L is the wave length. The wave and soil properties are shown in the Table 3.1. In the present numerical simulation, second-order Stokes waves are generated in the numerical wave flume based on the wave properties in the experiment, according to Jeng et al. (2013a).

The present numerical results are compared with the experimental data in Figure 3.2 and Figure 3.3, and they are in good agreement. Some discrepancies for the lowest pressure between the present numerical results and the measured data by Tsai and Lee (1995) can be observed. Vertical distribution of pore pressure amplitude by experimental measurement and the present numerical simulation are compared in Figure 3.4. The amplitude of pore pressure in the soil p_s is normalized by the amplitude of the pressure on the

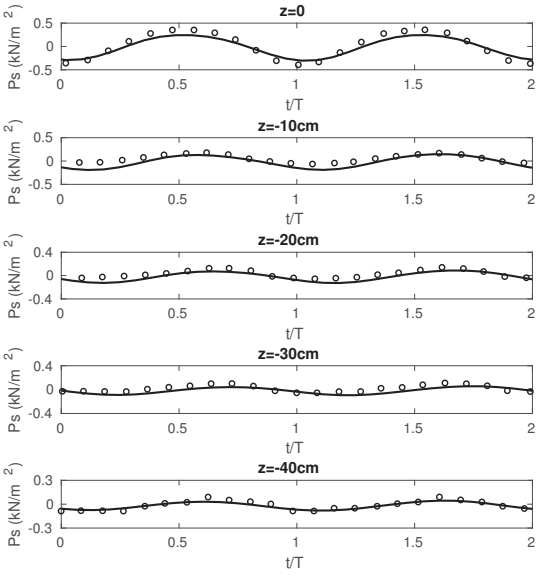

Figure 3.2 Comparisons of the pore pressure response at various depths, $kx = 0$ ($\circ$: measured data by Tsai and Lee (1995); – : numerical results solved by present numerical model).

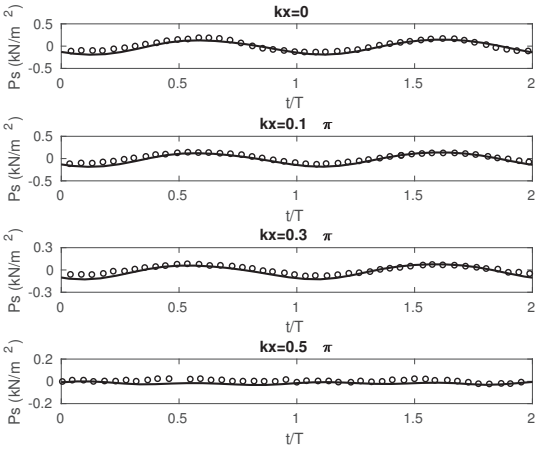

Figure 3.3 Comparisons of the pore pressure response at various positions parallel to the mudline in a depth of 10cm in the sand bed ($\circ$: measured data by Tsai and Lee (1995); – : present numerical results).

mudline p_0. It shows that the present numerical results are in good agreement with the measured data in terms of the time history data of wave-induced pore pressure and its vertical distribution.

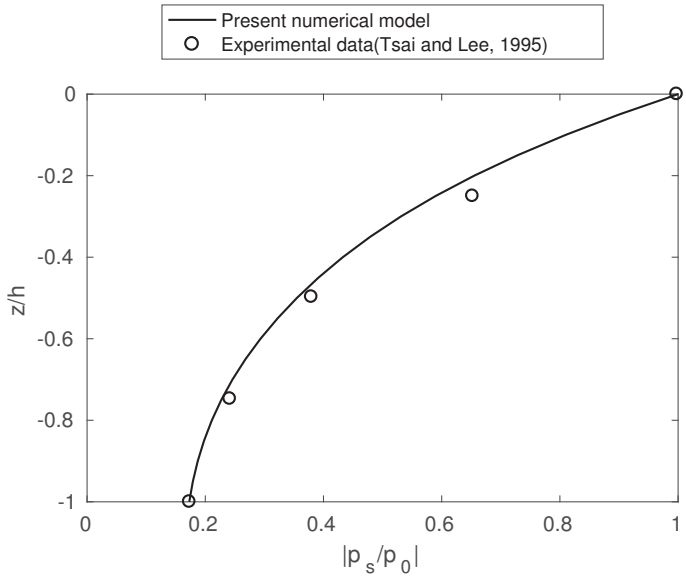

Figure 3.4 Comparison of the vertical distribution of the amplitude of pore pressure.

3.1.4 Model Application

The present numerical model is applied to a gravity-based offshore foundation with a hexagonal base and a pile shaft. The dimension of the foundation refers to the Lillgrund wind power plant (Jeppsson et al., 2008) and the simplification of the geometry refers to the work of Ong et al. (2016). Figure 3.5 presents an integrated layout of the numerical model containing three physical domains in terms of the waves, the structure and the seabed. The geometric parameters of the gravity-based offshore foundation are presented in Figure 3.6 in the real dimension. The height of the hexagonal caisson is 3 meters with 0.6

meters embedded in the seabed soil and 2.4 meters emerged out of the seabed (Hammar et al., 2010).

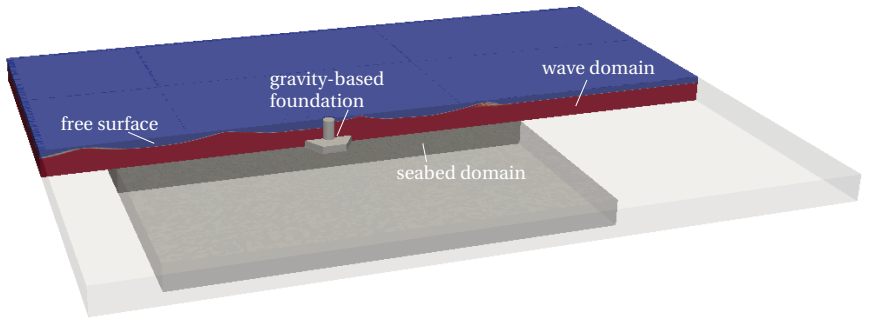

Figure 3.5 Illustration of the wave-structure-seabed interaction.

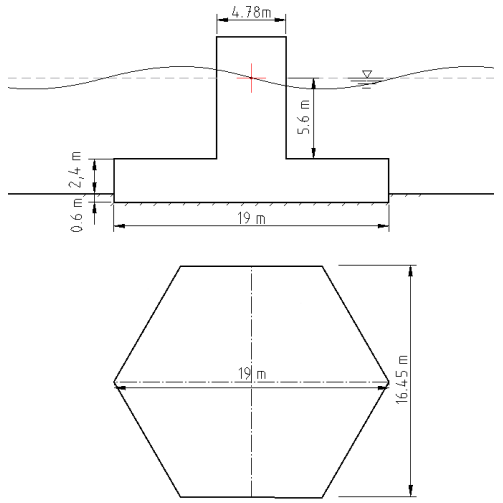

Figure 3.6 Geometry parameters of the hexagonal gravity-based foundation in the real dimension.

3.1.4.1 Numerical Wave Tank Settings

The entire numerical system is built in a uniform Cartesian coordinate system x, y, z, with $z = 0$ the undisturbed free surface, x positive toward wave propagation direction, y positive toward the left side of the wave propagation direction, and z positive upwards, as shown in Figure 3.7. Parameters of the waves modelled in the present work are shown in Table 3.2. The wave period T is 6.7 seconds, and the wave height H at the normal operating condition is 2.6 meters. More wave heights are considered in the parametric study. According to Fenton's Stokes wave theory (Fenton, 1985), the fifth-order Stokes wave model is applied for modeling the waves with wave heights at H=2.6m and 3.7m. Second-order Stokes wave model is applied for modeling the H=1.5m waves. Wave heights larger than 3.7m in the given water depth will exceed the breaking criterion according to Fenton's wave theory (Fenton, 1985); therefore, they are not considered in the present study.

The layout of the numerical tank is shown in Figure 3.7. The inlet relaxation zone is set to be one wave length (L). The working zone is set to be two wave lengths ($2L$). The outlet relaxation zone is set to be two wave lengths ($2L$) to ensure no wave reflection from the outlet boundary. A comprehensive explanation of the numerical wave tank relaxation techniques can be found in Jacobsen et al. (2012). The width of the wave tank (distance between front and back) is set to be four wave lengths ($4L$). The location of the structure is at the center of the working zone. The boundary conditions of the wave domain are specified as follows:

1) The velocity inlet value is specified as the theoretical wave velocity, while the outlet velocity is zero.

2) At four sides of the numerical wave tank, the pressure boundary condition is set to be 'zero-gradient', i.e., the normal gradient of the pressure at the boundary is zero.

3) At the atmosphere, the pressure is set to be atmosphere pressure (p_0) and the velocity is set to be 'zero-gradient'.

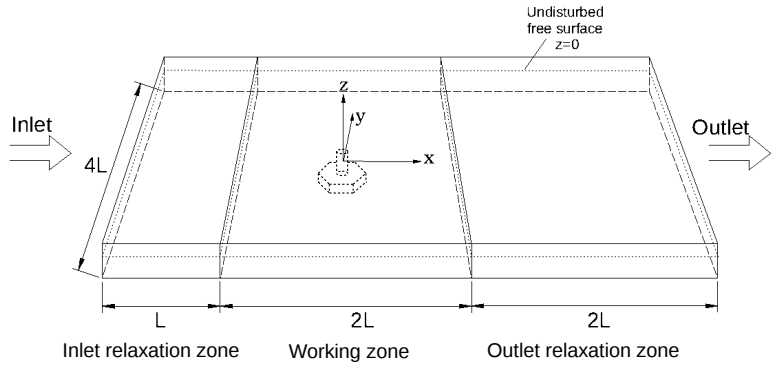

Figure 3.7 3D numerical wave tank layout.

4) At the wave-structure interface and the wave-seabed interface, no-slip velocity boundary is set. The normal gradient of the pressure is set to be zero. It is found in the present study that a slip or a no-slip velocity boundary condition at the wave bottom interface do not affect the bottom pressure results, so that a slip boundary condition can also be used for modeling our case, see also in Lin et al. (2017). Bottom boundary layer effect can thereby be neglected, and this is consistent with the invesitgation reported by Paulsen et al. (2014).

3.1.4.2 Structure Domain Settings

The gravity-based foundation submerges in the water and the soil and its shaft protrudes out of the free surface higher than the wave amplitude, as shown in Figure 3.6. Hence, there are no waves passing over the top of the structure. The structure is considered as linear elastic. The elastic properties of the foundation are set with $E = 22GPa$ and $\nu = 0.2$. Parameters of the structure are shown in Table 3.2.

As the structure passes the dynamic wave loadings to the seabed, the boundary conditions on the structure surface are nonuniform and time-varying.

The dynamic wave pressure is imposed on the structure through the wave-structure interface. Then, the wave-induced structural response is calculated in order to obtain the time-varying stress in the structure along the time. The time-varying wave-induced structural stress at the structure-seabed interface is therefore read by the soil solver to compute the compatible time-varying displacement gradient boundary for the seabed.

3.1.4.3 Seabed Domain Settings

The numerical domain of the porous seabed is three wave lengths $3L \times 3L$ long and wide, and $0.5L$ thick. The porous seabed parameters are based on the typical values of the North sea soil measurements by Kjekstad and Lunne (1981) with reasonable assumptions concerning the anisotropic properties. The soil porosity n is 0.3 and the saturation factor S_r is set to 0.975. The anisotropic parameter settings are shown in Table 3.2. The boundary conditions of the seabed domain are specified as follows:

1) At the wave-seabed interface, the effective soil stresses vanish so that the soil has zero traction at the seabed surface. The pore pressure at the wave-seabed interface is equal to the dynamic wave pressure on the seabed.

2) At the structurle-seabed interface, it is considered that the structure is impermeable. Thus, the pore pressure condition is zero normal gradient, according to Darcy's flow equation. The displacement of the soil at the structure-seabed interface is induced by the structural force, while the structural force is originally induced by the surface waves.

3) At the bottom and lateral boundaries of the seabed, the soil skeleton is allowed to slip and the normal pore pressure gradient is zero.

Table 3.2 Parameter settings for wave-structure-seabed interaction modeling in the present work.

Wave parameters			
Wave height H (m)	1.5	2.6	3.7
Wave period T (s)	6.7		
Water depth h_w (m)	8		
Wave length L (m)	52.235	53.184	54.197
Parameter settings for wave-structur Wave number k	0.120	0.118	0.116
Non-dimensional depth kh_w	0.962	0.945	0.927
Wave steepness H/L	0.029	0.049	0.068
Wave type	Stokes-second	Stokes-fifth	Stokes-fifth
Structure parameters			
Density ρ (kg/m^3)	2400		
Young's modules (N/m^2)	2.2×10^{10}		
Poisson's ratios	0.2		
Seabed parameters		Directional values	
Young's modules (N/m^2)	$E_x = 1.2 \times 10^7$	$E_y = 1.2 \times 10^7$	$E_z = 2 \times 10^7$
Poisson's ratios	$\nu_{xy} = 0.2$	$\nu_{yz} = 0.24$	$\nu_{zx} = 0.4$
Shear modulus (N/m^2)	$G_{xy} = 5 \times 10^6$	$G_{yz} = 1.2 \times 10^7$	$G_{zx} = 1.2 \times 10^7$
Permeability(m/s)	$k_x = 0.005$	$k_y = 0.005$	$k_z = 0.001$

3.1.5 Convergence studies

3.1.5.1 Wave Calibration

For the simulated wave condition, the water depth is intermediate compared to the wave length and the targeted waves are nonlinear. Convergence studies are performed to verify the generated waves, as shown in Figure 3.8 and Table 3.3. Three sets of simulations are conducted with increasing numbers of grid points. The maximum Courant number is set to 0.25.

Numerical results of wave elevations at a wave gauge located at the center of the Cartesian coordinate system with two wave lengths from the inlet are compared in Figure 3.8. Table 3.3 shows that mesh No.A2 and mesh

Table 3.3 Grid convergence for wave calibration with T=6.7s and H=2.6m in a water depth D=8.0m.

Mesh	Number of grids	Grids number per wave length	Wave crest amplitude	Wave through amplitude	Wave height	Percentage difference of the wave heights
No.A1	40698	80	1.488	-0.917	2.405	-7.50%
No.A2	131813	150	1.507	-0.957	2.464	-5.23%
No.A3	182413	250	1.511	-0.983	2.494	-4.07 %
Analytical solution			1.600	-1.000	2.600	

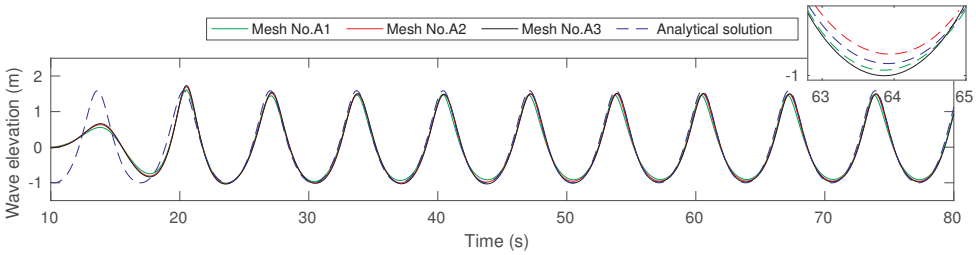

Figure 3.8 Grid convergence for wave calibration with T=6.7s and H=2.6m in a water depth D=8.0m.

No.A3 are in a reasonable accuracy with a percentage difference of 5.23% and 4.07%, respectively, compared to the analytical solution. From mesh No.A2 to mesh No.A3, as the grid number increases by 38%, the difference ratio reduces by only 1.23%, indicating the number of grid points in mesh No.A2 is sufficient to achieve good numerical accuracy. The wave convergence study is performed in 2D to calibrate the free surface. For the 3D simulation of the gravity-based foundation in waves, the free surface mesh is extended from mesh No.A2, with 150 grid points at a wave length and 64 grid points at a wave height. The discrepancy between the numerical results and the analytical solution is resulted from both physical and numerical aspects. Such

discrepancy is mainly seen in the cases with intermediate water depth and nonlinear waves. Detailed illustrations and explanations for this phenomenon were discussed in Seng (2012).

3.1.5.2 Grid Convergence for Dynamic Wave Pressure on the Seabed

A 3D grid convergence study for wave pressure on the seabed surface in the presence of the gravity-based foundation is conducted with four sets of meshes. The mesh is refined by increasing the grid resolution around the foundation horizontally and vertically. Numerical results of dynamic wave pressure p_d are compared at the location on the seabed surface (z=-h_w) with 0.5 wave length (x=-0.5L, y=0) upstream to the foundation bottom center. Figure 3.9 shows that mesh No.B3 and mesh No.B4 present very close results with minor shift between two curves. Relative changes of the pressure range between each mesh and mesh No.B4 are presented in Table 3.4. The relative change between mesh No.B3 and mesh No.B4 is only 0.66%, indicating 21.6 million of grid points in mesh No.3 is sufficient to achieve good numerical accuracy. The mesh No.B3 is used in the present numerical analysis.

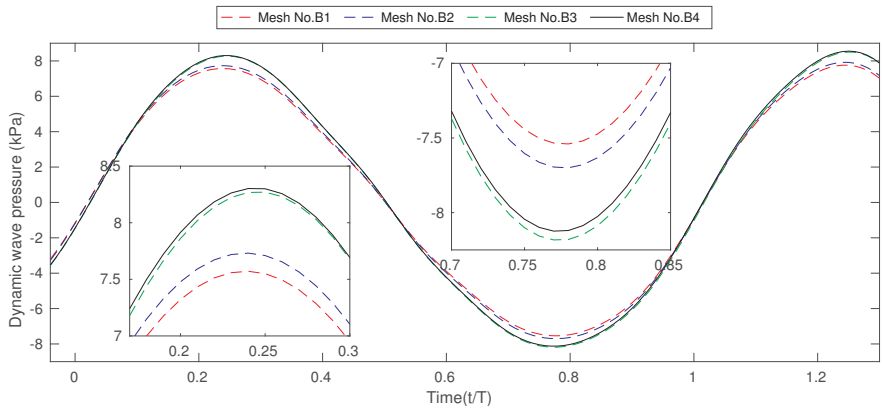

Figure 3.9 Grid convergence for dynamic wave pressure on the seabed in the existing of the structure (results for location (-0.5L, 0, -d) in the Cartesian coordinate system).

Table 3.4 Grid convergence for dynamic wave pressure on the seabed in the existing of the structure (results for location (-0.5L, 0, -d) in the Cartesian coordinate system).

Mesh	Number of grid points	Maximum pressure (kPa)	Lowest pressure (kPa)	Relative change
No.B1	9.6×10^6	7.7593	-7.5400	8.23%
No.B2	16.2×10^6	7.9193	-7.7000	6.31%
No.B3	21.6×10^6	8.5031	-8.1832	0.66%
No.B4	25.2×10^6	8.5530	-8.1241	

3.1.5.3 Grid Convergence for Seabed Pore Pressure

A grid convergence study is conducted for the soil domain with three sets of meshes. The dynamic pore pressure at 3m under the foundation bottom center is compared between 1.1 million, 2.0 million and 3.6 million of the grid points. Figure 3.10 presents the pore pressure curves of the three meshes. It is shown that as the number of grid points increases, the pore pressure converges to a lower amplitude. This implies that an insufficient number of grid points may overestimate the pore pressure in the seabed. In the present study, the set of 3.6 million mesh is used.

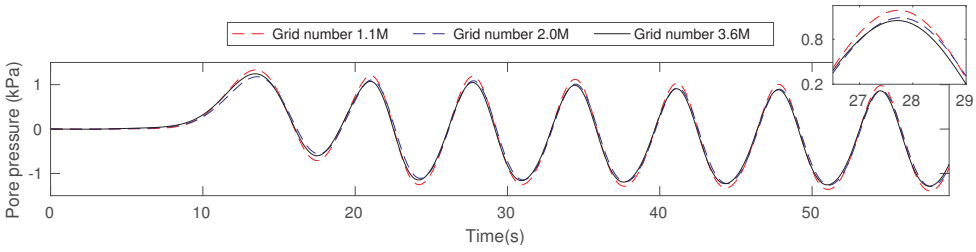

Figure 3.10 Grid convergence for pore pressure in the seabed (results for the location at 3m under the center of foundation).

3.1.6 Results and discussion

3.1.6.1 Consolidation

The construction of the marine structure on the seabed can significantly increase the effective stress in the surrounding soil. Once the structure is built on the seabed, the nearby soil will experience the gradual dissipation of the excess pore pressure and compression of the soil skeleton, induced by the gravitational forces from the structure and the soil itself. The soil consolidation behavior will further influence potential risk of dynamic wave-induced soil liquefaction (Sui et al., 2017; Ulker et al., 2010; Zhao et al., 2017a). Therefore, it is essential to perform the consolidation analysis before investigating the momentary liquefaction of the seabed around the gravity-based foundation.

The seabed consolidation behavior in this work is different from the consolidation behavior below a breakwater. As Sui et al. (2017) pointed out, as a part of the foundation is embedded in the seabed, it will cause a more complex seabed-structure interaction with a 3D interface.

Figure 3.11 shows the vertical soil displacement U_z after the completion of the consolidation process. A negative U_z indicates the soil skeleton is compressed and moves downward. It is obviously seen that around the foundation, the soil skeleton has been largely compressed compared to the far field. Figure 3.12 shows the distribution of the vertical effective stresses $\sigma_z^{'}$ in the soil when the consolidation process is completed. It is noted that in Figure 3.12, a negative value of $\sigma_z^{'}$ indicates the compression of the soil skeleton. In the present work, tension is taken as positive while compression is taken as negative. During the long-time consolidation, the gravity force from the foundation is gradually transferred to the supporting soil skeleton. It shows that right below the foundation, the vertical effective stress in the soil is amplified compared to the far field.

Figure 3.13 shows a cross-sectional view of vertical soil effective stress at z=-8.6m (structure bottom level). It is observed that the compressive stress at

the vertices is higher than that at the hexagonal edges. Since the foundation is embedded in the seabed with 0.6m, the sharp corners in the seabed cause stress concentration in the surrounding soil. The vertical effective stresses σ_z' computed from the consolidation process will be used as an initial condition for the analysis of momentary liquefaction.

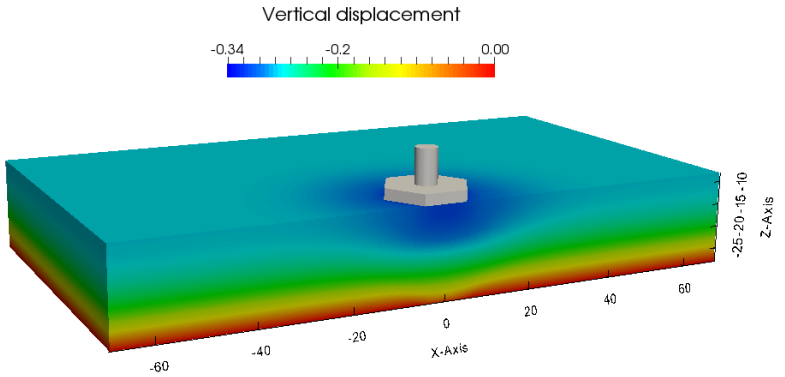

Figure 3.11 Vertical soil displacement U_z (m) after the completion of the consolidation process (x, y, z are in the unit of m).

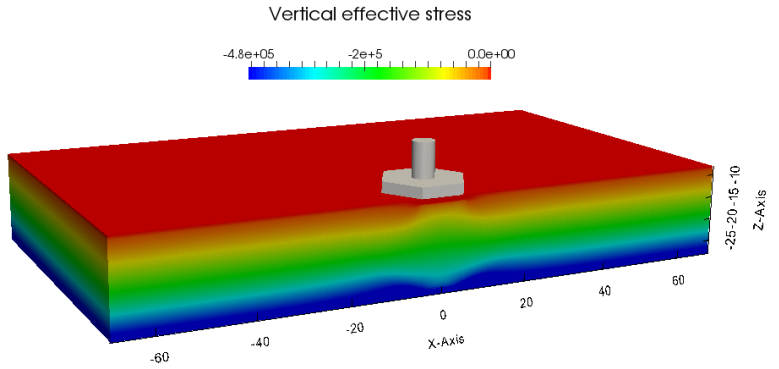

Figure 3.12 Vertical effective stresses σ_z' (Pa) after the completion of the consolidation process (x, y, z are in the unit of m).

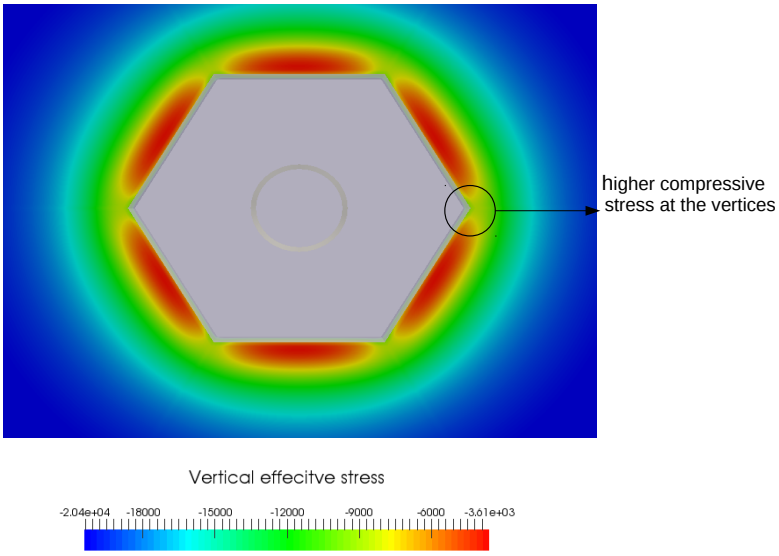

Figure 3.13 A cross-sectional view of the vertical soil effective stress (Pa) around the structure

3.1.6.2 Wave-Induced Seabed and Structure Responses

Dynamic Wave Pressure: Results of the dynamic wave pressure, the structure response and the soil response under the normal operating condition with T=6.7s, H=2.6m are presented as follows. Dynamic wave pressure on the seabed and the structure at two time instants are shown in Figure 3.14. Figure 3.14a shows the wave crest passes the structure at t/T=8. Figure 3.14b shows the wave trough passes the structure at t/T=8.5. The highest and lowest dynamic wave pressure in the legend shows the range of dynamic wave pressure on the seabed surface. The pressure magnitude on the structure is larger than that on the seabed due to the smaller depth.Dynamic wave pressure p_d is influenced by the wave diffraction effect around the foundation. p_d at three locations A1, A2, A3 in Figure 3.15 are presented in a time series in Figure 3.16. At the location A1, flow propagates closer to the foundation. Then at the location A2, flow hits the corner of the hexagon so that the velocity

reduces and the pressure increases compared to A1. After the flow passes through the foundation to the other side, it reaches location A3. Comparing between A3 and A2, it shows that the dynamic wave pressure amplitude at the downstream side of the foundation is slightly lower than that at the upstream side. Figure 3.17 provides a 3D illustration of the wave-induced pressure in the seabed when the wave trough approaches the upstream of the foundation. It is obviously seen that the wave-induced pressure increases dramatically at the upstream of the foundation.

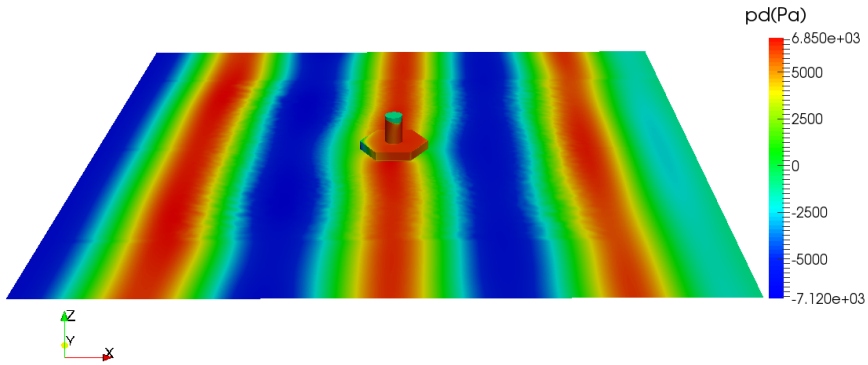

(a) Wave pressure on the structure and seabed at the time step t/T=8 (wave crest passing the structure).

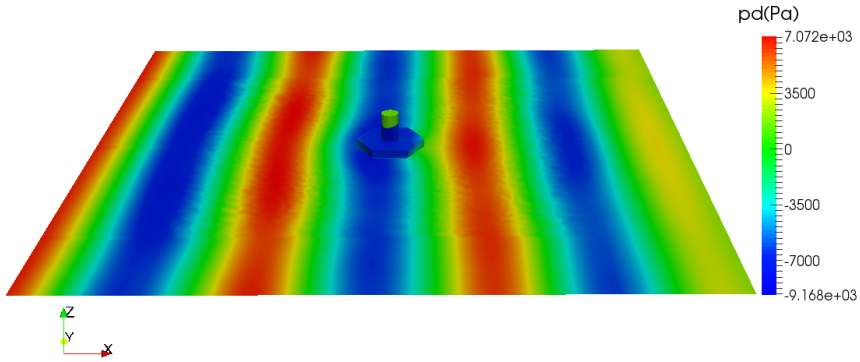

(b) Wave pressure on the structure and seabed at the time step t/T=8.5 (wave trough passing the structure).

Figure 3.14 Dynamic wave pressure on the structure and seabed (H=2.6m).

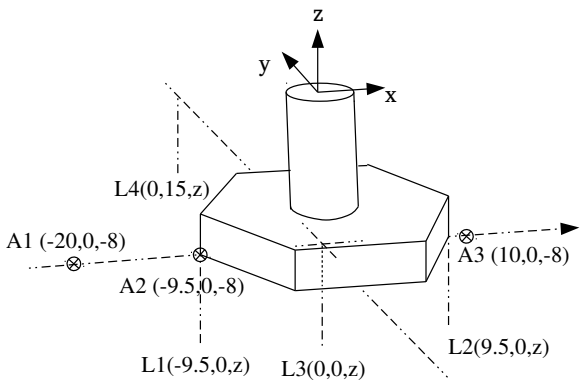

Figure 3.15 Locations of points along the seabed and the structure surface.

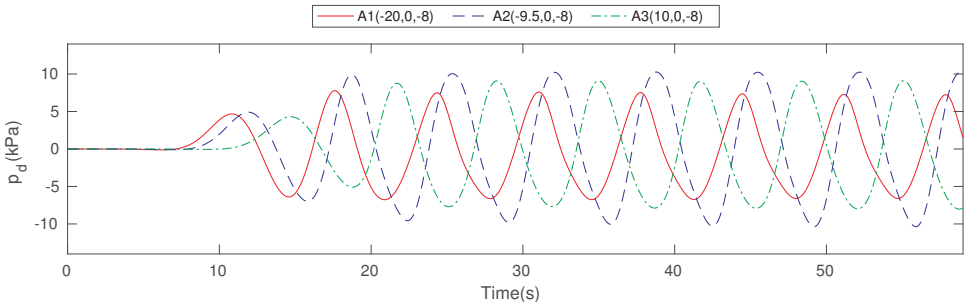

Figure 3.16 Dynamic wave pressure on the seabed in a time series (H=2.6m).

Structure Response: In the present work, the wave-induced structural response is solved in order to obtain the instantaneous stress of the structure at the structure-seabed interface. The previous studies assumed that the structure imposes a uniform force on the seabed or solve the structure and the seabed as a whole system (Ulker et al., 2010; Ye, 2012b; Ye et al., 2013). Nevertheless, the present study treats the structure and seabed as independent systems and includes an internal structure-seabed interface. The time-varying wave-induced structural stress imposed on the seabed is assessed. Figure 3.18 provides an insight of the computed structural responses in terms of

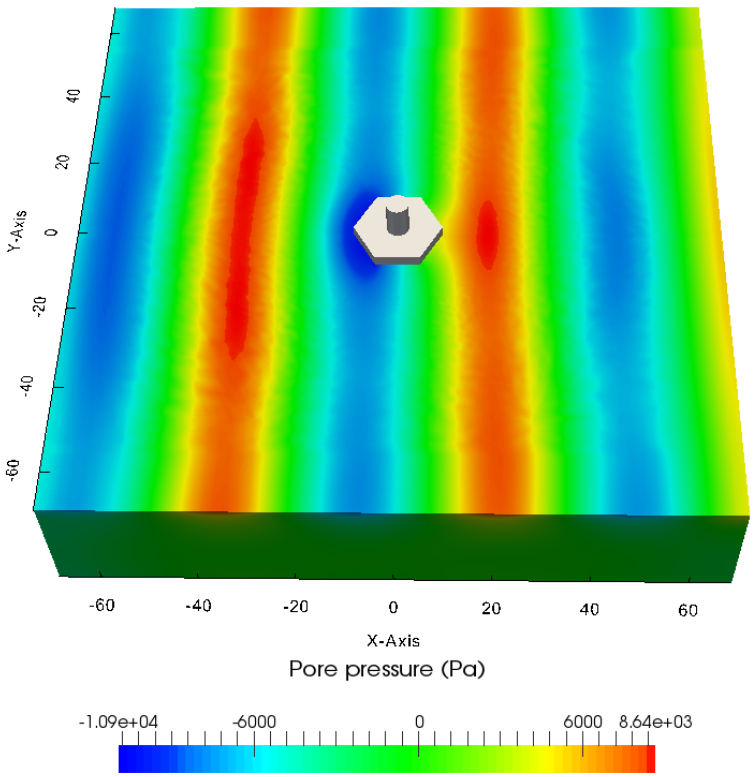

Figure 3.17 Illustration of the pore pressure increase at the upstream of the foundation due to wave diffraction effect (t/T=8.25).

the equivalent shear stress measurement σ_{eq} and the magnitude of structure displacement U. σ_{eq} is calculated by:

$$\sigma_{eq} = \sqrt{2/3\mathbf{s} : \mathbf{s}} \tag{3.15}$$

where $\mathbf{s}$ is the deviatoric stress tensor, $\mathbf{s} = \boldsymbol{\sigma} - 1/3(\mathrm{tr}\boldsymbol{\sigma})\mathbf{I}$. Shear stresses in the structure are resulted from the dynamic wave pressure variations. It is shown in Figure 3.18 that the highest shear stress occurs at the joint between the caisson and shaft. Since the structure bottom is fixed on the seabed, the shear stress can only be compensated at the joint. The total displacement resulted from the dynamic wave pressure gradient is insignificant, supporting the previously mentioned one-way wave-structure-seabed interaction assumption. Figure 3.19 shows the equivalent shear stress at the structure-seabed interface. The wave-induced structural shear stress tensor at the structure-seabed interface $\boldsymbol{\sigma}$ is then imposed on the seabed.

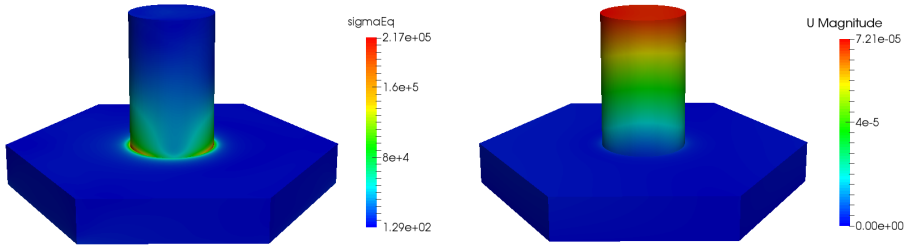

(a) Equivalent shear stress σ_{eq}. (b) Structure displacement magnitude U.

Figure 3.18 Structure responses at the time of t/T=8.5 seconds.

Seabed Response: Figure 3.20 shows the wave-induced shear stress σ_{xz} in the gravity-based foundation and in the seabed soil. It is observed that the highest σ_{xz} in the seabed occurs right beneath the foundation. The wave-induced seabed shear stress σ_{xz} is less significant in the field away from the structure, compared to the concentrated shearing zones around the foundation

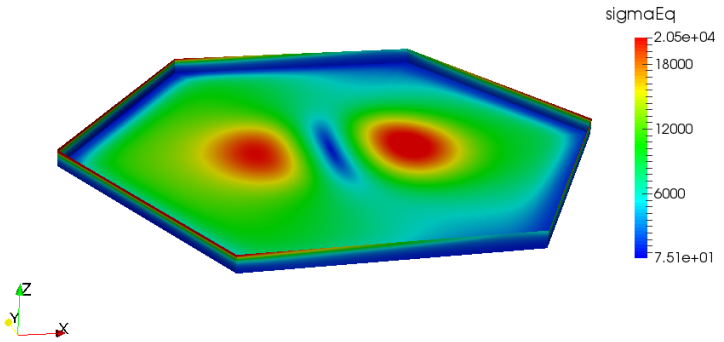

Figure 3.19 Equivalent shear stress at the structure-seabed interface

edges. This indicates that the presence of the structure on the seabed significantly affects the soil responses by amplifying the wave-induced shearing effect on the underlying seabed. The seabed zone with high shear stress may have the highest possibility of local plastic failure. Figure 3.21 shows the transient pore pressure and seepage flow in the seabed at the time instant of t/T=8.25 when the wave trough passes the upstream side of the foundation. The demonstrated wave height is 2.6m. Notable upward seepage flows are created underneath the structure upstream side. When the upward seepage forces exceed the vertical initial effective stress, the momentary soil liquefaction can occur and further affect the structure safety. More discussion of the seabed responses is presented in the parametric study shown in Section 3.1.6.3.

3.1.6.3 Parametric Study

A series of wave heights are simulated to impose various dynamic wave pressure amplitudes on the structure and the seabed. The changes of soil displacement, pore pressure distribution and liquefaction risk around the gravity-based foundation are investigated. Soil responses at wave heights H=1.5m, 2.6m and 3.7m and wave period T=6.7s are discussed in this section.

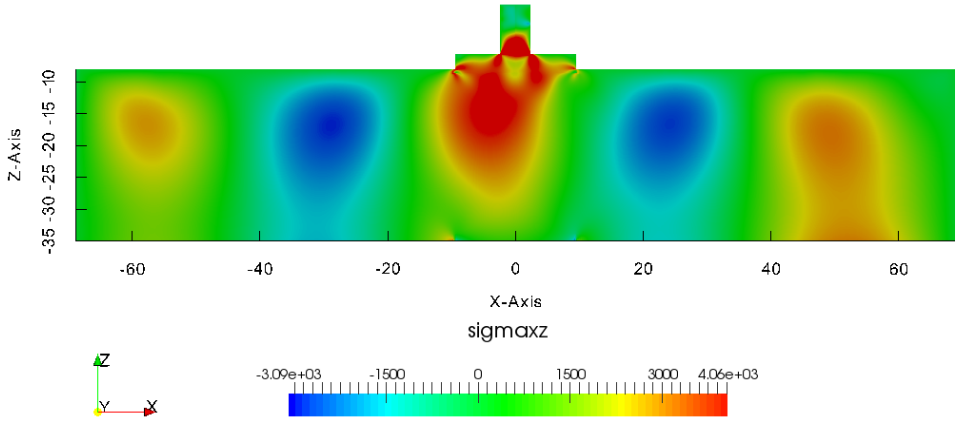

Figure 3.20 Shear stress σ_{xz} distribution in the structure and seabed at a time instant of t/T=5.25 (H=2.6m).

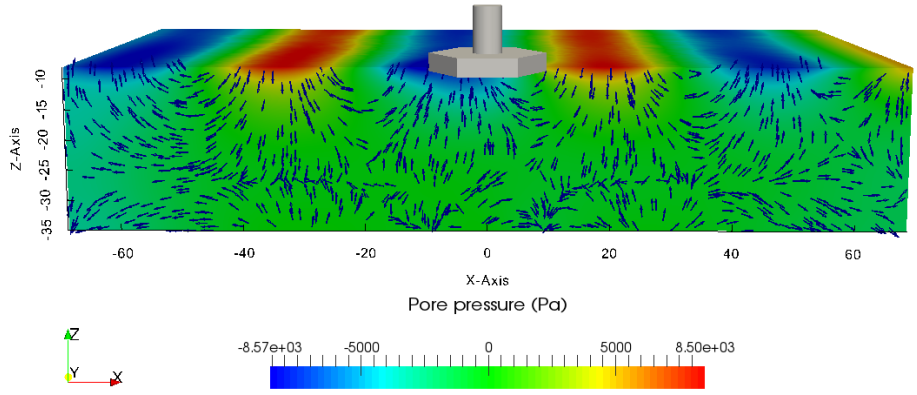

Figure 3.21 Transient pore pressure and seepage flow at the time of t/T=5.25 (H=2.6m).

The anisotropic poro-elastic soil model applied in this work focuses on the investigation of the momentary liquefaction risk around the structure. The linear elastic assumption was also used for liquefaction analysis in the previous studies, providing satisfactory results (Jeng et al., 2013a; Li et al., 2011; Lin et al., 2017). However, during long time scale action of extreme waves, the nonlinear plastic soil behavior might be dominant so that the plasticity may need to be modelled.

Soil Displacement: The change of dynamic wave pressure imposed on the flat horizontal seabed surface affects the change of vertical soil displacement. In Figure 3.22, locations at the upstream side of the foundation along L1(-9.5, 0, z), at the downstream side of the foundation along L2(9.5, 0, z), under the center of the foundation along L3(0,0,z) and farther from the foundation center along L4(0, 15, z) are investigated. Locations of the vertical lines L1, L2, L3 and L4 are illustrated in Figure 3.15. Figure 3.22 shows the vertical distributions of the maximum vertical soil displacement $|Uz|_{max}$ within a wave cycle at different wave heights. The distance of the vertical location to the seabed surface $z^{'}$ is normalized by the seabed thickness D_s. The amplitude of the vertical soil displacement $|Uz|_{max}$ is normalized by the structure embedded depth D_e. Higher waves impose higher pressure on the surface of the seabed and trigger larger soil displacement. It is observed that the vertical soil displacements in the vicinity of the foundation are higher than that at the far field. Under the center of the foundation, the decrease of $|Uz|_{max}$ along the depth is insignificant. It shows that the existence of the gravity-based foundation amplifies the wave-induced vertical soil displacement surrounding the foundation.

Pore Pressure Distribution: Figure 3.23 shows the vertical profiles of the amplitude of the negative pore pressure $|p|_{max}$ at different wave heights at locations L1, L2, L3 and L4. The amplitude of the maximum negative pore pressure in a wave cycle $|p|_{max}$ is normalized by the static water pressure

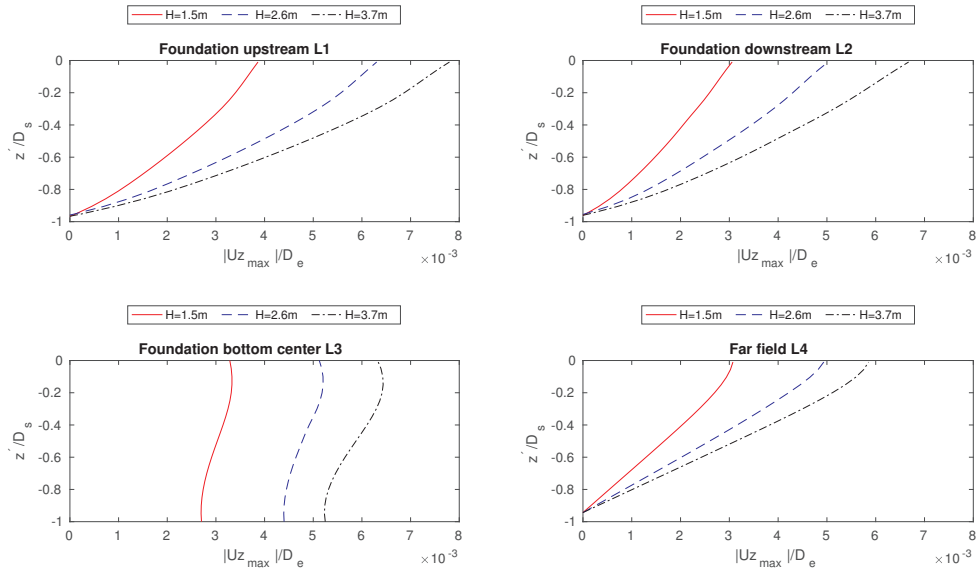

Figure 3.22 Vertical distributions of displacement amplitude $|u_z|_{max}$ in various locations at different wave heights.

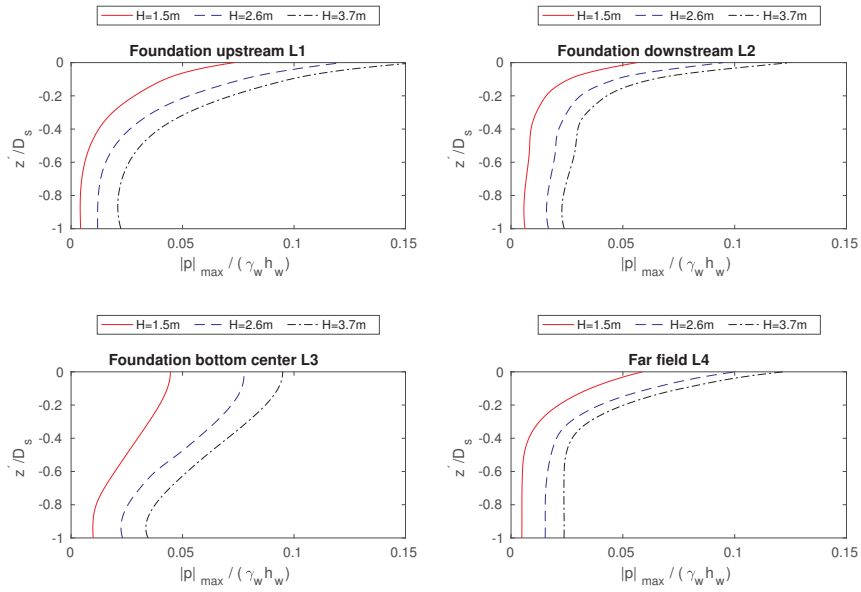

Figure 3.23 Vertical distributions of pore pressure amplitude $|p|_{max}$ in various locations at different wave heights.

$\gamma_w h_w$ at the seabed surface. As the wave height increases, both amplitude and gradient of the pore pressure increase, leading to more severe soil liquefaction around the foundation. The upstream side of the foundation experiences higher pore pressure amplitude and higher pore pressure gradient than the downstream side, due to the wave diffraction effect. It is also seen that the vertical gradient of $|p|_{max}$ along the depth under the foundation center is less significant than that at the other locations. As mentioned in Lin et al. (2017), the presence of the foundation has a so-called 'shielding effect': the soil beneath the foundation is shielded from the wave-induced pore pressure, so that the pore pressure underneath the foundation bottom has relatively small changes. Liquefaction is less likely to happen in the soil beneath the foundation bottom.

Liquefaction Analysis: According to the open literature, various liquefaction criteria for investigating the momentary liquefaction have been proposed based on the effective stress (Okusa, 1985; Tsai, 1995) or the excess pore pressure (Jeng, 1997c; Zen and Yamazaki, 1990b). Ye (2012a) has performed a comparison study of these liquefaction criteria. The liquefaction criterion adopted in the present work is a modified form from Zen and Yamazaki (1990b). They proposed an 1D liquefaction criterion based on the excess pore pressure:

$$p - p_b \geq -(\gamma_s - \gamma_\omega)z \tag{3.16}$$

which further extended by Jeng (1997a) to 3D cases:

$$p - p_b \geq -\frac{1+2K_0}{3}(\gamma_s - \gamma_\omega)z \tag{3.17}$$

where p_b is the pore wave pressure at the seabed surface, γ_s and γ_ω are the unit weight of soil and water respectively, K_0 is the coefficient of lateral earth pressure. However, Eqn. 3.17 is only applicable to the cases without a structure. In the present work, where a marine structure is built on the seabed,

the momentary liquefaction is examined by:

$$p - p_b \geq \sigma_{z0}^{'} \tag{3.18}$$

where $\sigma_{z0}^{'}$ is the initial vertical effective stress induced by the gravitational forces from the consolidation process. The same criterion is also used in the work of Sui et al. (2017) and Zhao et al. (2017a), which provides satisfactory results. At a certain wave length, the liquefaction risk increases with the wave heights. Figure 3.24 illustrates the maximum liquefaction depths in a wave cycle around the hexagonal foundation at the wave heights of 1.5m, 2.6m and 3.7m. The liquefaction depth D_L is normalized by the embedded depth D_e ($D_e = 0.6m$). It is shown that the liquefaction depth is symmetric with respect to the x-axis ($\theta = 0, 2\pi$). It is interesting to see that the liquefaction depth has its sudden change at the corners. At the four vertices (2, 3, 5, 6) beside x-axis, the liquefaction depth is 0 when H=1.5m and has small values when H=2.6m and 3.6m. Since the hexagonal foundation is embedded in the seabed with a depth, the sharp corners cause the stress concentration in the seabed during the consolidation process. Therefore, the initial effective stress at the vertices is much higher compared to the stress at the hexagon edges. However, due to the wave diffraction effect, the wave-induced pressure amplitude increases at the upstream and downstream vertices (1, 4). Therefore, liquefaction is observed at these two vertices. In the operating environment, the scour protection around the hexagonal foundation can encounter liquefaction risk. Chang and Jeng (2014) investigated seabed protection methodology and provided a suggestion of replacing the existing layers of the surrounding soil with higher permeability materials to reduce the liquefaction risk.

3.1.6.4 Effect of Anisotropic Permeability

The permeability of soil is a measurement of how rapidly fluid is transmitted through the void space in the soil. The specification of the soil permeability

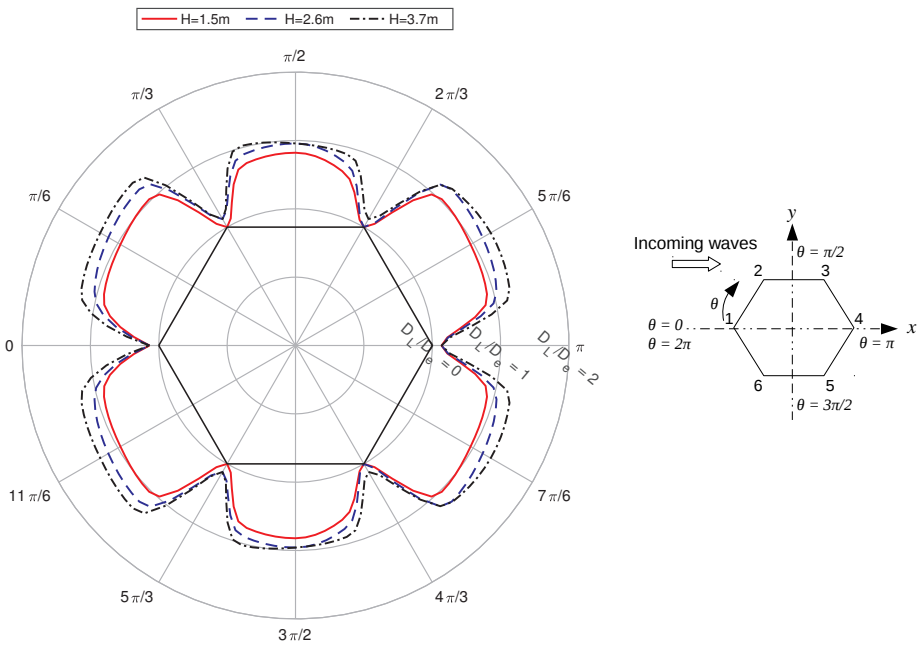

Figure 3.24 Maximum liquefaction depth around the gravity-based foundation at different wave heights.

Table 3.5 Parameter settings for the permeability study.

Parameter	Find sand	Medium sand	Coarse sand
G_{xy} (N/m^2)	5×10^6	1.2×10^7	1.2×10^7
G_{yz},G_{xz} (N/m^2)	1.2×10^6	2×10^7	2×10^7
Isotropic $k_{x,y}$ (m/s)	0.0001	0.001	0.01
Anisotropic $k_{x,y}$ (m/s)	0.0005	0.005	0.05
k_z(m/s)	0.0001	0.001	0.01
n	0.3	0.3	0.43

may largely affect the numerical results of the soil response. The seabed sand in the present simulation (medium sand), and other two different soil sediments in terms of fine sand, coarse sand are studied. The properties of the three soil sediments are specified in Table 3.5. The magnitude of the permeability and porosity ratio n are referred to the work of Lin and Jeng (1997). In the anisotropic permeability settings, the horizontal permeability is set to 5 times of the vertical permeability, i.e., $k_x = k_y = 5k_z$. This is based on the formation of the seabed layer, the horizontal permeability is generally ranging from 2 to 40 times of the vertical permeability, according to the work of Maasland (1957).

The distribution of the transient pore pressure along the vertical axis below the foundation center is compared at the time instant of t/T=4.75. Figure 3.25 shows the comparison between isotropic permeability (solid line) and anisotropic permeability (dash line) of three sets of soil sediments, i.e., fine sand, medium sand and coarse sand. $|z^{'}|/D_s = 0$ denotes the vertical position at the center of the structure bottom (structure-seabed interface). The vertical distance $|z^{'}|$ away from the center of the structure bottom is normalized by the thickness of seabed D_s, while the pore pressure p in the seabed is normalized by pore pressure of the isotropic permeability p_{i0} at the structure bottom.

For the fine sand, the pore pressure between isotropic and anisotropic permeabilities varies less than the others. This is because the pore fluid in the

fine sand is more difficult to move between the fine sand solids due to the low permeability. The comparison of the medium sand and coarse sand shows that the pore pressure results vary between isotropic permeability and anisotropic permeability settings. Therefore, it is suggested to perform the soil analysis with anisotropic consideration for these soil sediments. For the medium sand which is modelled in this work, the highest difference ratio of pore pressure distribution between isotropic and anisotropic permeability settings is 26%, see in Figure 3.25 (medium sand). Therefore, the anisotropic permeability has been considered for medium sand in the present study.

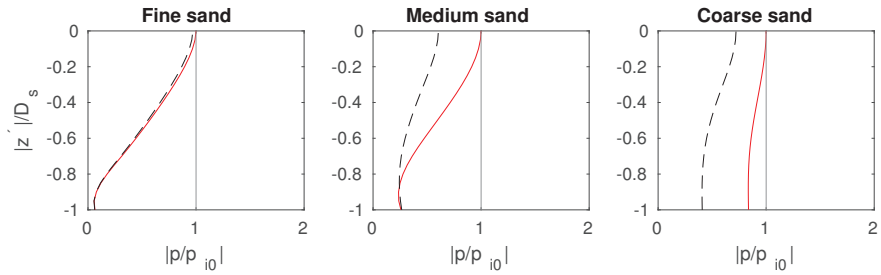

Figure 3.25 Comparison of transient pore pressure profiles in different soil sediments between isotropic(solid line) and anisotropic(dash line) permeabilities.

3.1.7 Conclusions

This paper has investigated the wave-induced soil response and liquefaction risk around a hexagonal gravity-based offshore foundation. A 3D FVM-based wave-structure-seabed interaction model has been applied. The present numerical model has been validated against the experimental data reported by Tsai and Lee (1995), and they are in good agreement. Grid convergence studies have been performed to verify the numerical sub-models. Parametric studies of wave heights have been carried out to study the changes of the soil response in the vicinity of the foundation. Anisotropic and isotropic

permeability settings have been compared for the soil analysis. Following conclusions can be drawn from the present study:

1) In the seabed soil, the highest shear stress occurs right beneath the foundation. The presence of the foundation on the seabed significantly affects the soil responses by amplifying the wave-induced shearing effect on the underlying seabed. The area with high shear stress may have the high possibility of local plastic failure.

2) The presence of the foundation on the seabed also amplifies the wave-induced vertical soil displacement in the vicinity.

3) The soil underneath the foundation has a smaller pore pressure gradient than that beside the foundation. Liquefaction is less likely to happen in the soil right beneath the foundation bottom.

4) A higher wave height causes higher momentary liquefaction risk around the foundation. For the hexagonal foundation, the sharp corners cause the stress concentration in the consolidation process. Therefore, the momentary liquefaction at the vertices is not significant due to the high initial effective stress.

5) The settings of isotropic and anisotropic soil permeabilities demonstrate that for the simulated seabed soil in the present study, the consideration of the anisotropic permeability is suggested. Modeling of other soil sediments should be based on their soil natures.

In the wave-structure-seabed interaction model, the seabed soil has been considered as elastic which does not account for the soil strength limitation and plastic deformation. An incorporation of the nonlinear soil model may result in different soil response results. More experimental data is required before a conclusion regarding the validity of the present numerical results can be given. Meanwhile, the present method should be useful as an engineering tool for predicting the wave-induced soil response around offshore foundations.

Acknowledgment

This study was supported in part with computational resources provided by the Norwegian Metacenter for Computational Science (NOTUR), under Project No: NN9372K.

3.2 Paper II: The effects of slab geometries and wave directions on the steep wave-induced soil response and momentary liquefaction around gravity-based offshore foundations

Yuzhu Li[a], Muk Chen Ong[a], Ove Tobias Gudmestad[a]
and Bjørn Helge Hjertager[a]
[a] Department of Mechanical and Structural Engineering and Materials Science, University of Stavanger, N-4036 Stavanger, Norway

Abstract*: Gravity-based offshore foundations generally consist of a bottom slab and one or more cylindrical shafts on top of it. The geometry of the foundation can strongly affect the surrounding flow pattern, dynamic wave pressure distribution and further soil response and the soil liquefaction risk. In the present study, the effects of the slab geometry and the incoming wave angle to the foundation on the surrounding soil response are investigated. The gravity-based foundations with bottom slabs of cylindrical shape and hexagonal prismatic shape are considered. For the hexagonal foundation, two different incoming wave angles, i.e., propagating to the hexagon corner and to the hexagon edge, are simulated. The waves are fully nonlinear steep non-breaking waves and are modeled by fifth-order stream functions. The present nonlinear wave-structure interaction model and wave-seabed interaction model are validated against the experiments respectively. Soil consolidation behavior in the presence of the foundations is investigated. It is found that the slab geometry has a strong effect on the initial effective stress distribution around the foundation. Steep wave-induced pore pressure distributions and momentary liquefaction depths around the foundations are predicted. It is found that both the slab geometry and incoming wave angle

*This is a journal paper accepted by Ships and Offshore Structures.

can affect the pore pressure distribution and liquefaction depth distribution in the surrounding soil.

keywords: steep wave; soil response; liquefaction; gravity-based; offshore foundations

3.2.1 Introduction

Offshore foundations are installed in an environment that may encounter steep and nonlinear waves. The wave-induced soil liquefaction around the offshore foundations may cause severe soil and further structure failures. The prediction of the wave-induced soil response and liquefaction risk around the offshore foundation is critical in the engineering design. In the recent years, most of the wave-structure-seabed interaction studies have focused on the coastal and offshore structures such as breakwaters (Celli et al., 2019; Jeng, 1997c; Ulker et al., 2010; Ye, 2012b) and monopile foundations (Chang and Jeng, 2014; Li et al., 2011; Lin et al., 2017; Sui et al., 2016; Zhang et al., 2015; Zhao et al., 2017a; Zhu et al., 2018), but very few literature studies have considered the wave-structure-seabed interaction of gravity-based foundations with more complex three-dimensional geometries. Recently, Li et al. (2018) studied the seabed consolidation and liquefaction around a hexagonal foundation using an integrated wave-structure-seabed interaction model developed in OpenFOAM. Stokes wave theories were applied to model the incoming waves in their work. As an extension to their study, the present work focuses on the investigation of the steep, non-breaking wave-induced soil response and liquefaction risk around gravity-based foundations of different geometries and incoming wave angles. The incoming waves in the present study are fully nonlinear and are modeled by fifth-order stream functions, according to Rienecker and Fenton (1981) and Fenton (1988). The nonlinear wave-structure interaction model is validated by comparing the free-surface elevation and the inline force with the experimental data conducted by Grue

and Huseby (2002). The wave-seabed interaction model has been validated in the work of Li et al. (2018) by reproducing the laboratory experiment of Tsai and Lee (1995) of standing wave induced pore pressure under a vertical wall. A good agreement was obtained.

In the present work, gravity-based foundations with bottom slabs of cylindrical shape (a circular foundation) and hexagonal prismatic shape (a hexagonal foundation) are investigated. Fine-grained sandy seabed is modeled. At first, the soil consolidation states in the presence of the foundations in the static water are assessed. The initial effective stress in the soil is calculated. Then, the nonlinear waves are imposed. The nonlinear wave-induced pore pressure and liquefaction depth around the foundations are investigated for the hexagonal and circular foundations. For the hexagonal foundation, two different incoming wave angles with 0 degrees and 90 degrees, i.e., waves propagate to the hexagon corner and to the hexagon edge, are considered. The effect of the incoming wave angle on the liquefaction distribution around the hexagonal foundation is investigated.

3.2.2 Mathematical Models and the Coupling Algorithm

3.2.2.1 Free Surface Wave Model

The wave domain is governed by the incompressible Navier-Stokes equations including the continuity equation and the momentum equations.

$$\nabla \cdot \mathbf{u} = 0 \tag{3.19}$$

$$\frac{\partial \mathbf{u}}{\partial t} + (\mathbf{u} \cdot \nabla)\mathbf{u} = -\frac{1}{\rho}\nabla p + \mathbf{g} + \frac{1}{\rho}\nabla \cdot \boldsymbol{\tau} \tag{3.20}$$

where $\mathbf{u}$ is the velocity vector with three components in the x,y,and z directions respectively; $\mathbf{g}$ is the gravitational acceleration; ρ is the fluid density, p is the pressure and $\boldsymbol{\tau}$ (in Einstein notation τ_{ij}) is the viscous stress tensor. For

Newtonian fluid,

$$\tau_{ij} = 2\mu\sigma_{ij} \tag{3.21}$$

where μ is the dynamic molecular viscosity σ_{ij} is defined by

$$\sigma_{ij} = \frac{1}{2}(\frac{\partial u_i}{\partial x_j} + \frac{\partial u_j}{\partial x_i}) \tag{3.22}$$

where $i, j \in$ [1,2,3]. u_i and u_j are the velocity components in x, y and z direction respectively.

The equations are solved for the two immiscible fluids, i.e., air and water simultaneously. The fluids are tracked by using a scalar field α. $\alpha = 0$ for air and $\alpha = 1$ for water. The distribution of α is modeled by an advection equation

$$\frac{\partial \alpha}{\partial t} + \nabla \cdot \alpha \mathbf{u} + \nabla \cdot [\alpha(1-\alpha)\mathbf{u}_r] = 0 \tag{3.23}$$

The last term on the left-hand side is a compression term, which limits the smearing of the interface, and $\mathbf{u}_r$ is a relative velocity which can be referred to Berberović et al. (2009).

Using α, the spatial variation in any fluid property can be expressed through the weighting

$$\Phi = \alpha\Phi_{water} + (1-\alpha)\Phi_{air} \tag{3.24}$$

Φ is a fluid property, such as μ and ρ.

3.2.2.2 Linear Elastic Structure Model

The structure domain is governed by a linear momentum balance equation,

$$\nabla \cdot \boldsymbol{\sigma} = \nabla \cdot [2\mu\boldsymbol{\varepsilon} + \lambda \mathrm{tr}(\boldsymbol{\varepsilon})\mathbf{I}] = 0 \tag{3.25}$$

and the isotropic linear elastic strain-displacement relations

$$\boldsymbol{\varepsilon} = 1/2(\nabla \mathbf{U} + \nabla \mathbf{U}^T) \tag{3.26}$$

where $\boldsymbol{\sigma}$ is the stress tensor; $\boldsymbol{\varepsilon}$ is the small strain tensor; $\mathbf{U}$ is the structural displacement vector consisting of three coupled components. tr is the trace of an square matrix which is the sum of the elements on the main diagonal, $\mathrm{tr}(\boldsymbol{\varepsilon}) = \sum_{i=1}^{n} \varepsilon_{ii}$. μ and λ are the Lamé's coefficients of elastic material properties which relate to commonly used Young's modulus E and Poisson's ratio ν. The finite volume-based solution to the coupled equations can be referred to the work of Jasak and Weller (2000) and Li et al. (2018).

3.2.2.3 Anisotropic Biot's Poro-Elastic Soil Model

The seabed model is based on assumptions that the sandy seabed is horizontally flat, fully saturated, with anisotropic permeabilities in vertical and horizontal directions. The soil skeleton generally obeys Hooke's law with elastic properties, therefore the classical Biot's consolidation equations (Biot, 1941) can be adopted. For anisotropic soil materials, the orthotropic elastic stress-strain relation can be expressed in a 6×6 matrix notation:

$$\boldsymbol{\sigma}' = \begin{pmatrix} \sigma'_{xx} \\ \sigma'_{yy} \\ \sigma'_{zz} \\ \sigma_{xy} \\ \sigma_{yz} \\ \sigma_{xz} \end{pmatrix} = \begin{bmatrix} A_{11} & A_{12} & A_{31} & 0 & 0 & 0 \\ A_{12} & A_{22} & A_{23} & 0 & 0 & 0 \\ A_{31} & A_{23} & A_{33} & 0 & 0 & 0 \\ 0 & 0 & 0 & A_{44} & 0 & 0 \\ 0 & 0 & 0 & 0 & A_{55} & 0 \\ 0 & 0 & 0 & 0 & 0 & A_{66} \end{bmatrix} \begin{pmatrix} \varepsilon_{xx} \\ \varepsilon_{yy} \\ \varepsilon_{zz} \\ \varepsilon_{xy} \\ \varepsilon_{yz} \\ \varepsilon_{xz} \end{pmatrix} = \mathbf{C} : \boldsymbol{\varepsilon} \tag{3.27}$$

where $\boldsymbol{\sigma}'$ is the effective stress tensor. In the present work, tension is taken as positive while compression is taken as negative. According to Demirdžić et al. (2000), the 9 independent coefficients A_{ij} are calculated from Young's

modulus E_i and Poisson's ratio ν_{ij} and shear modulus G_{ij}. The calculation of the coefficients A_{ij} can be referred to Li et al. (2018).

The soil domain is governed by a quasi-static momentum balance equation and a mass balance equation based on Darcy's law.

Quasi-static momentum balance equation for the soil mixture is expressed as:

$$\nabla \cdot [\mathbf{C} : \frac{1}{2}(\nabla \mathbf{U} + (\nabla \mathbf{U})^T)] - \nabla p = 0 \tag{3.28}$$

where $\mathbf{U}$ is the soil (skeleton) displacement, p is the pore fluid pressure and $\mathbf{C}$ is the fourth-order elastic stiffness tensor.

Mass balance equation for the pore fluid is expressed as:

$$\frac{n}{K'}\frac{\partial p}{\partial t} - \frac{1}{\gamma_w}\nabla \cdot (\mathbf{k} \cdot \nabla p) + \frac{\partial}{\partial t}(\nabla \cdot \mathbf{U}) = 0 \tag{3.29}$$

where n is the soil porosity, γ_w is the specific weight of water in soil, and $\mathbf{k}$ is the diagonal permeability tensor with values of k_x, k_y and k_z. The bulk modulus of the compressible pore flow $K^{'}$ is approximately computed by the formulation Vafai and Tien (1981):

$$\frac{1}{K'} = \frac{1}{K_w} + \frac{1 - S_r}{p_a} \tag{3.30}$$

where S_r is the degree of soil saturation, K_w is the bulk modulus of pure water and p_a is the absolute pore water pressure.

The wave, structure and seabed domains are coupled by the data transfer at the common boundaries. A one-way coupling algorithm is adopted, as illustrated in Figure 3.26. The data is transferred in a single direction and the structure and seabed deformations do not alter the wave domain. This is because that the present study is focused on the steep wave-induced momentary liquefaction, which means the phenomenon that investigated is an instantaneous phenomenon. Therefore, the time-dependent effect of wave-induced

structure vibration on the wave and seabed domains and the effect of seabed deformation on the structure and wave domains are neglected.

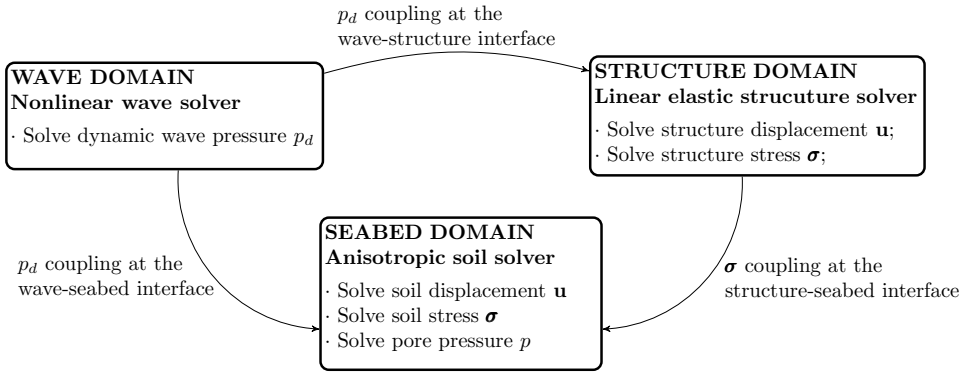

Figure 3.26 One-way boundary coupling algorithm of wave-structure-seabed interaction.

3.2.3 Model Validation

3.2.3.1 Validation of Nonlinear Wave-Structure Interaction

The present nonlinear wave-structure interaction model is validated against the experiment conducted by Grue and Huseby (2002). Their test of regular steep waves propagating towards a vertical circular cylinder (Figures 3(c) and 3(d) in Grue and Huseby (2002)) is reproduced. The free surface elevation and the inline force on the cylinder are compared between the present numerical simulation and the experimental data. The parameter setting for reproducing the experiment is shown in Table 3.6. D is the diameter (characteristic length) of the cylinder, h_w is the water depth, η_m is the wave crest elevation and k is the wave number. The fully nonlinear stream function wave theory is used in the numerical wave generation. A slip boundary condition is set at the cylinder surface and the seabed. The number of grid points for the free surface is 32 in the present study.

Figure 3.27 presents the comparison between the numerical results and the experimental measurements. Both the free surface elevation and the inline force are in good agreement (converging to 1-3% discrepancy as the waves develop). The experimental measurement contains second-order spurious waves from first-order wave generation. In the numerical simulation, the second-order spurious waves are avoided in the fully nonlinear stream function wave model, as pointed out by Paulsen et al. (2014).

Table 3.6 Parameters of the steep wave propagation experiment of Grue and Huseby (2002)

D (m)	h_w (m)	T (s)	$k\eta_m$	H (m)	η_m
0.06	0.6	0.86	0.34	0.11	0.662

3.2.3.2 Validation of Wave-Seabed Interaction

The present wave-induced seabed response model has been validated in the work of Li et al. (2018). The experiment performed by Tsai and Lee (1995) of standing wave-induced soil response in the vicinity of a vertical wall was reproduced. It showed that the present numerical results are in good agreement with the measured data.

3.2.4 Model Application

3.2.4.1 Numerical Settings

The present work focuses on two types of gravity-based foundations. The geometries of the foundations are shown in Figure 3.28.

The entire multi-physic numerical system is established in the 3D Cartesian coordinate system. $z = 0$ is located at the undisturbed free surface. x positive towards the wave propagation direction, y positive towards the left

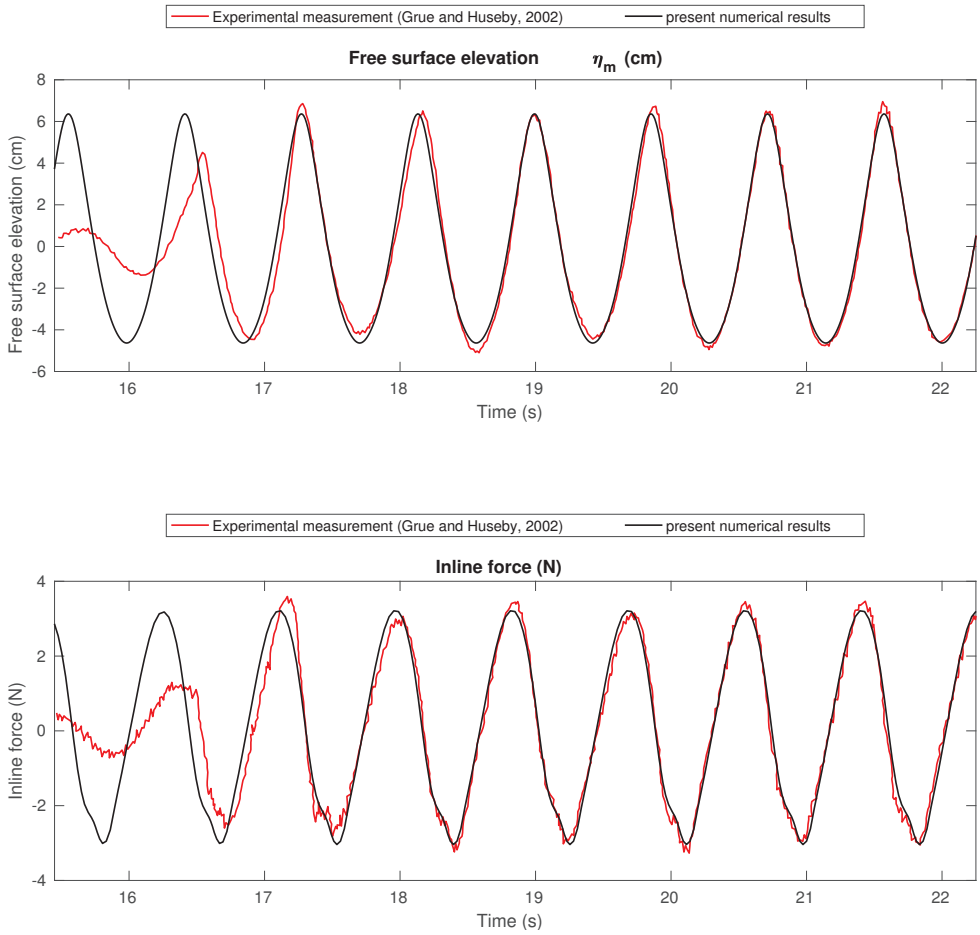

Figure 3.27 Validation study of nonlinear wave propagation to a vertical structure by comparing to the experimental data of Grue and Huseby (2002).

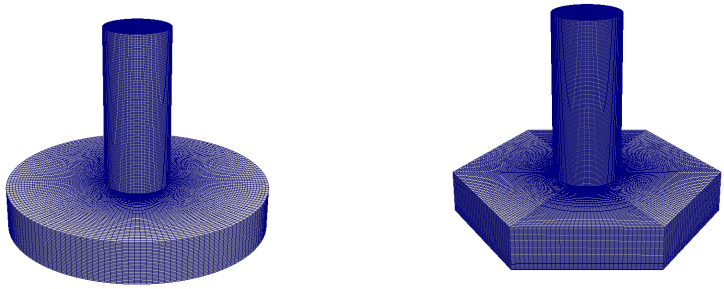

(a) Foundation with cylindrical slab.

(b) Foundation with hexagonal prismatic slab.

Figure 3.28 Geometries and meshes of the structures.

side of the wave propagation direction, and z positive upwards. The layout of the numerical system is shown in Figure 3.29. The wave inlet relaxation zone (Jacobsen et al., 2012) is set to be one wave length. The wave outlet relaxation zone is set to 1.25 wave lengths to absorb waves and ensure no reflection from the outlet boundary. The width of the wave tank (distance between the sides of the tank) is set to be two wave lengths.

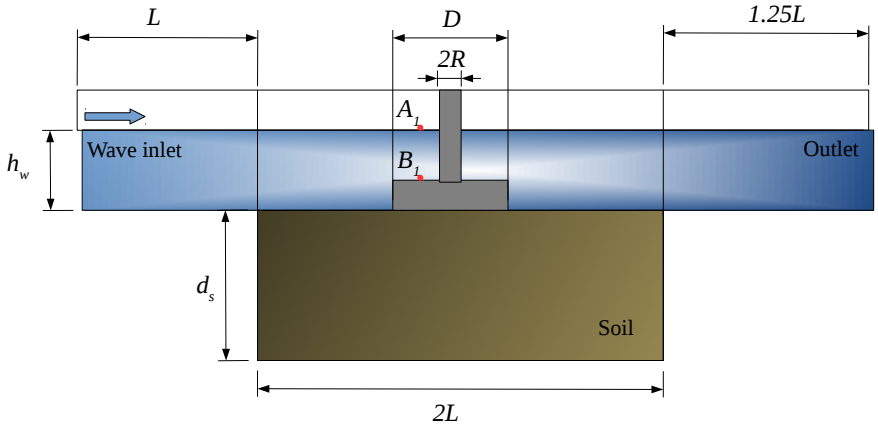

Figure 3.29 A sketch of the numerical layout for the wave-structure-seabed interaction model.

Table 3.7 gives the parameter settings in the present work. The water depth is $h_w = 10m$, the wave height is $H = 4m$ and the wave period is $T = 10s$. According to Le Mehaute (2013), the present wave condition exceeds the modeling ranges of linear wave theory and Stokes wave theory. It should be modeled by using the fifth-order stream function theory (Dean, 1965; Fenton, 1988) for the steep non-breaking waves. The Keulegan-Carpenter number (KC number) (Journée and Massie, 2000) for the simulated condition is 1.70, which is a small value that indicates the drag force which comes from the viscosity is negligible compared to inertial forces. Hence, turbulence modeling is not considered.

For the hexagonal foundations, two wave angles are considered in terms of waves come towards the hexagon corner (wave angle of 0 degrees) and waves come towards the hexagon edge (wave angle of 90 degrees), respectively. As shown in Figure 3.30, three points P1, P2 and P3 around the foundation are identified. The characteristic length of the foundation D is defined as the distance between P1 and P3 .

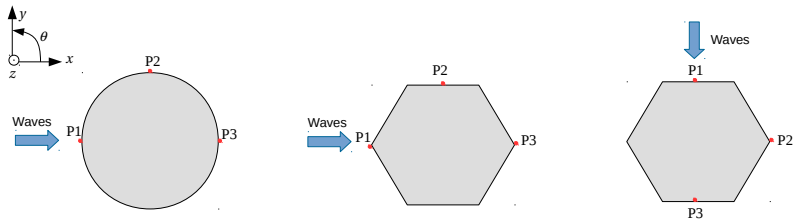

(a) circular foundation (wave angle=0°). (b) hexagonal foundation (wave angle=0°). (c) hexagonal foundation (wave angle=90°).

Figure 3.30 Top views of waves incoming to the circular and hexagonal foundations.

3.2.4.2 Boundary Conditions

Boundary conditions for the multi-physic model are specified as follows.

Wave domain:

Table 3.7 Parameter settings for wave-structure-seabed interaction modeling in the present study.

Wave parameters			
Wave height H (m)	4.0		
Wave period T (s)	10.0		
Water depth h_w (m)	10.0		
Wave length L (m)	98.2		
KC number	1.70		
Structure parameters			
Characteristic length D (m)	19.0		
Bottom slab height h_b (m)	3.0		
Shaft radius R (m)	2.25		
Density ρ (kg/m^3)	2400		
Young's modules (N/m^2)	2.2×10^{10}		
Poisson's ratio	0.2		
Seabed parameters		Directional values	
Young's modules (N/m^2)	$E_x = 1.2 \times 10^7$	$E_y = 1.2 \times 10^7$	$E_z = 2 \times 10^7$
Poisson's ratios	$\nu_{xy} = 0.2$	$\nu_{yz} = 0.24$	$\nu_{zx} = 0.4$
Shear modulus (N/m^2)	$G_{xy} = 5 \times 10^6$	$G_{yz} = 1.2 \times 10^7$	$G_{zx} = 1.2 \times 10^7$
Permeabilities(m/s)	$k_x = 0.0005$	$k_y = 0.0005$	$k_z = 0.0001$
Saturation factor S_r	0.98		
Porosity n	0.3		

At the inlet boundary, the velocity is specified as the input wave velocity. At the outlet boundary, the velocity is set to zero. At four sides of the numerical wave tank, the normal gradient of the pressure is set to zero, i.e. $\frac{\partial p}{\partial n} = 0$. At the atmosphere, the pressure is set to be atmosphere pressure $p = p_0$. At the wave-structure interface and the wave-seabed interface, slip velocity boundary is set since the viscous effects at the walls are negligible.

Structure domain:

The structure transfers the dynamic wave loading to the seabed. At the wave-structure interface, the nonuniform and time-varying dynamic wave pressure is imposed on the structure. At the structure-seabed interface, the

instantaneous structural stress is read by the soil solver to compute the compatible time-varying displacement gradient boundary for the seabed.

Seabed domain:

At the wave-seabed interface, the soil has zero effective shear stress while the pore pressure is equal to the dynamic wave pressure. At the structure-seabed interface, it is considered that the structure is impermeable. Thus, the pore pressure has zero normal gradient, according to Darcy's flow equation. At the bottom and lateral boundaries of the seabed, a slip boundary is applied for the soil skeleton. The normal pore pressure gradient is zero.

3.2.5 Results and Discussions

3.2.5.1 Consolidation

Once the structure is placed on the seabed, the gravitational forces will induce the compression of the soil skeleton and the gradual dissipation of the excess pore pressure. The soil consolidation behavior will further affect the potential risk of wave-induced soil liquefaction (Sui et al., 2017; Ulker et al., 2010; Zhao et al., 2017a). Therefore, it is essential to do consolidation analysis before investigating the momentary liquefaction of the seabed around the foundations. In the present work, the consolidation process is simulated for each type of the structure. According to the 1D Terzaghi's consolidation theory, the time for completing 90% consolidation can be expressed as (Wang, 2017):

$$t_{90} = T_v \frac{H_d^2}{c_v} \tag{3.31}$$

where H_d is the drainage distance of the layer, $T_v = 0.848$ is the vertical consolidation time factor for 90% consolidation, c_v is the consolidation coefficient calculated by

$$c_v = \frac{2Gk_z(1-\nu)}{\gamma_w(1-2\nu)} \tag{3.32}$$

where k_z is the vertical permeability and γ_w is the bulk specific weight of the pore water. In the present study, the longest time for reaching the 90% consolidation state is estimated as 3230s.

Figure 3.31 shows the vertical soil displacement U_z after the completion of the consolidation in the presence of the circular foundation. A negative value of U_z means the soil skeleton is compressed and moving downward. It is seen that around the foundations, the soil skeleton has been largely compressed. Compared to the circumstance without a structure, the presence of the foundation changes the surrounding soil displacement behavior.

Figure 3.32 presents the distribution of the initial vertical effective stresses $\sigma_z^{'}$ in the soil after the consolidation process. A negative value of $\sigma_z^{'}$ indicates the compression of the soil skeleton. In the long-time consolidation process, the gravity forces gradually transfer to the supporting soil skeleton. It shows that the initial vertical effective stress below the foundation is amplified compared to the far field. Similar soil consolidation behavior can be observed in the presence of the hexagonal foundation, as shown in Figure 3.33a and 3.33b.

A cross-sectional view of vertical soil effective stress at z=-10.1m (0.1m below the seabed surface) is shown in Figure 3.34. It is observed that for the circular foundation, the initial vertical effective stress is evenly distributed in the surrounding soil. However, for the hexagonal foundation, the compressive stress at the corners is higher than that at the edges. This is because that the sharp corners of the hexagon cause stress concentration in the soil. The initial vertical effective stress $\sigma_z^{'}$ at the end of the consolidation process will be used as an initial condition to evaluate the momentary liquefaction risk.

It is worthwhile to mention that the 'pre-shear history' of sand may have effect on its liquefaction resistance. Ye et al. (2015a) studied the liquefaction risk of the sand with different initial shear stress $\sigma_{\theta z}$ ($\sigma_{\theta z}$ correspond to clockwise shear load). They found that a high initial shear stress ratio (i.e., $\sigma_{\theta z}$ / mean effective stress) can speed up the liquefaction process. However, in

the present study, the initial shear stress that is triggered by the consolidation process is negligible compared to the initial vertical effective stress. As shown in Figure 3.35, the magnitudes of initial shear stress σ_{xz0} and initial vertical effective stress σ'_{z0} beneath the corner of the hexagonal foundation are compared. It is observed that the magnitude of σ_{xz0} is negligible compared to σ'_{z0}, which means that the initial shear stress ratio is very small. Therefore, the effect of 'pre-shear history' of sand on the liquefaction analysis is not considered in the present work.

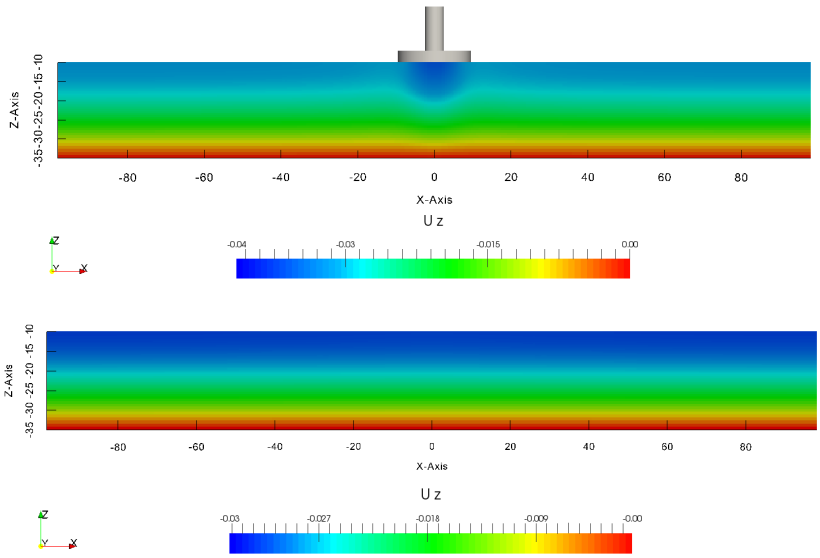

Figure 3.31 Initial vertical displacement (m) of the seabed after the completion of the consolidation with and without the circular foundation.

3.2.5.2 Nonlinear Wave-Induced Soil Response

Nonlinear steep waves are imposed on the structure and seabed. Figure 3.36 presents the time histories of free surface elevation at the location A1 and the corresponding bottom wave pressure at B1. The locations of the points are shown in Figure 3.29. It is observed that the interaction between the waves

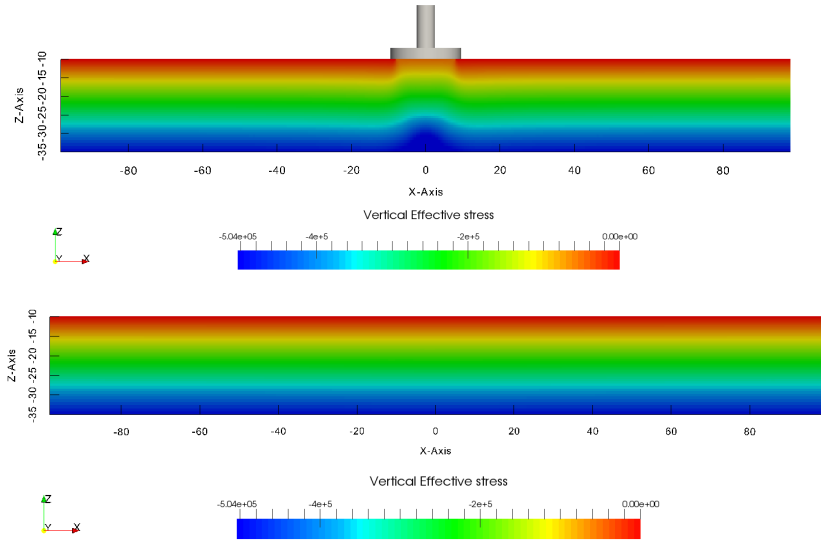

Figure 3.32 Initial vertical effective stress (N/m^2) in the seabed after the completion of the consolidation with and without the circular foundation.

and the foundations triggers strong nonlinearity of free surface elevation. It affects the bottom wave pressure, which shows a similar nonlinear effect.

The wave diffraction effect causes various pore pressure distributions at different locations around the foundation. According to Li et al. (2018), the soil beneath the foundation is shielded from the dynamic waves, so that the pore pressure underneath the foundation bottom has relatively small variations. Therefore, liquefaction is less likely to happen under the foundation bottom. The present work focuses on investigating the pore pressure distribution around the foundations. The vertical profiles of transient pore pressure at three typical locations surrounding the foundation are shown in Figure 3.37. P1 is at the upstream side of the foundation when waves first hit the surface of the foundations. P2 is at the location of 90 degrees from the upstream. P3 is at the downstream side of the foundation.

In Figure 3.37, vertical pore pressure profiles at time instants of t/T=8 and t/T=8.5 are presented. The vertical distance to the seabed surface $z^{'}$ is

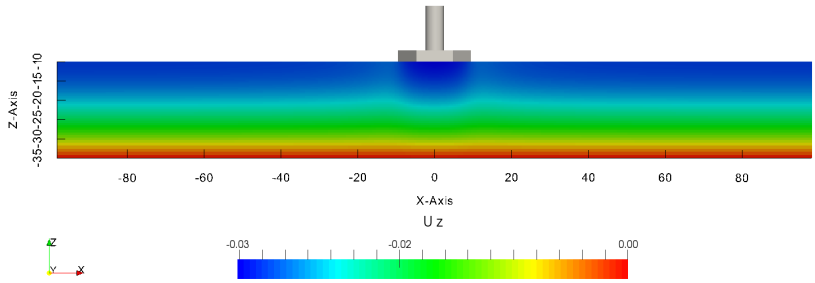

(a) Initial vertical displacement (m) of the seabed beneath the hexagonal foundation.

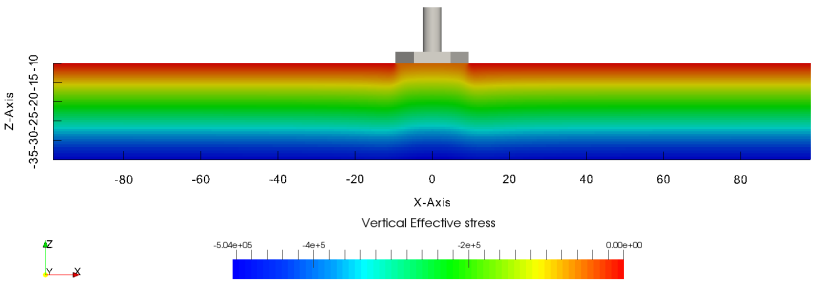

(b) Initial vertical effective stress (N/m^2) in the seabed beneath the hexagonal foundation.

Figure 3.33 Initial vertical displacement (m) and initial vertical effective stress (N/m^2) in the seabed after the completion of the consolidation with the hexagonal foundation.

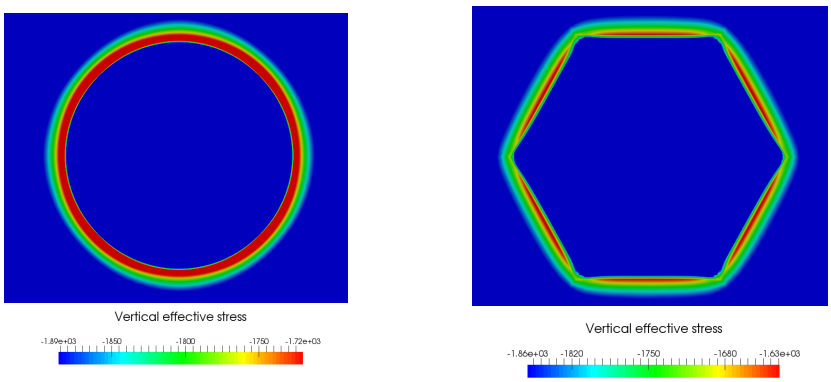

Figure 3.34 A cross-section of the initial vertical effective stress (N/m^2) of the seabed after the completion of the consolidation at 0.1m below the seabed surface (z=-10.1m).

normalized by the seabed thickness D_s. Figure 3.37 shows that the magnitude of pore water pressure decreases rapidly from the seabed surface to approximately $z^{'}/D_s = -0.25$. Then, the magnitude remains almost unchanged until to the seabed bottom ($z = -D_s$). Comparing between the three curves in each sub-figure, it is observed that the pore pressure profiles at P1 (upstream) has the highest changes from the seabed surface to a depth at $z^{'}/D_s = -0.25$. This indicates that the pore pressure gradient at the upstream of the foundations are generally higher than that at the downstream of the foundations. Therefore, the liquefaction risk at the upstream can be relatively higher. The same phenomenon is found in the work of Lin et al. (2017). Their study showed that the liquefaction depth at the upstream side of the monopile is around 15%-20% higher than that at the downstream side. However, this conclusion can only be drawn when the soil consolidation process is not considered. In fact, when the structure is placed on the seabed, the effective stress in the surrounding soil can significantly increase, which further influences the momentary liquefaction depth around the foundation (Sui et al., 2017; Ulker et al., 2010; Zhao et al., 2017a).

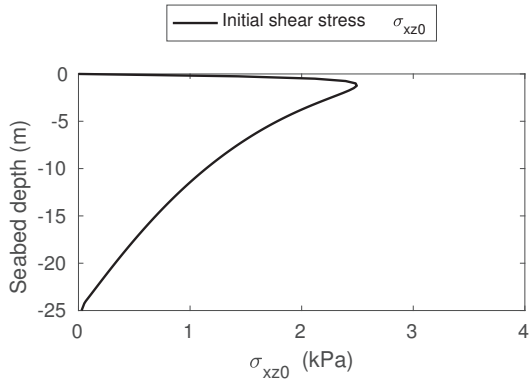

(a) Initial shear stress σ_{xz0} beneath the corner of the hexagonal foundation.

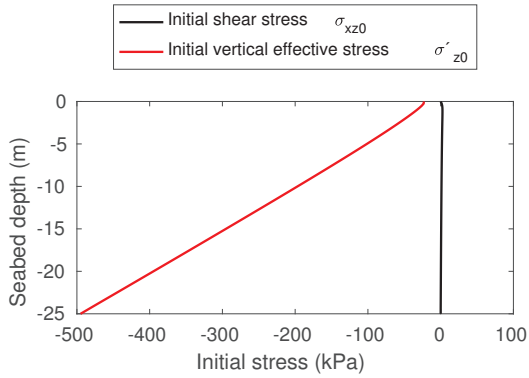

(b) Comparing the magnitudes of initial shear stress σ_{xz0} and initial vertical effective stress σ'_{z0} beneath the corner of the hexagonal foundation.

Figure 3.35 Vertical distributions of initial shear stress and initial vertical effective stress after the consolidation process. It is observed that the magnitude of σ_{xz0} is negligible compared to σ'_{z0}.

(a) circular foundation (wave angle=0°).

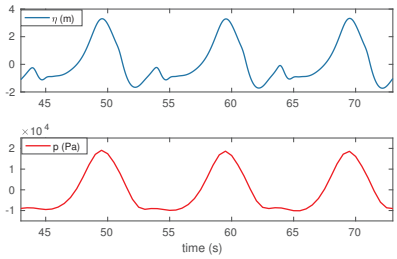

(b) hexagonal foundation (wave angle=0°).

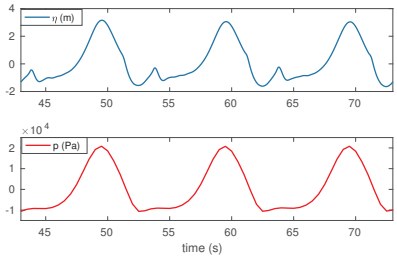

(c) hexagonal foundation (wave angle=90°).

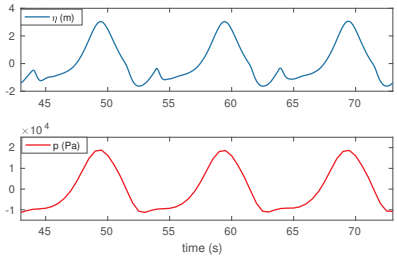

Figure 3.36 Time histories of the free surface elevation and the corresponding bottom wave pressure.

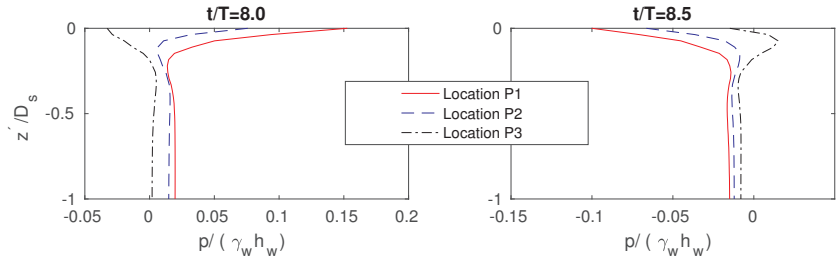

(a) Transient pore pressure distribution around the circular foundation.

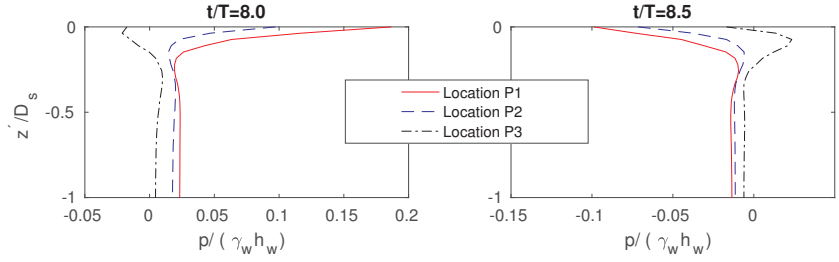

(b) Transient pore pressure distribution around the hexagonal foundation with 0 degrees incoming waves.

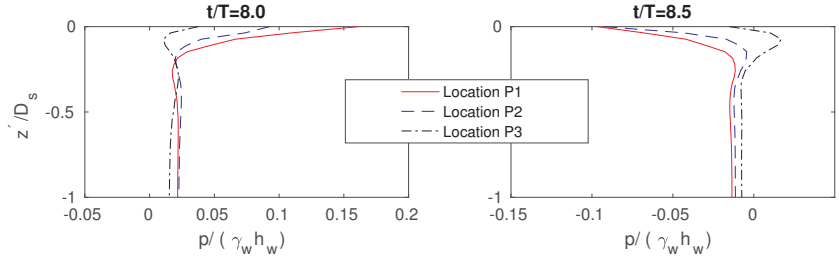

(c) Transient pore pressure distribution around the hexagonal foundation with 90 degrees incoming waves.

Figure 3.37 Transient pore pressure distribution at two time instants around the offshore foundations.

Momentary liquefaction happens periodically under the wave trough. At this moment, upward seepage flows are generated. Figure 3.38 shows the vertical distribution of the maximum amplitude of negative pore pressure within a wave cycle. It is observed that, when incoming waves are perpendicular to the edge of the hexagonal foundation (Figure 3.38 (c)), the vertical gradient of the pore pressure is the highest among the three cases. In Figure 3.38 (b), incoming waves first hit the corner of the hexagon. The pore pressure and vertical pore pressure gradient at location P1 are smaller than that in Figure 3.38 (c). This is because when waves hit the corner, the change of wave velocity in the wave propagating direction is smaller than when waves hit the edge. In the latter case, when waves hit the edge of the hexagon, the wave velocity component perpendicular to the edge becomes zero, so that the pressure is significantly increased. For the circular foundation, the change of the wave velocity is milder when waves diffract around the circular geometry, so that the pore pressure gradient around the circular foundation is generally smaller than that around the hexagonal foundations.

Based on the discussion above, the upstream of the hexagonal foundations can experience a higher pore pressure gradient than the circular foundation. If the initial effective stress caused by the seabed consolidation process is not considered, the liquefaction risk at the upstream of the hexagonal foundation should be higher than that at the upstream of the circular foundation.

3.2.5.3 Liquefaction

So far in the literature, various liquefaction criteria for investigating the momentary liquefaction have been proposed based on the either the effective stress (Okusa, 1985; Tsai, 1995), or the excess pore pressure (Jeng, 1997c; Zen and Yamazaki, 1990b). Ye (2012a) performed a comparison study of different liquefaction critera. For the liquefaction analysis considering the seabed consolidation around a marine structure, a modified criterion based on

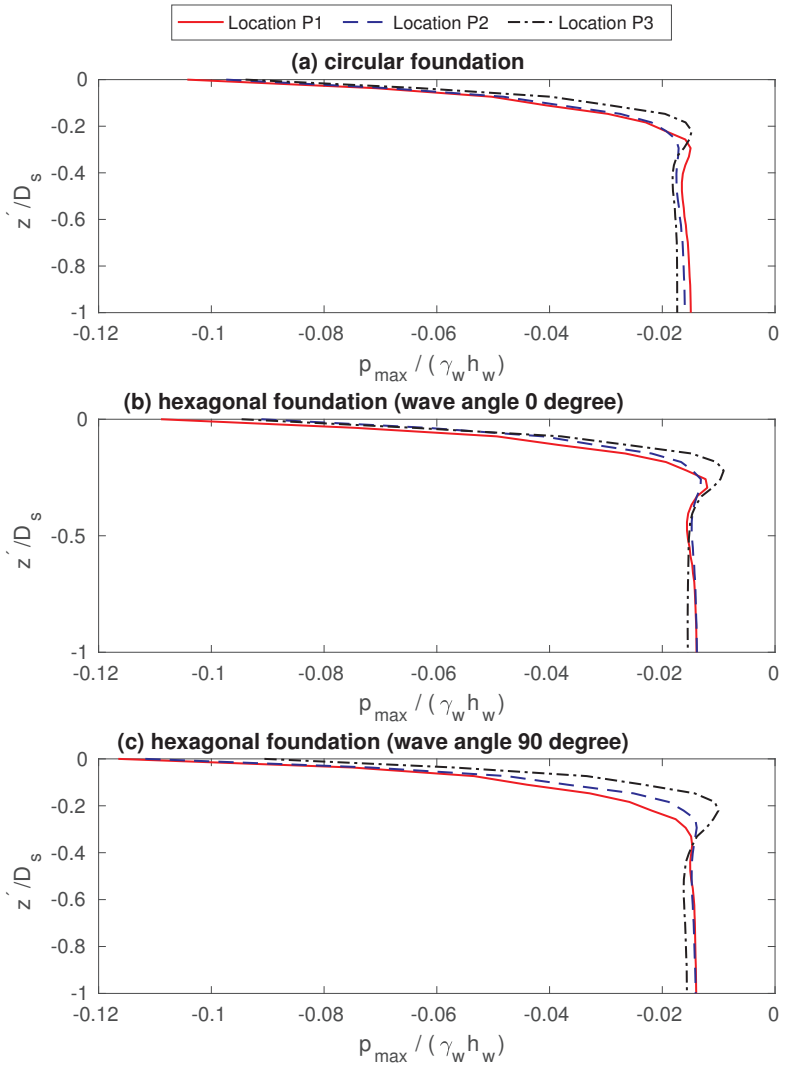

Figure 3.38 Vertical distribution of the amplitude of the negative pore pressure.

Zen and Yamazaki (1990b) is recommended. The criterion is given by:

$$p - p_b \geq \sigma_{z0}^{'} \tag{3.33}$$

where $\sigma_{z0}^{'}$ is the initial vertical effective stress induced by the gravitational forces from the consolidation process.

Maximum liquefaction depth in a wave cycle around the hexagonal foundations and the circular foundation are presented in Figure 3.39. It is seen that for the circular foundation, the liquefaction depth is approximately averagely distributed around the circular foundation. The upstream side has a sightly higher liquefaction depth than the downstream side. The reason is explained in the Section of Nonlinear Wave-Induced Soil Response.

For the hexagonal foundations, the initial soil effective stress around the corners is higher than that around the edges, so that liquefaction is less likely to happen around the hexagon corners, as shown in Figure 3.39 (b)(c). However, when incoming waves propagate towards the hexagon corner (Figure 3.39 (b)), the high pore pressure gradient can cause notable upward seepage flow. Therefore, liquefaction happens at the upstream corner in Figure 3.39 (b). When incoming waves propagate 90° to the hexagon edge, as shown in Figure 3.39 (c), no liquefaction is observed at the hexagon corners.

In the real ocean environment, the waves are nonuniform and non-unidirectional, so that both the corners and edges of the hexagonal foundation can experience liquefaction and therefore need specific protections. Chang and Jeng (2014) studied the seabed protection methodology and suggested to replace the existing layers of the surrounding soil with materials of higher permeability to mitigate the liquefaction risk. It is noted that the process of soil liquefaction can be closely related to scour. In the experiment by Sumer et al. (2007), liquefaction and scour around a monopile were observed in one experiment. As discussed in Whitehouse (1998), since a liquefied bed has almost no shear strength, the sediment can be eroded more easily than a non-liquefied bed. In the engineering practice, gravity-based structures are usually fitted with a skirt

to prevent the hydraulic process of scour channels penetrating underneath the structure.

3.2.6 Conclusions

The present study has investigated the soil consolidation, steep wave-induced soil response and the momentary liquefaction risk around gravity-based offshore foundations. Two different geometries are considered in terms of a circular foundation and a hexagonal foundation. For the hexagonal foundation, two different incoming wave angles are investigated in terms of waves come towards the hexagon corner and waves come towards the hexagon edge. A 3D FVM-based wave-structure-seabed interaction model has been applied. The nonlinear wave-structure interaction model and wave-seabed interaction model have been validated against existing experimental data. Good agreement has been obtained. An anisotropic poro-elastic model has been applied for the soil analysis. The following conclusions can be drawn from the present study:

1) The presence of the foundations on the seabed leads to the compression of the soil in the vicinity of the structure during the consolidation process. The initial vertical effective stress in the surrounding soil is increased. The slab geometry of the foundation affects the initial effective stress distribution. For the circular foundation, the initial vertical effective stress is evenly distributed in the surrounding soil. However, for the hexagonal foundation, the geometry triggers stress concentration in the soil around the corners. The compressive stress at the corners is much higher than that at the edges.

2) Generally, when waves propagate towards the foundations, the pore pressure gradient at the upstream of the foundations is higher than that at the downstream. Therefore, the liquefaction risk at the upstream of the foundation can be relatively higher. This is due to the wave diffraction effect.

3) For the circular foundation, the liquefaction depth is approximately averagely distributed around the circular foundation, except that the upstream

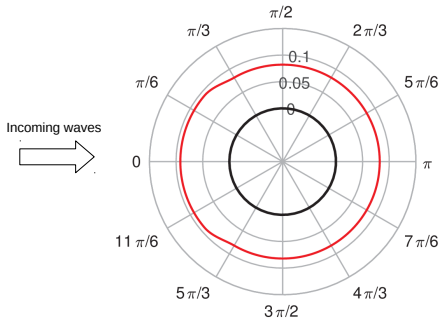

(a)

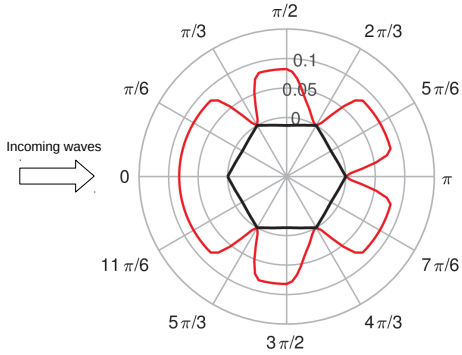

(b)

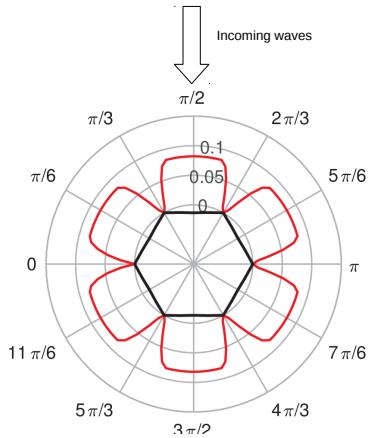

(c)

Figure 3.39 Maximum liquefaction depth (m) in a wave cycle around the circular foundation (a) and the hexagonal foundations (b)(c).

side has a sightly higher liquefaction depth than the downstream side. For the hexagonal foundations, the distribution of the initial soil effective stress from the consolidation process affect the liquefaction zone distribution. The momentary liquefaction is less likely to happen around the hexagon corners due to high initial effective stress.

4) Wave direction affects the pore pressure and the liquefaction distribution around the hexagonal foundation. When incoming waves propagate towards the hexagon corner, the high pore pressure gradient can cause notable upward seepage flow. Although the initial effective stress at the hexagon corners is high, significant upward excess pore pressure can still trigger liquefaction around the upstream corner. However, when incoming waves propagate 90° to the hexagon edge, no liquefaction is observed at the hexagon corners.

5) In the real ocean environment, the waves are nonuniform and non-unidirectional, so that both the corners and edges of the hexagonal foundation can experience liquefaction and therefore need liquefaction protections.

More experimental data is required before a final conclusion can be given. Meanwhile, the present method could be useful as an engineering tool for predicting the wave-induced soil response and momentary liquefaction risk around offshore foundations.

3.2.7 Acknowledgement

This study was supported in part with computational resources provided by the Norwegian Metacenter for Computational Science (NOTUR), under Project No: NN9372K.

3.3 Paper III: The role of submerged berms on the momentary liquefaction around conventional rubble mound breakwaters

Daniele Celli[a], Yuzhu Li[b], Muk Chen Ong[b]
and Marcello Di Risio[c]
[a] Department of Civil, Environmental, Territory, Building and Chemical Engineering, Technical University of Bari, Bari, Italy
[b] Department of Mechanical and Structural Engineering and Materials Science, University of Stavanger, Stavanger, Norway
[c] Department of Civil, Construction-Architectural and Environmental Engineering, University of L'Aquila, L'Aquila, Italy

Abstract*: Berms deployed at the toe of conventional rubble mound breakwaters can be very effective in improving the stability of the armor layer. Indeed, their design is commonly tackled by paying attention to armor elements dimensioning. Past research studies showed how submerged berms can increase the stability of the armor layer if compared to straight sloped conventional breakwaters without a berm. To fill the gap of knowledge related to the interaction between breakwaters with submerged berm, waves and soil, this research aims to evaluate how submerged berms configuration influences the seabed soil response and momentary liquefaction occurrences around and beneath breakwaters foundation, under dynamic wave loading. The effects of submerged berms on the incident waves transformation have been evaluated by means of a phase resolving numerical model for simulating non-hydrostatic, free-surface, rotational flows. The soil response to wave-induced seabed pressures has been evaluated by using an ad-hoc anisotropic poro-elastic soil solver. Once the evaluation of the seabed consolidation state due to the presence of the breakwater has been performed, the dynamic interaction

*This is a journal paper published in Applied Ocean Research 85 (2019): 1-11.

among water waves, soil and structure has been analyzed by using a one-way coupling boundary condition. A parametric study has been carried out by varying the berm configuration (i.e. its height and its length), keeping constant the offshore regular wave condition, the berm and armor layer porosity values, the water depth and the elastic properties of the soil. Results indicate that the presence of submerged berms tends to mitigate the liquefaction probability if compared to straight sloped conventional breakwater without a berm. In addition, it appears that the momentary liquefaction phenomena are more influenced by changing the berm length rather than the berm height.

keywords: Breakwaters; Berm; SWASH; Momentary liquefaction; Numerical models

3.3.1 Introduction

Conventional rubble mound breakwaters are widely used all over the world, mainly to provide protection for harbors (e.g. Van Der Meer, 1988) and to preserve coastal areas (Di Risio et al., 2010; Lamberti et al., 2005; Saponieri et al., 2018b) from currents and wave actions. Therefore, the design of the breakwaters is aimed to ensure stability against such environmental loads. Furthermore, in order to limit the scour induced by the coastal currents (e.g. Saponieri et al., 2018a) and the storm surge (e.g. Pasquali et al., 2015), and to increase the stability of the armor layer (e.g. Celli et al., 2018; Van Gent, 2013), it can be appropriate to modify the straight slopes of conventional breakwaters, by deploying a submerged berm marked by a higher length than usual. As reported in literature (e.g. Chung et al., 2006; Elsafti and Oumeraci, 2016b, 2017; Franco, 1994; Oumeraci, 1994; Zhao et al., 2017b), some of the failures experienced by coastal structures are likely due to geotechnical causes, such as the wave-induced liquefaction. It could be hence interesting to evaluate the performances of submerged berms of reducing the liquefaction probability in the soil, in the vicinity of the breakwaters.

When water waves propagate over a non-cohesive seabed and interact with coastal structures, excess pore pressure can be generated, enabling the rise of two different types of liquefaction (Nago et al., 1993): the "residual" liquefaction and the "momentary" liquefaction. The "residual" liquefaction is caused by compression-relaxation cycles under wave crests and wave troughs, respectively. It generates shear stresses in the soil and the consequent buildup of pore water pressure that could exceed the value of the overburden pressure, making the soil grains totally unbound (Sumer, 2014a). The "momentary" liquefaction occurs during the passage of wave troughs if the upward pore pressure gradient (strictly related to seepage forces) exceeds the initial vertical effective stress. When a pore pressure gradient exists, a seepage flow arises (e.g. Zen and Yamazaki, 1990a). It generates seepage forces on the soil skeleton in the direction of the flow, as seen from Figure 13 and 14 in Ye et al. (2014). At the passage of wave crests are hence associated pressure gradients acting downwards, enhancing the grain compaction, excluding liquefaction occurrences. On the contrary, upward pressure gradients, generated under the wave troughs, may uplift the soil, inducing seabed instability (Jeng and Ye, 2012).

The work proposed herein deals with rubble mound breakwaters with submerged berms. The potential structure failure of rubble mound breakwaters may result from both residual and transient pore pressure generation. The present work is focused on the evaluation of submerged berms configuration only upon momentary liquefaction occurrences.

In the past decades, research studies have been carried out on the interaction between waves, seabed and structures (hereinafter referred to as WSSI). In this regard, Mase et al. (1994) and Hur et al. (2010) used the classic Biot's poro-elastic theory to investigate the seabed response around a composite caisson-type breakwater by using numerical tools. Ulker et al. (2010), Ye et al. (2015c, 2014) and Zhao et al. (2017b) simulated the presence of a composite caisson-type breakwater in their numerical models, showing that the

assessment of the consolidation process, in presence of marine structures, is essential for the liquefaction analysis. In particular, Ulker et al. (2010) studied the instability of the porous seabed-rubble foundation due to the momentary liquefaction, by adopting three different formulations for the Biot's equations. Ye et al. (2014) investigated the interaction between breaking waves, seabed foundation and composite breakwater, by carrying out a parametric study about the maximum momentary liquefaction depth as a function of the soil properties and the wave characteristics. Furthermore, Ye et al. (2015c) and Zhao et al. (2017b) focused their attention on the residual liquefaction around the structure, under the combined action of both waves and caisson rocking motions. To remain within the breakwater framework, Zhao and Jeng (2015) carried out a parametric study on the effects of wave and soil characteristics, as well as bed slopes, on the wave-induced residual liquefaction in the vicinity of a breakwater. Liao et al. (2018a,b) used both a three-dimensional integrated numerical scheme to evaluate the WSSI around a slope-type breakwater head. Their results showed that the breakwater slope has significant effects on the seabed response. In particular, an increase of the breakwater slope could intensify the soil response and the liquefaction probability around the breakwater head. Zhao et al. (2018) developed a numerical model to investigate the interactions between waves, currents, a submerged rubble mound breakwater and its poro-elastic seabed foundations. Their results showed the significant influences of currents on the local hydrodynamic process and the resulting dynamics of seabed foundation around a submerged rubble mound breakwater.

To date, the effects of submerged berms on the liquefaction phenomenon around rubble mound breakwaters have been given little attention in the literature. Therefore, the aim of the present research is to investigate the wave-induced soil response and momentary liquefaction probability around and beneath rubble mound breakwaters with submerged berm. A parametric study has been carried out by varying the berm configuration in terms of its length

and its height, keeping constant the elastic properties of the soil, the berm and the armor layer porosity values, the water depth and the offshore regular wave condition. This is to assess if the introduction of a submerged berm will provide improvements in terms of reduction of liquefaction probability, if compared to the case of straight sloped conventional breakwaters without a berm. The adopted rationale, based on a parametric-comparative study, makes reasonable the regular wave assumption, despite irregular waves always occur in real ocean environments. The features of the present work are:

i) the water waves hydrodynamic properties have been evaluated by means of SWASH, an open source phase resolving numerical model for simulating non-hydrostatic, free-surface, rotational flows (Zijlema et al., 2011), due to its efficiency;

ii) an open-source poro-elastic soil solver including both consolidation and liquefaction analysis has been adopted for the present study. The soil model was developed within the Finite Volume Method (hereinafter referred to as FVM)-based OpenFOAM framework by Li et al. (2018) and was already employed for the detection of momentary liquefaction occurrences within the WSSI framework. It takes into account the anisotropy since most of the natural soils show some degree of anisotropy, i.e., having different elastic and hydraulic properties in different directions, according to Hsu and Jeng (1994b). The interaction between the multiple physical phases has been implemented by using the seabed dynamic pressure as one-way coupling boundary condition for the poro-elastic anisotropic soil model;

iii) a parametric study has been carried out to investigate the efficiency of a berm in reducing the momentary liquefaction phenomena. The optimal berm configuration has been identified from the parametric study.

Since the parametric study has involved 62 numerical simulations, SWASH is used to calculate the hydrodynamic properties associated to wave propagation

in presence of porous structure (e.g. Celli et al., 2018) in a fast way and with low computational cost (about 2 hours of wall clock time adopting 16 cores and 58 MB of pressure data per simulation produced). The usage of this type of tool enables to carry out an extensive parametric study in a reasonable time window.

3.3.2 Mathematical models and the coupling algorithm

3.3.2.1 The wave numerical model

The numerical model SWASH has been used to compute the water wave hydrodynamic properties within the wave-structure interaction framework. It is an open source phase resolving numerical model for simulating non-hydrostatic, free surface, rotational flows (Zijlema et al., 2011). The model has been widely validated and used within several research studies, including the interaction among waves and both impermeable (Marmoush and Mulligan, 2016; Suzuki et al., 2017) and porous structures (Alabart et al., 2014; Celli et al., 2018; van den Bos et al., 2015, 2014). In the followings, only a synthetic description of the model is illustrated. For further details, the reader can refer to the model manual (The SWASH team, 2017). The model solves the shallow water equations including a non-hydrostatic pressure term that can be derived from the incompressible Navier-Stokes equations and a module for porous flow on the basis of Forchheimer's formulations. The former relationships are included in the porous momentum equations by means of two extra dissipative terms, f_l (laminar) and f_t (turbulent), equal to:

$$f_l = \alpha_0 \frac{(1-n)^3}{n^2} \frac{\nu}{D_{n50}^2} \qquad f_t = \beta_0 \frac{(1-n)}{n^3} \frac{1}{D_{n50}} \tag{3.34}$$

where α_0 and β_0 are the Forchheimer's coefficients, n is the porosity and D_{n50} represents the nominal diameter.

In the research described herein, the numerical model has been employed by using three terrain-following layers in the vertical direction in the one-dimensional case. Then, the layer-integrated continuity equation for layer $1 \leq k \leq K$ $(K = 3)$ reads as follows (Zijlema and Stelling, 2005):

$$\frac{\partial h_k u_k}{\partial x} - u \frac{\partial z}{\partial x}\bigg|_{z_{k-1/2}}^{z_{k+1/2}} + w_{k+1/2} - w_{k-1/2} = 0 \tag{3.35}$$

where x is the horizontal coordinate, h_k is the thickness of the layer k, z is the elevation of the interface between two layers (being $z_{k-1/2}$ the interface between the layer $k-1$ and the layer k and $z_{k+1/2}$ the interface between the layer k and the layer $k+1$), u is the layer-integrated horizontal velocity, $w_{k\pm1/2}$ is the vertical velocity at the interfaces between two layers.
The layer-integrated horizontal momentum equation reads as follows:

$$\begin{aligned}\frac{\partial h_k u_k}{\partial t} + \frac{\partial h_k u_k^2}{\partial x} + \bar{u}^z_{k+1/2}\omega_{k+1/2} - \bar{u}^z_{k-1/2}\omega_{k-1/2} + \\ + g h_k \frac{\partial \zeta}{\partial x} + \frac{\partial h_k \bar{q}^z_k}{\partial x} - q_{k+1/2}\frac{\partial z_{k+1/2}}{\partial x} + q_{k-1/2}\frac{\partial z_{k-1/2}}{\partial x} = 0\end{aligned} \tag{3.36}$$

where t is the elapsed time, $\bar{u}^z_{k\pm1/2}$ is the horizontal velocity estimated at the layer interfaces $z_{k\pm1/2}$, $\omega_{k\pm1/2}$ is the vertical velocity relative to layer interface $z_{k\pm1/2}$ (defined as the difference between the vertical velocity along the streamline and the vertical velocity along the interface), g is the gravitational acceleration, ζ is the free surface elevation, $q_{k\pm1/2}$ is the non-hydrostatic pressure defined at the layer interfaces, $\bar{q}^z_k$ is the arithmetic mean of the non-hydrostatic pressure at the layer interfaces $z_{k\pm1/2}$.
The layer-integrated vertical momentum equation reads as follows:

$$\frac{\partial h_{k+1/2} w_{k+1/2}}{\partial t} + \frac{\partial h_{k+1/2}\bar{u}^z_{k+1/2} w_{k+1/2}}{\partial x} + \bar{w}^z_{k+1}\bar{\omega}^z_{k+1} - \bar{w}^z_k\bar{\omega}^z_k + 2\bar{q}^z_k = 0 \tag{3.37}$$

where $h_{k+1/2}$ is the arithmetic mean of the layer thicknesses h_k and h_{k+1}, $\bar{w}^z_{k(+1)}$ is the arithmetic mean of the vertical velocities at the layer interfaces $z_{k(+1)\pm 1/2}$, $\bar{\omega}^z_{k(+1)}$ is the arithmetic mean of the vertical velocities relative to the layer interface at the layer interfaces $z_{k(+1)\pm 1/2}$.
The details of numerical procedures and boundary conditions can be referred to Zijlema and Stelling (2005, 2008) and Smit et al. (2013)

3.3.2.2 The soil numerical model

Within the soil model framework, the following assumptions have been made (Li et al., 2018):

i) the seabed has constant thickness;

ii) the soil is nearly saturated;

iii) the soil skeleton obeys to Hooke's law (i.e. is characterized by elastic properties);

iv) the Young's modulus, the Poisson's ratio and the constant soil permeability are different in vertical and horizontal directions (i.e. anisotropic condition).

The classical Biot's consolidation equations (Biot, 1941) are adopted to model the coupled soil behavior with the interaction between the solid skeleton and the pore fluid, considering the anisotropic soil characteristics. The soil domain is governed by the quasi-static momentum balance equation for soil mixture and the mass balance equation of the pore fluid based on Darcy's law.

Quasi-static momentum balance equation is presented in Equation (3.38):

$$\nabla \cdot \left[\mathbf{C} : \frac{1}{2} \left(\nabla \mathbf{U} + (\nabla \mathbf{U})^T \right) \right] - \nabla p = 0 \tag{3.38}$$

where $\mathbf{U}$ is the soil (skeleton) displacement, p is the pore fluid pressure and $\mathbf{C}$ is the elastic stiffness tensor. For anisotropic soil materials, the two

dimensional (hereinafter referred to as 2D) orthotropic elastic stress-strain relation can be expressed in a 3 x 3 matrix notation:

$$\sigma' = \begin{pmatrix} \sigma'_{xx} \\ \sigma'_{zz} \\ \sigma_{xz} \end{pmatrix} = \begin{bmatrix} A_{11} & A_{12} & 0 \\ A_{12} & A_{22} & 0 \\ 0 & 0 & A_{33} \end{bmatrix} \begin{pmatrix} \varepsilon_{xx} \\ \varepsilon_{zz} \\ \varepsilon_{xz} \end{pmatrix} = \mathbf{C} : \varepsilon \tag{3.39}$$

where σ' is the effective stress tensor. The 4 independent coefficients A_{ij} are calculated from Young's modulus E_i, Poisson's ratio ν_{ij} and the shear modulus G_{ij} as follows:

$$\begin{aligned} A_{11} &= \frac{E_x}{1-\nu_{xz}\nu_{zx}} \\ A_{22} &= \frac{E_z}{1-\nu_{zx}\nu_{xz}} \\ A_{12} &= \frac{\nu_{xz}E_z}{1-\nu_{zx}\nu_{xz}} \\ A_{33} &= G_{xz} \end{aligned} \tag{3.40}$$

The mass balance equation of the pore fluid reads as follows:

$$\frac{n}{K'}\frac{\partial p}{\partial t} = -\frac{1}{\gamma_w}\nabla\cdot(\mathbf{k}\cdot\nabla p) + \frac{\partial}{\partial t}(\nabla\cdot\mathbf{U}) \tag{3.41}$$

where n denotes the soil porosity, γ_w represents the specific weight of the water in the soil, and $\mathbf{k}$ denotes the diagonal permeability tensor with values k_x and k_z. The bulk modulus of the compressible pore flow K' is approximated through the formulation proposed by Vafai and Tien (1981):

$$\frac{1}{K'} = \frac{1}{K_w} + \frac{1-S_r}{p_a} \tag{3.42}$$

where S_r represents the degree of soil saturation, K_w denotes the bulk modulus of pure water ($\approx$ 2 GPa), and $p_a = \rho_f g d$ is the absolute pore water pressure.

A description of the boundary conditions adopted to solve the governing equations are discussed in the Section of Numerical investigations.

3.3.2.3 Boundary coupling algorithm

The coupling procedure requires the information exchange in terms of dynamic wave pressure between the different domains involved in the WSSI, via the common boundary. Similar approach was adopted by Ye et al. (2015c) (see their Figure 1) within the FSSI-CAS 2D model. Then, two physical domains are selected: the first one is addressed to the interaction between waves and porous structures, whilst the second one is dedicated to the seabed response to the waves loads. The common boundary is at the seabed surface. The minor motion of the seabed soil does not alter the wave-porous structure domain, as depicted in Figure 3.40. The dynamic wave pressure p_d, computed at the seabed layer and beneath the porous structure, transfers to the soil domain as a dynamic boundary condition. In the model, time-varying boundary conditions are implemented at the interface, by interpolating the values from the supplied domain in space and time. Since the grid sizes and time steps for the two domains are allowed to be various, it increases the efficiency of solving the coupled system and allows the usage of different numerical tools.

3.3.3 Model verifications

The present numerical models have been validated in the previous studies. The SWASH model to simulate the interaction of submerged berms and the incident waves has been validated by Celli et al. (2018), through a comparison with the experimental data (see their Figure 3). The poro-elastic soil model in OpenFOAM to simulate the wave-induced seabed response, has been validated by Li et al. (2018), through a comparison with the experimental data provided by Tsai and Lee (1995) (e.g. see their Figures 2,3 and 4). To

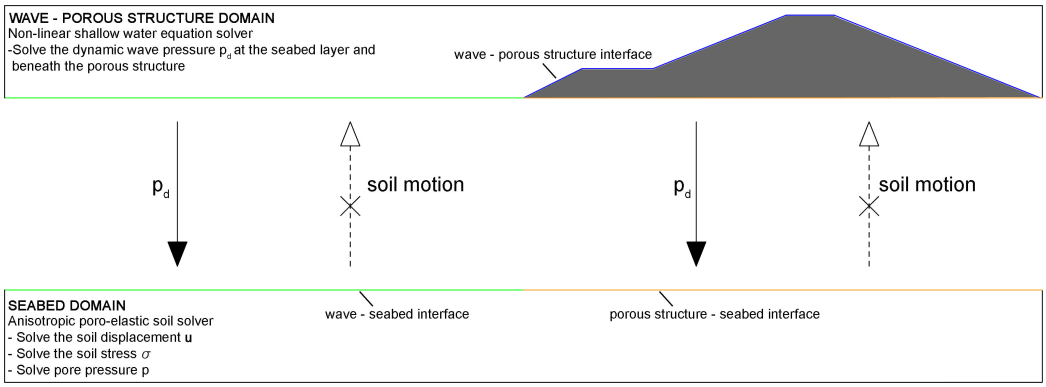

Figure 3.40 One-way boundary coupling algorithm of wave-structure-seabed interaction.

further verify the numerical models for the present problems, grid convergence studies have been performed with SWASH and with the porous soil solver, respectively. In particular, the numerical model SWASH has been used to compute the wave-induced seabed pressure within the wave-porous structure interaction framework. At first, a series of preliminary tests have been carried out to evaluate the sensitivity of the results for different computational grid sizes. A rubble mound breakwater interacting with regular waves (H = 2 m, T = 7 s) has been simulated considering a domain length equal to 411 m and a series of computational grid spatial resolutions, ranging from 0.1 m up to 0.5 m. The water level and the seabed dynamic pressure time series have been collected at the same location for comparison purposes. Then zero-crossing analysis has been carried out and the mean values of the water wave heights and wave pressure heights have been evaluated. For a selected location (similar results are achieved for other points), Figure 3.41 shows the normalized values of the water wave heights, i.e. $H_{dxi}/H_{dx0.1}$ (left panel) and the normalized values of the wave pressure heights i.e. $P_{dxi}/P_{dx0.1}$ (right panel), taking as a reference the results obtained for the finest grid resolution (i.e. $H_{dx0.1}$ and $P_{dx0.1}$).

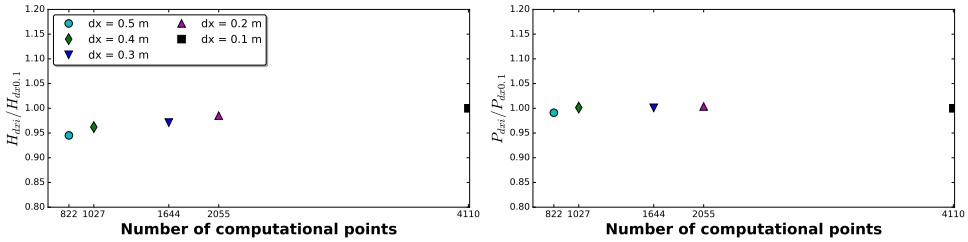

Figure 3.41 Variation of the normalized water wave height $H_{dxi}/H_{dx0.1}$ (left panel) and of the normalized wave pressure height $P_{dxi}/P_{dx0.1}$ (right panel), as a function of the numbers of computational points of the mesh.

With respect to the finest grid, it appears that the difference of the results computed by adopting dx = 0.2 m is equal to 1.5% and 0.37% for the mean water wave heights and the mean wave pressure heights, respectively. Therefore, adopting a computational grid spatial resolution equal to 0.2 m suffices to achieve reliable numerical accuracy.

A grid convergence study has been carried out also for the soil model, simulating a 30 m thick and 450 m long portion of soil (Figure 3.42), subjected to wave-induced seabed pressure acting on the upper boundary, adopting three different sets of meshes (see Table 3.8). The dynamic pore pressures, collected in the sample point (see Figure 3.42), have been compared as shown in Figure 3.43.

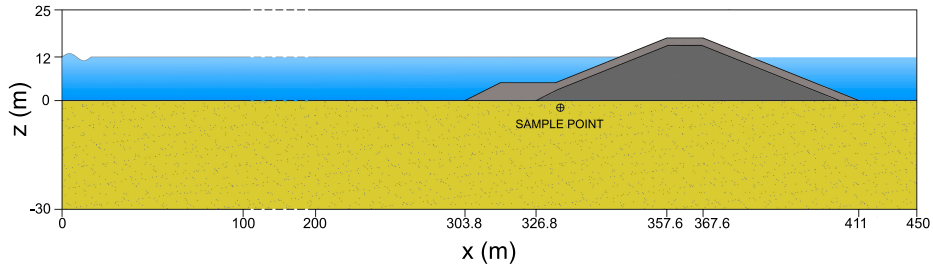

Figure 3.42 Sketch of the computational domain implemented for the soil model convergency study. It is shown the sample point (x = 330.2 m , z = -2 m), where the pore pressures are collected.

It appears that as the number of grid points increases, the pore pressure converges to a higher amplitude (in absolute value). This implies that an insufficient number of points may underestimate the pore pressure in the seabed. As illustrated in Table 3.8, the relative change of minimum pressure derived from the finest tested mesh (Mesh No.3) and the medium tested mesh (Mesh No.2) is 0.45%. Then, 2.7 x 10^5 grid points (i.e. Mesh No.2) have been used to perform the parametric study described herein.

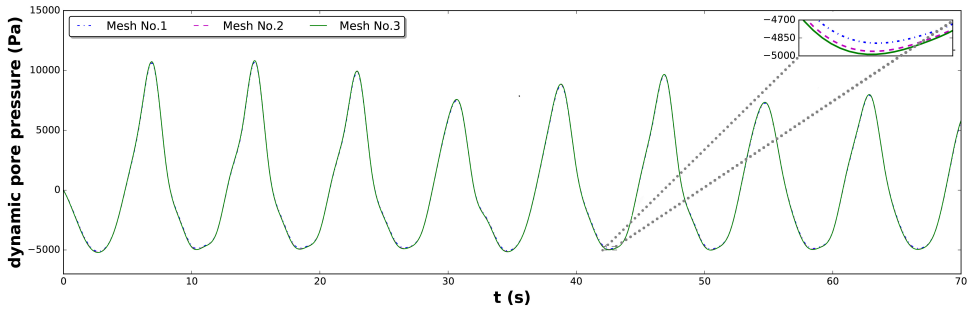

Figure 3.43 Grid convergence for dynamic pore pressure in the seabed (sample point coordinates: x = 330.2 m , z = -2 m)

.

Table 3.8 Mesh parameters for the soil model convergency study (relative change is evaluated with respect to the finest Mesh No.3).

Mesh	Number of grid points	Minimum pressure (Pa)	Relative change
No.1	8.43 x 10^4	-5116.88	1.28%
No.2	2.70 x 10^5	-5183.30	0.45%
No.3	6.75 x 10^5	-5206.84	

3.3.4 Numerical investigations

Momentary liquefaction occurs in very dense elastic seabed foundation and it is unlikely able to produce the total collapse of structures, if any. This

does not mean the absence of potential serious damage that could be suffered by structures. Indeed, the momentary liquefaction can enhance the scouring process in front of rubble mound breakwaters, causing the partial failure of the armor layer. The damage could even reach the core, if a bedding layer is not used. The deployment of submerged berms could be hence very positive for the structure stability, since they are able to reduce the momentary liquefaction occurrences and the scouring process as well.

Therefore, the aim of this paper is to evaluate the performances of submerged berms in reducing the momentary liquefaction depths around and beneath a rubble mound breakwater. The results have been compared to those associated with the presence of a straight sloped conventional breakwater without a berm. In both cases, the absence of a transition layer beneath the armour layer and the berm is assumed by considering the rocks in direct contact with the seabed, loading the soil in a discontinuous way. It should be emphasized that various experimental (e.g. Kudella et al., 2006b) and numerical (e.g. Ye et al., 2015c) studies indicated the absence of momentary liquefaction occurrences underneath the breakwater, where the overburdened pressure is significantly enhanced by the self-gravity of the structure. In the work presented herein, all the momentary liquefaction occurrences appearing under the breakwaters are due to the discontinuous load acting on the soil, aimed to describe the absence of a transition layer under the berm. Therefore, under the assumption of bedding layer absence, the berm rocks load is transferred to the soil only in correspondence of the contact area (see Figure 3.44). In the former zone, the vertical effective stresses, increased due to the weight of the rocks, decrease the liquefaction probability. On the other hand, the presence of unloaded areas (i.e. zones among two contiguous rocks) makes the soil potentially prone to momentary liquefaction occurrences. The former assumptions find justification if a safe rationale is employed.

Then, a parametric study has been carried out by varying the berm configuration (i.e. its length, L_b, and the water depth over the berm, h_b, see Figure

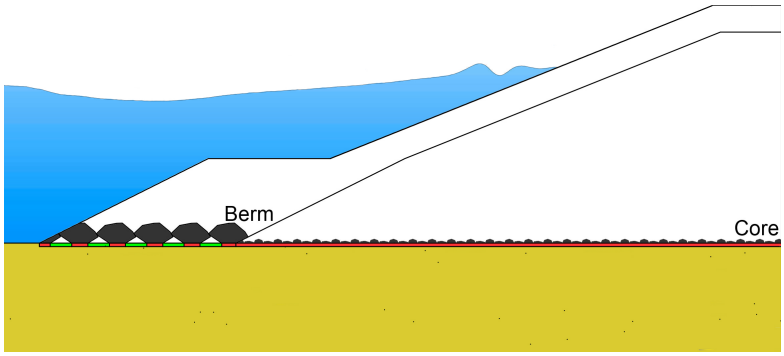

Figure 3.44 Sketch of assumed load distribution under a porous structure: red zones refer to contact areas, where the load is transferred to the soil. Green zones refer to unloaded areas.

3.45), keeping constant the offshore regular wave condition, the water depth and the elastic properties of the soil (see Table 3.9). A series of preliminary tests have been carried out to evaluate the sensitivity of dynamic seabed pressure to the armor layer porosity parameter variation. It was observed that a higher porosity of the armor layer leads to a higher amplitude of dynamic pressure on the underneath seabed. According to US Army Corps of Engineers (USACE) (2002) and CIRIA/CUR/CETMEF (2007), typical values of rock armor layer porosity are at most equal to 0.4. Therefore, n = 0.4 is selected for modeling the berm and the armor layer in the present study. The value of the ratio h_b/h_t (being h_t the water depth at the toe of the berm) ranges from 0.2 up to 0.8, whilst the ratio L_b/L_w (being L_w the wave length at the toe of the berm) ranges from 0.040 up to 0.356 for a total of 62 simulations.

With the aim to evaluate the wave-induced seabed pressure for different submerged berm configurations (i.e. by varying the berm length L_b and the water depth over the berm h_b), the simulations have been carried out by using SWASH numerical model, validated as described in the previous section.

Figure 3.45 shows one of the used computational domain. As for the simulations carried out for the calibration of the model, the total length of the computational domain is set at 411 m and the cell size in the x-direction at

Table 3.9 Parameter settings for wave-structure-seabed interaction.

Wave parameters		
Wave height H (m)	4.0	
Wave period $T(s)$	8.0	
Water depth h_t (m)	12.0	
Wave length L_w (m)	75.8	
Seabed parameters (directional values)		
Young's modulus (N/m^2)	E_x = 1.2 x 10^7	E_z = 2.0 x 10^7
Poisson's ratios	$\nu_{zx} = 0.40$	
Shear modulus (N/m^2)	G_{zx} = 5 x 10^6	
Permeability (m/s)	$k_x = 0.005$	$k_z = 0.001$

0.2 m. The model is run with three layers in the vertical direction, in order to properly describe the wave frequency dispersion. The offshore boundary is considered as weakly reflective and a water level time series, reproducing regular waves (see Table 3.9), is imposed. For each test case, almost 90 waves have been simulated. At the onshore boundary, the Sommerfeld radiation condition is applied.

For each tested berm configuration, the computed seabed dynamic pressure time series have been collected and used as coupling boundary condition for the anisotropic Biot's porous soil model.

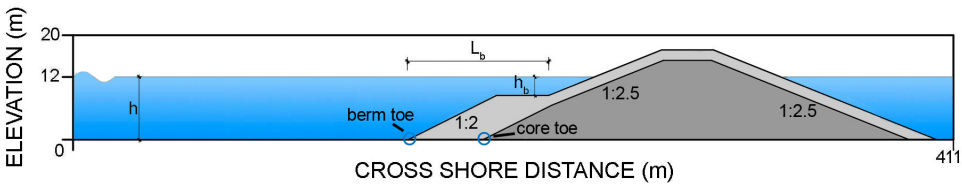

Figure 3.45 Geometric parameters definition of conventional rubble mound breakwater with a berm. The berm and core toe positions could vary among the simulated test cases.

The numerical domain of the porous seabed is 450 m long and 30 m thick. In order to avoid unwanted lateral boundary effects, a preliminary sensitivity study to evaluate the best structure location, inside the computational domain, has been carried out. Therefore, it has been decided to place the porous structure at a distance equal to almost 4 λ from the left side of the computational domain (where λ is the wave length at the toe of the berm, equal to 75.83 m). Moreover, the soil domain was extended of a quantity equal to 39 m starting from the breakwater end, in order to further limit the effect of the onshore boundary.

The properties of the seabed sand sediment are based on the measurements of the North sea soil by Kjekstad and Lunne (1981), with reasonable assumptions concerning the anisotropic properties. Since the comparative nature of the present work, based on the evaluation of the submerged berms configuration effects on the momentary liquefaction occurrences, the importance of simulating several soil properties is not crucial. In the shallow coastal area, the presence of the breakwater will make it more likely to have air content in the soil due to breaking waves and therefore the penetration of air into the soil. Therefore, the saturation factor S_r in the present work is set to 0.975. The soil porosity n is set to 0.3. The anisotropic parameter settings are shown in Table 3.9. The boundary conditions of the seabed domain are specified as follows.

1) At the wave-seabed and the porous structure-seabed interfaces (see Figure 3.40), the effective soil stresses vanish, hence the soil has zero traction at the seabed surface. The pore pressure, at the aforementioned interfaces, is equal to the dynamic wave pressure acting on the seabed and beneath the porous structure.

2) At the bottom and lateral boundaries of the seabed, the soil skeleton is allowed to slip and the normal pore pressure gradient is zero.

3.3.5 Results and discussion

3.3.5.1 Consolidation

The deployment of the breakwaters can significantly increase the effective stresses in the surrounding soil. Once the structure is built on the seabed, the self-weight of a breakwater is initially transferred to the pore water in the seabed foundation, resulting in the generation of excess pore pressure. Then, the soil will experience the gradual dissipation of the excess pore pressure. Consequently, the breakwater load is gradually transferred from the pore water to the soil skeleton. At the end of the process, the seabed foundation reaches an equilibrium consolidation status. Therefore, the determination of the initial consolidation status of seabed foundation under hydrostatic pressure and breakwater weight is an essential step in the evaluation of structures stability (Jeng and Ye, 2012), since it is able to influence the potential probability of dynamic wave-induced soil liquefaction (e.g. Sui et al., 2017; Ulker et al., 2010; Zhao et al., 2017b).

Figure 3.46 (upper panel) shows the vertical soil displacement U_z after the completion of the consolidation process for the simulated test cases with $h_b/h_t = 0.19$ and $L_b/L_W = 0.35$. A negative value of U_z indicates that the soil skeleton is compressed and moves downward. It appears that beneath the structure, the soil skeleton has been largely compressed compared to the far field. The vertical soil displacement under the berm is lower (in absolute value) than that under the breakwater core due to the berm reduced weight.

The lower panel of Figure 3.46 shows the distribution of the vertical effective stresses σ_z' in the soil, at the end of the consolidation process. A negative value of σ_z' indicates the compression of the soil skeleton. It appears that the gravity of the structure is gradually transferred to the supporting soil skeleton. The portion of soil beneath the breakwater is characterized by higher (absolute) values of vertical effective stresses if compared to the far field. The lower panel of Figure 3.46 also shows a compressive stress concentration at the berm-core interface as well as at the end of the breakwater.

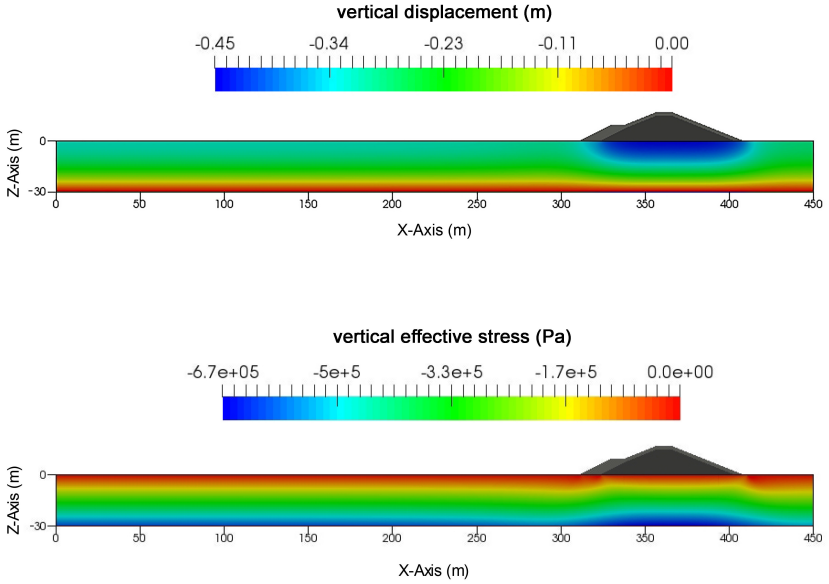

Figure 3.46 Consolidation process results with reference to a breakwater with submerged berm characterized by $h_b/h_t = 0.19$ and $L_b/L_W = 0.35$. Upper panel: vertical soil displacement U_z after the completion of the consolidation process. Lower panel: vertical effective stress σ'_z after the completion of the consolidation process.

This effect is justified by the different gravitational load distributions between the submerged berm and the core, as well as between the loaded and unloaded areas at the end of the breakwater.

The vertical effective stresses σ'_z computed at the end of the consolidation process have been used as an initial condition for the momentary liquefaction analysis. It should be stressed that during the construction phase, when the consolidation state has not been reached, the vulnerability of the structure to liquefaction occurrences could be higher.

3.3.5.2 Wave-induced seabed response

Figure 3.47 (upper panel) shows the wave-induced transient pore pressure and the seepage flow in the seabed at the time instant t = 676 s, for one of the simulated test cases (i.e. $h_b/h_t = 0.59$ and $L_b/L_W = 0.3$).

As expected, the passage of wave crests induces positive transient pore pressures, whilst the transient pore pressures become negative under the wave troughs. The same big picture could be drawn focusing on the seepage flow. Its direction is directly related to the wave phases (e.g. Jeng et al., 2013b). The seepage flow is directed downward during the passage of wave crests and is directed upward during the passage of wave troughs. In particular, when the upward pore pressure gradient (strictly related to the seepage forces) exceeds the vertical initial effective stress, the momentary soil liquefaction is likely to occur and further affects the structure stability. More discussion about the liquefaction analysis is presented in the next section.

Figure 3.47 (lower panel) shows the wave-induced shear stresses σ_{xz} in the seabed. By neglecting the seabed response close to the left boundary of the computational soil domain, affected by the lateral boundary proximity, it could be observed that under the periodic wave loading, the shear stresses σ_{xz} values switch from positive to negative periodically. In the present work, the shear failure is not investigated. Nevertheless, it should be stressed that the wave-induced cyclic dynamic shear stresses could be a crucial factor for the stability

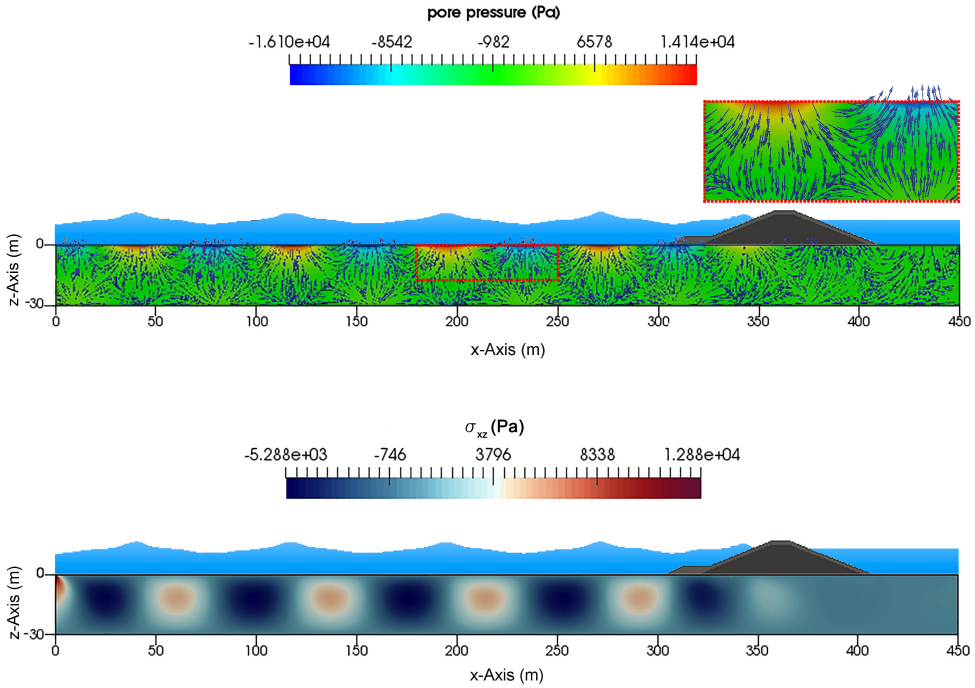

Figure 3.47 Wave-induced seabed response with reference to a breakwater with submerged berm characterized by $h_b/h_t = 0.59$ and $L_b/L_W = 0.3$. Upper panel: transient pore pressure and seepage flow at the instant t = 676 s (H = 4 m). Lower panel: Shear stress σ_{xz} distribution in the seabed at the time instant t = 676 s (H = 4 m).

of breakwaters (Ye et al., 2016). They can lead to the progressive buildup pore pressure that may eventually be large enough to result in significant deformation of the soil (Nataraja and Gill, 1983).

3.3.5.3 Momentary liquefaction analysis

The liquefaction criterion adopted in the present work is a modified version from Zen and Yamazaki (1990a). The latter authors proposed a 1D

liquefaction criterion based on the excess pore pressure:

$$p(z,t) - p(0,t) \geq -(\gamma_s - \gamma_w)\, z \tag{3.43}$$

afterwards extended by Jeng (1997b) to the 3D cases:

$$p(z,t) - p(0,t) = \geq -\frac{1+2K_0}{3}(\gamma_s - \gamma_w) \tag{3.44}$$

where $p(z,t)$ is the pore pressure in the seabed, $p(0,t)$ is the pore pressure at the seabed surface, γ_s and γ_w are the unit weight of soil and water respectively, K_0 is the coefficient of lateral earth pressure. It should be stressed that Equation (3.44) is only applicable in absence of any structure. As for this work, if rubble mound breakwaters are concerned, the adopted momentary liquefaction criterion reads as follows:

$$p(z,t) - p(0,t) \geq \sigma'_{z0} \tag{3.45}$$

where σ'_{z0} represents the initial vertical effective stress induced by the gravitational forces from the consolidation process. The present criterion was used in the works of Sui et al. (2017), Zhao et al. (2017b) and Li et al. (2018). In order to investigate the effects of submerged berm deployment, the adopted rationale imposes a comparison among the aforementioned series of results deriving from the deployment of a rubble mound breakwater without a berm. Figure 3.48 shows the liquefaction depth achieved in the presence of the rubble mound breakwater without the submerged berm.

As for the rubble mound breakwaters with submerged berms, the simulation considers the armor layer rocks in direct contact with the seabed. Their arrangement leads to the existence of loaded areas (i.e. just beneath the rocks) and unloaded areas (i.e. zones between two contiguous rocks). Therefore, the rocks load is transferred to the soil only in correspondence of the contact area (see Figure 3.44). In the former zone, the vertical effective stresses, increased

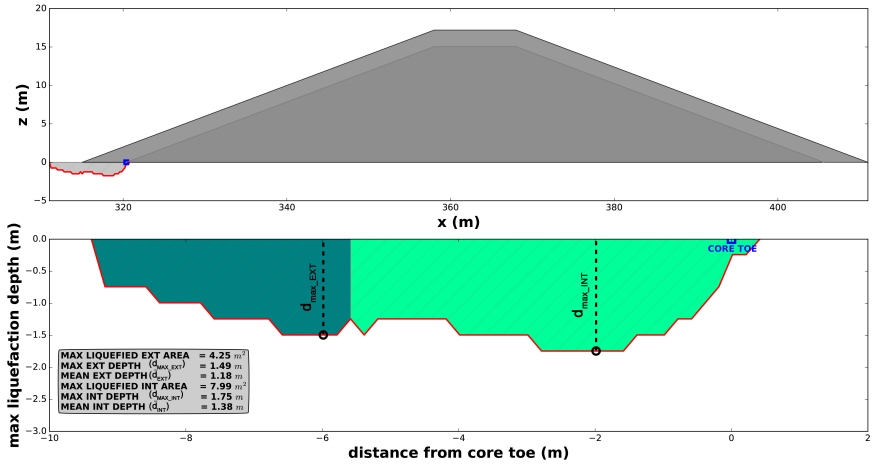

Figure 3.48 Wave-induced momentary liquefaction with reference to a breakwater without submerged berm. Upper panel: momentary liquefaction maximum depth around and beneath the structure. Lower panel: zoom of the momentary liquefaction maximum area splits in two subareas, according to the location of the liquefaction occurrences. Dark green subarea refers to maximum liquefaction depth in front of the structure up to the breakwater toe. Light green subarea refers to maximum liquefaction depth beneath the structure.

due to the weight of the rocks, decrease the liquefaction probability. On the other hand, the presence of unloaded areas leads to a higher possibility of soil liquefaction compared to the loaded zones. The upper panel of Figure 3.48 shows the maximum values of liquefaction depth around and beneath the structure, whereas in the lower panel, the maximum liquefied area has been divided into two subareas: the internal subarea (i.e. light green zone) shows what happens beneath the structure, whilst the external one (i.e. dark green zone) shows what happens in front of the structure, up to the breakwater toe. In the lower panel of Figure 3.48, the origin of the coordinate system is located at the core toe. For each of the detected subareas, the maximum and the mean local depth (i.e. obtained dividing the subarea value by its superficial length) have been evaluated. From the inspection of Figure 3.48 it

appears that the maximum internal liquefaction depth (hereinafter referred to as d_{maxint}), equal to 1.75 m, is greater than the external one (hereinafter referred to as d_{maxext}) equal to 1.49 m. Also the comparison among the mean maximum values (hereinafter referred to as $\overline{d}_{ext}$ and $\overline{d}_{int}$) confirms that in a rubble mound breakwater without submerged berm, the most exposed part to the momentary liquefaction occurrences is the area beneath the armor layer. Hence, the probability of the structure damage triggering is high in that location.

For the comparison purpose, Figure 3.49 shows the maximum liquefaction depths in presence of a rubble mound breakwater with two different submerged berms characterized by $h_b/h_t = 0.59$, $L_b/L_w = 0.17$ (left panels) and $h_b/h_t = 0.59$, $L_b/L_w = 0.30$ (right panels), respectively.

The inspection of Figure 3.49 reveals the positive effects of submerged berms deployment on the reduction of momentary liquefaction depth. From the comparison between the left panels of Figure 3.49 and Figure 3.48, it appears that even though d_{maxint} remains the same, $\overline{d}_{int}$ decreases down to 1.16 m, less than what is achieved in absence of berm (i.e. 1.38 m). Similar consideration applies for $\overline{d}_{ext}$ that drops down to 0.54 m. The big picture description further improves looking at the right panels of Figure 3.49. The deployment of a longer submerged berm implies a reduction of d_{maxint} that drops down to 1.24 m as well as $\overline{d}_{int}$ that is equal to 0.64 m. In contrast, d_{maxext} and $\overline{d}_{ext}$ grow up reaching values equal to 0.99 m and 0.77 m, respectively. The latter phenomenon is likely due to the upward wave-induced pore pressure gradient rather than to a reduced initial vertical stress distribution, in view of the increased distance from the breakwater core. It should be emphasized that the behavior of maximum liquefaction depths under the porous structures is not smooth, as observable in the right panel of Figure 3.49. This is due to the rocks arrangement aimed to simulate the absence of the transition layer under both the berm and the armor layer. Looking again at Figure 3.48, it appears that the maximum liquefied area for the straight sloped rubble

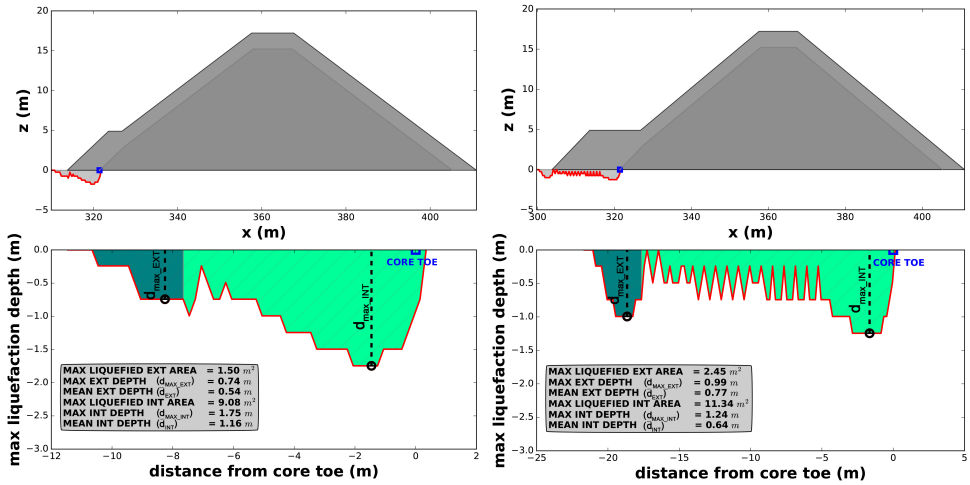

Figure 3.49 Wave-induced momentary liquefaction with reference to breakwaters with submerged berms characterized by $h_b/h_t = 0.59$ and $Lb/Lw = 0.17$ (left panels), $Lb/Lw = 0.30$ (right panels). Upper panels: momentary liquefaction maximum depth around and beneath the structure. Lower panels: zoom of the momentary liquefaction maximum area splits in two subareas, according to the location of the liquefaction occurrences. Dark green subareas refers to maximum liquefaction depth in front of the structure, up to the breakwater toe. Light green subareas refers to maximum liquefaction depth beneath the structure.

mound breakwater is lower if compared to the liquefied areas of Figure 3.49 where submerged berms are employed. Of course this is expected, since the contact length among the seabed and the structure increases as the berm length increases. However, this does not imply a growth of potential structure failure.

Basically, the longer the berm, the lower the momentary liquefaction probability near the breakwater core, and the higher the momentary liquefaction probability at the toe of the berm, where the stability of the armor layer is not compromised. The submerged berm could be hence intended as the expendable part of the structure. This concept could be better caught looking at the upper panel of Figure 3.50, where d^* represents the ratio of $\overline{d}_{ext}$ to

$\overline{d}_{int}$, as a function of the dimensionless berm length L_b/L_w. Except for the lowest berms (i.e. characterized by $h_b/h_t = 0.9$), the lengthening of the berm tends to push away the liquefaction probability from the zone beneath the breakwater to the area in front of the structure. Just for instance, the longest berms characterized by the ratio h_b/h_t equal to 0.49 and 0.59, lead to $d^* > 1$, i.e. $\overline{d}_{ext} > \overline{d}_{int}$. Nevertheless, the positive effects of the berm lengthening do not apply for the lowest berms, for which d^* remains almost constant varying the berm length. The inspection of the lower panel of Figure 3.50 confirms that within the framework of long berms (i.e. roughly $L_b/L_w \geqslant 0.20$), the best performances belong to those marked by h_b/h_t equal to 0.49 and 0.59. For short berms, roughly marked $L_b/L_w \leq 0.1$, d^* is almost constant for different dimensionless water depth over the berm h_b/h_t values, i.e. a variation of the berm height does not induce appreciable modification on the area where liquefaction phenomena are likely to occur.

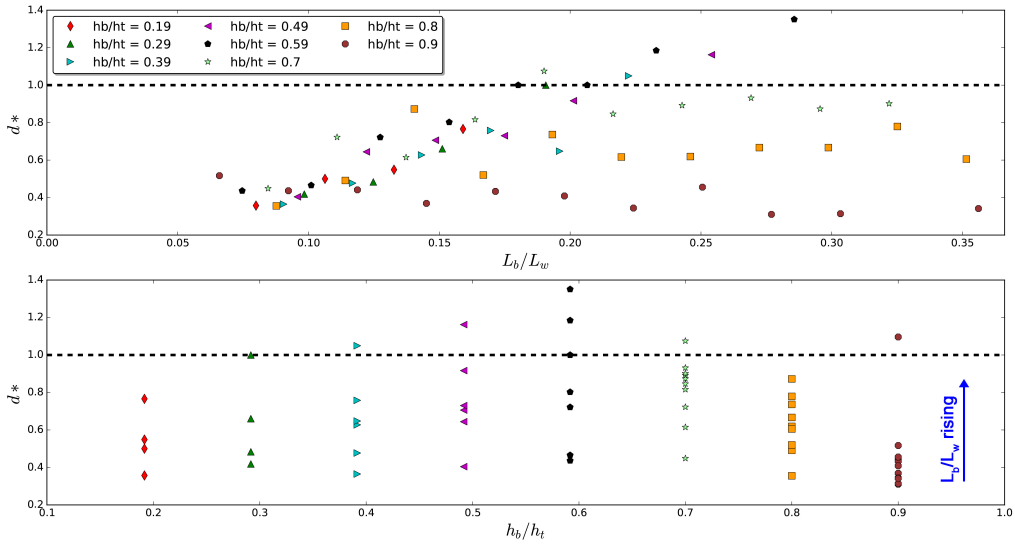

Figure 3.50 Variation of d^*, (i.e. the ratio $\overline{d}_{ext}$ / $\overline{d}_{int}$) as a function of the dimensionless berm length (L_b/L_w, upper panel) and of the dimensionless water depth over the berm (h_b/h_t, lower panel).

By focusing on the general behavior of submerged berms in influencing the liquefaction phenomena, the evaluation of the mean maximum liquefaction depth d_m, computed considering the whole liquefied area, could be helpful. By taking the mean maximum liquefied depth (d_{m0}), achieved in presence of a straight sloped conventional breakwater without a berm as reference, Figure 3.51 shows the variation of the ratio d_m/d_{m0} as a function of the dimensionless berm length L_b/L_w (upper panel) and of the dimensionless water depth over the berm h_b/h_t (lower panel).

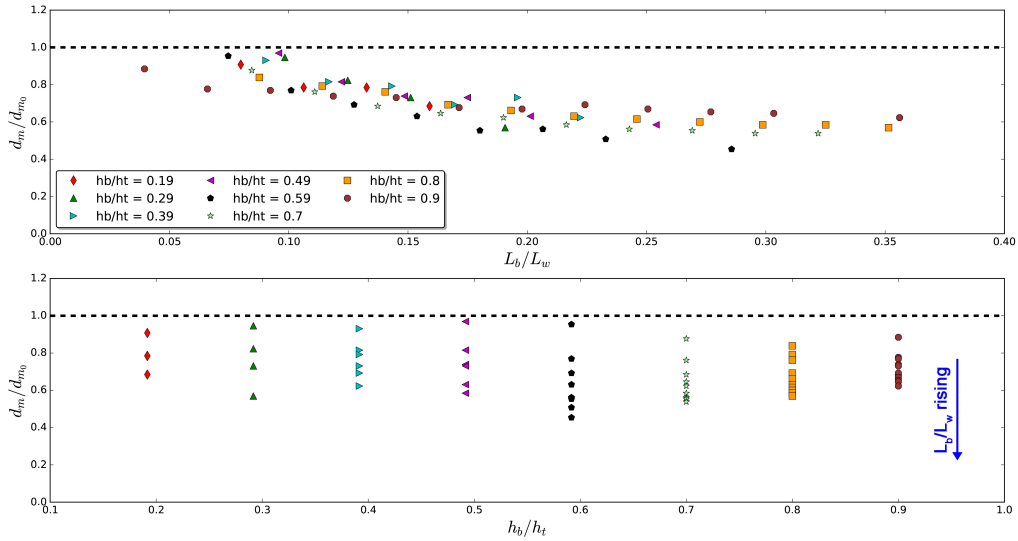

Figure 3.51 Variation of the normalized mean maximum liquefaction depth d_m/d_{m0} as a function of the dimensionless berm length (L_b/L_w, upper panel) and of the dimensionless water depth over the berm (h_b/h_t, lower panel).

In particular, from the inspection of the upper panel of Figure 3.51 it is confirmed that, for the same water depth over the berm, the longer the berms, the higher the reduction of liquefaction depths around and beneath the structure. It has to be emphasized that even though high berms (i.e. characterized by lower values of h_b/h_t) strongly affect the wave propagation (e.g. Celli et al., 2018), the strongest influence on the momentary liquefaction occurrence belongs again to the berms characterized by the ratio $h_b/h_t = 0.59$.

Higher berms tend to better attenuate the wave-induced pore pressure at the seabed interface, however, being heavier than the low ones, they enhance a stronger initial vertical effective stress reduction in the unloaded areas, i.e. where the armour elements are not in direct contact with the seabed. On the other hand, low berms (i.e. characterized by the ratio h_b/h_t ranging from 0.7 up to 0.9), being lighter than the high ones, marginally influence the initial vertical effective stress reduction, while at the same time, have no significant effect on the attenuation of the wave-induced pore pressure at the seabed interface. The influence of low berms length on momentary liquefaction attenuation is therefore negligible, being the ratio d_m/d_{m0} almost constant varying the ratio L_b/L_w.

The long berms, characterized by the ratio $h_b/h_t = 0.59$, could be hence intended as the right balance in terms of seabed pore pressure attenuation and initial vertical effective stress reduction. Therefore, within the range of the tested configurations, they could be regarded as the best design choice to limit the liquefaction phenomena. On a final note, the lower panel of Figure 3.51 confirms that for short berms with a given length, the change of the berm height has no significant influence on the liquefaction occurrences, being the ratio d_m/d_{m0} almost constant varying the ratio h_b/h_t.

3.3.6 Concluding remarks

Berms deployed at the toe of conventional rubble mound breakwaters may be useful for various purposes, i.e. (i) to reduce wave loads acting on the breakwater armor elements, (ii) to reduce wave overtopping, (iii) to reduce momentary liquefaction occurrences under the structure, (iv) to protect from the scouring the breakwater toe. This research has numerically investigated the wave-induced soil response and the liquefaction probability around and beneath rubble mound breakwaters with submerged berm. Two numerical tools have been used for this study: the effects of submerged berms on the dynamic pressure acting on the seabed have been evaluated by means of

SWASH, whereas the seabed responses to the wave-induced seabed pressures have been evaluated by using an ad-hoc anisotropic poro-elastic soil solver, developed in OpenFOAM (Li et al., 2018). A parametric study has been carried out by changing the berm configuration, to find out their performances in attenuating momentary liquefaction probability, especially under the breakwater core, where a partial failure could lead to a severe damage for the whole structure. For all the tested configurations, the effects of the consolidation process on the wave-induced soil response, have been taken into account. Within the range of the tested configurations, the main conclusions are drawn as follows.

1. The presence of any berm tends to attenuate momentary liquefaction occurrences if compared to the case of a straight sloped conventional breakwater without a berm.

2. Except for the lowest tested berm (i.e. characterized by $h_b/h_t = 0.9$), the lengthening of the berm tends to move the location where liquefaction probability is high, from the zone beneath the breakwater to the area in front of the structure,i.e. where a potential damage is less dangerous. Then, the main role of submerged berms is to protect the armor layer from momentary liquefaction occurrences and scouring process consequently. Basically, they could be intended as the expendable part of the structure.

3. High berms tend to better attenuate the wave-induced pore pressure at the seabed interface, however, being heavier than the low ones, they enhance a stronger initial vertical effective stress reduction in the unloaded areas. Consequently, the momentary liquefaction attenuation is limited.

4. Low berms, being lighter than the high ones, slightly influence the initial vertical effective stress reduction, while at the same time, have

no significant effects on the attenuation of the wave-induced pore pressure at the seabed interface. The resulting momentary liquefaction attenuation is limited.

5. The greater momentary liquefaction attenuation is given by long berms characterized by the ratio $h_b/h_t = 0.59$, i.e. an intermediate height within the considered range, at least for the tested wave condition. They could be intended as the right balance in terms of seabed pore pressure attenuation and initial vertical effective stress reduction. Therefore, they could be regarded as the optimal design choice to prevent the liquefaction phenomena, within the tested conditions.

The present work has been carried out in a regular wave condition. More parametric studies on irregular waves will be covered in the future works.

3.3.7 Acknowledgment

This study was supported in part with computational resources provided by the Norwegian Metacenter for Computational Science (NOTUR), under the project No: NN9372K.

Chapter 4

Further development on the modeling of wave-induced momentary liquefaction around offshore foundations

This chapter presents a paper submitted to Ocean Engineering on the further development of wave-induced seabed response model and liquefaction analysis module. The partial-dynamic form ($u-p$ approximation form) of anisotropic poro-elastic soil model is implemented to achieve a good efficiency and accuracy. Two types of liquefaction criteria are implemented and compared in the present study. The parametric study in the paper follows the systematic sequence of consolidation analysis, WSSI analysis and liquefaction assessment.

4.1 Paper IV: A numerical toolbox for wave-induced seabed response analysis around marine structures in the OpenFOAM framework

Yuzhu Li[a], Muk Chen Ong[a], Tian Tang[b]
[a]Department of Mechanical and Structural Engineering and Materials Science, University of Stavanger, N-4036 Stavanger, Norway
[b]Bekaert Technology Center, Deerlijk, 8 540, Belgium

Abstract*: An open-source numerical toolbox for modeling the porous seabed interaction with waves and structures is implemented in the finite-volume-method (FVM) based OpenFOAM® framework. The toolbox includes a soil consolidation model, a wave-structure-seabed interaction (WSSI) model, and the liquefaction assessment module. In the present work, one-way coupling algorithm is applied for the WSSI analysis. The coupling effect between different physical domains is achieved by time-varying data mapping via the common boundaries. The consolidation model is governed by the quasi-static Biot's equations and is verified against the theoretical solution for the Terzaghi's classical consolidation test. The anisotropic wave-induced porous seabed response model is governed by the Biot's equations in the partial-dynamic form, i.e. $u-p$ approximation form, to achieve a good efficiency and accuracy. The FVM-based $u-p$ model is validated against the existing experimental data of standing wave-induced seabed response near a vertical wall. The integrated WSSI model is validated against existing experiment of wave-soil-pile interaction with wave data and soil response data. Good agreement is obtained. Two case studies are performed using the present numerical toolbox. The first case is an investigation of two-dimensional (2D) nonlinear wave-seabed interaction. The second case is a parametric study of three-dimensional (3D) wave-induced seabed response analysis around

*This is a journal paper submitted to Ocean Engineering.

gravity-based offshore foundations with different designs of shaft diameters. The 3D parametric study follows the sequence of consolidation analysis, WSSI analysis and momentary liquefaction assessment. Two types of liquefaction criteria are implemented and compared in the present study. The toolbox is made publicly available through the foam-extend community.

keywords: wave-structure-seabed interaction; numerical solver; consolidation; momentary liquefaction

4.1.1 Introduction

For offshore foundations and coastal structures, soil liquefaction is one of the essential concerns which may cause the structural failure. In order to prevent the liquefaction risk around the offshore foundations and coastal structures, the investigation of wave-induced seabed response in the vicinity of the structures is important. The modeling of the interaction problem incorporating multiple physical domains including the fluid domain of waves and the solid domain(s) of the seabed (and the structure).

To date, most of the studies in the open literature followed the manner of using the volume of fluid (VOF) method or boundary element method (BEM) to solve the wave domain and a separate code or software based on the finite element method (FEM) or finite difference method (FDM) to solve the soil domain (Jeng et al., 2013a; Sui et al., 2016; Ye, 2012b; Zhang et al., 2015). For example, Jeng et al. (2013a) proposed a model for the wave-induced seabed response around marine structures. In their work, the VOF method is applied to model the waves and the FEM is applied for the soil analysis. However, to couple different numerical methods/tools for each physical domain, the external data exchange and time-step update can incur a high usage of computational memory and a low efficiency. Jeng (2012) reviewed the numerical methods for wave-seabed interaction in terms of FDM (Sui et al., 2019; Zen and Yamazaki, 1990a,b), FEM(Gatmiri, 1990; Jeng and

Hsu, 1996; Jeng and Lin, 2000; Okusa, 1985) and BEM((Raman-Nair et al., 1991), respectively. Among them, the FEM method has been most commonly used. In recent years, with the development of open-source software, the FVM-based OpenFOAM becomes a platform for multi-physic solver development. Using the same numerical method within the same framework, the time and computational memory required by the data exchange between different physical domains can be reduced. Liu et al. (2007) first discretized the Biot's equations in an FVM manner within OpenFOAM. They investigated the wave-induced response around submerged objects but without parallel computing. Tang et al. (2014) implemented a three-dimensional FVM-based anisotropic poro-elastic Biot's model in the quasi-static form. Elsafti and Oumeraci (2016a) developed a hydro-geotechnical model named *geotechFoam* to model the wave-structure-seabed interaction around the marine gravity structures. The quasi-static anisotropic poro-elastic solver by Tang et al. (2014) was validated and applied in the work of Li et al. (2018) in which the anisotropic consideration was proved to be practical for modeling the seabed of medium and coarse sand. Recently, Zhang et al. (2016) and Sui et al. (2018) have carried out studies on non-homogeneous soil response in waves using the aforementioned FDM model.

The present study focuses on the momentary liquefaction in the poro-elastic seabed. In the work of Ulker et al. (2009b) and Ulker et al. (2010), three forms of the Biot's poro-elastic model were discussed, in terms of the quasi-static form, the partial dynamic form (i.e., the $u-p$ formulation), and the fully dynamic form. The difference between the forms is based on the consideration of including inertial terms associated with the motion of fluids and solids. The fully dynamic Biot's model contains the terms associated with the acceleration of the soil and relative acceleration of the fluid compared to the soil. However, it was reported that the fully dynamic solution could provide a good prediction but the solutions were lengthy and difficult to be applied in engineering practice, as discussed in the work of Jeng and Rahman

(2001) and Jeng and Cha (2003). The one-dimensional $u-p$ approximation model was proposed by Zienkiewicz et al. (1980) based on Biot's poro-elastic theory(Biot, 1956). The pore fluid acceleration relative to the solid phase is neglected, in order to reduce the computational effort compared to the fully dynamic form. The one-dimensional $u-p$ approximation (Zienkiewicz et al., 1980) was further extended to 2D by Jeng and Rahman (2000). The $u-p$ formulation can be more accurate than the quasi-static form for the dynamic cases with moderate frequencies. It also reduces the computational effort compared to the fully dynamic form of the Biot's model.

The present work implements the $u-p$ approximation Biot's model in the FVM-based framework with anisotropic considerations. The finite volume (FV) soil solver is named `anisoUpFoam` and is coupled with FV wave solver and structure solver to investigated the WSSI interaction. The present FV $u-p$ model is validated against experimental data of standing wave-induced pore pressure in the soil by Tsai and Lee (1995). To validate the integrated WSSI analysis model, the experiment of wave-pile-soil interaction (Qi, 2018; Qi and Gao, 2014) is reproduced. The experimental data used in this work were not presented in the paper of Qi and Gao (2014). Through personal contact with Qi (2018), the unpublished data were used in the present work to validate the WSSI model.

To analyze the momentary liquefaction risk in the seabed, the assessment of soil consolidation behavior in the presence of marine structures is essential. A consolidation solver named `elasticBiotConsolidationFoam` in the quasi-static form accounting for the gravitational forces of the marine structure is developed in the present work. The consolidation solver is verified against the theoretical solution for the one-dimensional Terzaghi's consolidation test by Wang (2017). For the liquefaction analysis, various liquefaction criteria have been proposed based on the effective stress (Okusa, 1985; Tsai, 1995) or the excess pore pressure (Jeng, 1997c; Zen and Yamazaki, 1990b). The liquefaction assessment module in the present toolbox incorporates the

proposed criteria based on both the vertical effective stress and the excess pore pressure.

The present toolbox is then applied to two case studies. The first one is a 2D nonlinear wave-seabed interaction case without the presence of the structure. In the second one, a 3D parametric study of wave-induced seabed response investigation around offshore foundations with various designs is carried out, following the sequence of consolidation analysis, WSSI analysis and momentary liquefaction assessment. Two liquefaction criteria are applied and compared.

The toolbox can be used to investigate the seabed response and momentary liquefaction risk around offshore foundations and marine structures in waves. It is built with a series of solvers and utilities, including a consolidation solver, an anisotropic soil response solver with liquefaction assessment module, a linear structural response solver, and interface data mapping utilities. Each specific solver requires minimized parameter specification and can be used independently for the specific analysis of consolidation or soil response. Parallel running is allowed for each solver. The present FVM model can model arbitrary 3D geometry of the structure. Using parallel running, a large domain can be solved in a fast manner. The toolbox is made publicly available through the foam-extend community (Li et al., 2019).

4.1.2 Theoretical Background

4.1.2.1 Free Surface Wave Model

In the wave-structure-seabed analysis, the wave domain is governed by the incompressible Navier-Stokes equations including the continuity equation and the momentum equations.

$$\nabla \cdot \mathbf{u} = 0 \tag{4.1}$$

$$\frac{\partial \mathbf{u}}{\partial t} + (\mathbf{u} \cdot \nabla)\mathbf{u} = -\frac{1}{\rho_f}\nabla p_d + \mathbf{g} + \frac{1}{\rho_f}\nabla \cdot \boldsymbol{\tau} \tag{4.2}$$

where $\mathbf{u}$ denotes the velocity vector with three components in the x,y,and z directions respectively; $\mathbf{g}$ denotes the gravitational acceleration; ρ_f is the fluid density which can represent the air ρ_a or the water ρ_w. p_d is the dynamic wave pressure which is defined as $p_d = p_t - \rho_f \mathbf{g} \cdot \mathbf{x}$, where p_t is the total pressure and the $\mathbf{x} = (x, y, z)$ is the Cartesian coordinate vector. $\boldsymbol{\tau}$ is the viscous stress tensor with Einstein notation of τ_{ij}. For Newtonian fluid,

$$\tau_{ij} = 2\mu\sigma_{ij} \tag{4.3}$$

where μ is the dynamic molecular viscosity with μ_{air} for the air and μ_{water} for the water. σ_{ij} is defined by

$$\sigma_{ij} = \frac{1}{2}\left(\frac{\partial u_i}{\partial x_j} + \frac{\partial u_j}{\partial x_i}\right) \tag{4.4}$$

where $i, j \in$ [1,2,3]. u_i and u_j denote the velocity components in x, y and z direction respectively.

The equations are solved for the two immiscible fluids simultaneously, where the fluids are tracked using a scalar field α. α is 0 for air and 1 for water, and any intermediate value is a mixture of the two fluids. The distribution of α is modelled by an advection equation

$$\frac{\partial \alpha}{\partial t} + \nabla \cdot \alpha\mathbf{u} + \nabla \cdot [\alpha(1-\alpha)\mathbf{u}_r] = 0 \tag{4.5}$$

The last term on the left-hand side is a compression term, which limits the smearing of the interface, and $\mathbf{u}_r$ is a relative velocity (Berberović et al., 2009).

Using α, one can express the spatial variation in any fluid property, through the weighting

$$\Phi = \alpha\Phi_{water} + (1-\alpha)\Phi_{air} \tag{4.6}$$

Φ is a fluid property, such as ρ_f and μ.

4.1.2.2 Linear Elastic Structure Model

The structure domain is modelled as a linear elastic media and is governed by a linear momentum balance equation and isotropic linear elastic strain-displacement relations. The equations and the solving of the equations can be referred to Section 3.1.2.3 in Chapter 3 or Li et al. (2018).

4.1.2.3 Anisotropic Biot's Consolidation Model

In the present work, the soil behavior is modelled by the classical Biot's consolidation equations (Biot, 1941) with the interaction between the solid skeleton and the pore fluids, considering the anisotropic soil characteristics. The seabed is assumed to be fully saturated and the soil skeleton generally obeys Hooke's law with elastic properties.

- **Constitutive relations:**

  In the present work, the tension stress is defined as positive while the compression stress is defined as negative, in compliance with the tradition in computational continuum mechanics. The total stress for the saturated porous medium is defined by

  $$\boldsymbol{\sigma} = \boldsymbol{\sigma}^{'} - p\mathbf{I} \tag{4.7}$$

  where $\boldsymbol{\sigma}^{'}$ is the effective stress tensor of the soil skeleton, $\boldsymbol{\sigma}$ is the total stress tensor of soil mixture, p is the pore fluid pressure, and $\mathbf{I}$ is the identity tensor.

Effective stress-strain relation by the generalized Hooke's law is expressed as

$$\boldsymbol{\sigma}^{'} = C : \boldsymbol{\varepsilon} \tag{4.8}$$

The strain-displacement relation is expressed as

$$\boldsymbol{\varepsilon} = \frac{1}{2}(\nabla \mathbf{U} + (\nabla \mathbf{U})^T) \tag{4.9}$$

where $\boldsymbol{\varepsilon}$ is the strain tensor, $\mathbf{U}$ is the soil skeleton displacement vector.

For anisotropic soil materials, the orthotropic elastic stress-strain relation can be expressed in a 6×6 matrix notation:

$$\boldsymbol{\sigma}^{'} = \begin{pmatrix} \sigma^{'}_{xx} \\ \sigma^{'}_{yy} \\ \sigma^{'}_{zz} \\ \sigma_{xy} \\ \sigma_{yz} \\ \sigma_{xz} \end{pmatrix} = \begin{bmatrix} A_{11} & A_{12} & A_{31} & 0 & 0 & 0 \\ A_{12} & A_{22} & A_{23} & 0 & 0 & 0 \\ A_{31} & A_{23} & A_{33} & 0 & 0 & 0 \\ 0 & 0 & 0 & A_{44} & 0 & 0 \\ 0 & 0 & 0 & 0 & A_{55} & 0 \\ 0 & 0 & 0 & 0 & 0 & A_{66} \end{bmatrix} \begin{pmatrix} \varepsilon_{xx} \\ \varepsilon_{yy} \\ \varepsilon_{zz} \\ \varepsilon_{xy} \\ \varepsilon_{yz} \\ \varepsilon_{xz} \end{pmatrix} = \mathbf{C} : \boldsymbol{\varepsilon} \tag{4.10}$$

where $\boldsymbol{\sigma}^{'}$ is the effective stress tensor. According to the work of Demirdžić et al. (2000), the 9 independent coefficients A_{ij} are calculated from Young's modulus E_i and Poisson's ratio ν_{ij} and shear modulus G_{ij} as follows:

$$\begin{aligned} A_{11} &= \frac{1-\nu_{yz}\nu_{zy}}{JE_yE_z}, & A_{22} &= \frac{1-\nu_{xz}\nu_{zx}}{JE_xE_z}, & A_{33} &= \frac{1-\nu_{yx}\nu_{xy}}{JE_yE_x}, \\ A_{12} &= \frac{\nu_{xy}+\nu_{zy}\nu_{xz}}{JE_xE_z}, & A_{23} &= \frac{\nu_{yz}+\nu_{yx}\nu_{xz}}{JE_xE_y}, & A_{31} &= \frac{\nu_{zx}+\nu_{yx}\nu_{zy}}{JE_yE_z}, \\ A_{44} &= 2G_{xy}, & A_{55} &= 2G_{yz}, & A_{66} &= 2G_{zx} \end{aligned} \tag{4.11}$$

where

$$J = \frac{1 - \nu_{xy}\nu_{yx} - \nu_{yz}\nu_{zy} - \nu_{xz}\nu_{zx} - 2\nu_{yx}\nu_{zy}\nu_{xz}}{E_x E_y E_z} \tag{4.12}$$

- **Quasi-static model for consolidation analysis:**

  The Biot's model contains two governing partial differential equations:

  - One vector equation for the momentum equilibrium.
  - One scalar equation for the mass conservation.

  In the consolidation analysis, a static gravitational force is imposed on the seabed; therefore, the Biot's model in the quasi-static form is applied because the frequency of the process is very low. The soil domain in the consolidation analysis is governed by a quasi-static momentum balance equation for the soil mixture and a mass balance equation for the pore fluid based on Darcy's law. The quasi-static momentum balance equation is presented in Eqn. 4.13:

$$\nabla \cdot [\mathbf{C} : \frac{1}{2}(\nabla \mathbf{U} + (\nabla \mathbf{U})^T)] - \nabla p + \rho \mathbf{g} = 0 \tag{4.13}$$

  where $\mathbf{U}$ is the soil (skeleton) displacement, p is the pore fluid pressure, ρ is the density of the soil mixture, $\mathbf{g}$ is the gravitational acceleration vector with components of $(0,0,g)$, and $\mathbf{C}$ is the fourth-order elastic stiffness tensor. The density of the soil mixture, or submerged density of the soil is calculated by

$$\rho = n\rho_f + (1-n)\rho_s \tag{4.14}$$

  where n is the porosity, ρ_s is the soil density and ρ_f is the water density. The mass balance equation of the pore fluid based on Darcy's law is shown in Eqn. 4.15:

$$\frac{n}{K'}\frac{\partial p}{\partial t} - \frac{1}{\gamma_w}\nabla \cdot (\mathbf{k} \cdot \nabla p) + \frac{\partial}{\partial t}(\nabla \cdot \mathbf{U}) + \frac{\mathbf{k}}{g} \cdot (\nabla \cdot \mathbf{g}) = 0 \tag{4.15}$$

where n denotes the soil porosity, γ_w denotes the specific weight of water in soil, and $\mathbf{k}$ denotes the diagonal permeability tensor with values of k_x, k_y and k_z. The bulk modulus of the compressible pore flow $K^{'}$ is approximately computed by using the formulation of Vafai and Tien (1981):

$$\frac{1}{K^{'}} = \frac{1}{K_w} + \frac{1 - S_r}{p_a} \tag{4.16}$$

where S_r denotes the degree of soil saturation, K_w denotes the bulk modulus of pure water ($\approx$ 2GPa), and $p_a = \rho_f g h_w$ denotes the absolute pore water pressure at the seabed.

- **u-p approximation model for wave-induced seabed response:**

  The partial dynamic $u - p$ formulation is more accurate compared to the quasi-static form for the oscillating problems and is more efficient compared to the fully-dynamic form for most of the engineering problems. Therefore, it is adopted for the wave-induced seabed response modeling in the present work. Satisfactory accuracy has been reported by the previous work such as Ye et al. (2013).

  The wave-induced soil response analysis starts from the status that the gravity structure has been installed in place and the consolidation process has been completed. At this stage, the seabed soil has adjusted itself in equilibrium with the massive weight of the gravity structure. The governing equations for the $u - p$ approximation model to analyze the wave effect on the soil is given as follows:

$$\nabla \cdot [\mathbf{C} : \frac{1}{2}(\nabla \mathbf{U} + (\nabla \mathbf{U})^T)] - \nabla p - \rho \frac{\partial^2 \mathbf{U}}{\partial t^2} = 0 \tag{4.17}$$

$$\frac{n}{K^{'}} \frac{\partial p}{\partial t} - \frac{1}{\gamma_w} \nabla \cdot (\mathbf{k} \cdot \nabla p) + \frac{1}{g} \nabla \cdot (\mathbf{k} \cdot \frac{\partial^2 \mathbf{U}}{\partial t^2}) + \frac{\partial}{\partial t} (\nabla \cdot \mathbf{U}) = 0 \tag{4.18}$$

It is noted that the gravitational term $\rho \mathbf{g}$ is not incorporated in Eqn. 4.17 for the force balance. It is because that the partial dynamic $u-p$ approximation form is applied for the pure wave-induced soil response analysis, which starts from an equivalent status between the structure and the soil. Therefore, in the Eqn. 4.17, the external force is only the dynamic wave pressure, incorporated in the term p.

4.1.2.4 Liquefaction Criteria

As mentioned before, there are various liquefaction criteria in the open literature based on the effective stress (Okusa, 1985; Tsai, 1995) or the excess pore pressure (Jeng, 1997c; Zen and Yamazaki, 1990b). Ye (2012a) compared different liquefaction criteria for the seabed without marine structure built on it. Ye (2012a) concluded that among those liquefaction criteria based on the effective stress, the criteria of Okusa (1985) provides most appropriate engineering solution and among those liquefaction criteria based on the excess pore pressure, the criteria of Zen and Yamazaki (1990b) provide the best engineering solution.

However, these criteria are all applicable to the cases without a structure. In the case of momentary liquefaction around a gravity structure, the initial effective stress from the consolidation stage should be taken into consideration. In the present work, following modified liquefaction criteria considering the presence of the structure are incorporated in the liquefaction assessment module, including:

- **Criterion A:** The modified form from Okusa (1985),

$$\sigma_z^{'} \geq |\sigma_{z0}^{'}| \tag{4.19}$$

where $\sigma_{z0}^{'}$ is the initial vertical effective stress induced by the gravitational forces from the consolidation process. The applications of this

criterion can be referred to the work of Jeng et al. (2013a) and Ye et al. (2014).

- **Criterion B:** The modified form from Zen and Yamazaki (1990b),

$$p - p_b \geq |\sigma'_{z0}| \tag{4.20}$$

where p_b is the wave-induced pressure on the seabed surface. The applications of this criterion can refer to the work of Sui et al. (2017), Zhao et al. (2017a) and Sui et al. (2019).

The right hand sides of Eqn. 4.19 and Eqn. 4.20 express the downward gravitational forces including the soil weight and the external gravitational forces. The left hand sides of the liquefaction equations express the upward wave-induced hydraulic forces. In the present work, the two liquefaction criteria above are implemented. The present study will evaluate and compare the two representative criteria (A and B) in the application section (Section 4.1.5) with a gravity-based structure built on the seabed.

4.1.2.5 Finite Volume Method Based Approach

In the Biot's model, the momentum and mass balance equations are strongly coupled. In the FVM analysis, the coupling of the three displacement components U_x, U_y, U_z and pressure p are handled by using a 'segregated strategy' (Demirdžić and Martinović, 1993; Demirdžić and Muzaferija, 1994). The equations are split into the 'implicit' and 'explicit' discretization parts, where the 'explicit' parts contain all the coupling effect from the other variables and shall be evaluated from the previous iteration or the initial condition.

The cross-component coupling in Eqn. 4.10 can be decomposed into implicit and explicit components:

$$\boldsymbol{\sigma}' = \mathbf{C} : \boldsymbol{\varepsilon} = \underbrace{\mathbf{K} \cdot \nabla \mathbf{U}}_{\text{implicit}} + \underbrace{\mathbf{C} : \boldsymbol{\varepsilon} - \mathbf{K} \cdot \nabla \mathbf{U}}_{\text{explicit}}. \tag{4.21}$$

where the $\mathbf{K}$ is a 3×3 diagonal stiffness tensor given by

$$\mathbf{K} = \begin{bmatrix} A_{11} & 0 & 0 \\ 0 & A_{22} & 0 \\ 0 & 0 & A_{33} \end{bmatrix} \tag{4.22}$$

In this way, Eqn. 4.13 and Eqn. 4.15 can be rearranged into the FVM implicit-explicit format:

$$\underbrace{\nabla \cdot (\mathbf{K}\nabla\mathbf{U})}_{\text{implicit}} = \underbrace{\nabla \cdot [\mathbf{C} : \frac{1}{2}(\nabla\mathbf{U} + \nabla\mathbf{U}^T)] + \nabla \cdot (\mathbf{K}\nabla\mathbf{U}) - \nabla p + \rho\mathbf{g}}_{\text{explicit}} \tag{4.23}$$

$$\underbrace{\frac{n}{K'}\frac{\partial p}{\partial t} - \frac{1}{\gamma_w}\nabla \cdot (\mathbf{k} \cdot \nabla p)}_{\text{implicit}} = \underbrace{-\frac{\partial}{\partial t}(\nabla \cdot \mathbf{U}) - \frac{\mathbf{k}}{g} \cdot (\nabla \cdot \mathbf{g})}_{\text{explicit}} \tag{4.24}$$

Similarly, the FVM implicit-explicit format for the $u - p$ approximation model to apply to the wave effect analysis is written as:

$$\underbrace{\nabla \cdot (\mathbf{K}\nabla\mathbf{U})}_{\text{implicit}} = \underbrace{\nabla \cdot [\mathbf{C} : \frac{1}{2}(\nabla\mathbf{U} + \nabla\mathbf{U}^T)] + \nabla \cdot (\mathbf{K}\nabla\mathbf{U}) - \nabla p - \rho\frac{\partial^2\mathbf{U}}{\partial t^2}}_{\text{explicit}} \tag{4.25}$$

$$\underbrace{\frac{n}{K'}\frac{\partial p}{\partial t} - \frac{1}{\gamma_w}\nabla \cdot (\mathbf{k} \cdot \nabla p)}_{\text{implicit}} = \underbrace{-\frac{\partial}{\partial t}(\nabla \cdot \mathbf{U}) - \frac{1}{g}\nabla \cdot (\mathbf{k} \cdot \frac{\partial^2\mathbf{U}}{\partial t^2})}_{\text{explicit}} \tag{4.26}$$

The iterative procedure for solving the Biot's models are shown in Figure 4.1. Equations are solved iteratively until the solution changes less than a pre-defined tolerance. As pointed out in the work of Jasak and Weller (2000), the finite-volume(FV) discretization to the linear stress analysis problem uses small matrices for the three components of displacement, rather than using

one large matrix that seen in the FEM. In this way, the usage of the computer memory can be significantly reduced.

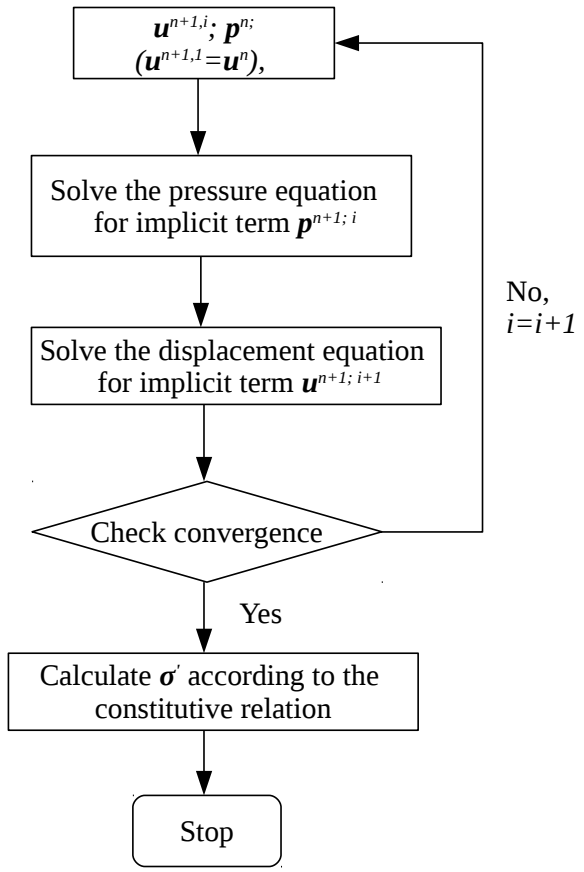

Figure 4.1 Iteration procedure for solving the Biot's model.

4.1.3 The FVM-Based WSSI Toolbox

4.1.3.1 The Solvers

The present FVM-based toolbox can be applied to soil consolidation analysis, WSSI analysis, and momentary liquefaction assessment. An outline of the

toolbox and an illustration of the systematic analysis procedure is presented in Figure 4.2. The present toolbox reads wave pressure data from a free-surface solver. There is no restriction on selecting the free-surface modeling tools. In the OpenFOAM CFD library, various solvers can be adopted, such as `interFoam` solver in OpenFoam, toolboxes of `waves2Foam` (Jacobsen et al., 2012) and `iHFoam` (Higuera et al., 2013). In the present work, the `waves2Foam` is adopted for modeling the wave generation and absorption.

For the soil consolidation analysis, a new solver `biotConsolidationFoam` is developed in the present work. It reads the static gravitational force from the structure and computes the initial vertical effective stress in the soil. In the WSSI analysis, the new solver named `anisoUpFoam` is developed to consider the anisotropic soil property and the inertial force of the soil skeleton. For the momentary liquefaction assessment, a module is developed to read data from the consolidation analysis and the WSSI analysis. Criteria extended from Okusa (1985) and Zen and Yamazaki (1990a) are implemented. Since the toolbox is based on the poro-elastic soil model, the momentary liquefaction is assessed.

4.1.3.2 Boundary Conditions

- **Boundary conditions for consolidation analysis:**

  Boundary conditions for consolidation analysis are presented in Figure 4.3a. In the consolidation analysis, the static gravitational force from the structure $-\sigma_0$ is read as the boundary condition at the structure-seabed interface.

  $$-\sigma_0 = -(W - B)/A \tag{4.27}$$

  where W is the weight of the structure, B is the buoyant force and A is the area of the structure-seabed interface.

  A Neumann type boundary for the displacement at the structure-seabed interface is specified with a traction-displacement relation $\nabla \mathbf{U} = \mathrm{f}(\mathbf{T})$.

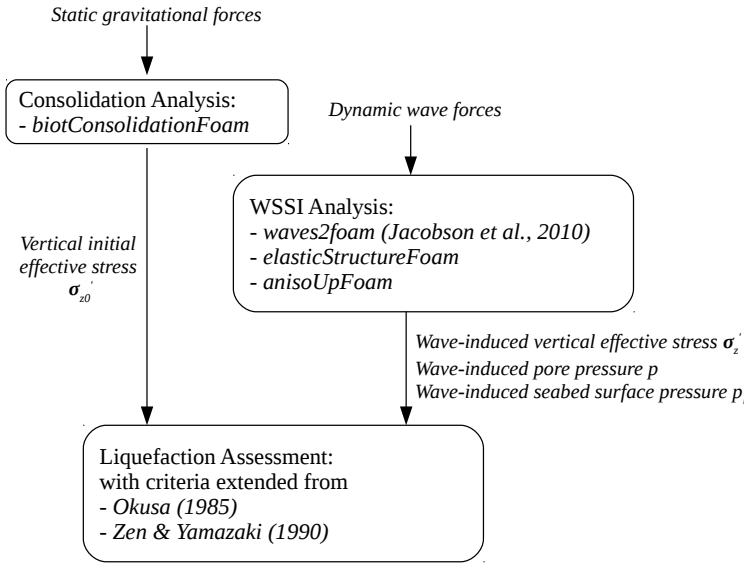

Figure 4.2 An outline of the FVM-based WSSI toolbox.

The traction $\mathbf{T}$ is defined by

$$\mathbf{T} = \boldsymbol{\sigma} \cdot \mathbf{n} \tag{4.28}$$

where $\mathbf{n}$ is the surface normal vector. The traction-displacement relation is expressed as

$$\mathbf{T} = \left[\mu \nabla \mathbf{U} + \mu (\nabla \mathbf{U})^T + \lambda \mathbf{I} tr(\nabla \mathbf{U})\right] \cdot \mathbf{n} \tag{4.29}$$

Therefore, a displacement gradient boundary can be derived from Eqn. 4.29 as

$$(\nabla \mathbf{U}) \cdot \mathbf{n} = \frac{\mathbf{T} - [\mu (\nabla \mathbf{U})^T + \lambda \mathbf{I} tr(\nabla \mathbf{U}) - (\mu + \lambda) \nabla \mathbf{U}] \cdot \mathbf{n}}{(2\mu + \lambda)} \tag{4.30}$$

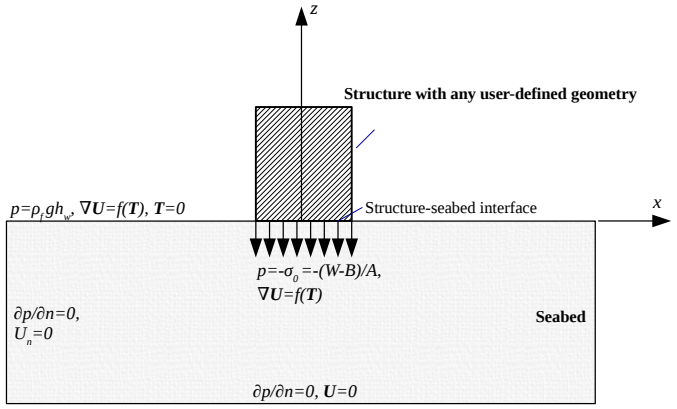

(a) Consolidation analysis.

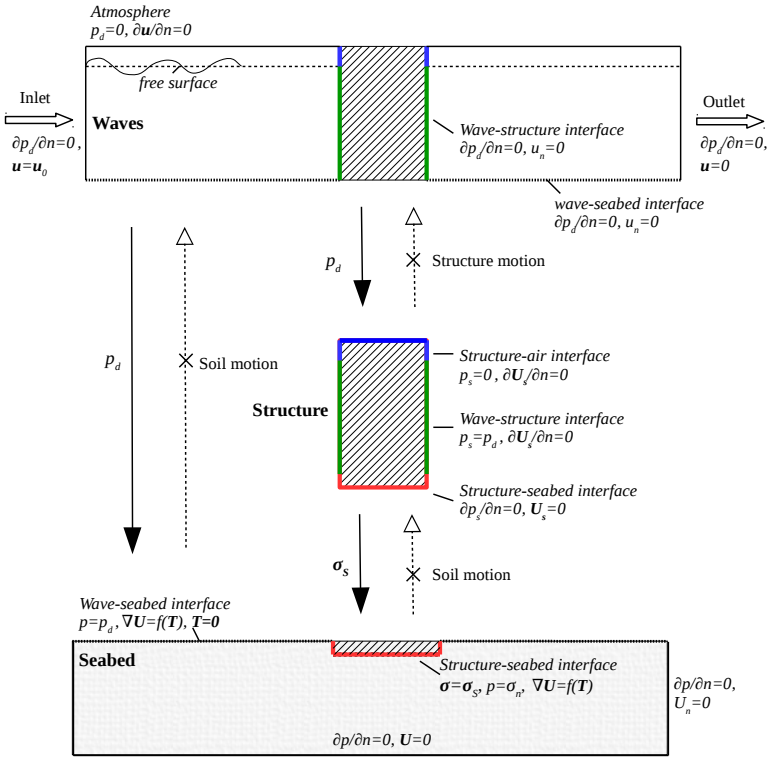

(b) Wave-structure-seabed interaction (WSSI) and the one-way boundary coupling.

Figure 4.3 Boundary conditions of consolidation analysis and wave-structure-seabed interaction (WSSI) analysis.

The term $[\mu(\nabla \mathbf{U})^T + \lambda \mathbf{I} tr(\nabla \mathbf{U}) - (\mu + \lambda)\nabla \mathbf{U}]$ on the right-hand side is treated explicitly. Iterations are used to compute the compatible displacement gradient $(\nabla \mathbf{U})$ with known $\mathbf{T}$.

At the seabed surface, a zero-traction boundary is specified where $\mathbf{T} = 0$. A static water pressure $p = \rho_f g h_w$ is applied on the seabed boundary. At the seabed bottom, a stiff layer of clay is assumed to be underneath the sand sediments so that the pore pressure p has zero normal gradient and the displacement is zero. At the seabed lateral sides, the pore pressure p has zero normal gradient. A slip boundary is specified at the seabed lateral sides for the displacement where the normal displacement to the boundary U_n is zero.

- **Boundary conditions for WSSI analysis:**

  In the dynamic WSSI analysis, one-way coupling algorithm is considered, due to the small magnitudes of wave-induced structure vibration and soil deformation compared to the wavelength. The time-varying data transfer in a single direction at the interfaces, i.e., from waves to the structure, from waves to the seabed and from the structure to the seabed. The small structure and seabed motions do not alter the wave domain. The dynamic wave pressure p_d imposes directly on the seabed through the wave-seabed interface and imposed indirectly on the seabed through wave-structure and structure-seabed interfaces. The schematic one-way coupling procedure for the dynamic WSSI analysis and the corresponding boundary conditions are presented in Figure 4.3b.

  Boundary conditions for wave modeling are specified as follows.

  - The inlet velocity is specified as the input wave velocity $\mathbf{u} = \mathbf{u_0}$, while the outlet velocity is $\mathbf{u} = 0$. The pressure at the inlet and outlet has zero normal gradient.
  - At four sides of the numerical wave tank, the pressure has zero normal gradient. A slip boundary is set for the velocity at the

lateral sides where the flow is passing along the walls and the normal flow velocity u_n is zero.

- At the atmosphere, the dynamic wave pressure p_d is zero and the velocity has zero normal gradient.
- At the wave-structure interface and the wave-seabed interface, the pressure has zero normal gradient. A slip boundary is set for the velocity. Bottom boundary layer effect is neglected since it has insignificant effect on the dynamic wave pressure results.

Boundary conditions for structure analysis are specified as follows.

- At the structure-air interface, the dynamic pressure on the structure is zero. The structure displacement U_s has zero gradient.
- At the wave-structure interface, the dynamic pressure p_s is read from the dynamic wave pressure p_d. The structure displacement has zero normal gradient.
- At the structure-seabed interface, the dynamic pressure p_s has zero normal gradient. The structure displacement is set to zero based on the assumption that the structure is rigid and the seabed can provide a valid support to the structure.

Boundary conditions for seabed analysis are specified as follows.

- At the wave-seabed interface, the soil has zero traction. The displacement boundary at the wave-seabed interface is computed via the traction-displacement relation. The pore pressure is equal to the dynamic wave pressure on the seabed.
- At the structure-seabed interface, the pore pressure has zero normal gradient since the structure is impermeable. The soil displacement at the structure-seabed interface is triggered by the structural force, while the structural force is wave-induced. The

displacement boundary at the structure-seabed interface is also computed via the traction-displacement relation.

- At the lateral sides of the seabed, the pore pressure has zero normal gradient. The soil skeleton is allowed to slip.
- At the seabed bottom, a stiff layer of clay is assumed to be underneath the sand sediments and the pore pressure has zero normal gradient. The soil skeleton has zero displacement.

For solving the multi-physic WSSI problems, different physical domains can have different demands on the time step and grid size, based on the convergence and stability requisitions. For the WSSI problem, the time steps and the grid sizes needed for the linear-elastic soil and structural domains are relatively larger than what is needed for the nonlinear wave domain(Li, 2016). Therefore, it not efficient to calculate the multiple domains with the same grid size and to loop at the same time step. In the present model, time-dependent (time-varying) boundary conditions are applied for the data mapping at the interfaces. First, the values at the interfaces of the supplied domain are interpolated in space and time. Then, the interpolated values are mapped to the targeted domain interface with a reversed normal vector. In the present work, linear interpolation is applied. The boundary data are first interpolated in space for every face center and then interpolated linearly between the time instants.

4.1.4 Validation and Verification

4.1.4.1 Verification of the FV Biot's Consolidation Solver

The present FV consolidation solver is verified against Terzaghi's classical consolidation test (Terzaghi, 1944; Wang, 2017). In Terzaghi's classical consolidation test, a constant stress $-\sigma_0$ is applied suddenly on the surface $z = 0$ of a saturated sample of length L_s. Here, z is positive in the downward

direction. The piston applying the load is permeable so that the top boundary is drained. The sample consolidates gradually as fluid flows out from the top drain. The setup of the test is shown in Figure 4.4. The input parameters for the present numerical simulation is presented in Table 4.1.

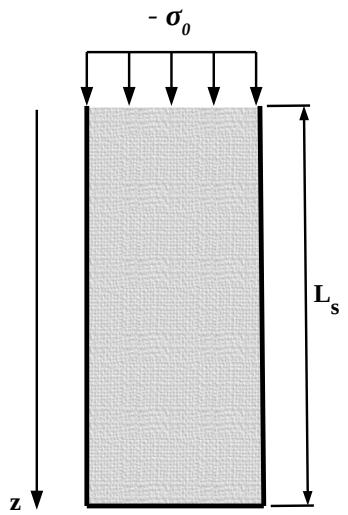

Figure 4.4 Test setup of Terzaghi's classical consolidation test.

The boundary conditions for reproducing the test is specified as follows:
At $z = 0$,

$$\sigma_z = -\sigma_0, \quad p = 0 \tag{4.31}$$

At $z = L_s$,

$$\frac{\partial p}{\partial z} = 0, \quad u_z = 0 \tag{4.32}$$

At four sides of the column, the boundary condition is defined as 'empty', i.e., the x and y directions are not solved, to achieve a one-dimensional problem.

Table 4.1 Parameter setting in the present numerical simulation for the 1D Terzaghi's consolidation test

Parameters	Values
L_s (m)	20
σ_0 (kPa)	10
Permeability k (m/s)	10^{-5}
Youngs modulus E (N/m^2)	10^8
Saturation degree S_r	0.995
Poissonsratio ν	0.25
Porosity n	0.3

Wang (2017) provided the non-dimensional analytical solutions for Terzaghi's consolidation theory. Figure 4.5 shows the comparison of pore pressure between the present numerical results and the analytical solution at certain time instants during the consolidation process. In the figure, the pressure p is normalized by the initial undrained response $p_0 = \Upsilon\sigma_0$, where Υ denotes the loading efficiency according to Wang (2017). Υ is 0.725 in the present simulation. The time instant t is normalized by L_s^2/c where c is the hydraulic diffusivity that governs the time lag. As shown in Figure 4.5, under the constant stress, the soil is consolidated along the time. The excess pore pressure is dissipated gradually from time instant $ct/L^2 = 0.01$ to 1.0. The present numerical results are consistent with the analytical solutions.

4.1.4.2 Validation of the FV $u-p$ Approximation Soil Solver

The present FV $u-p$ approximation soil solver is validated against the experimental data of Tsai and Lee (1995). Their experiment investigated the standing waves induced pore pressure in the sand bed in the vicinity of a vertical wall. In the work of Li et al. (2018), the same experiment was adopted to validate the quasi-static Biot poro-elastic solver. The present work reproduces the experiment of Tsai and Lee (1995) by using the $u-p$ approximation soil solver. The present numerical results are compared with

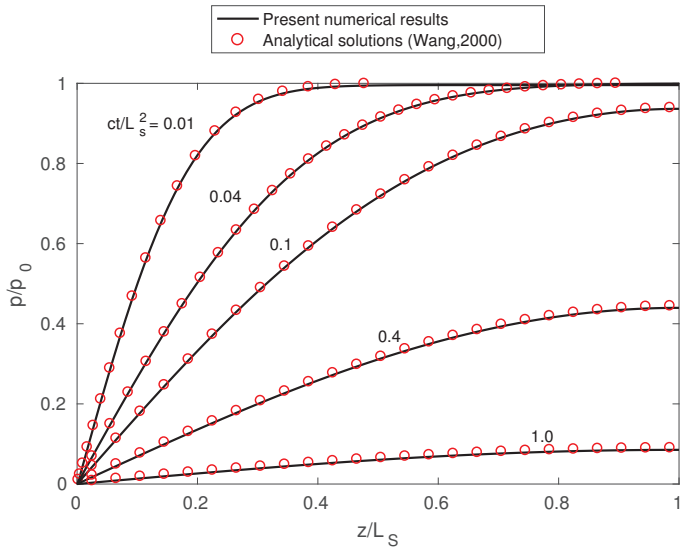

Figure 4.5 Verification of the consolidation model by comparing the present numerical results (biotConsolidationFoam) to the analytical solutions (Wang, 2017).

the experimental data of Tsai and Lee (1995) and the numerical results by the quasi-static Biot poro-elastic solver in Li et al. (2018).

The experimental setup by Tsai and Lee (1995) is shown in Figure 4.6. Waves propagated to the sand bed region in a flume and reflected at a vertical smooth wall at the end of the wave flume. In the sand bed, nine pore pressure transducers were placed vertically and horizontally below and close to the vertical wall, as shown in Figure 4.6. Five of the pressure transducers were installed vertically below the wall from the sand bed surface with 10 cm distance in between. Another four were installed horizontally at a depth of 10 cm in the sand with distances of $kx = 1/10\pi$, $2/10\pi$, $3/10\pi$, $4/10\pi$ and $5/10\pi$ to the wall, where k is the wave number. The sand was in medium firmness and the properties are presented in Table 4.2. The present numerical simulation uses the second-order Stokes wave theory to model the propagating waves based on the given wave properties. The amplitude of pore pressure

in the soil p_s is normalized by the amplitude of the pressure on the sand bed surface p_0. Figure 4.7 shows the comparison of pore pressure in the seabed between the present numerical results and the experimental data. They are in good agreement.

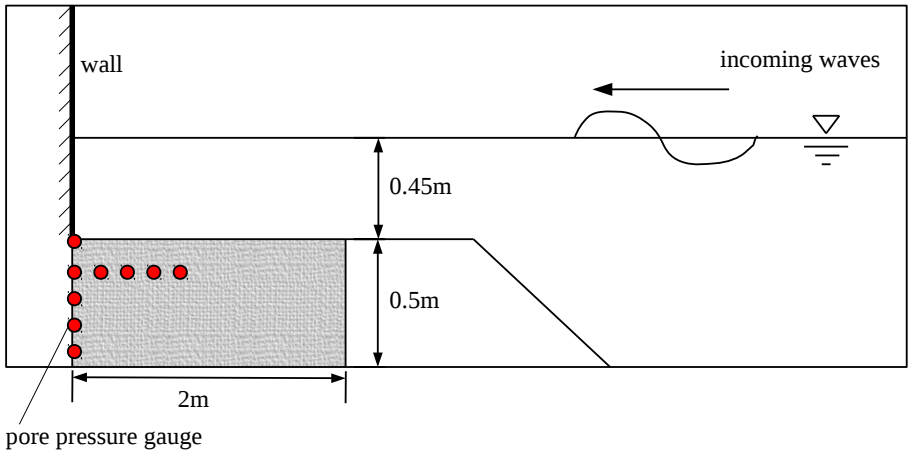

Figure 4.6 Experimental setup of Tsai and Lee (1995).

Table 4.2 Physical properties of the wave and soil for model validation (experiment conducted by Tsai and Lee (1995)).

Wave parameters		Soil parameters			
Wave height H (cm)	5.1	Permeability k (m/s)	1.2×10^{-4}	Young's modules E (N/m^2)	6.86×10^{7}
Wave period T (s)	1.5	Porosity n	0.38	Shear modulus G (N/m^2)	2.64×10^{7}
Wave type	second-order	Poisson's ratio ν	0.3	Saturation degree S_r	0.98

The present numerical results of FV $u-p$ model is also compared with the numerical results of FV quasi-static model by Li et al. (2018), as shown in Figure 4.8. It is seen that the present partial dynamic $u-p$ model gives

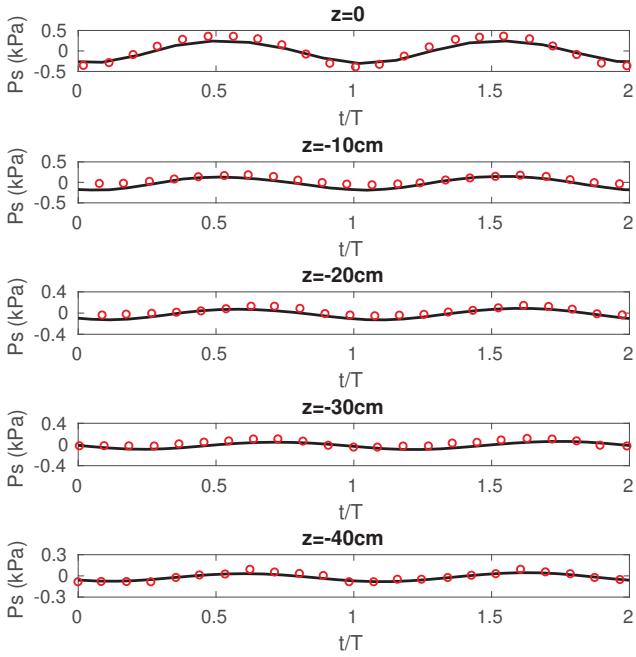

(a) Pore pressure at various depths, $kx = 0$.

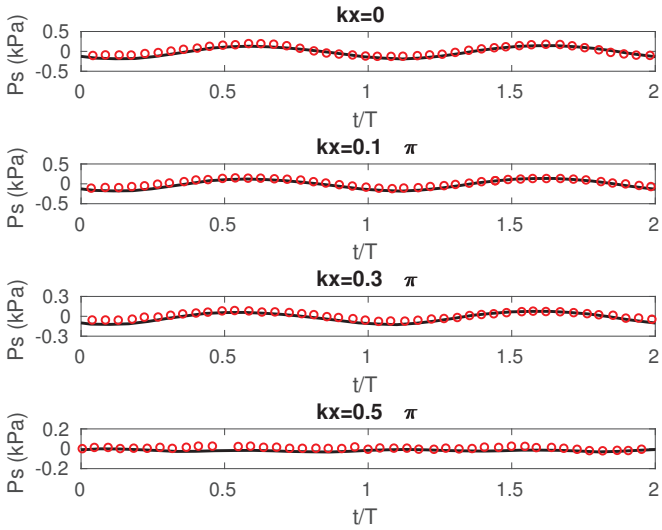

(b) Pore pressure at various horizontal positions, $z = -10$ cm.

Figure 4.7 Comparisons of the pore pressure response between measured data by Tsai and Lee (1995) and the numerical results by present FV $u-p$ approximation solver (○ : measured data by Tsai and Lee (1995); – : present numerical results by $u-p$ approximation solver.)

slightly higher prediction of the pore pressure than the quasi-static model, and is closer to the experimental measurement. The difference between quasi-static model and $u-p$ model is not very significant in this case (with a maximum difference ratio of 8.6% at the sand bed bottom), due to the mild wave condition. Nevertheless, the $u-p$ model shows a better prediction than the quasi-static model for this experiment, as compared to the experimental measurement. In rough sea or breaking wave cases, the difference between two numerical models can be more significant due to higher acceleration (Ulker et al., 2009a). Since the predicted excess pore pressure by $u-p$ model is higher than the quasi-static model, the $u-p$ model is able to provide a more conservative solution for the engineering problems.

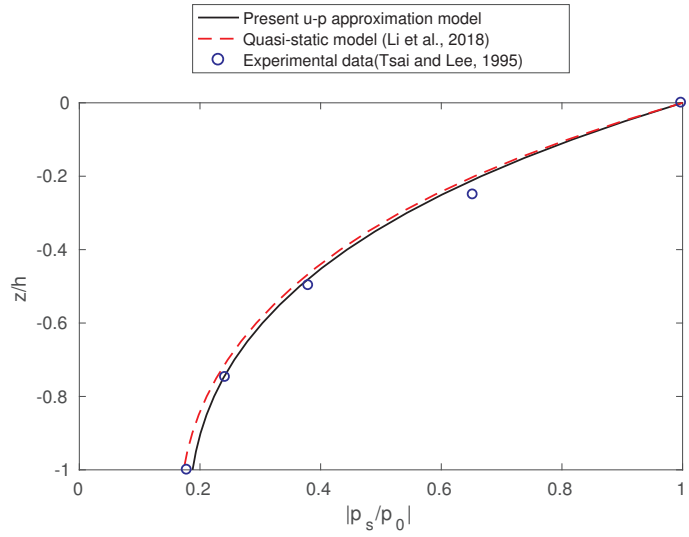

Figure 4.8 Comparisons of the pore pressure at various depths, $kx = 0$.

4.1.4.3 Validation of the WSSI Model

The present WSSI model including FV $u-p$ approximation soil solver coupled with wave generation tool `waves2Foam` is validated against existing experimental data. Qi and Gao (2014) performed a series of experiments to investigate the local-scour and pore pressure responses around a large-diameter monopile in combined waves and current. In their work, the pore pressure and the time development of scour depth around the monopile under the conditions of wave-only, current-only and wave-plus-current were measured. However, in the paper of Qi and Gao (2014), only the experimental data under wave-plus-current and under current-only were presented. The experimental data under wave-only conditions provided by Qi (2018) are processed and presented in this work to validate the present WSSI numerical model. The test condition of the wave-only case is given in Table 4.3. The experimental set-up is shown in Figure 4.9. Wave elevation data measured by three wave gauges are presented, with W1 in the far filed, W2 at 20 cm upstream to the pile and W3 at 10 cm upstream to the pile. Pore pressure data measured by four pressure gauges at two sides of the pile are presented. P1, P2 and P3 are located at the upstream side of the pile with 10 cm vertical gap in between. P4 is located at the downstream side of the pile. In view of the fact that the pile was installed before the sand box was filled in the experiment, the consolidation analysis is not required in the numerical reproduction of this experiment.

Comparisons of wave elevation and pore pressure between the present numerical simulation and the experimental data is shown in Figure 4.10 and Figure 4.11, respectively. Stokes second-order wave model is adopted for simulating the present waves. A good agreement is observed for the wave elevation results, with minor discrepancy in the wave trough amplitudes. The numerical results of the pore pressure also agree with the experimental data in the time series, with an average discrepancy of 6.9%. The present WSSI model is valid and is applicable to the case studies in Section 4.1.5.

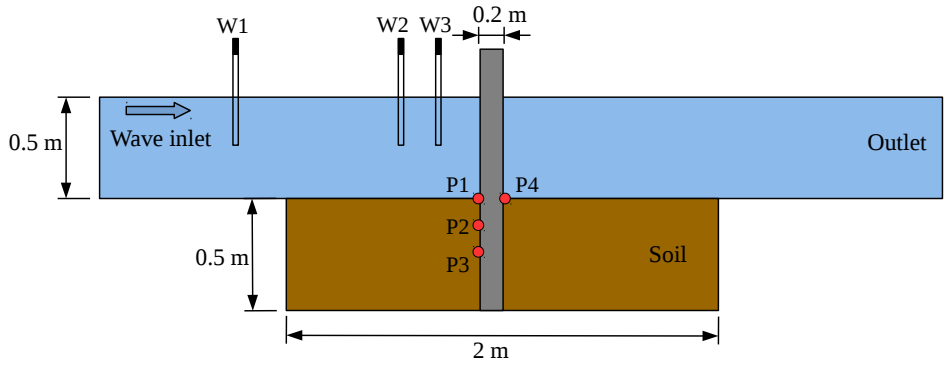

Figure 4.9 Experimental set-up of wave-pile-soil interaction (Qi and Gao, 2014).

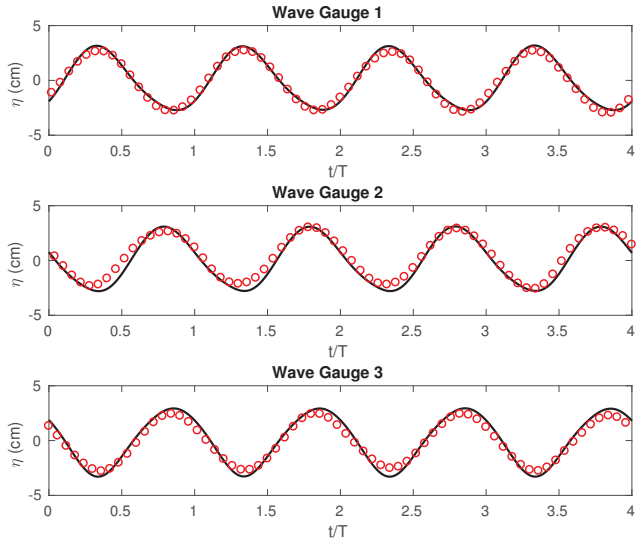

Figure 4.10 Comparison of the wave elevation.

Table 4.3 Parameter settings of the wave-pile-soil interaction experiment by Qi and Gao (2014).

Wave parameters	
Wave height H (cm)	5
Wave period T (s)	1.0
Water depth h_w (m)	0.5
Seabed parameters	
Seabed thickness d_s (m)	0.5
Young's modules E (N/m^2)	2.6×10^7
Poisson's ratio ν	0.3
Permeabilities(m/s) k	1.88×10^{-4}
Saturation factor S_r	0.997
Porosity n	0.435

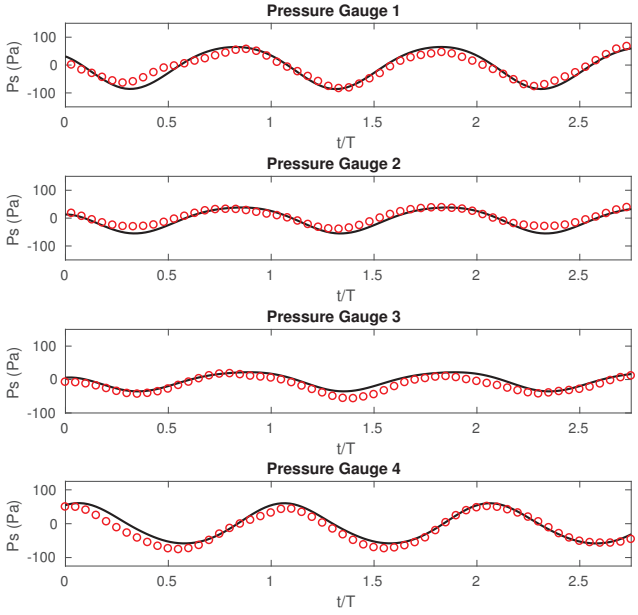

Figure 4.11 Comparison of pore pressure around the pile.

4.1.5 Applications

4.1.5.1 Nonlinear Wave-Induced Soil Response

The present `wssi` toolbox is applied to investigate the wave-induced soil response with and without the presence of the structure. A case study of 2D nonlinear wave-induced soil response is performed with wave height H=0.5 m, water depth H_w = 3 m and wave period T =2 s. According to the work of Fenton (1985), the fifth-order Stokes wave theory is applied to model the propagating waves considering the wave condition. A wave flume of 36-meter long is simulated by using the OpenFoam wave generation tool `waves2Foam` with inlet and outlet relaxation techniques (Jacobsen et al., 2012) to ensure the accuracy and no influence from the reflected waves. The soil domain is 30-meter long and 3-meter thick. The soil parameters in the Tsai and Lee (1995)'s experiment, as shown in in Table 4.2, are adopted with an anisotropic permeability consideration of $k_x = k_y = 5k_z = 6 \times 10^{-4}$ m/s.

Figure 4.12 (a) shows the dynamic wave pressure in the numerical wave flume and the pore pressure in the sand bed at a time instant of t/T = 15. When waves propagating over the and sand bed, a wave crest generates a positive pore pressure while a wave trough generates a negative pore pressure in the sand bed. The horizontal wave velocity field is presented in Figure 4.12 (b) together with the vertical effective stress in the sand bed. The positive vertical effective stress (tension) results from the wave trough. Figure 4.13 shows the time series of wave elevation and pore pressure in the sand bed. A phase-lag in the pore pressure diffusion is seen from a depth of 0 to 0.2 meters in the sand bed. The phase-lag in the present case from sand bed surface to a 0.2-meter depth is around one-sixth of the wave period. It has been proved that a phase lag exists in wave-induced soil response in a nearly saturated sea-bed of finite thickness (Jeng and Hsu, 1996) and also a cross-anisotropic seabed of infinite thickness (Jeng, 1998).

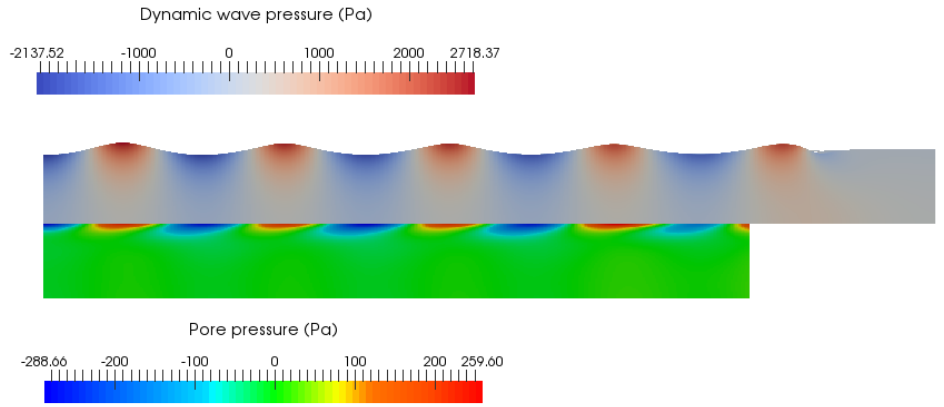

(a) Dynamic wave pressure in the wave flume and pore water pressure in the sand bed .

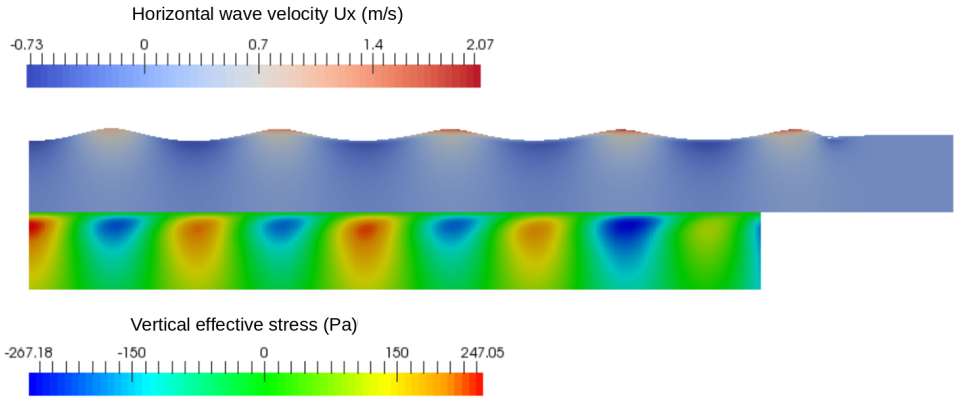

(b) Horizontal wave velocity in the wave flume and vertical effective stress in the sand bed.

Figure 4.12 Numerical model of nonlinear wave-seabed interaction.

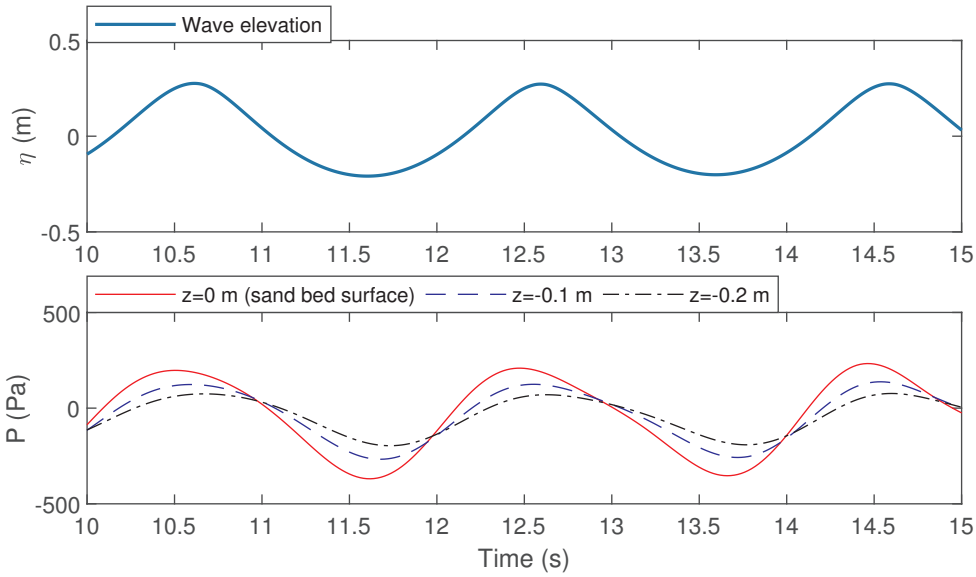

Figure 4.13 Time series of wave elevation and the corresponding pore pressure in the sand bed.

4.1.5.2 Wave-Structure-Seabed Interaction Modeling for Offshore Foundations

The integrated toolbox including the consolidation solver, WSSI solvers and the liquefaction module is applied to investigate the soil response and momentary liquefaction around offshore gravity-based foundations in a steep non-breaking wave condition. Gravity-based foundations for offshore wind turbines are normally installed close to the shore in a limited water depth. When waves travel into shallower water in the coastal areas, they are affected by the ocean bottom. The crest becomes higher and waves become steeper (Zhang et al., 2016). The gravity-based foundations are often exposed to steep waves while the linear wave theory is not applicable. Meanwhile, the gravity-based foundations have various designs that can result in different surrounding flow patterns and seabed pressure distributions after interacting with the incoming waves. The design of the gravity-based foundations usually

consists of a slab (with a diameter D) and a shaft (with a diameter $D^{'}$) on top of it, as shown in Figure 4.14b. A different ratio of $D^{'}/D$ will directly affect the wave diffraction pattern and further affect the dynamic wave pressure and seabed response around the slab bottom. In this section, a parametric study on wave-structure-seabed interaction around gravity-foundations with different $D^{'}/D$ from 0.25 to 0.75 is performed. Simplified models of the gravity-based foundations are shown in Figure 4.14b, while $D^{'}/D = 0.25$ resembles the diameter ratio of Lillgrund foundation in Jeppsson et al. (2008), $D^{'}/D = 0.5$ resembles the diameter ratio of the third generation of GBS concepts in Esteban et al. (2015). The slab height of $h_b = 0.189D$ is referred to the design of the Lillgrund foundation (Jeppsson et al., 2008). The design with $D^{'}/D = 1$ tends to be a monopile, which should be inserted into the seabed; therefore, it is not considered in the gravity-based circumstance. However, the $D^{'}/D = 1$ case is still computed in the present study to give a reference of the upper limit in the momentary liquefaction risk assessment.

The numerical setup of the parametric study is shown in Figure 4.14a. The entire system is built in a Cartesian coordinate system x, y, z, with $z = 0$ at the static free surface, x positive in the wave propagating direction, y positive toward the back of the tank, z positive upward. The width of the wave tank (distance between the sides of the tank) is set to be two wavelengths. Wave inlet and outlet relaxation zones (Jacobsen et al., 2012) are set to be 1 and 1.5 wave lengths, respectively. Wave parameters are set as follows. The wave steepness is $H/L = 0.095$. The relative water depth is $h_w/L = 0.175$ ($h_w/L \leq 0.1$ is considered as shallow water and $h_w/L \geq 0.5$ is considered as deep water). The water depth h_w is assumed as $1.75D$ and the corresponding wave length is $L = 10D$ and the wave height is $H = 0.95D$. Due to high nonlinearity of the incoming waves, 5th-order stream function wave theory (Dean, 1965) is utilized to model the waves. The structural material is considered as concrete with a density of 2400 kg/m^3. To examine the effect of $D^{'}/D$ of the foundation, the soil condition is kept constant. The seabed

Table 4.4 Parameter settings of the parametric study of wave-structure-seabed interaction. D is the characteristic diameter of the foundation slab with $D = 1$ in the present parametric study.

Wave parameters			
Water depth h_w (m)	$1.75D$		
Wave height H (m)	$0.95D$		
Wave length L (s)	$10D$		
Wave period T (m)	2.6 s for $D = 1$		
Structure parameters			
Characteristic length D (m)	1		
Bottom slab height h_b (m)	$0.189D$		
Shaft diameter $D^{'}$ (m)	$0.25 - 0.75D$		
Density ρ (kg/m^3)	2400		
Young's modules (N/m^2)	2.2×10^{10}		
Poisson's ratio	0.2		
Seabed parameters			
Seabed thickness d_s (m)	$5D$		
Young's modules (N/m^2)	$E_x = 1.2 \times 10^7$	$E_y = 1.2 \times 10^7$	$E_z = 2 \times 10^7$
Poisson's ratios	$\nu_{xy} = 0.2$	$\nu_{yz} = 0.24$	$\nu_{zx} = 0.4$
Permeabilities(m/s)	$k_x = 0.0005$	$k_y = 0.0005$	$k_z = 0.0001$
Saturation factor S_r	0.975		
Porosity n	0.3		

thickness is $d_s = 5D$. The soil property is referred to the measurement of the North sea soil by (Kjekstad and Lunne, 1981), with reasonable anisotropic considerations. The numerical parameters are given in Table 4.4.

The parametric study begins with the consolidation analysis, in order to check the initial vertical effective stress in the soil after the foundation is built on the seabed. Then, the WSSI analysis is performed. The wave-induced seabed response around the structure is investigated. Finally, momentary liquefaction assessment is performed with a comparison of two liquefaction criteria. Results and discussions are as follows.

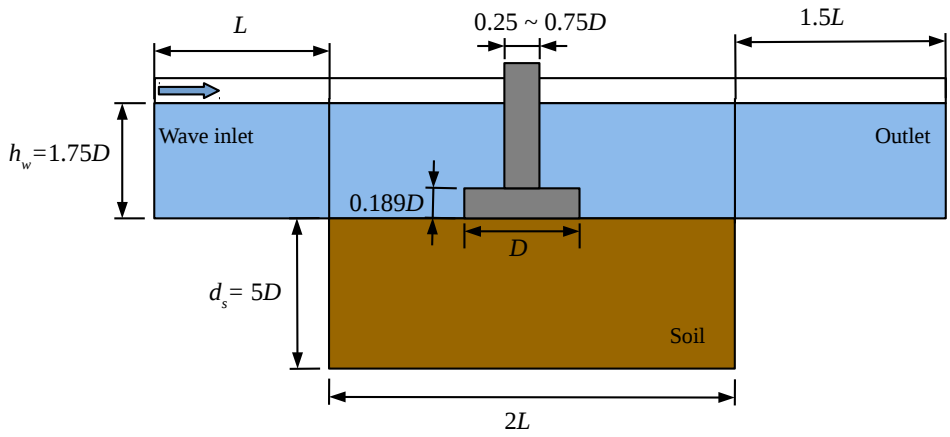

(a) Numerical layout of wave-structure-seabed interaction.

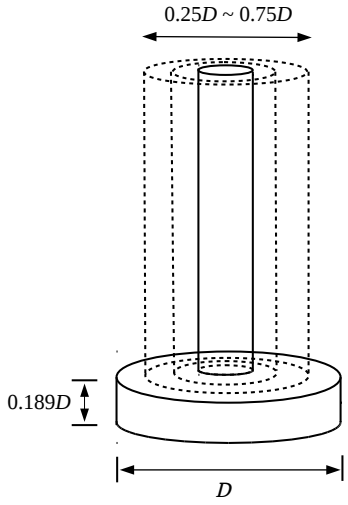

(b) Geometries of the structures.

Figure 4.14 Numerical models of the parametric study.

- **Consolidation:**

  When the structure is built on the seabed, the gravitational forces will induce a gradual dissipation of the excess pore pressure and a compression of the soil skeleton. The effective stress distribution in the surrounding soil will be significantly changed. According to the 1D Terzaghi's consolidation theory, the time for completing 90% consolidation can be expressed as (Wang, 2017):

$$t_{90} = T_v \frac{H_d^2}{c_v} \tag{4.33}$$

  where H_d is the drainage distance of the layer, $T_v = 0.848$ is the vertical consolidation time factor for 90% consolidation, c_v is the consolidation coefficient calculated by

$$c_v = \frac{2Gk_z(1-\nu)}{\gamma_w(1-2\nu)} \tag{4.34}$$

  where k_z is the vertical permeability and γ_w is the bulk specific weight of the pore water. In the present consolidation analysis, the gravitational force of the foundation reduced by the the buoyant force is applied on the interface between the structure bottom and the seabed. Figure 4.15 presents the distribution of the vertical effective stresses $\sigma_z^{'}$ and the vertical soil displacement U_z in the soil when the consolidation process is completed. A negative value of $\sigma_z^{'}$ indicates the compression of the soil skeleton. During the long-time consolidation, the gravity force from the foundation is gradually transferred to the supporting soil skeleton. It shows that below the foundation, the vertical effective stress and soil displacement are both amplified compared to those at the far field. Figure 4.16 shows the vertical effective stress and the vertical displacement on horizontal lines. The red curves are the $\sigma_{z0}^{'}$ and U_z at the seabed surface. It is seen that after the completion of the consolidation,

the vertical effective stress at the seabed surface beside the foundation becomes zero. Below the structure bottom, the vertical effective stress is a constant of $(W-B)/A$. In a deeper soil, the effective stress (shown as the blue dashed curve in Figure 4.16a) is higher than that at the seabed surface since the gravity force is transferring downward. On the other hand, the vertical soil displacement U_z is gradually decreasing in a deeper seabed and the maximum deformation is right beneath the center of the structure bottom.

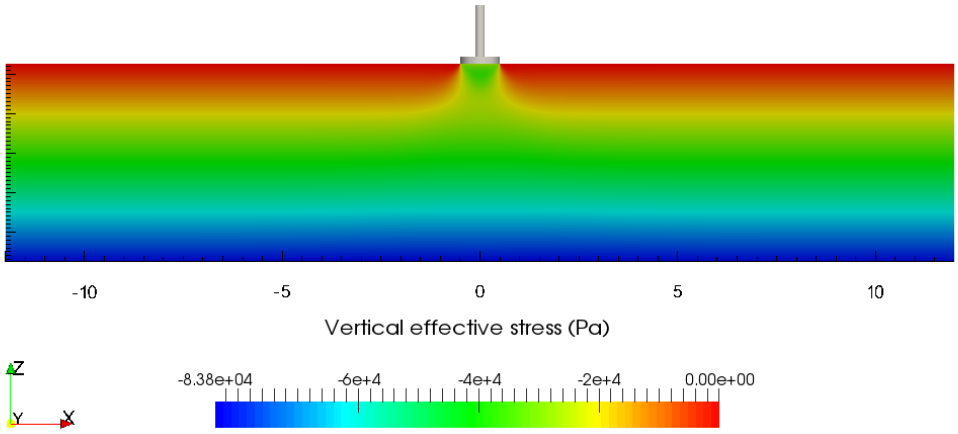

(a) Initial vertical soil effective stress σ'_{z0} (Pa) after the completion of the consolidation.

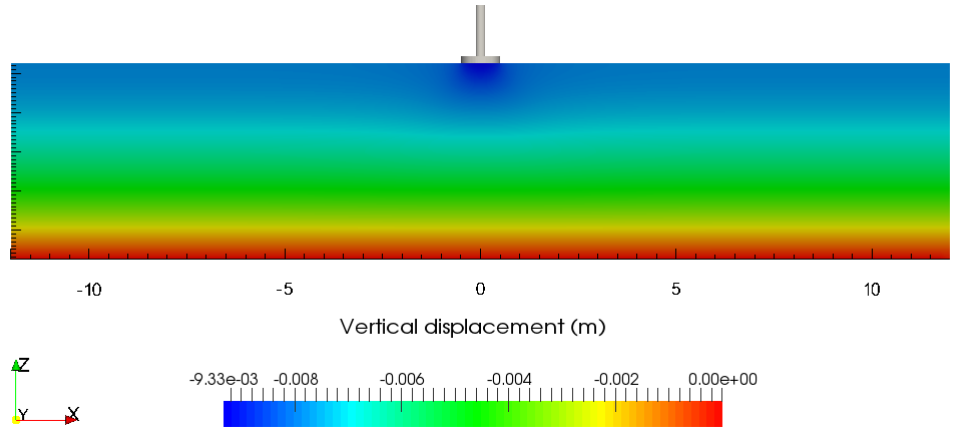

(b) Vertical soil displacement U_z (m) after the completion of the consolidation.

Figure 4.15 Soil condition after the completion of the consolidation.

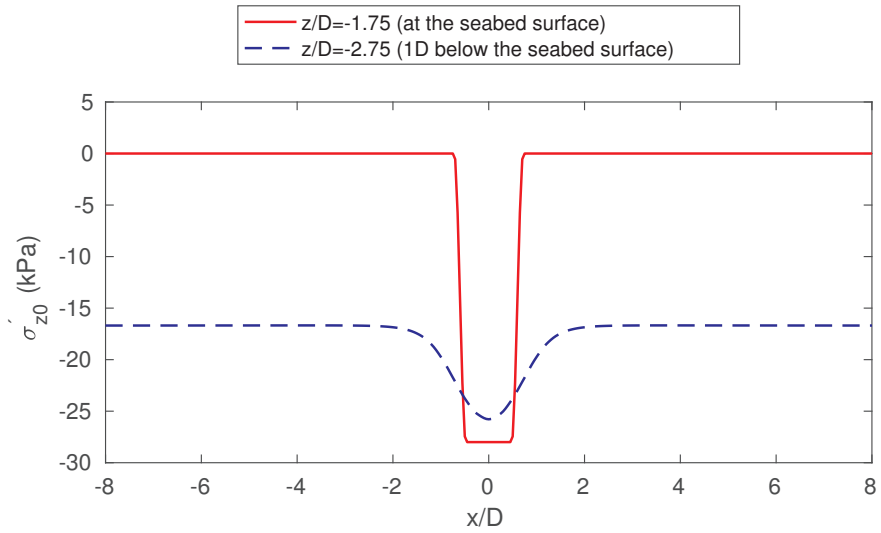

(a) Vertical soil effective stress σ'_{z0} (Pa) along horizontal lines in the seabed.

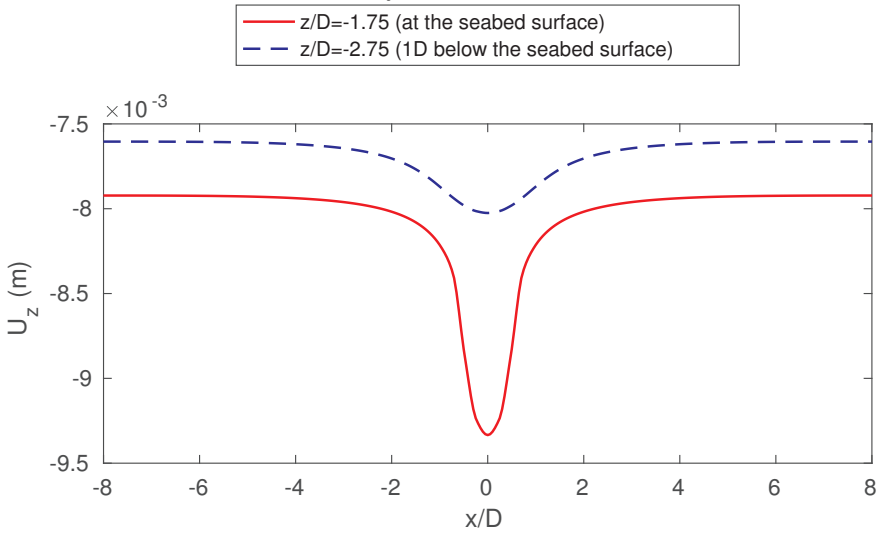

(b) Vertical soil displacement U_z (m) along horizontal lines in the seabed.

Figure 4.16 Soil condition after the completion of the consolidation along the horizontal lines: $y/D = 0, z/D = -1.75$ and $y/D = 0, z/D = -2.75$.

- **WSSI analysis:**

  After the consolidation analysis, the steep waves are simulated to propagate over the seabed. Figure 4.17 presents the wave elevation and the dynamic wave pressure on the seabed at locations upstream to the foundation with $5D$ and $1D$ distance to the foundation center (i.e., $x/D = -5$ and $x/D = -1$). It is shown that for the foundation with $D^{'}/D = 0.25$, the wave elevation at $x/D = -1$ is just slightly higher than that at $x/D = -5$, so does the dynamic wave pressure on the seabed. With $D^{'}/D = 0.5$, the difference is still not significant. When $D^{'}/D$ continuously increases to 0.75, both wave crest and wave trough become visibly steeper at $x/D = -1$ and the wave amplitude increases. Figure 4.17 also shows the wave elevation and seabed pressure with $D^{'}/D = 1$, where the wave crest becomes sharper and the pressure amplitude at $x/D = -1$ is apparently higher than that at $x/D = -5$. A larger $D^{'}/D$ will apparently increase the wave reflection in the near field of the foundation and also the wave pressure on the seabed near the foundation slab. When waves further approaches the structure, the wave elevation is even more increased. However, the initial vertical effective stress in the seabed close to the structure will also be very high because of the consolidation process, so that the momentary liquefaction may not happen. Thereby, the WSSI analysis and following liquefaction analysis focuses on the location with a $0.5D$ distance to the slab surface, e.g. $x/D = -1$ in Figure 4.17.

  In the present study, the structure is considered as a medium which transfers the wave effect to the seabed. Previous studies assumed a uniform structural force on the seabed or consider the structure and the seabed as the same type of porous media (Ulker et al., 2010; Ye, 2012b; Ye et al., 2013). However, in the present study, the structure and the seabed are treated as independent systems. Therefore, the effect of the structure as a medium which transfers the wave effect to the seabed can

be assessed. The wave-induced structural response is solved by a linear elastic structure solver to obtain the instantaneous structural stress at the structure-seabed interface. The structural shear stress tensor $\boldsymbol{\sigma}$ at the structure bottom is then imposed on the seabed as a time-varying boundary condition. Figure 4.18 shows the dynamic wave pressure in the wave domain and the vertical effective stress in the soil domain when wave crest is reaching the the foundations with $D^{'}/D = 0.5$ and 0.75. At this moment, a wave crest with high velocity is reaching the upstream side of the foundation, causing high pressure on the upstream side of the foundation and low pressure on the downstream side of the foundation. The foundation is experiencing a tilting force towards its downstream side at this instantaneous moment. To balance this tilting force, the foundation is compressing the soil at its downstream side and releasing the soil at its upstream side from the compression. In the soil, it is seen that the vertical effective stress under the structure bottom has opposite signs to its surrounding soil. On the contrary, when the wave trough approaches the foundation, it causes tension force in the seabed upstream to the foundation. A tension force can trigger momentary liquefaction in the soil. However, at the same time, the structure experiences a tilting force towards its upstream side so that it causes compression force in the upstream nearby soil. Therefore, the wave-induced structural stress can have a mitigating effect on the momentary liquefaction in the soil very close to the foundation bottom. Figure 4.18 also shows that with $D^{'}/D = 0.75$, the effect of the wave-induced structural stress on the underneath soil is stronger than that with $D^{'}/D = 0.5$.

Figure 4.19 shows the transient pore pressure and seepage flow in the seabed at the time instant of t/T=9.45. The arrows in the seabed denote the vector of the pore pressure gradient, illustrating the seepage flow in the physical behavior. It is seen that at this time instant, wave trough is

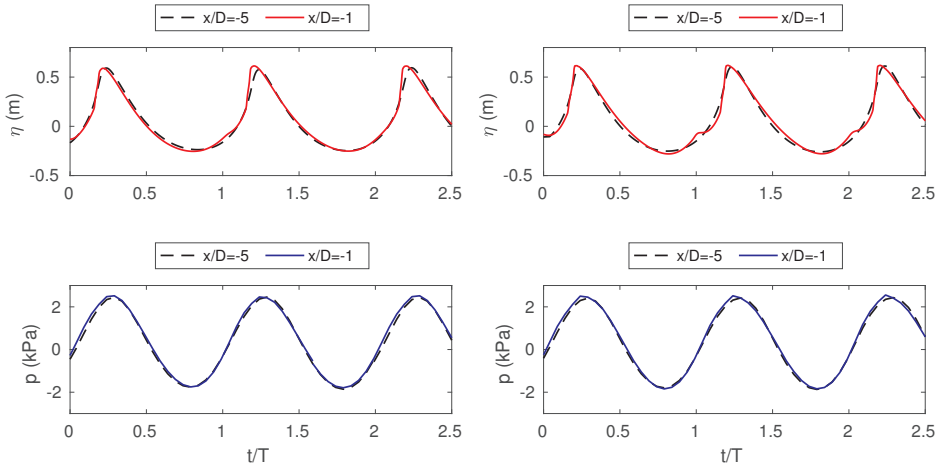

(a) $D^{'}/D = 0.25$. (b) $D^{'}/D = 0.5$.

(c) $D^{'}/D = 0.75$. (d) $D^{'}/D = 1$.

Figure 4.17 Surface elevation and wave pressure on the seabed at a far-field location and a near-field location to the structure.

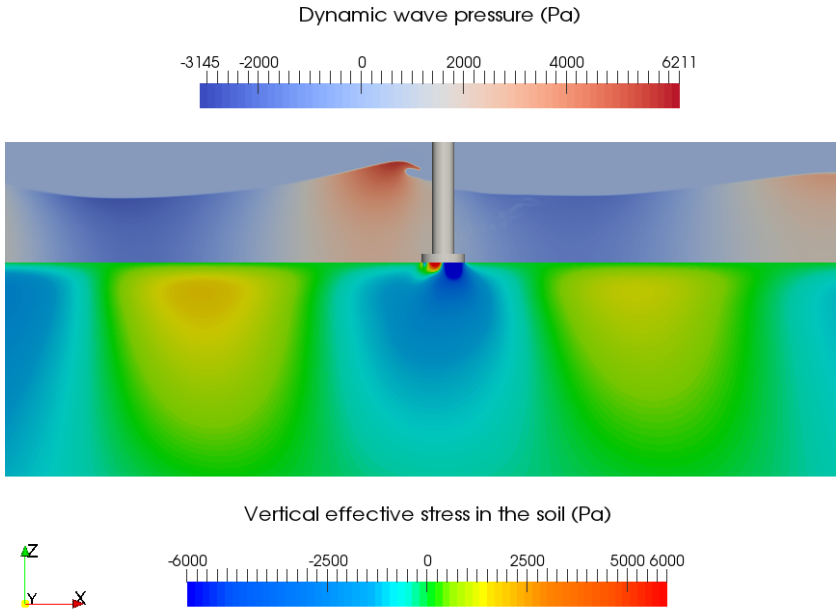

(a) Wave crest approaches the structure with $D^{'}/D = 0.5$.

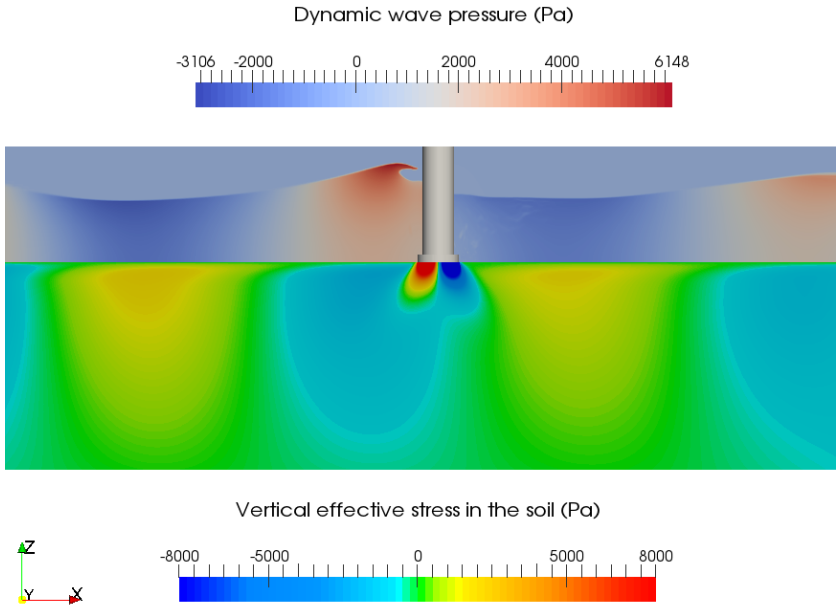

(b) Wave crest approaches the structure with $D^{'}/D = 0.75$.

Figure 4.18 Wave crest approaches the foundations and generate high opposite vertical stress beneath the structure bottom σ_z (Pa) compared to the nearby field.

passing the foundation. The pressure gradient triggers notable upward seepage flows in the vicinity of the foundation. Once the upward seepage forces exceed the initial vertical effective stress, the momentary liquefaction will occur and influence the safety of the foundation. It is also seen that the dynamic waves only affect a certain depth of the seabed. The excess pore pressure vanishes in a deeper soil skeleton.

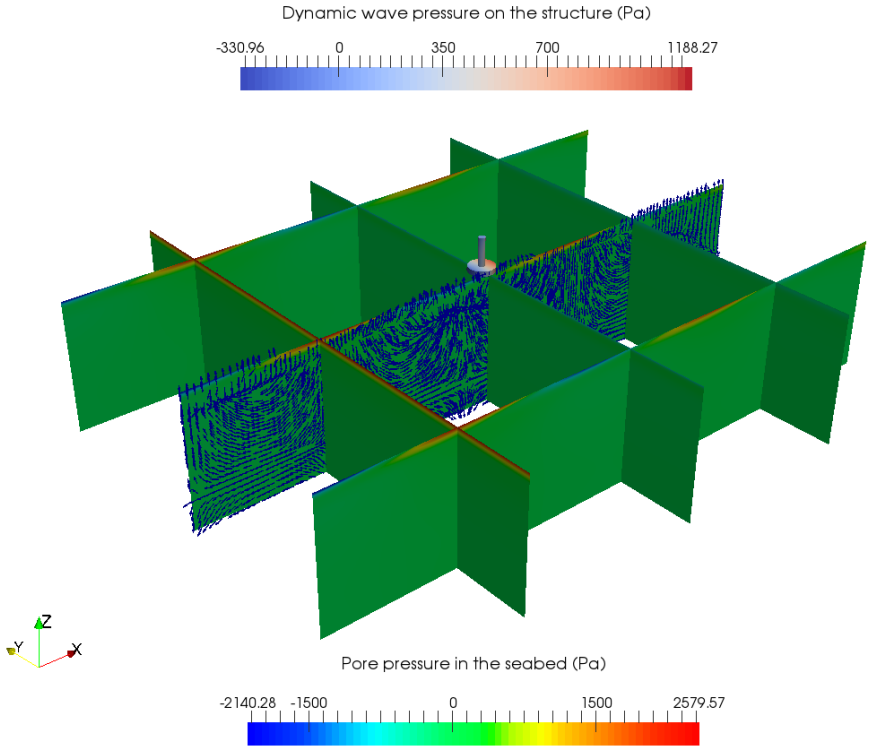

Figure 4.19 Transient pore pressure and seepage flow at the time of t/T=9.45.

- **Liquefaction:**

  For 1D quasi-static Biot's model, the criterion based on the excess pore pressure and that based on the vertical effective stress should lead to the same result (Sumer, 2014a), since the vertical effective stress $\sigma_z^{'}$ is theoretically the same as $p - p_b$ due to the force balance in the vertical direction. However, for the present 3D partial dynamic Biot's model with inertia force of the soil skeleton, the two criteria will lead to different assessment results. Figure 4.20 shows the maximum liquefaction depths d_L in a wave cycle along the x-axis evaluated by 3D liquefaction criteria modified from Okusa (1985) and Zen and Yamazaki (1990b) (criterion A and B), respectively. The maximum momentary liquefaction depths around foundations in different $D^{'}/D$ are compared. It is seen that as $D^{'}/D$ increases from 0.25 to 0.75, the liquefaction risk in terms of the maximum liquefaction depth and the liquefaction amplified distance near the foundation generally increases. The dashed line is the maximum liquefaction depth with $D^{'}/D = 1$, providing an upper limit reference for the present parametric study. In a dimensional case, for a gravity-based foundation with a slab diameter D of 19 meters and a shaft parameter $D^{'}$ of 9.5 meters as an example, the maximum momentary liquefaction depth at the given steep wave condition can reach 2.4 meters.

  For both criteria A and B, the highest momentary liquefaction risk happens at a location of $x/D = -1 \pm 0.25$ upstream to the foundation. It is because that the momentary liquefaction risk is determined by two factors, i.e., the wave effect and the initial vertical effective stress in the soil. As waves propagate to the foundation, the dynamic wave pressure is increasing due to the decreasing of the wave velocity when approaching to the foundation, according to the Bernoulli equation. The increase of the wave pressure and further the pore pressure gradient in the seabed will cause a higher momentary liquefaction risk in the seabed.

However, at the same time, the initial vertical effective stress in the seabed also increases when approaching to the foundation. The increase of the initial vertical effective stress will cause a lower momentary liquefaction risk in the seabed. Two factors have opposite effect on the momentary liquefaction risk as getting closer to the foundation. It is observed in Figure 4.20 that the wave effect is dominant at $x/D = -1.25$ to -0.75 and the initial vertical effective stress is dominant at $x/D = -0.75$ to -0.5. When it is very close to the foundation slab ($x/D = \pm 0.5$), the initial vertical effective stress due to the consolidation is very high so that the momentary liquefaction would not happen near the slab surface. At the downstream of the structure, the maximum liquefaction depths predicted by criterion A are the same for all $D^{'}/D$, while criterion B gives a higher prediction of maximum liquefaction depths with $D^{'}/D = 1$.

The maximum liquefaction depths d_L around the foundation from 0 to 360 degrees in a circle with $r/D = 1$ (i.e., $0.5D$ to the slab surface) is investigated, as shown in Figure 4.21. It appears that the upstream side has a higher liquefaction depth than the downstream side. It is general found that the upstream side of the offshore foundation is more vulnerable to the momentary liquefaction risk (also seen in the work of Lin et al. (2017) and Li et al. (2018)), therefore needs more protection. Chang and Jeng (2014) investigated the liquefaction protection methodology and they suggested to replace the existing layers of the surrounding soil with higher permeability materials to reduce the liquefaction risk. In the engineering practice, gravity-based structures are usually fitted with skirts to prevent the hydraulic process of scour channels penetrating underneath the structure, which can also be helpful to prevent the seepage flow penetration and further liquefaction risk around the foundations. Based on the parametric study, it is found that the design of a smaller $D^{'}/D$ is able to alleviate the

momentary liquefaction risk around the foundation in the steep coastal waves.

It appears that criterion A and B provide similar results of maximum liquefaction distribution. However, criterion B based on the excess pore pressure (modified from Zen and Yamazaki (1990b)) gives relatively higher momentary liquefaction risk prediction than criterion A based on the effective stress (modified from Okusa (1985)). Also, the length of the amplified liquefaction zone predicted by criterion B is larger than that predicted by criterion A. Criterion B can be a better choice for engineering design since it provides more conservative solution.

4.1.6 Conclusions

An open-source CFD toolbox for simulating the wave-induced seabed response and momentary liquefaction around the marine structures including the consolidation analysis, WSSI analysis, and liquefaction assessment has been presented in the present work. The whole model is implemented in the FVM-based OpenFOAM framework. The coupling between the multiphysics is achieved by the data interpolating and mapping via the common boundaries. The FV partial dynamic soil model is modified from Biot's consolidation theory accounting for the anisotropic seabed properties.

The present model has been verified and validated against the theoretical solution and experimental data. The consolidation solver is verified by the analytical solution for the one-dimensional Terzaghi's consolidation test (Terzaghi, 1944; Wang, 2017). The dynamic wave-induced seabed response solver is validated against the experimental data of standing wave-induced pore pressure under a vertical wall (Tsai and Lee, 1995). The integrated WSSI model is validated against the wave data and soil pore pressure data of a wave-pile-soil interaction experiment (Qi, 2018; Qi and Gao, 2014). Two case studies have been conducted in the present work in terms of the analysis of

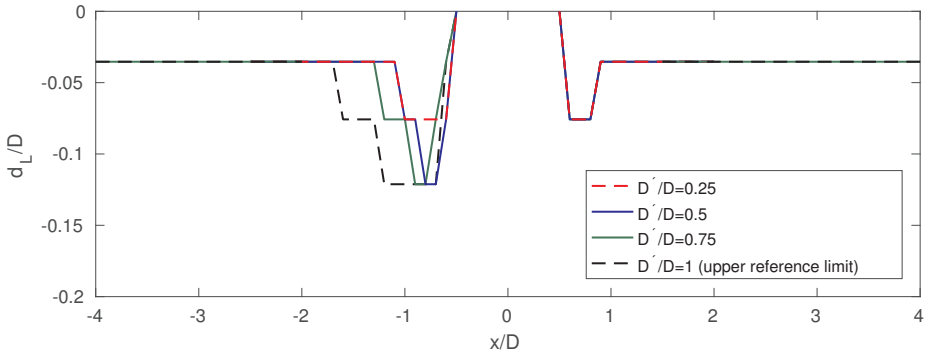

(a) Evaluated by liquefaction criterion A based on the effective stress.

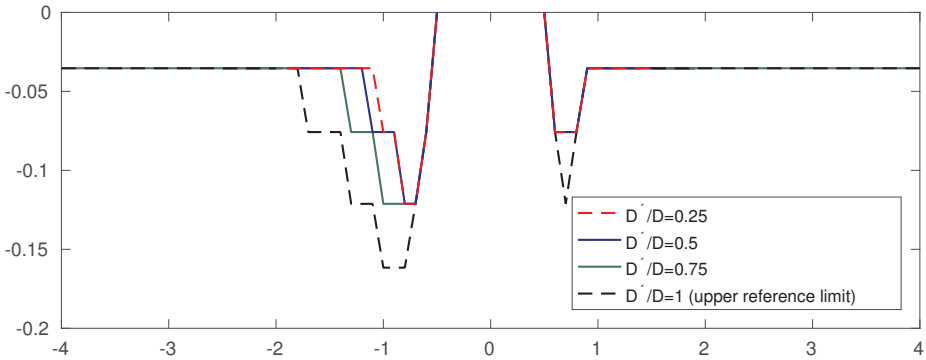

(b) Evaluated by liquefaction criterion B based on the excess pore pressure.

Figure 4.20 Maximum liquefaction depths in a wave cycle beside the foundation along x-axis. The curves are plotted with sampled points at every x/D=0.1.

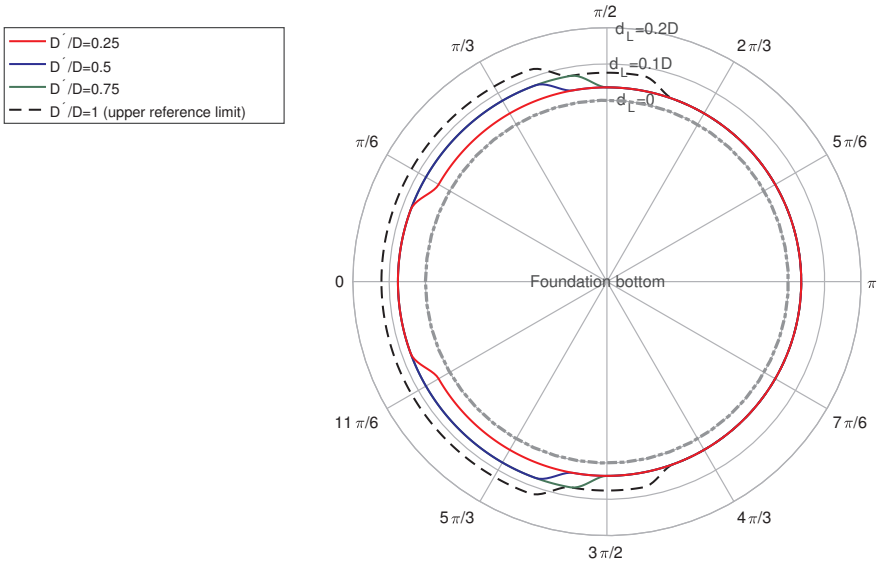

(a) Evaluated by liquefaction criterion A modified from Okusa (1985) based on the effective stress.

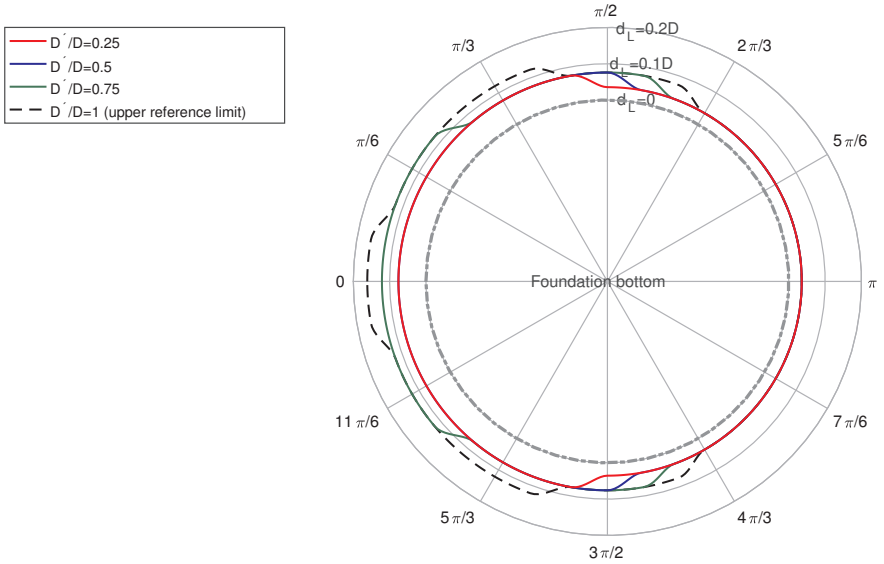

(b) Evaluated by liquefaction criterion B modified from Zen and Yamazaki (1990b) based on the excess pore pressure.

Figure 4.21 Maximum momentary liquefaction depth in a wave cycle around the foundation bottom with a distance of $0.5D$ to the slab surface.

2D nonlinear wave-soil interaction and the investigation of 3D wave-structure-seabed interaction around gravity-based foundations. For the latter case study, a systematic investigation process including consolidation analysis, wave-induced seabed response and momentary liquefaction assessment has been performed. Two liquefaction criteria based on the effective stress and based on the excess pore pressure have been applied and compared. It is recommended to use the criteria modified from Zen and Yamazaki (1990b) based on the excess pore pressure as it provides more conservative solution for evaluating the liquefaction risk around the offshore foundations.

The present model can be applied to the seabed response analysis around the marine structures and offshore foundations in various wave conditions, providing safety assessment based on the practical assumptions. The present toolbox in the FVM-based OpenFOAM framework allows structured and unstructured meshing for either simple or complex geometries. The segregated approach and parallelism provide a fast and memory-efficient solution to certain coastal and offshore engineering problems.

Acknowledgment

This study was supported in part with computational resources provided by the Norwegian Metacenter for Computational Science (NOTUR), under Project No: NN9372K. The authors acknowledge Dr. Wen-Gang Qi from Chinese Academy of Sciences for providing the experimental data.

Chapter 5

Scour prediction beneath submarine pipelines

This chapter presents a paper submitted to Coastal Engineering on scour beneath two tandem pipelines in wave-plus-current conditions. A fully-coupled hydrodynamic and morphologic model developed in the previous work is applied.

5.1 Paper V: Numerical investigation of wave-plus-current induced scour beneath two submarine pipelines in tandem

Yuzhu Li[a], Muk Chen Ong[a], David R. Fuhrman[b], Bjarke Eltard Larsen[b]
[a] Department of Mechanical and Structural Engineering and Materials Science, University of Stavanger, N-4036 Stavanger, Norway
[b] Section of Fluid Mechanics, Department of Mechanical Engineering, Technical University of Denmark, DK-2800 Kongens, Lyngby, Denmark

Abstract* Two-dimensional (2D) local scour beneath two submarine pipelines in tandem under wave-plus-current conditions is investigated numerically. A fully-coupled hydrodynamic and morphologic model based on unsteady Reynolds-averaged Navier-Stokes (URANS) equations with the $k-\omega$ turbulence closure is applied. The model is validated against existing experimental measurements involving live-bed scour beneath a single pipeline and beneath two pipelines in tandem, respectively. The model is then employed to simulate scour beneath two tandem pipelines under wave-plus-current conditions for a variety of Keulegan-Carpenter (KC) numbers and relative current strengths. Horizontal gap ratios (the horizontal gap distance between two pipelines divided by the pipeline diameter) ranging from 1 to 4 are modelled. It is found that for conditions involving waves plus a low-strength current, the scour pattern beneath two pipelines behaves like that in the pure-wave condition. Conversely, when the current has equal strength to the wave-induced flow, the scour pattern beneath two pipelines resembles that in the pure-current condition. It is also observed that in the pure-wave condition the equilibrium scour depth beneath each pipeline is affected by both KC and the horizontal gap ratio, except for $KC = 5.6$. For such a small KC, the horizontal gap ratio has insignificant influence on the equilibrium scour depth, since vortex shed-

*This is a journal paper submitted to Coastal Engineering.

ding does not occur. When the current strength relative to the waves is low, the scour development beneath the upstream and the downstream pipelines are similar. However, when the current has equal strength to the waves, the scour development beneath the downstream pipeline has a different pattern to that upstream. Namely, smaller horizontal gap ratios result in delayed scour beneath the downstream pipeline.

keywords: scour; pipelines in tandem; wave and current; turbulence modeling

5.1.1 Introduction

In the submarine environment hydrodynamic loads from waves and currents can act on submarine pipeline systems simultaneously. Once pipelines are installed on the seabed, the local flow patterns will be changed and the sediment transport capability can be increased. Significant local scour has been observed during surveys of submarine pipelines in service. The development of scour beneath such pipelines can cause free spanning of the pipeline, which can increase structural fatigue and damage. To predict the local scour under pipelines, research has been conducted mainly in three forms: (1) empirical models based on experimental data, e.g., Mao (1986), Sumer and Fredsøe (1990, 1996), (2) numerical models based on potential flow theory, e.g., Chao and Hennessy (1972), Chiew (1991), Li and Cheng (1999), and (3) numerical models capable of describing turbulent flows, e.g., Brørs (1999), Li and Cheng (2000), Liang et al. (2005), Fuhrman et al. (2014) and Larsen et al. (2016).

Mao (1986) performed a series of experiments involving scour beneath pipelines under a variety of flow conditions. It was found that the equilibrium scour depth divided by the pipeline diameter S_e/D is a weakly varying function of the Shields parameters θ for the live-bed conditions. An empirical formula for the equilibrium scour depth based on Mao (1986)'s experimental measurement was established by Sumer and Fredsøe (2002).

In the clear-water regime, the variation in scour depth with θ was large, and therefore no simple formula exists. In the live-bed regime, the empirical relation $S_e/D = 0.6 \pm \sigma$ was proposed, where $\sigma = 0.2$ is the standard deviation (Sumer and Fredsøe, 2002). For scour in waves, Sumer and Fredsøe (1990) investigated the variation of the scour depth with the Keulegan–Carpenter number (KC). Experimental results were fitted with the empirical equation $S_e/D = 0.1\sqrt{KC}$ in the live-bed regime. In the case of combined waves and currents, Sumer and Fredsøe (1996) conducted experiments covering a wide range of KC and the relative current strength m were considered (here m is taken as the current velocity magnitude at the pipeline center divided by the total combined velocity magnitude including the near-bed orbital velocity amplitude of the oscillating flow and the current velocity magnitude at the pipeline center). It was found that the scour depth may increase or decrease in wave-plus-current conditions relative to pure-wave conditions, depending on both KC and m. They also found that when $m > 0.7$ (i.e. strong currents), the equilibrium scour depth S_e/D is the same as in the current-alone case.

In addition to experimental studies, early attempts on numerically modelling the scour beneath pipelines were based on potential flow theory, according to Sumer (2007) and Sumer (2014b). The studies of Chao and Hennessy (1972), Chiew (1991) and Li and Cheng (1999) could predict the maximum scour depth and the upstream slope. However, the potential flow theory cannot capture the flow separation and formation of lee-wake vortices, which are responsible for a more gentle downstream slope (Sumer and Fredsøe, 2002)

More recent attempts at the numerical modelling of scour beneath submarine pipelines have been based on the complete Navier-Stokes equations, with turbulence modelling in the form of either Reynolds-averaged formulations or Large Eddy Simulations (LES). Li and Cheng (2000, 2001) have used LES to model the local scour beneath a pipeline. Their studies modeled the scour development using local amplification of the bed shear stress, but they did not model the sediment transport process. Brørs (1999) used a $k-\varepsilon$ turbulence

model to solve the Reynolds-averaged Navier-Stokes (RANS) equations and established a numerical model to describe the flow, sediment transport and morphology in steady currents. Liang et al. (2005) compared a $k-\varepsilon$ turbulence model and LES. They found that both turbulence models provided good results, while the $k-\varepsilon$ turbulence model performed better. However, as demonstrated in the work of Lee et al. (2016), the $k-\varepsilon$ turbulence model cannot reproduce the vortex shedding so that the lee-wake erosion stage cannot be properly modelled. Liang and Cheng (2005) carried out a numerical study of scour in waves and used a $k-\omega$ turbulence model for closure. The $k-\omega$ turbulence model is able to capture the vortex shedding. Fuhrman et al. (2014) likewise used a $k-\omega$ turbulence model (Wilcox, 2006, 2008) to solve the unsteady RANS equations and simulated both the scour development, as well as backfilling, that occurs for various KC. Larsen et al. (2016) simulated the scour around a pipeline in wave-plus-current conditions with the same model. In their work, similar trends as seen in Sumer and Fredsøe (1996) were obtained for the variation of the equilibrium scour depth with the relative current strength. Bayraktar et al. (2016) also utilized the model to simulate wave-induced backfilling from a current generated scour hole and achieved equilibrium depths and time scales in line with their experimental results.

Extensive studies have been performed to predict the scour around a single submarine pipeline, though pipelines may also be laid in tandem. In such tandem arrangements, in addition to the usual environmental loads, the spacing between multiple pipelines can also affect the resulting flow and scour patterns. Zhao et al. (2015) performed numerical studies involving the local scour around two pipelines in tandem in steady currents. In their work, the numerical model was validated against experiments. Specifically, horizontal gap ratios (defined as the horizontal gap distance separating the two pipelines G divided by their diameter D) ranging from 0.5 to 5 were investigated numerically for current-alone cases. It was found that the scour depth increases with horizontal gap ratios between 0.5 to 2.5, reaching a max-

imum at $G/D = 2.5$. Zhang et al. (2017) carried out a series of experiments involving scour beneath two tandem pipelines in steady currents with G/D ranging from 0 to 5.9. They found that for horizontal gap ratios between 0 and 3, the equilibrium scour depth beneath the downstream pipeline is slightly larger than that upstream. However, for larger gap ratios between 3 to 5.9, the equilibrium scour depth beneath the downstream pipeline is slightly smaller than that upstream. Their results also showed that the time scale of scour beneath the downstream pipeline is generally larger (by up to a factor 4) than that for the upstream pipeline.

The present work focuses on the numerical investigation of local scour beneath two tandem pipelines subject to wave-plus-current conditions, which has not been previously studied in a detailed manner. A fully-coupled hydrodynamic and morphologic model based on RANS equations coupled with the $k-\omega$ turbulence closure is applied. The same turbulence models have been successfully used in previous scour studies of Fuhrman et al. (2014), Baykal et al. (2015), Larsen et al. (2016), Bayraktar et al. (2016) and Larsen et al. (2017). The model will be validated against existing experimental measurements involving pure-current induced scour beneath a single pipeline in the live-bed regime (Mao, 1986) as well as against experimentals involving live-bed scour beneath two pipelines in tandem (Zhao et al., 2015). The present model will then be applied to simulate the local scour beneath two tandem pipelines in the wave-plus-current conditions for a variety of KC and relative current strengths m. Various horizontal gap ratios ranging from $G/D = 1$ to 4 will be considered.

5.1.2 Numerical Model Description

5.1.2.1 Hydrodynamic and turbulence models

The present numerical model solves the incompressible unsteady Reynolds-averaged Navier-Stokes (URANS) equations with the $k-\omega$ turbulence model

(Wilcox, 2006, 2008) as the closure. The equations governing the flow in the Cartesian coordinate system include a continuity equation and incompressible URANS equations:

$$\frac{\partial u_i}{\partial x_i} = 0 \tag{5.1}$$

$$\frac{\partial u_i}{\partial t} + u_j \frac{\partial u_i}{\partial x_j} = -\frac{1}{\rho}\frac{\partial p}{\partial x_i} + \frac{\partial}{\partial x_j}[2\nu S_{ij} + \frac{\tau_{ij}}{\rho}] + F_i \tag{5.2}$$

where u_i are the mean velocities, x_i are the Cartesian coordinates, $\rho = 1000$ kg/m^3 is the fluid density, p is the pressure, $\nu = 10^{-6}$ m^2/s is the fluid kinematic viscosity, F_i is the external body force used to drive the flow, S_{ij} is the mean-strain-rate tensor defined as

$$S_{ij} = \frac{1}{2}(\frac{\partial u_i}{\partial x_j} + \frac{\partial u_j}{\partial x_i}) \tag{5.3}$$

τ_{ij} is the Reynolds stress tensor that defined according to the constitutive relation given by

$$\frac{\tau_{ij}}{\rho} = -\overline{u_i' u_j'} = 2\nu_T S_{ij} - \frac{2}{3}k\delta_{ij} \tag{5.4}$$

where δ_{ij} is the Kronecker delta, k is the turbulent kinetic energy density expressed as

$$k = \frac{1}{2}\overline{u_i' u_i'} \tag{5.5}$$

and ν_T is the eddy viscosity. In the present work this is defined by

$$\nu_T = \frac{k}{\tilde{\omega}} \tag{5.6}$$

where the $\tilde{\omega}$ is defined by

$$\tilde{\omega} = \max\{\omega, C_{\text{lim}}\sqrt{\frac{2S_{ij}S_{ij}}{\beta^*}}\}, \qquad C_{\text{lim}} = \frac{7}{8} \tag{5.7}$$

The two-equation $k-\omega$ turbulence model is used in the present study as a closure for the URANS equations. The model includes the transport equation of the turbulent kinetic energy k and the specific dissipation rate ω (Wilcox, 2006):

$$\frac{\partial k}{\partial t}+u_j\frac{\partial k}{\partial x_j}=\frac{\tau_{ij}}{\rho}\frac{\partial u_i}{\partial x_j}-\beta^* k\omega+\frac{\partial}{\partial x_j}[(\nu+\sigma^*\frac{k}{\omega})\frac{\partial k}{\partial x_j}] \tag{5.8}$$

$$\frac{\partial \omega}{\partial t}+u_j\frac{\partial \omega}{\partial x_j}=\alpha\frac{\omega}{k}\frac{\tau_{ij}}{\rho}\frac{\partial u_i}{\partial x_j}-\beta\omega^2+\frac{\sigma_d}{\omega}\frac{\partial k}{\partial x_j}\frac{\partial \omega}{\partial x_j}+\frac{\partial}{\partial x_j}[(\nu+\sigma\frac{k}{\omega})\frac{\partial \omega}{\partial x_j}] \tag{5.9}$$

where

$$\sigma_d=H\{\frac{\partial k}{\partial x_j}\cdot\frac{\partial \omega}{\partial x_j}\}\sigma_{d0} \tag{5.10}$$

where $H\{\cdot\}$ denotes the Heaveside step function, which takes value 1 if the argument is positive and takes 0 otherwise. The standard closure coefficients are: $\alpha=0.52$, $\beta=0.0708$ (constant for two-dimensional problems), $\beta^*=0.09$, $\sigma=0.5$, $\sigma^*=0.6$, $\sigma_{d0}=0.125$. In Eqn. 5.2, the body force F_i is implemented to drive the flow. In the present work, preliminary one-dimensional vertical (1DV) pure flow simulations driven by the body force without morphology are carried out, in order to achieve a fully developed wave-plus-current boundary inlet. The one-dimensional body force of combined waves and current is given by (Larsen et al., 2016):

$$F_1=U_m\frac{2\pi}{T_w}\cos\left(\frac{2\pi}{T_w}t\right)+\frac{U_{fc}^2}{h} \tag{5.11}$$

where U_m is the near-bed orbital velocity amplitude of the oscillating flow, T_w is the wave period, U_{fc} is the desired friction velocity of the pure-current, and h is the domain height. After the 1DV flow simulation reaches the equilibrium state, the velocity field, k and ω at the inlet boundary are applied as the boundary inlet for the scour simulations. The body force is then set to zero in

the scour simulations as the flow will be driven by the Dirichlet condition at the inlet.

5.1.2.2 Sediment transport and morphological models

Bed load transport: The present sediment transport model consists of a bed load transport model and a suspended load transport model. A full description and numerical implementation of the model can be found in Jacobsen (2011) and Jacobsen and Fredsoe (2014). The bed load transport model is based on the work of Roulund et al. (2005) which is a generalized three-dimensional extension of the transport formulation by Engelund and Fredsøe (1976). The bed load sediment transport rate q_B can be written as (Fredsøe and Deigaard, 1992)

$$q_B = \frac{\pi}{6} d^3 \frac{p_{EF}}{d^2} U_B \tag{5.12}$$

where d is the median grain diameter, U_B is the bed load particle moving velocity, for which the detailed derivation can be found in Fredsøe and Deigaard (1992) and Roulund et al. (2005). In the present two-dimensional context, the expression for U_B is given by

$$U_B = aU_f \left(1 - 0.7\sqrt{\frac{\theta_{c0}}{\theta}(cos(\gamma) - \frac{1}{\mu_d} sin(\gamma))}\right) \tag{5.13}$$

where $a \approx 10$ is a non-dimensional coefficient and U_f is the friction velocity, such that αU_f denotes the flow velocity at a distance of the order of magnitude d from the bottom (Fredsøe and Deigaard, 1992). γ is the slope angle; p_{EF} is the percentage of particles in motion in the surface layer of the bed, expressed by Engelund and Fredsøe (1976)

$$p_{EF} = \left[1 + \left(\frac{\frac{1}{6}\pi\mu_d}{\theta - \theta_c}\right)^4\right]^{-1/4} \tag{5.14}$$

where μ_d is the dynamic friction coefficient. In the present work, the value of μ_d is specified as 0.7, following Fuhrman et al. (2014) and Larsen et al. (2016). The Shields parameter θ is defined by

$$\theta = \frac{U_f^2}{(s-1)gd} \tag{5.15}$$

where $s = \rho_s/\rho$ is the specific gravity of the sediment grains, with ρ_s being the density of the sediment grains. The critical Shields parameter θ_c for the incipient motion of the particles is taken as (appropriate for two-dimensional problems):

$$\theta_c = \theta_{c0}\left(\cos(\gamma) - \frac{1}{\mu_s}\sin(\gamma)\right) \tag{5.16}$$

where θ_{c0} is the critical Shields parameter for a horizontal bed and μ_s is the static friction coefficient. In the present study, $\theta_{c0} = 0.045$ and $\mu_s = 0.65$ are utilized, as in Larsen et al. (2016).

Suspended load transport: The suspended load is computed by solving a turbulent-diffusion equation based on the continuity of the concentration (Fredsøe and Deigaard, 1992; Jacobsen, 2011).

$$\frac{\partial c}{\partial t} + (u_j - w_s\delta_{j3})\frac{\partial c}{\partial x_j} = \frac{\partial}{\partial x_j}\left[(\nu + \beta_s\frac{k}{\omega})\frac{\partial c}{\partial x_j}\right] \tag{5.17}$$

where c is the suspended sediment concentration, w_s is the settling velocity, β_s is the factor that is dependent on the grain size and level of turbulence which describes the ratio between sediment particle diffusivity and the eddy viscosity (Rijn, 1984). $\beta_s = 1$ is used in the present study, the same as that in Fuhrman et al. (2014). A reference concentration c_b is used at the reference level b. In the present work, $b = 3.5d$ is utilized following Fuhrman et al. (2014). For c_b, the formulation proposed by Engelund and Fredsøe (1976) is

utilized:

$$c_b = \frac{c_0}{(1+\frac{1}{\lambda_b})^3} \tag{5.18}$$

where $c_0 = 0.65$ is the maximum value for volumetric concentration, and λ_b is the linear concentration expressed by

$$\lambda_b^2 = \frac{\kappa^2 \alpha_1^2}{0.013 s\theta}(\theta - \theta_c - \frac{\pi}{6}\mu_d p_{EF}) \tag{5.19}$$

The settling velocity w_s is calculated according to Fredsøe and Deigaard (1992):

$$w_s = \sqrt{\frac{4(s-1)gd}{3c_D}} \tag{5.20}$$

where the drag coefficient is $c_D = 1.4 + 36/R$, and the settling Reynolds number is defined by $R = \frac{w_s d}{\nu}$.

Morphology: The morphological model is based on the sediment continuity (Exner) equation:

$$\frac{\partial h_b}{\partial t} = \frac{1}{1-n}\left[-\frac{\partial q_{Bi}}{\partial x_i} + D + E\right], i = 1,2 \tag{5.21}$$

where h_b is the bed height, n is the porosity which take 0.4 in the present study, D is the deposition and E is the erosion:

$$D = (w_s - v)c_b \tag{5.22}$$

$$E = (\nu + \beta_s \frac{k}{\omega})\frac{\partial c}{\partial x_3}|_{x_3=b} \tag{5.23}$$

In the present simulations, the morphological time step is the same as the hydrodynamic time step i.e. no morphological acceleration of any kind is utilized. To prevent the excess steepness of the bed, the sand slide model of Niemann et al. (2010) in two-dimensional is incorporated in the present study

with the angle of repose of 32°. The sand slide model uses a geometrical approach (Marieu et al., 2008; Niemann et al., 2010) to prevent the un-physical steepening of the scour shape. The implementation of the sand slide model is described in Jacobsen (2011).

5.1.2.3 Boundary conditions

The hydrodynamic boundary conditions are specified as follows.

- At the seabed and pipeline surfaces, no-slip boundary conditions are used, i.e., the velocities at the walls are zero. The seabed is modelled as a hydraulically rough wall where the friction velocity U_f is determined by the tangential velocity at the nearest cell center based on an assumed logarithmic velocity distribution, as described in Fuhrman et al. (2014). The pipeline surface is modelled as a hydraulically smooth wall where the friction velocity U_f is determined based on the profile proposed by Cebeci and Chang (1978). The generalized wall functions for k and ω are presented in Fuhrman et al. (2014).

- At the top boundary, a frictionless lid is modelled at which the vertical velocity is zero and the horizontal velocities and other hydrodynamic quantities have zero normal gradients.

- At the inlet boundary, a Dirichlet boundary is specified with time-varying u, k and ω, taken from the preliminary 1DV simulations. The outlet boundary is specified by a Neumann condition with zero normal velocity gradient and zero pressure.

For the sediment transport model, the boundary conditions for the suspended sediment concentration c is specified as follows.

- At the top and pipeline boundaries, a zero-flux condition for c is specified.

- At the bottom seabed boundary, a reference concentration is specified, as presented in Eqn. 5.18. The reference concentration is not imposed at the bottom wall but is at a reference distance of $3.5d$ from the seabed.
- At the inlet and outlet boundaries, c is specified with a zero normal gradient.

5.1.3 Model Validation

The present numerical model has been validated in Fuhrman et al. (2014) and Larsen et al. (2016). Fuhrman et al. (2014) validated the present model for scour around a pipeline in waves against the measurement of Sumer and Fredsøe (1990). Larsen et al. (2016) validated the present model for scour around a pipeline in the current against Mao (1986) and in the wave-plus-current condition against the experimental findings of Sumer and Fredsøe (1996). The present work uses the same model but with new mesh for the single pipeline case. Therefore, additional validations are conducted in the present study.

The computational meshes in the present study for a single pipeline and two pipelines in tandem are shown in Figure 5.1 (sub-plots (a) and (b), respectively). A small initial scour hole $S_0/D = 0.15$ is needed to ensure that there are cells beneath the pipeline. First, the computational mesh setup for a single pipeline will be validated by reproducing the live-bed scour experiment of Mao (1986). The time series of the non-dimensional scour depth S/D development and the scour profiles at two time instants will be compared to the experimental data in section 5.1.3.1. Then, the computational mesh for a single pipeline is extended for two pipelines in tandem, as shown in Figure 5.1a. For this purpose, the present model will be validated against the experiments of Zhao et al. (2015), involving live-bed scour around two tandem pipelines in a current. The bed profiles at the corresponding time instants will be compared in section 5.1.3.2. In all the cases, the smallest

cells near the pipeline have a height of $0.003D$ and the smallest cells near the seabed have a height of $0.5d$.

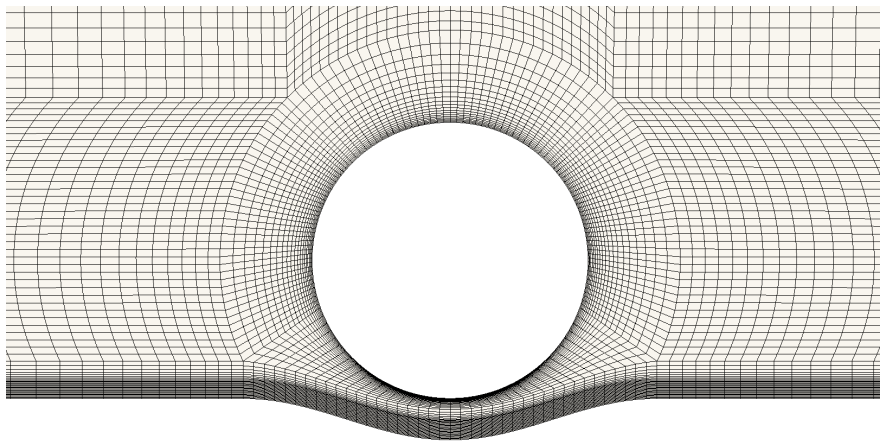

(a) Mesh around a single pipeline.

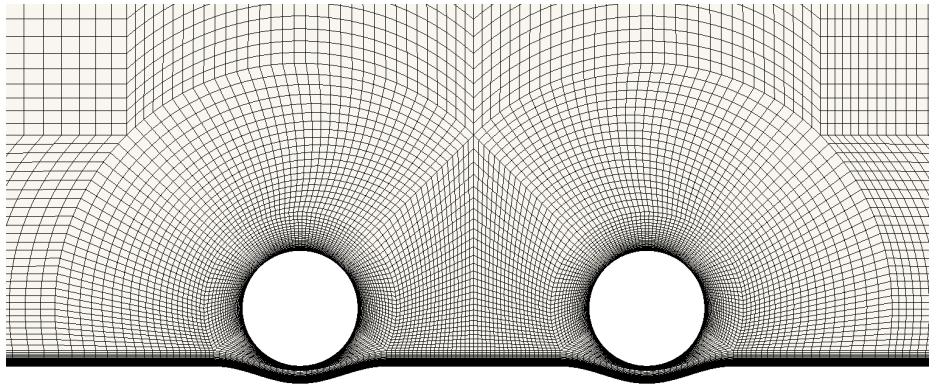

(b) Mesh for two pipelines in tandem.

Figure 5.1 Mesh setup

5.1.3.1 Validation against the experiment of scour beneath a single pipeline

In this section the live-bed scour experiment in Mao (1986) is reproduced using the present model and mesh. The Shields parameter θ is 0.098 for both the experiment and the present simulation. The pipeline diameter and

the grain size in Mao (1986) is $D = 0.1$ m and $d = 0.36$ mm. In the present simulation, $D = 0.03$ m and $d = 0.19$ mm. Following the arguments of Larsen et al. (2016), this is justifiable as non-dimensional comparison between the present numerical simulation and the experiment of Mao (1986) are performed in terms of S/D over the non-dimensional time t^* which is expressed as

$$t^* = \frac{\sqrt{g(s-1)d^3}}{D^2}t \tag{5.24}$$

where t is the physical time. It is ensured that the non-dimensional scour developments are comparable between two different scales once the Shields parameter is kept the same. The friction velocity U_f is calculated using Eqn. 5.15 and is equal to 0.017 m/s in the present simulation. The specific gravity of the sediment grains is $s = 2.65$ for both the experiment (Mao, 1986) and the present simulation. An initial hole of $S_0/D = 0.15$ is specified in the numerical simulation. Therefore, an approximation time that is used to develop the initial hole is added to compare the numerical time series to the corresponding experimental results of Mao (1986). The approximation time for the initial hole development is estimated by computing the initial scour rate dS/dt. The shift time is then calculated by $t_0 = \frac{S_0/D}{dS/dt}$.

The non-dimensional scour depths S/D over the non-dimensional time t^* from the present numerical simulation and the experiment of Mao (1986) are compared in Figure 5.2a. It is shown in Figure 5.2a that the present numerical results are in good agreement with the experimental measurement by Mao (1986). The final equilibrium scour depth reaches around $0.7D$ for both the numerical simulation and the experiment. As mentioned before, the expected equilibrium scour depth should be approximately constant (Sumer and Fredsøe, 1990) as $\frac{S_e}{D} = 0.6 \pm 0.2$. Figure 5.2a compares the profiles between the numerical prediction and the experimental measurement. It shows that the predicted downstream shoulder is slightly smaller than the experiment at the first time instant ($t^* = 0.24$) and slightly larger than the

experiment at the second time instant ($t^* = 4.86$). The predicted profiles are generally consistent with the experimental measurement and the scour depths beneath the pipeline are highly matched.

5.1.3.2 Validation against the experiment of scour beneath two pipeline in tandem

To further validate the present model, the experiments conducted by Zhao et al. (2015) will be considered, involving scour around two pipelines in a steady current. In Zhao et al. (2015), two laboratory tests were conducted with two identical pipelines having $D = 0.15$ m, having two different horizontal gap ratios $G/D = 0.5$ and 3. The sediment that was used in the model test has a median diameter d of 0.24 mm and a specific gravity of $s = 2.65$. The incoming steady flow velocity is 0.65 m/s at a height of 0.15 m above the sand bed surface, which corresponds to $U_f = 0.029$ m/s and $\theta = 0.218$.

The present study first conducted the 1DV simulation to ensure that the incoming flow at the inlet reaches its equilibrium state. Then the scour simulations are conducted for both the $G/D = 0.5$ and $G/D = 3$ cases. The bed profiles computed from the numerical simulations at different time instants are compared with the experimental data reported by Zhao et al. (2015) in Figure 5.3. It shows that the bed profiles solved by the present numerical model are in a reasonable agreement with Zhao et al. (2015)'s experimental measurements. For the $G/D = 0.5$ case, the maximum scour depth is located in between the two pipelines. No ripples are observed between two pipelines after the test time of 5 min. For the $G/D = 3$ case, the numerical result of scour depth beneath the downstream pipeline is slightly smaller than the experimental data by Zhao et al. (2015) at $t = 6.4$ min. At $t = 96.3$ min, the berm in between the two pipelines from the numerical simulation is more obvious than that from the experiment. However, the final scour depths below the centers of two pipelines are generally in good agreement with the experimental data.

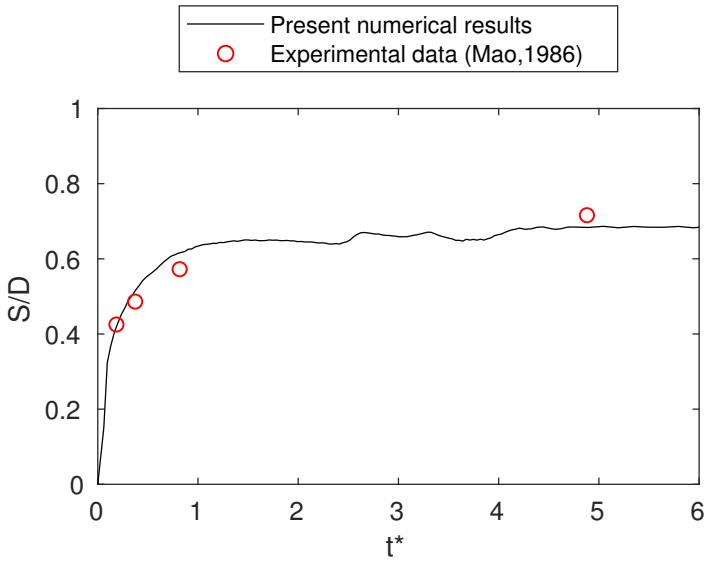

(a) Time series.

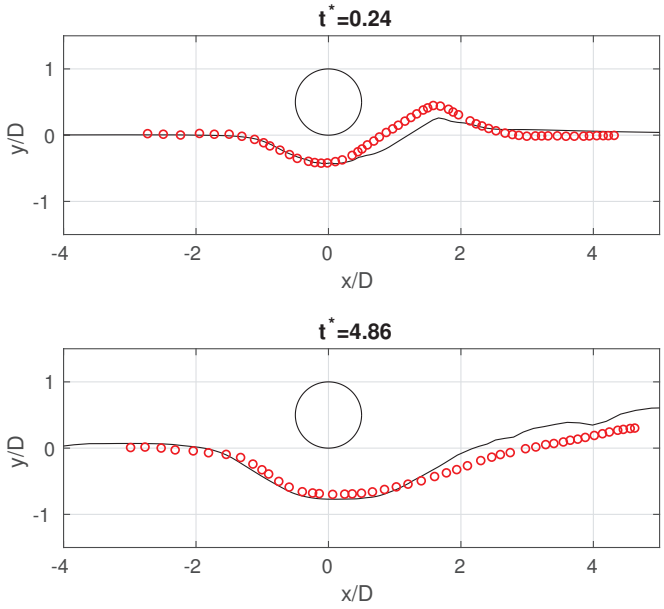

(b) Scour profiles.

Figure 5.2 Comparison of the present numerical results of scour depth development to the experimental data of Mao (1986), with $\theta = 0.098$ for both the experiment and the present simulation.

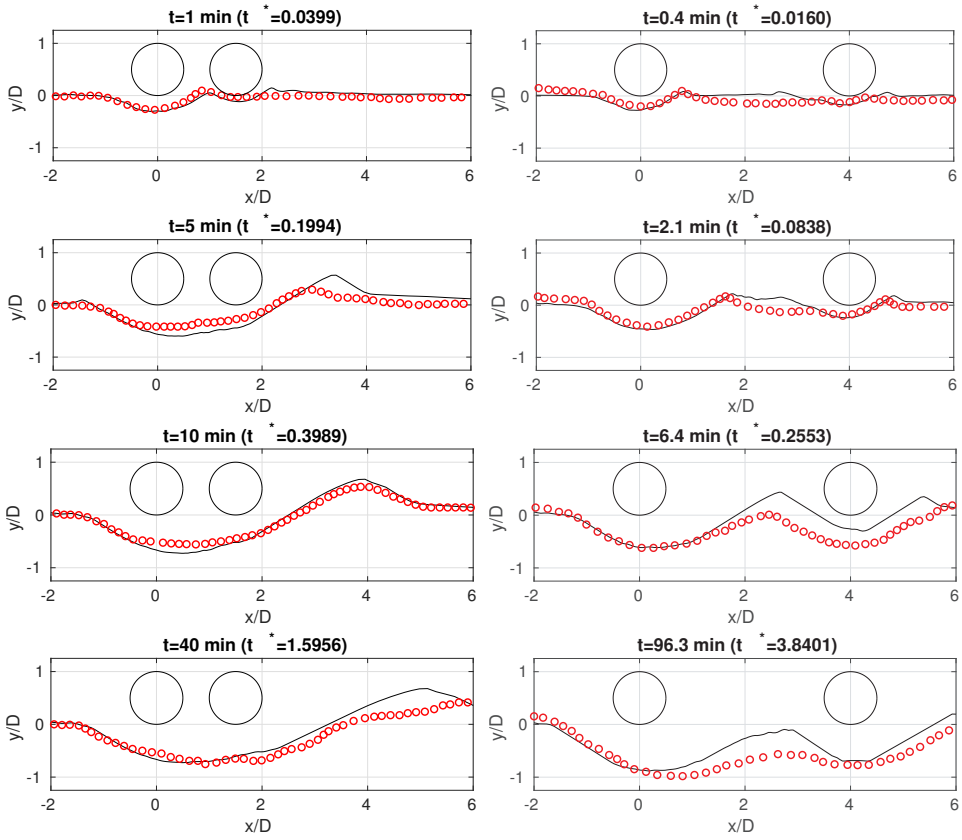

(a) Horizontal gap ratio $G/D = 0.5$. (b) Horizontal gap ratio $G/D = 3$.

Figure 5.3 Comparison of the bed profiles between the present numerical simulations and the experimental measurement of Zhao et al. (2015). Left column: $G/D = 0.5$; Right column: $G/D = 3$.

5.1.4 Model Application

A sketch of the present numerical model of scour beneath two pipelines in tandem is shown in Figure 5.4. The pipelines are placed on the seabed with the upstream pipeline's bottom at the origin (x, y) = (0, 0). The horizontal gap ratio, i.e., the horizontal gap distance between the two pipelines over the pipeline diameter G/D takes the values of 1, 2, 3 and 4 in the present study. An initial hole with a depth of $S_0/D = 0.15$ is set for both pipelines. In the present simulations, the pipeline diameter is $D = 0.03$ m and the grain size is $d = 0.19$ mm. The specific gravity of the sediment grains is $s = 2.65$.

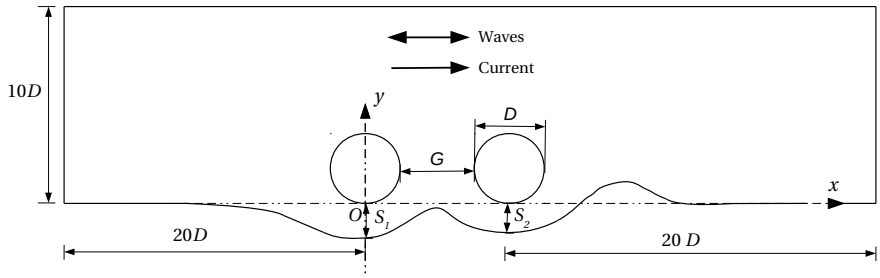

Figure 5.4 A sketch of the numerical layout for scour beneath two pipelines in tandem.

The wave-plus-current conditions simulated in the present work are given in Table 5.1, with six different KC ranging from 5.6 to 30, combined with three different current strengths for each KC. In Table 5.1, U_c is calculated while the relative current strength m is 0, 0.25 and 0.5, with m defined by

$$m = \frac{U_c}{U_c + U_m} \tag{5.25}$$

where U_m is the near-bed orbital velocity amplitude of the oscillating flow and U_c is the current velocity at the center of the pipeline. With this definition

Table 5.1 Wave-plus-current conditions in the present study. Each KC and its corresponding T_w and U_m are taken from the references. KC =5.6, 19.6 and 25.3 are referred to Fredsøe et al. (1991); KC =11 and 15 are referred to Sumer and Fredsøe (1990); KC =30 is referred to Fuhrman et al. (2014). The present study simulates wave-plus-current conditions by adding different levels of U_c to the pure-wave conditions. U_c is calculated while the relative current strength m is 0, 0.25 and 0.5.

KC	T_w (s)	U_m (m/s)	U_c (m/s)			θ_{cw}		
			m=0	m=0.25	m=0.5	m=0	m=0.25	m=0.5
5.6	1.1	0.153	0	0.051	0.153	0.119	0.125	0.161
11	1.22	0.24	0	0.080	0.240	0.177	0.191	0.269
15	2.5	0.177	0	0.059	0.177	0.091	0.099	0.141
19.6	3	0.196	0	0.065	0.196	0.092	0.102	0.150
25.3	3.51	0.216	0	0.072	0.216	0.094	0.105	0.161
30	3.5	0.257	0	0.086	0.257	0.120	0.136	0.212

$m = 0$ corresponds to a pure-wave condition and $m = 1$ corresponds to a pure-current condition.

According to Sumer and Fredsøe (1996), when $m > 0.7$, (and similarly according to Larsen et al. (2016), when $m \geq 0.5$), the current effect is dominant, and the scour depths are very similar to those in the pure-current conditions. The pure-current ($m = 1$) induced scour beneath two tandem pipelines has been numerically simulated by Zhao et al. (2015) and experimentally investigated by Zhang et al. (2017). Therefore, the present work focuses on the range of $m = 0$ to 0.5, i.e., from pure-wave conditions ($m = 0$) to an essentially equal strength of the wave and current (corresponding to $m = 0.5$). Figure 5.5 shows the time series of free stream velocity at the pipeline center with $m = 0$, 0.25 and 0.5, for cases having $KC = 19.6$, as an example.

The far-field Shields parameter θ_{cw} for the wave-plus-current flow is calculated as follows (Fuhrman et al., 2013; Larsen et al., 2016; Soulsby, 1995).

$$\theta_{cw} = \theta_w + \theta_m \tag{5.26}$$

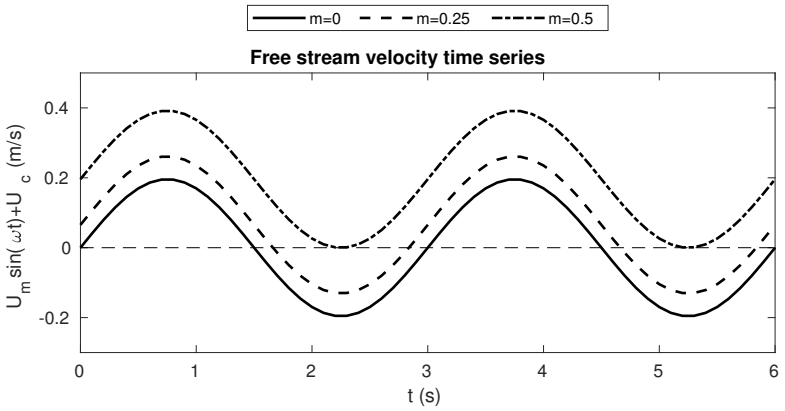

Figure 5.5 Free stream velocity of wave-plus-current in a time series.

where θ_w is the is the maximum Shields parameter of the oscillating flow. The maximum near-bed friction velocity induced by the oscillating flow is calculated by

$$U_{fw} = \sqrt{0.5 f_w} U_m \tag{5.27}$$

Here, following e.g. Larsen et al. (2016), f_w is calculated by taking the maximum among the laminar, smooth-turbulent, and rough-turbulent wave friction factors: f_w^{lam},f_w^{smooth},f_w^{rough}.

$$\begin{cases} f_w^{lam} = \frac{2}{\sqrt{Re}} \\ f_w^{smooth} = 0.035 Re^{-0.16} \\ f_w^{rough} = \exp(5.5(\frac{a}{k_s})^{-0.16} - 6.7) \end{cases} \tag{5.28}$$

where $Re = U_m \lambda / \nu$ is the Reynolds number, $\lambda = U_m T_w/(2\pi)$ is the characteristic amplitude of free stream orbital motion, the f_w^{smooth} expression is from Fredsøe and Deigaard (1992), and the f_w^{rough} expression is from Fuhrman et al. (2013). The mean Shields parameter θ_m is calculated by

$$\theta_m = \theta_{cur} \left(1 + 1.2 \left(\frac{\theta_w}{\theta_{cur} + \theta_w} \right)^{3.2} \right) \tag{5.29}$$

where θ_{cur} is the Shields parameter calculated from the pure current friction velocity U_{fc}. For all the simulated cases, a warm-up period (with morphology turned off) of $t = 10T_w$ is applied.

5.1.5 Results and Discussion

The discussion of the results will start from presenting the scour profile evolution and time series of scour depth development for representative cases with $m = 0$, $m = 0.25$ and $m = 0.5$, respectively. Then the equilibrium depths of all the cases will be summarized and discussed.

5.1.5.1 Profile evolution and time series

- **Pure-wave conditions $m = 0$:**

  When $m = 0$, i.e. pure-wave conditions, the scour profile in the vicinity of the upstream and the downstream pipelines is generally symmetric. Figure 5.6 shows the scour profiles in a pure-wave condition with $KC = 30$. It is seen that a small berm emerges between two pipelines at the initial time. For each G/D, the berm in between two pipelines is gradually eroded over time and becomes less visible than that at the beginning. When the horizontal gap ratio is larger, the berm is more visible during the equilibrium stage. It is also noted that the maximum scour depths of the final scour profile are not located right below the center of the pipelines. The maximum scour depths gradually move towards the middle of the two pipelines during the development.

  The time-averaged scour depth development with $m = 0$, $KC = 30$ can be seen in the left column of Figure 5.7, which depicts time series of the scour beneath two pipelines in tandem for varying horizontal gap ratios. It is shown that the time-averaged scour depths beneath the upstream and the downstream pipelines are generally symmetric.

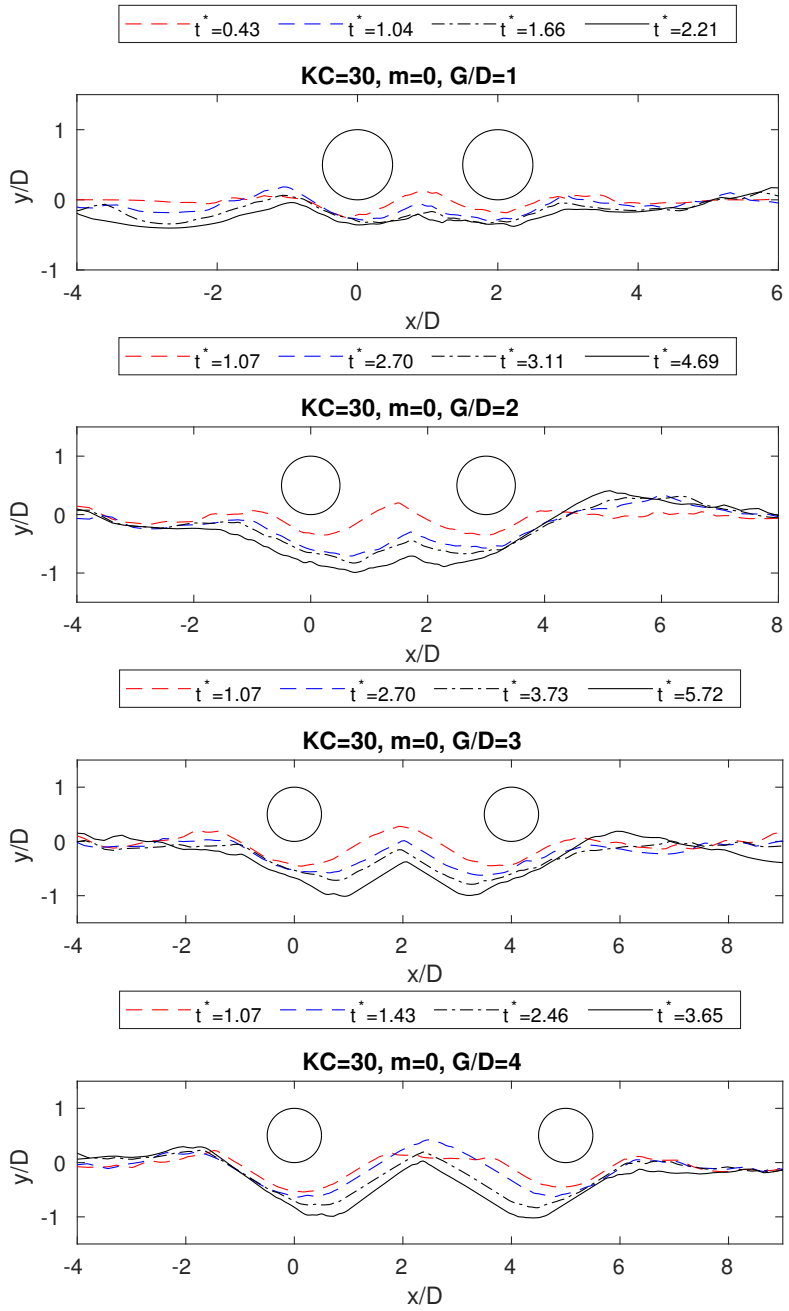

Figure 5.6 Scour profiles for $m = 0$, pure-wave condition with $KC = 30$.

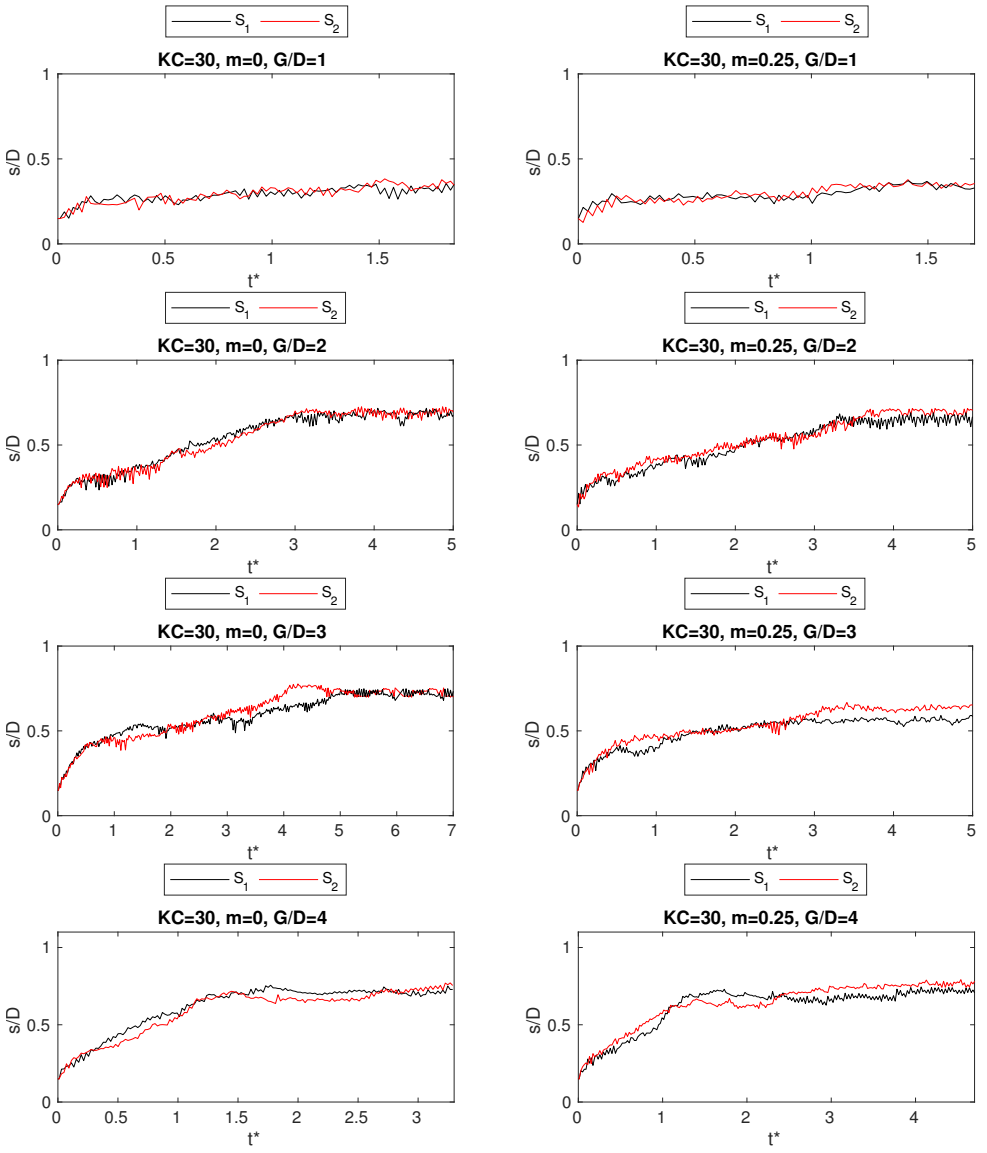

Figure 5.7 Time series of the scour depths beneath the upstream pipeline (S_1) and the downstream pipeline (S_2) with $KC = 30$. Left column: $m = 0$; Right column: $m = 0.25$.

It is noted that the number of the berms that are formed in between the tandem pipelines is influenced by both G/D and KC. As KC is proportional to the ratio of the amplitude of free stream orbital motion to the pipeline diameter, it is expected that for large horizontal gap ratios, more berms in between the two pipelines can be formed for a small KC. Figure 5.8 presents computed scour profiles with different KC during the equilibrium stage with large horizontal gap ratio, i.e. $G/D = 4$. It is seen that for $KC = 5.6$, three berms are formed between two pipelines at the equilibrium stage. For $KC = 15$, two berms are formed in between two pipelines. As KC increases to over 15, only one berm is observed between the tandem pipelines, as shown in Figure 5.8 e.g. with $KC = 25.3$. It should be mentioned that the asymmetric form of the berms in $KC = 15$ is a momentary phenomenon, since the profile still changes cyclically during the equilibrium stage. The number of berms that are formed between the pipelines can be related to the natural length of vortex ripples. Following Brøker (1985) and Fuhrman et al. (2014), the nature length of the vortex ripples is calculated by $\lambda_r/D = 1.2/(2\pi) \cdot KC$. For $KC = 5.6$, λ_r/D is calculated as 1.07, meaning that we can expect three vortex ripples between the pipelines at $G/D = 4$. For $KC = 15$, λ_r/D is calculated as 2.86, so there is maximum two vortex ripples between the pipelines with $G/D = 4$. For $KC = 25.3$, λ_r/D is 4.83 so that only one vortex ripple can be formed between the pipelines with $G/D = 4$.

- **Waves with weak current** $m = 0.25$**:**

  We will now consider waves with a relatively weak current, corresponding specifically to the flows with $m = 0.25$. Figure 5.9 presents a comparison of the scour profiles between the $m = 0$ and $m = 0.25$ cases with $KC = 15, G/D = 2$; $KC = 25.3, G/D = 2$ and $KC = 25.3, G/D = 4$. It is shown that with $m = 0.25$, the scour profiles resemble those under pure-wave conditions, but with slightly less symmetry. Especially, in

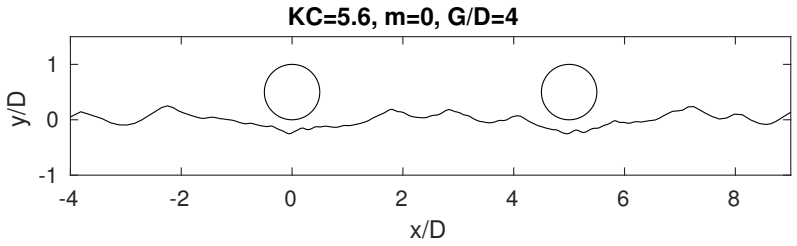

(a) Scour profile at the time instant of $t^* = 2.08$.

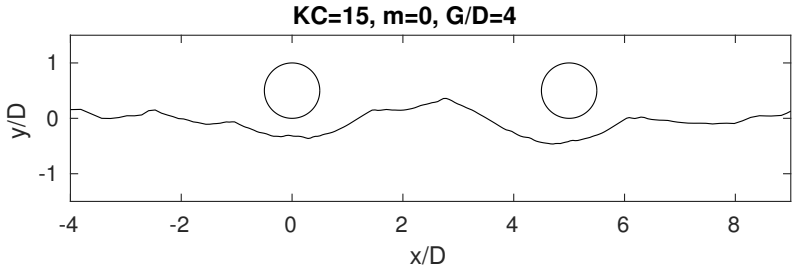

(b) Scour profile at the time instant of $t^* = 3.45$.

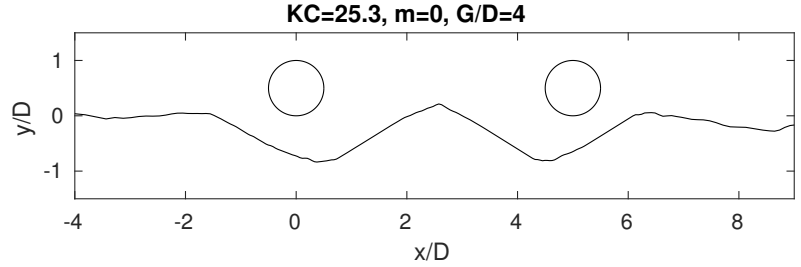

(c) Scour profile at the time instant of $t^* = 4.85$.

Figure 5.8 The number of berms formed in between two pipelines varies with KC at $G/D = 4$.

Figure 5.9c with $KC = 25.3, m = 0.25, G/D = 4$, the asymmetry of the scour profile is more apparent than those with $m = 0.25$ in Figure 5.9a and Figure 5.9b. Figure 5.9 demonstrates that for these three cases the shoulders at the downstream are more eroded with $m = 0.25$ compared to $m = 0$. Figure 5.9a and Figure 5.9b present the scour profiles with the same G/D but different KC. It is seen that the scour profile patterns (with $m = 0$ and 0.25, respectively) are similar with different KC. With a larger KC, the scour depth increases for both $m = 0$ and 0.25. Figure 5.9b and Figure 5.9c present the scour profiles with the same KC but different G/Ds. It is shown that the scour depth also increases when G/D increases from 2 to 4 for both $m = 0$ and 0.25.

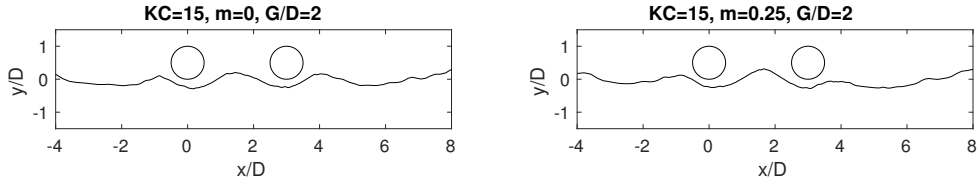

(a) Scour profiles at the time instant of $t^* = 2.92$.

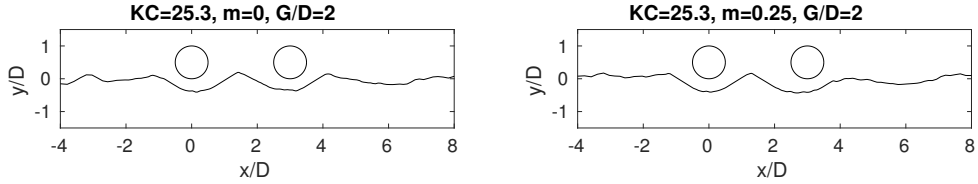

(b) Scour profiles at the time instant of $t^* = 2.84$.

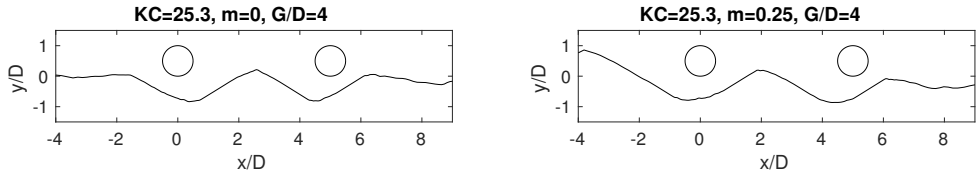

(c) Scour profiles at the time instant of $t^* = 4.85$.

Figure 5.9 A comparison of scour profiles during equilibrium stage between $m = 0$ and $m = 0.25$. Left column: $m = 0$; Right column: $m = 0.25$.

The scour time series with $m = 0.25$ are also compared with those with $m = 0$ in Figure 5.7 and Figure 5.10, respectively. It is generally observed that with $m = 0.25$, the scour depths at the equilibrium stage does not differ much from those with $m = 0$. The result is consistent with the findings in Larsen et al. (2016), who simulated the wave-plus-current induced scour beneath a single pipeline. They found that a low value of m leads to scour pattern quite close to pure-wave cases. It is seen that for the $G/D = 1$ cases, the scour time series with $m = 0.25$ are very close to those with $m = 0$, since the lee-wake vortex shedding is largely suppressed in between the two pipelines. However, it appears that when the horizontal gap ratio increases, the two pipelines eventually have different scour depths under the asymmetric effect of wave-plus-current conditions, although the difference is minor, as seen in Figure 5.7 and Figure 5.10 at $G/D = 2$, 3, and 4. Here, the downstream pipeline has a slightly larger scour depth than the upstream pipeline after reaching equilibrium.

- **Waves with strong current** $m = 0.5$**:**

  We will now consider waves with a strong current, corresponding specifically to the flows with $m = 0.5$. As shown before in Figure 5.5, when $m = 0.5$, the undisturbed free stream velocity is ≥ 0 at all times. This means that the undisturbed free stream flow behaves more like a unidirectional current flow with a fluctuating velocity from 0 to $2U_m$. Therefore, it is expected that with $m = 0.5$ the effect of the current should become more dominant compared to the effect of waves.

  Figure 5.11 presents the scour profile evolution and the time series with $m = 0.5$, $G/D = 1$ for the case having $KC = 19.6$ as an example. It is seen in Figure 5.11a that the scour holes beneath the two tandem pipelines are merged into one large scour hole while reaching equilibrium. This profile shape is similar to that in the validation case involving a steady current, as shown in Figure 5.3a. The same

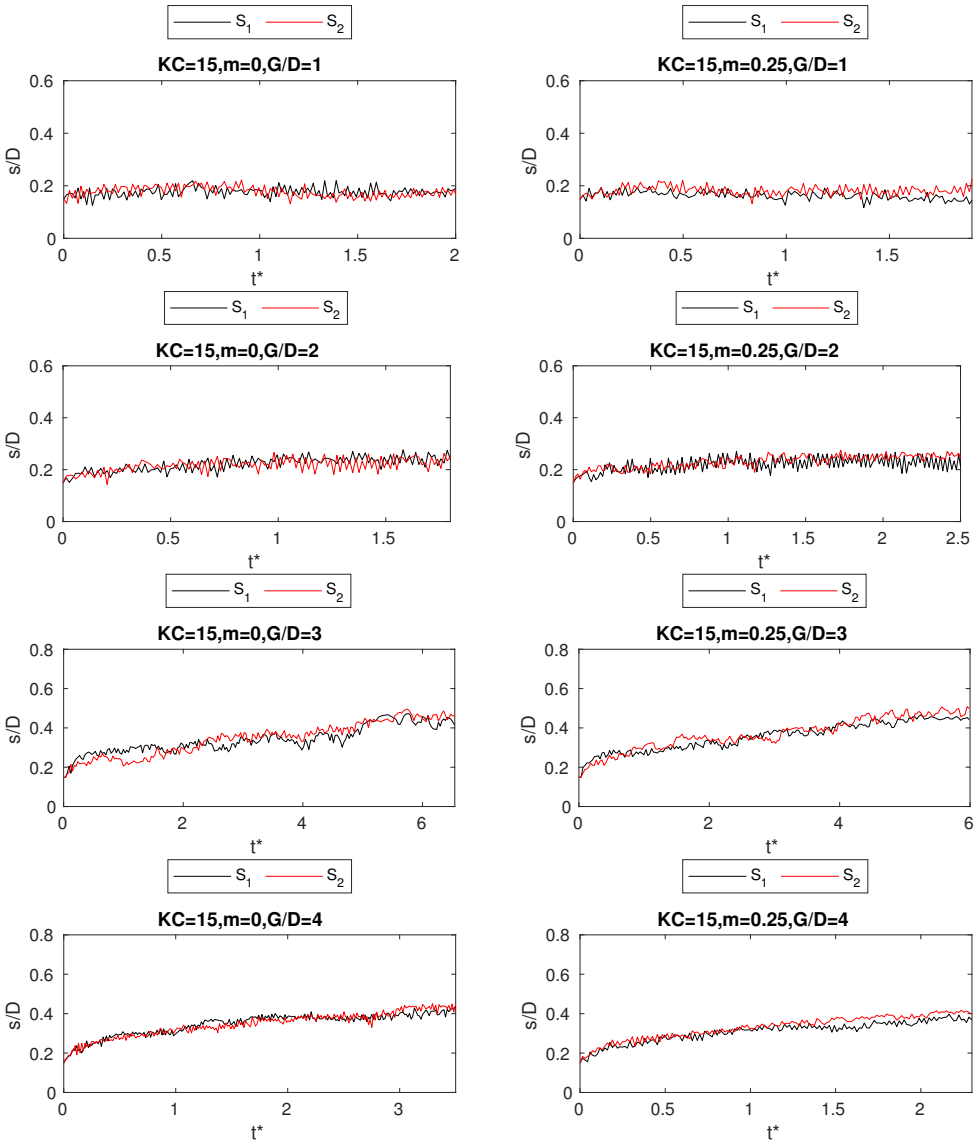

Figure 5.10 Time series of the scour depths beneath the upstream pipeline (S_1) and the downstream pipeline (S_2) with $KC = 15$. Left column: $m = 0$; Right column: $m = 0.25$.

phenomenon is observed for $m = 0.5$, $G/D = 1$ cases having all the KC except for $KC = 5.6$. Zhou and Yiu (2006) and Sumner (2010) investigated the flow around two pipelines in the pure current. They found that for $G/D \leq 1$, the two pipelines behave effectively as a single extended body so that the one large scour hole is formed beneath the two tandem pipelines while reaching equilibrium.

It is noticed in Figure 5.11 that the development of the scour profile with $m = 0.5$, $G/D = 1$ generally follows a four-stage pattern, as shown in Figure 5.11a. At the initial stage, the scour depths beneath the two pipelines are both increased. A berm is formed in between the two pipelines (e.g. $t^* = 0.09$ in Figure 5.11a, stage (1) in Figure 5.11b). Then, at the second stage, the berm migrates towards the downstream pipeline and the scour hole beneath the downstream pipeline is slightly buried by the sediments transported from upstream. The scour depth beneath the downstream pipeline slightly decreases at this stage (e.g. $t^* = 0.33$ in Figure 5.11a, stage (2) in Figure 5.11b). The reduction of the scour hole beneath the downstream pipeline at the second stage is explained in Figure 5.12 which shows the horizontal velocity field and the suspended sediment concentration at a time instant during this stage. As shown in Figure 5.12a, the berm in the gap causes flow separation at its lee-side. The main flow is transported along the stoss-side of the berm towards the upper side of the downstream pipeline. Only a small part of the flow pass through the tunnel beneath the downstream pipeline. Due to the low flow velocity and low shear stress in the downstream tunnel, the small amount of sediments transported from the upstream are mainly trapped inside the tunnel while very little can be transported out. Figure 5.12b shows the distribution of the suspended sediment concentration at the second stage. High suspended sediment concentration is observed at the lee-side of the berm. Suspended sediments are transported into the downstream tunnel. At the lee-side of

the downstream pipeline, the suspended sediment concentration is relatively low, indicating that very few suspended sediments are transported out of the downstream tunnel, causing a decrease of the scour depth beneath the downstream pipeline.

At the third stage, the height of the berm between the two pipelines is gradually decreased and the scour depths beneath the upstream and downstream pipelines are both increasing (e.g. $t^* = 2.77$ in Figure 5.11a, stage (3) in Figure 5.11b). Figure 5.13 shows the velocity field and the suspended load concentration at this stage. With the disappearance of the berm in the gap, the main flow is passing beneath the downstream pipeline, causing high velocity and shear stress at the downstream slope. The depth and width beneath the downstream pipeline are gradually increasing. At this stage, the scour depth beneath the upstream pipeline reaches equilibrium first, while the scour depth beneath the downstream pipeline is still under development. The sediments are transported to the downstream of both pipelines because of the vortex shedding behind the downstream pipeline. At the final stage, the scour profile reaches equilibrium with minor cyclic fluctuations (e.g. $t^* = 5.89$ in Figure 5.11a, stage (4) in Figure 5.11b). The time series and the corresponding four stages of the scour development with $KC = 19.6, m = 0.5$, $G/D = 1$ are shown in Figure 5.11b. The same phenomenon is seen at other KC except for $KC = 5.6$.

The final scour profile for $KC = 5.6, m = 0.5, G/D = 1$ is shown in Figure 5.14. It is seen that the berm in between the two pipelines is not eroded due to the small stroke of the wave motion. Also, for such a low KC, the T_w is also small so that the flow direction changes frequently with a small stroke of wave motion. Therefore, the scour depth does not develop much.

As the horizontal gap distance increases, two pipelines become more independent. Separate scour holes are formed beneath the two pipelines.

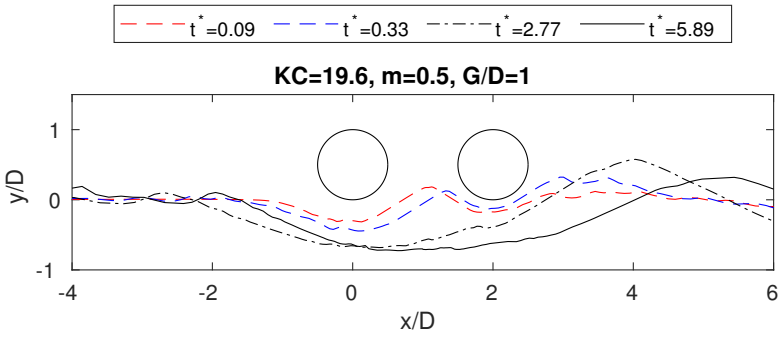

(a) Scour profile development.

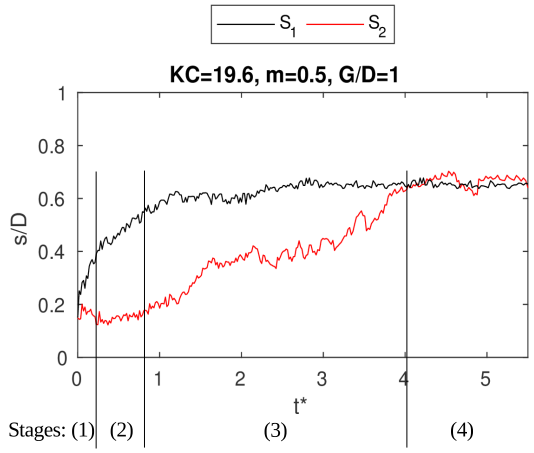

(b) Time series.

Figure 5.11 Scour profile development and time series of case $KC = 19.6$, $m = 0.5$, $G/D = 1$.

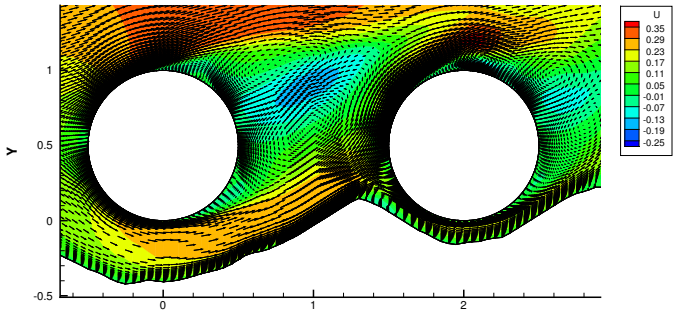

(a) Horizontal velocity field U_x (m/s).

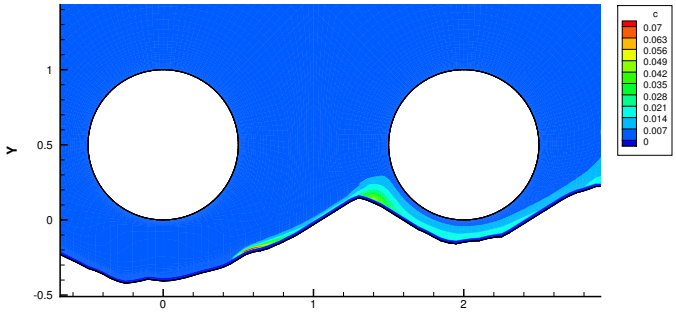

(b) Suspended sediment concentration.

Figure 5.12 Horizontal velocity field and suspended sediment concentration for case $KC = 19.6$, $m = 0.5$, $G/D = 1$. The time instant is $t^* = 0.26$, when the downstream pipeline experiences a decrease of the scour depth (corresponding to stage (2) in Figure 5.11b).

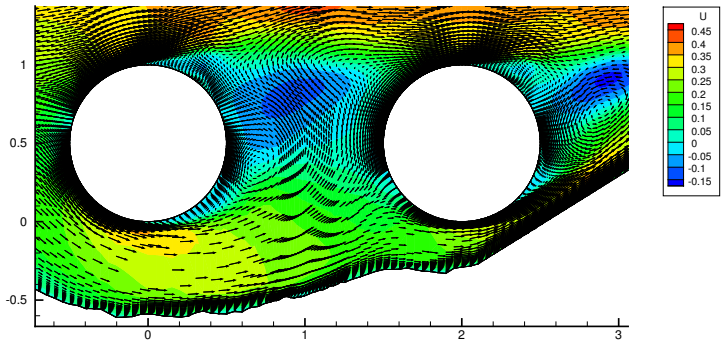

(a) Horizontal velocity field U_x (m/s).

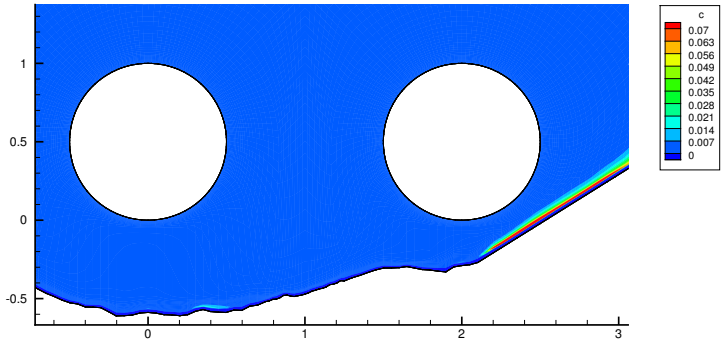

(b) Suspended sediment concentration.

Figure 5.13 Horizontal velocity field and suspended sediment concentration for case $KC = 19.6$, $m = 0.5$, $G/D = 1$. The time instant is $t^* = 1.52$, when the downstream pipeline experiences an increase of the scour depth (corresponding to stage (3) in Figure 5.11b).

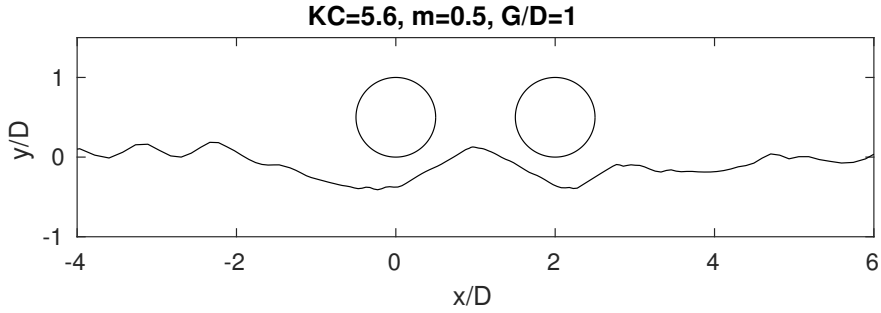

Figure 5.14 Scour profile at the equilibrium stage with $KC = 5.6$, $m = 0.5$, $G/D = 1$ at $t^* = 3.29$.

Therefore, the berm in between the two pipelines will not disappear even at the equilibrium stage. As shown in Figure 5.15 and Figure 5.16 (for $m = 0.5$ cases with $KC = 19.6$ and $KC = 25.3$, respectively), at the equilibrium stage, the berm is still present and is located close to the downstream pipelines. It is seen in Figure 5.15 that as the horizontal gap distance increases from 2 to 4, the berm height becomes higher after reaching equilibrium. It is also seen that the width of the scour hole beneath the upstream pipeline becomes larger as the horizontal gap distance increases.

Figure 5.17 and Figure 5.18 present the scour time series with $KC = 11, m = 0.5$ and $KC = 30, m = 0.5$ at G/D =1, 2, 3, and 4. It is observed that the time duration for the scour beneath the downstream pipeline to reach equilibrium is larger than that required for the upstream pipeline. It shows that with $G/D = 1$ the downstream pipeline experiences a greater delay of scour development compared to those with larger horizontal gap ratios. The same as the time series of $KC = 19.6, m = 0.5, G/D = 1$ in Figure 5.11b, it is also shown in Figure 5.17 and Figure 5.18 that for $m = 0.5, G/D = 1$ at different KC, the downstream pipeline experiences an initial increase of the scour depth (stage(1))

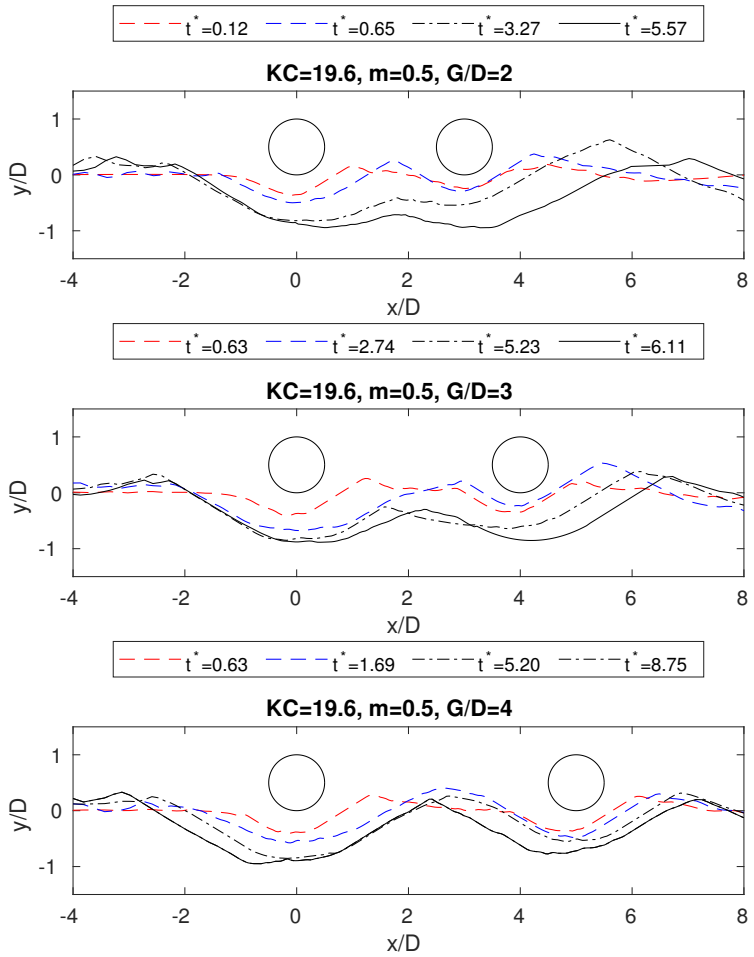

Figure 5.15 Scour profile development with $KC = 19.6$, $m = 0.5$, $G/D = 2, 3$ and 4.

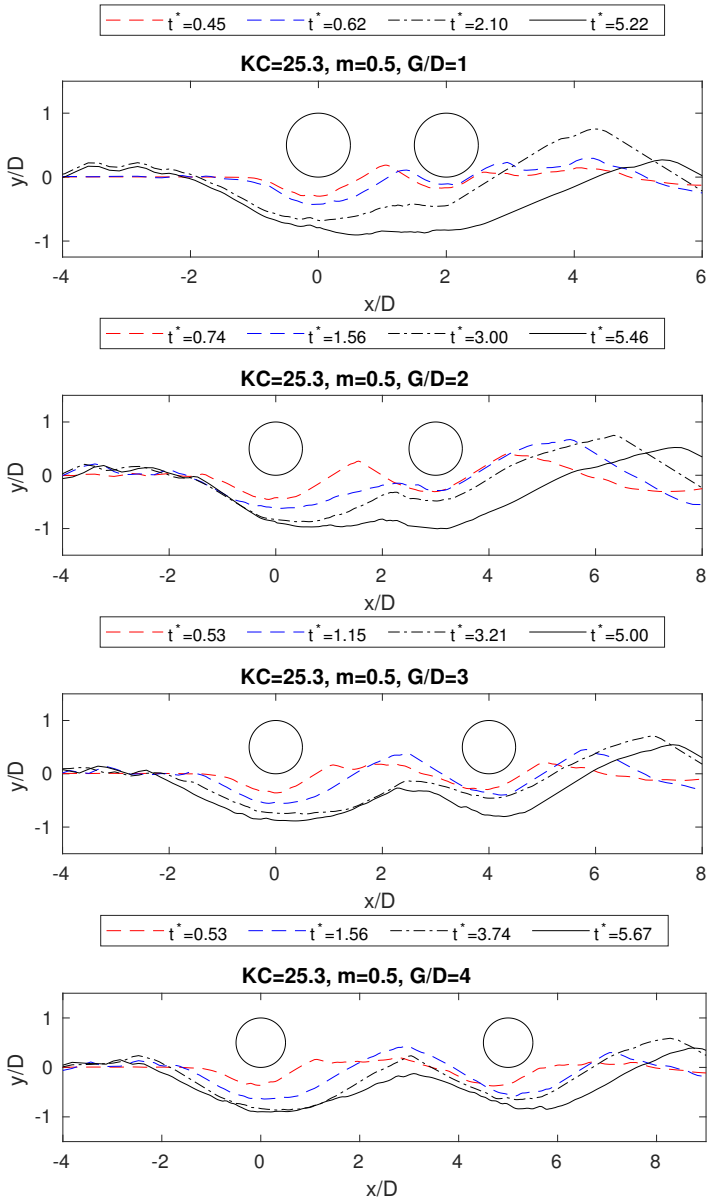

Figure 5.16 Scour profile development with $KC = 25.3$, $m = 0.5$, $G/D = 1$, 2, 3 and 4.

and then a decrease of the scour depth (stage(2)) during the scour development process.

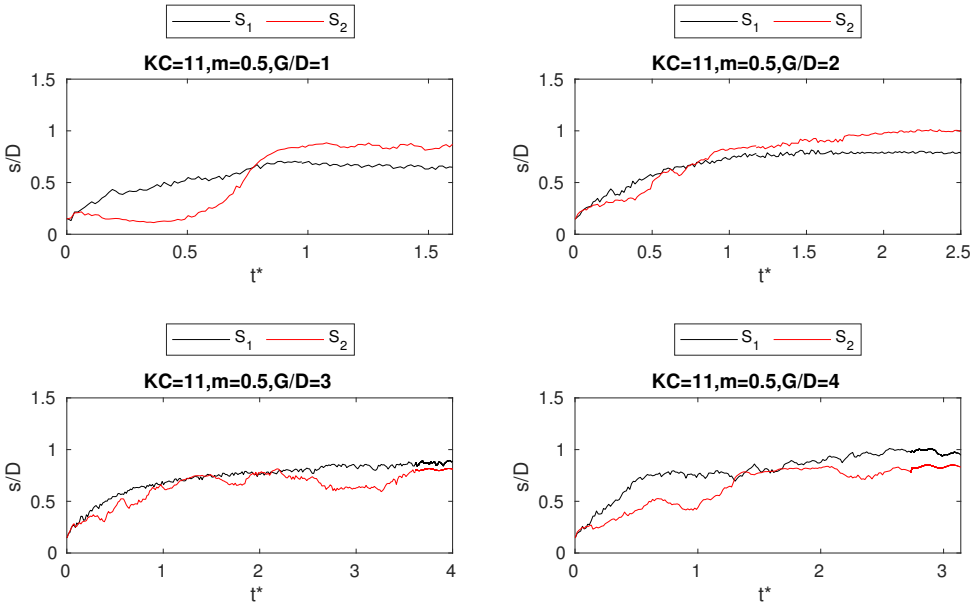

Figure 5.17 Scour time series with $KC = 11$, $m = 0.5$.

5.1.5.2 Equilibrium depths

For all the cases, the equilibrium scour depths beneath the centers of the upstream and downstream pipelines are shown in Figure 5.19–5.21. For $m = 0$ (a pure-wave condition), the time-averaged scour depth development is symmetric below two pipelines. Therefore, only one S_e is shown in Figure 5.19. Due to minor fluctuations of the scour depth at the equilibrium stage, S_e is calculated from $(\bar{S_1} + \bar{S_2})/2$, where $\bar{S_1}$ and $\bar{S_2}$ are the average scour depths beneath the upstream and the downstream pipelines over ten wave periods after reaching equilibrium. For a single pipeline in pure-wave conditions, the equilibrium scour depth is a function of the KC number (Sumer and Fredsøe, 1990), $S_e/D = f\{KC\}$, as expressed by the solid line in Figure 5.19.

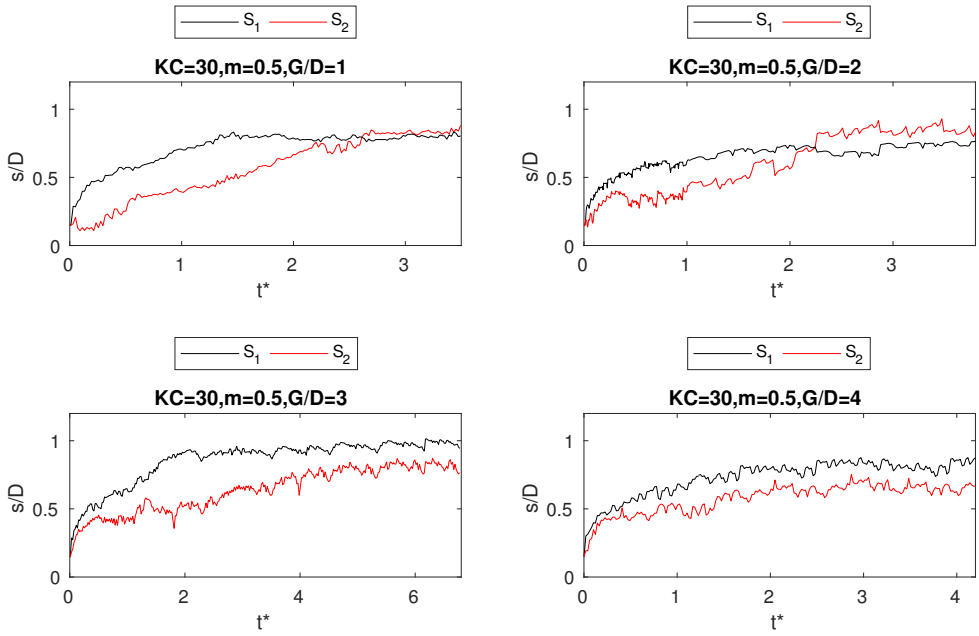

Figure 5.18 Scour time series with $KC = 30$, $m = 0.5$.

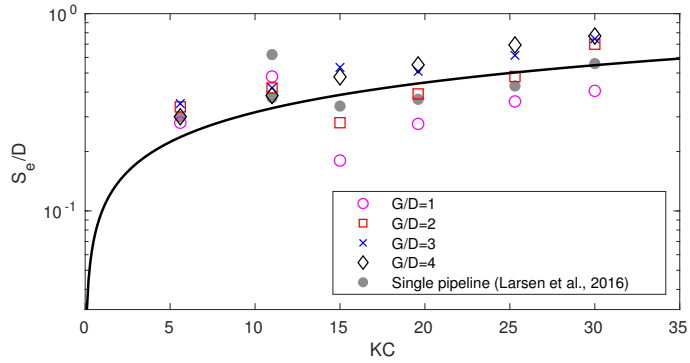

Figure 5.19 Equilibrium scour depths beneath the centers of the upstream and downstream pipelines at $m = 0$. The solid reference line is the empirical solution for a single pipeline in waves (Sumer and Fredsøe, 1990), $S_e/D = 0.1\sqrt{KC}$.

Figure 5.20 and Figure 5.21 present the equilibrium scour depths in combined waves and current with $m = 0.25$ and $m = 0.5$, where the reference lines in the figures correspond to the empirical expressions for the equilibrium scour depth for a single pipeline in combined waves and current given by Sumer and Fredsøe (1996):

$$S_e = S_c F \tag{5.30}$$

where S_c is the equilibrium scour depth in the pure current ($S_c/D = 0.6 \pm 0.2$). F is calculated by

$$F = \begin{cases} \frac{5}{3}(KC)^{a_m}\exp(2.3b_m), & 0 \le m \le 0.7 \\ 1, & m \ge 0.7 \end{cases} \tag{5.31}$$

where

$$a_m = \begin{cases} 0.557 - 0.912(m-0.25)^2, & 0 \le m \le 0.4 \\ -2.14m + 1.46, & 0.4 \le m \le 0.7 \end{cases} \tag{5.32}$$

$$b_m = \begin{cases} -1.14 + 2.24(m-0.25)^2, & 0 \le m \le 0.4 \\ 3.3m - 2.5, & 0.4 \le m \le 0.7 \end{cases} \tag{5.33}$$

- **Pure-wave conditions $m = 0$:**

  For a single pipeline in pure-wave conditions, the equilibrium scour depth is a function of KC (Sumer and Fredsøe, 1990), while for two tandem pipelines in pure waves the equilibrium scour depth must also potentially depend on the horizontal gap ratio G/D, i.e. such that:

$$\frac{S_e}{D} = f\left\{KC, \frac{G}{D}\right\} \tag{5.34}$$

  It is seen in Figure 5.19 that when $G/D = 1$ and 2, the trend in which the equilibrium scour depth for two tandem pipelines varies with KC

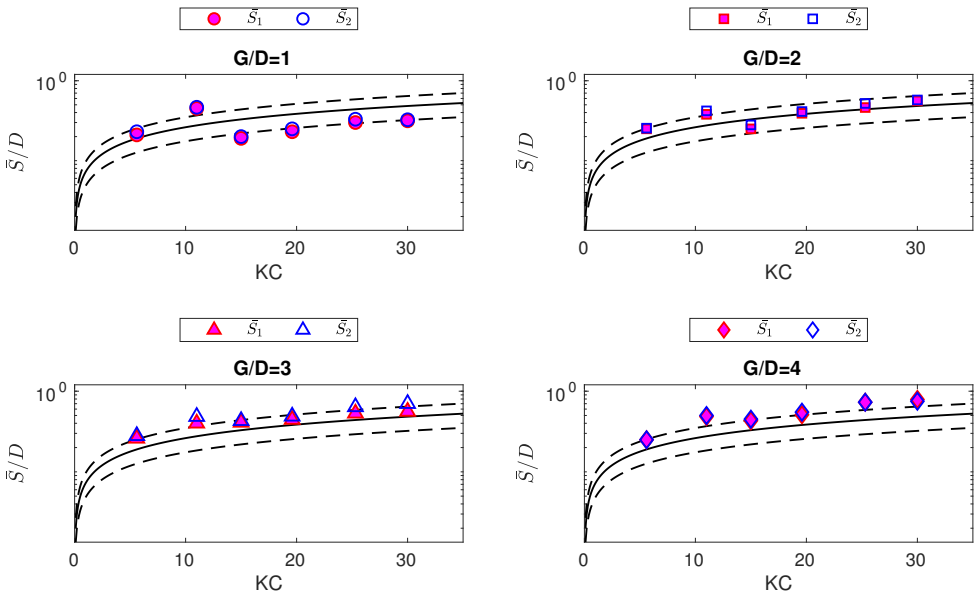

Figure 5.20 Equilibrium scour depths beneath the centers of the upstream and downstream pipelines at $m = 0.25$. The solid reference line is the empirical solution for a single pipeline in combined waves and current (Sumer and Fredsøe, 1996). The dashed lines are the empirical solution with the standard deviation.

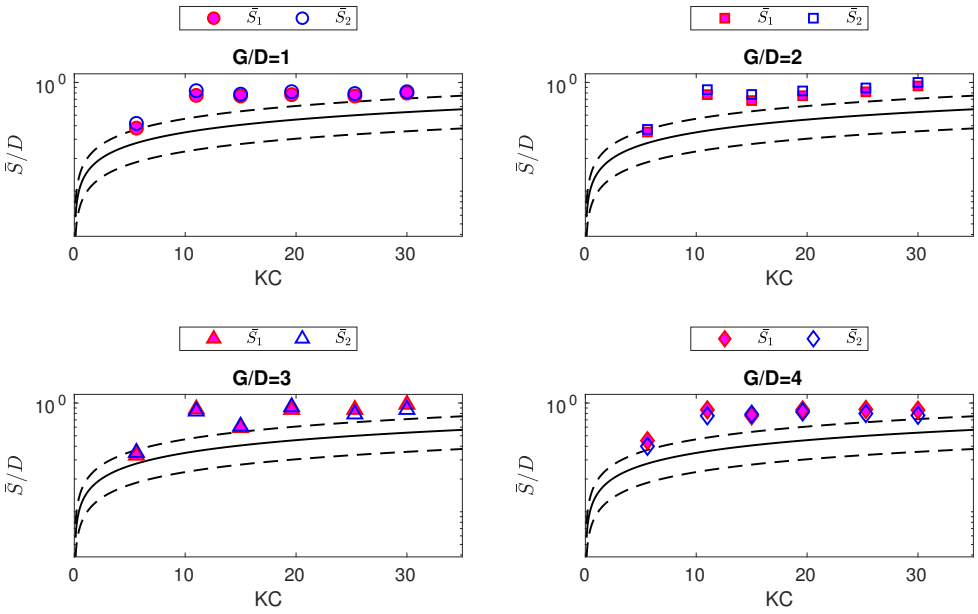

Figure 5.21 Equilibrium scour depths beneath the centers of the upstream and downstream pipelines at $m = 0.5$. The solid reference line is the empirical solution for a single pipeline in combined waves and current (Sumer and Fredsøe, 1996). The dashed lines are the empirical solution with the standard deviation.

is similar to that for single pipeline cases conducted by Larsen et al. (2016) but with a more significant drop in scour depth from $KC = 11$ to $KC = 15$. For $G/D = 3$ and 4, S_e/D increases with KC, which is in line with the trend of the empirical prediction for a single pipeline by Sumer and Fredsøe (1990).

For a given KC, the equilibrium scour depth generally increases with G/D. A special case is $KC = 11$, where the equilibrium scour depth with $KC = 11, G/D = 1$ is much higher than that with other KC at $G/D = 1$ and also higher than that with $KC = 11$ at other horizontal gap ratios. Similar phenomena were observed for a single pipeline with $KC = 11$ in simulations of Fuhrman et al. (2014) and Larsen et al. (2016). Fuhrman et al. (2014) explained the phenomenon as a resonance with the nature ripple length that is triggered within the model when KC is around 10 – 11. The profile develops a 'trough-to-trough' wavelength beneath the pipeline which closely matches with the nature length of vortex ripples. Therefore, the scour depth at around $KC = 10 - 11$ continually develops into a secondary stage and reached a final equilibrium. In Figure 5.19, for $KC = 11$ the two dots in grey from Larsen et al. (2016) are the scour depths beneath a single pipeline at the first temporary equilibrium stage and the secondary equilibrium stage, respectively. In the present simulations, the equilibrium depth of $KC = 11$ at each horizontal gap ratio is dominated by the resonance phenomenon within the model so that horizontal gap ratio has a relative small effect on $KC = 11$ compared to the other higher KC. It is worthwhile to mention that, in the present simulations, the equilibrium scour depths beneath two pipelines S_1 and S_2 are measured right below the center of the pipelines. The maximum scour depths in the scour hole may locate between two pipeline centers. Figure 5.22 presents the scour profile with $KC = 11, G/D = 1, m = 0$. The averaged equilibrium scour depth S_e/D is 0.48, while the averaged maximum scour depth

$S_{\max}/D$ is 0.625. In the study for a single pipeline in pure-waves by Larsen et al. (2016), the maximum scour depth locates right below the pipeline center, and the equilibrium scour depth is 0.62 at the secondary equilibrium stage. This explains why in Figure 5.19, the S_e/D with $KC = 11$ for two pipelines is lower than that for a single pipeline from Larsen et al. (2016) while the equilibrium scour status for this specific case is dominated by the resonance phenomenon. It is noted that the equilibrium scour depths for $KC = 5.6$ also varies insignificantly with G/D, which will be explained later. It is emphasized that, while the resonance phenomenon discussed above can occur in numerical models, it has yet to be observed in physical experiments, to the best of the authors' knowledge.

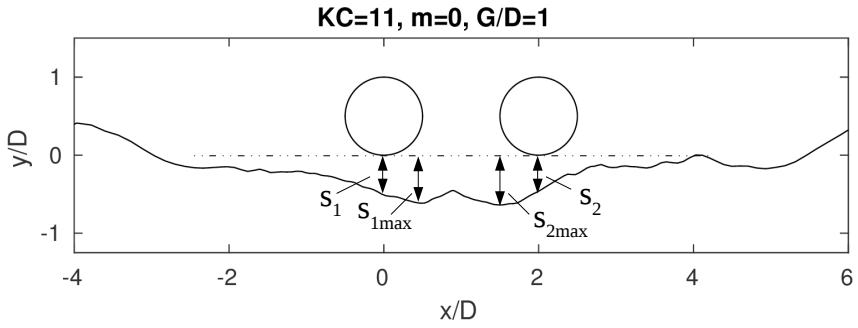

Figure 5.22 Scour profile with $KC = 11, G/D = 1, m = 0$ after reaching equilibrium. The averaged scour depth beneath the pipelines is $S_e/D = (\bar{S_1}/D + \bar{S_2}/D)/2 = 0.48$. The averaged maximum scour depth between the pipelines is $S_{\max}/D = (\bar{S_{1\max}}/D + \bar{S_{2\max}}/D)/2 = 0.625$. The equilibrium scour depth beneath a single pipeline with $KC = 11$ from Larsen et al. (2016) is $S/D = 0.62$.

For other KC (except for $KC = 5.6$ and 11), the equilibrium scour depth generally increases with G/D. For $G/D = 1$, the equilibrium scour depth beneath both pipelines is generally smaller than the empirical

prediction and also the simulation results (Larsen et al., 2016) for a single pipeline. The reduction of the scour depth with $G/D = 1$ can be explained by the suppression of the vortex shedding behind the upstream pipeline. The small spacing between the pipelines partially inhibits the shedding and further reduces the effect of the lee wake on the scour depth. However, the suppression of the vortex shedding will not happen for the $KC = 5.6$ case at $G/D = 1$. It is found that when $KC = 5.6$, the vortex shedding does not occur and the vortices remain attached to the pipelines during the half cycle of oscillating flow motions. Figure 5.23 presents the computed velocity field (U) in the x direction with $KC = 5.6$ and $G/D = 1$ during the scouring process. Snapshots at three time instants are presented: just after a change in flow direction direction at $t/T = \frac{\pi}{8}$, at maximum velocity at $t/T = \frac{\pi}{2}$, and during deceleration of the flow prior to changing direction at $t/T = \frac{7\pi}{8}$. These show that for $KC = 5.6$ the vortex at the lee-side of the upstream pipeline does not reach the downstream pipeline before the flow changes its direction. The vortex at the lee-side of the downstream pipeline remains attached to the pipeline during the first half of the wave cycle. Similar phenomenon was presented in Sumer and Fredsøe (2006), i.e., vortex shedding does not occur when $KC = 4$ in the oscillating flows. This explains the results shown in Figure 5.19, where the equilibrium scour depth computed with $KC = 5.6$ varies insignificantly with G/D ranging from 1 to 4. The equilibrium scour depth with $KC = 5.6$ is higher than the empirical predictions for a single pipeline but is consistent with the simulated result for a single pipeline in Larsen et al. (2016).

When the horizontal gap ratio increases to $G/D = 3$ and 4, the effect of KC is dominant. The equilibrium scour depths beneath two tandem pipelines are increased with KC in a similar way to the empirical prediction of scour beneath a single pipeline. It is seen in Figure

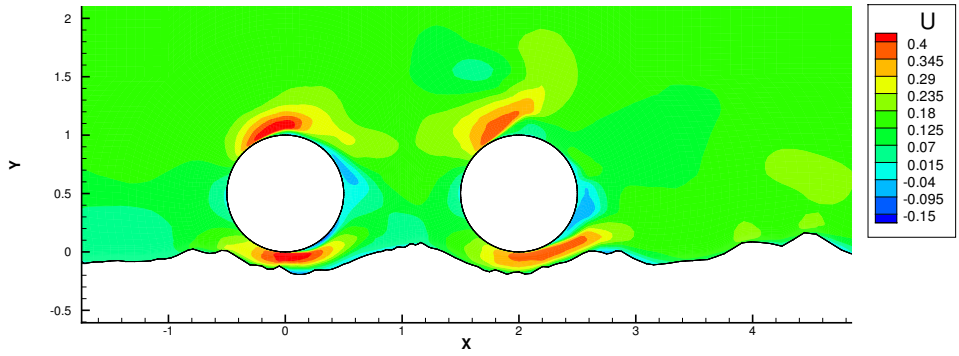

(a) $t/T = \frac{\pi}{8}$.

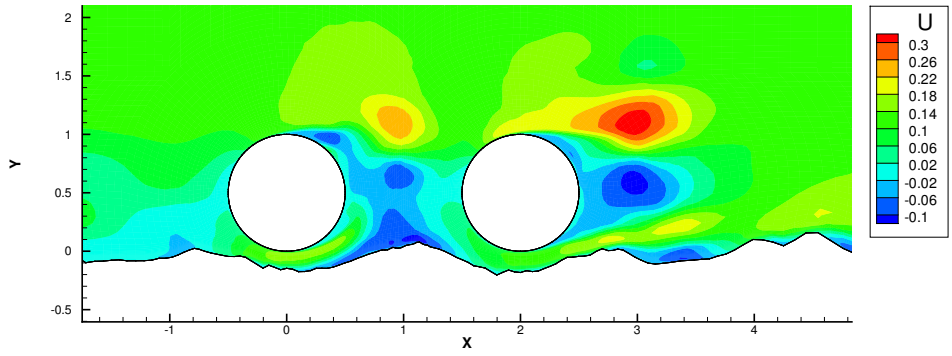

(b) $t/T = \frac{\pi}{2}$.

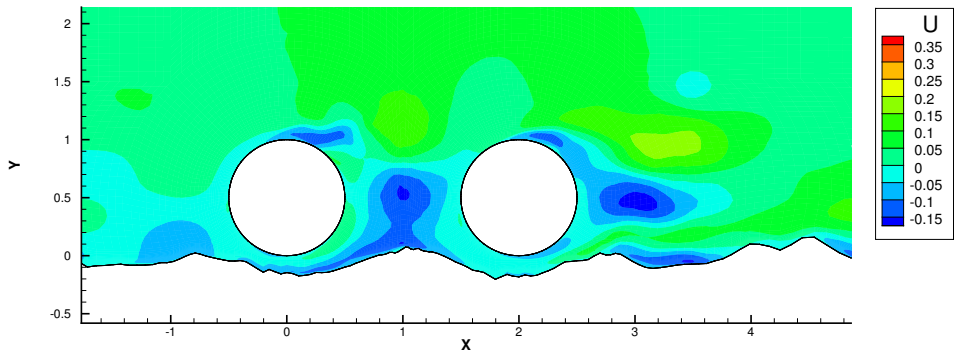

(c) $t/T = \frac{7\pi}{8}$.

Figure 5.23 Velocity field U (m/s) for two pipelines in tandem with $KC = 5.6$, $G/D = 1$, $m = 0$.

5.19 that the equilibrium scour depths for $G/D = 3$ and 4 beneath two pipelines are generally higher than that beneath a single pipeline in Larsen et al. (2016). This may be because of the mutual interaction of the lee-wake erosion from the upstream and the downstream pipelines in the oscillating flow.

- **Waves with weak current $m = 0.25$:**

  When the current of a relative strength $m = 0.25$ is added to the waves, the downstream pipeline can have a slightly higher equilibrium scour depth than the upstream pipeline, as shown in Figure 5.20. The difference of the equilibrium scour depths between the upstream and the downstream pipelines is relatively obvious for $G/D = 2$ and 3. These differences can arise because the current-induced lee-wake vortex behind the upstream pipeline may influence the downstream pipeline, and this influence appears to be more apparent when $G/D = 2$ and 3. Detailed studies and reviews of the gap effect on the flow around two tandem cylinders in a current can be found in Zhou and Yiu (2006) and Sumner (2010). Zhou and Yiu (2006) have discussed that when the horizontal gap ratio between two cylinders is between 0–1, two cylinders in the current behave like a single 'extended-body' and no vortex shedding occurs in between. Once the gap between two pipelines exceeds a critical value of between 2 and 2.5 (Zhao et al., 2015), vortex shedding from the upstream cylinder will occur. The vortices shed from the pipeline will sweep the bed and amplify the shear stress and the sediment transport. Therefore, the scour depth at the downstream pipeline is enhanced at the intermediate horizontal gap ratios. When G/D increases to 4, the influence from the vortex shedding behind the upstream pipeline on the downstream pipeline becomes less significant. The two pipelines then become more independent, so that at $G/D = 4$, the equilibrium scour depths beneath the upstream and downstream pipelines are very close to one another.

At each G/D, the trend of equilibrium scour depths varies with KC follows reasonably the empirical expression of Sumer and Fredsøe (1996). Furthermore, it is also worth noting that for $G/D = 1$ and 2, $m = 0.25$ in Figure 5.20, the trend of equilibrium scour depths varies with KC is very similar to that for pure waves, i.e., $G/D = 1$ and 2, $m = 0$ in Figure 5.19. Namely, a drop in scour depth from $KC = 11$ to $KC = 15$.

- **Waves with strong current $m = 0.5$:**

  With $m = 0.5$, it appears in Figure 5.21 that when KC is higher than 5.6, the equilibrium scour depth beneath the upstream pipeline is not affected by increases in KC. The equilibrium scour depths are generally located within the range of $S_e/D = 0.85 \pm 0.1$. These results tend to be similar to those in pure-current conditions. As discussed before that when $m = 0.5$, the free stream flow behaves like a unidirectional current flow. Mao (1986) investigated the equilibrium scour depth versus Shields parameter, and it is found that when $\theta > 0.15$, the equilibrium scour depths are generally larger than those with $\theta < 0.15$ and are in the range of $S_e/D = 0.8 - 0.9$. As presented in Table 5.1, the far-field Shields parameters θ_{cw} with $m = 0.5$ for each KC exceed 0.15 except for $KC = 15$. The finding is consistent with the results in Larsen et al. (2016). Their simulation results of a single pipeline showed that for $KC = 11 - 30$ and $m \geq 0.5$, the equilibrium scour depths were slightly larger than the empirical solutions predicted by Eqn. 5.30-5.33, being close to the equilibrium scour depth in pure-current conditions, i.e. with $m = 1$.

  Figure 5.21 shows that the equilibrium scour depth beneath the downstream pipeline is higher than that beneath the upstream pipeline at $G/D = 2$. At $G/D = 3$ and 4, the present work finds that the upstream and downstream pipelines have nearly equivalent scour depths, while the downstream pipeline does not always have a higher equilibrium

scour depth than the upstream pipeline. The finding is similar to the results of the experimental study on the scour beneath two tandem pipelines in pure-currents of Zhang et al. (2017).

5.1.6 Conclusions

The present study has investigated the local scour beneath two pipelines in tandem in the wave-plus-current conditions. A fully-coupled hydrodynamic and morphologic numerical model based on unsteady Reynolds-averaged Navier-Stokes (URANS) equations with k-ω turbulence closure has been applied. The model has been validated against existing experimental measurements of live-bed scour beneath a single pipeline (Mao, 1986) and as well as against experimental data involving live-bed scour beneath two pipelines in tandem (Zhao et al., 2015).

The scour profiles, scour time series and the equilibrium scour depths have been studied for two pipelines in tandem, with horizontal gap ratios ranging from 1 to 4, coupled with various KC and relative current strengths m. The following conclusions can be drawn from the present study.

- The effect of the Keulegan-Carpenter number, KC

  The effect of KC on the scour beneath two pipelines is dominant when the current strength is low ($m = 0$ and 0.25) and the horizontal gap ratio is high ($G/D \geq 3$). The present study found that in such conditions, the trend in which the equilibrium scour depths for two tandem pipelines varies with KC is similar to that for a single pipeline: the equilibrium scour depth increases proportionally with $\sqrt{KC}$. When KC is small, e.g. $KC = 5.6$, vortex shedding does not occur because the wave period is small and the flows change direction prior to vortices being shed. Therefore, the horizontal gap ratio has a less significant influence on the equilibrium scour depth. At a large horizontal gap ratio, i.e., $G/D = 4$ in the present study, KC also affects the number of berms that formed

in between two pipelines in pure-wave conditions. When $KC \leq 15$, two or more berms are formed in the gap between two pipelines. With $m = 0.5$, KC has insignificant effect on the scour depth and the results tend to be similar to those in the pure-current conditions.

- The effect of the relative current strength, m

  It is generally seen that with $m = 0$ and 0.25, the scour pattern is more similar to that in pure-wave conditions. With $m = 0.5$, the scour pattern is very similar to that in the pure-current conditions. With $m = 0$, i.e. pure-wave conditions, the time-averaged scour depth development is symmetric below the two tandem pipelines. At a relative high KC ($KC > 15$ in the present study), one berm is formed in between the two pipelines and the height of the berm gradually reduces during the scour process. However, it is still visible after reaching equilibrium for each horizontal gap ratio considered. The maximum scour depth is located in the gap between the two pipelines rather than below either of their respective centers. At a low current strength, the scour profiles still resemble those under pure-wave conditions, but with less symmetry. The downstream shoulder tends to be more eroded compared to pure-wave conditions. In waves plus strong-strength currents ($m = 0.5$), the flows effectively behave like a unidirectional current flow with a fluctuating "pumping" velocity from 0 to $2U_m$. Therefore, the scour pattern resembles that in pure current conditions. The scour depths are generally located in the range of $S_e/D = 0.85 \pm 0.1$ for the present cases. The scour beneath the downstream pipeline is delayed due to shielding from the upstream pipeline.

- The effect of the horizontal gap ratio, G/D

  The present study shows that in pure-waves, when $G/D = 1$ the vortex shedding behind the upstream pipeline is suppressed, except for $KC = 5.6$, where vortex shedding does not occur. At a low relative current

strength ($m = 0.25$), the scour depth beneath the downstream pipeline is slightly higher than that upstream when $G/D = 2$ and 3, since that the current-induced lee-wake vortex behind the upstream pipeline will have the most effective influence on the downstream pipeline. At $G/D = 4$, the upstream pipeline and the downstream pipeline tend to have very similar equilibrium scour depths. Under strong currents ($m = 0.5$), when the horizontal gap ratio is small, i.e. $G/D = 1$ in the present study, the scour hole below the tandem pipelines will eventually merge to one since the two pipelines effectively behave like a single extended body. As the horizontal gap ratio increases, the two pipelines become more independent and essentially separate scour holes are formed. The present study found that a smaller horizontal gap ratio, i.e., $G/D = 1$, can cause a greater delay of the scour beneath the downstream pipeline with $m = 0.5$. It is also seen that with $m = 0.5$ the width of the scour hole beneath the upstream pipeline becomes larger as the horizontal gap ratio increases.

Acknowledgment

This study was supported in part with computational resources provided by the Norwegian Metacenter for Computational Science (NOTUR), under Project No: NN9372K. The PhD project was financed by the Statoil Akademia program at the University of Stavanger.

Chapter 6

Numerical modeling of scour with upward seepage

Based on the fully-coupled hydrodynamic and morphologic model described in Chapter 5, this chapter proposes a numerical model of scour beneath subsea structures with considering the effect of upward seepage in the seabed. The coupled scour and seepage model is developed, validated and applied in the present work. The paper presented in this chapter has been submitted to Coastal Engineering.

6.1 Paper VI: CFD investigations of scour beneath a submarine pipeline with the effect of upward seepage

Yuzhu Li[a], Muk Chen Ong[a], David R. Fuhrman[b]
[a] Department of Mechanical and Structural Engineering and Materials Science, University of Stavanger, N-4036 Stavanger, Norway
[b] Section of Fluid Mechanics, Department of Mechanical Engineering, Technical University of Denmark, DK-2800 Kongens, Lyngby, Denmark

Abstract* A numerical model of scour beneath subsea structures considering the effect of upward seepage in the seabed is proposed. A small seepage can cause significant changes to the hydrodynamic force on the bed surface and stability of bed particles, which can further affect the sediment transport processes and scour patterns around subsea structures. The present model is developed based on a fully-coupled hydrodynamic and morphologic sediment transport model. The unsteady Reynolds-averaged Navier-Stokes (URANS) equations are solved together with the $k-\omega$ turbulence closure. In the presence of seepage, the bed friction velocity, the bed shear stress, and the bed load transport rate will be changed as compared to conditions without seepage. The sediment particle stability is also affected and the critical Shields parameter is changed. In the presence of upward seepage forces, the repose angle of the sediment is also reduced. The present model is validated against existing experiments in terms of streamwise flow velocity distribution subjected to upward seepage. The fully-coupled hydrodynamic and morphologic model is validated against existing experiments of scour beneath a pipeline in the live-bed regime and clear-water regime, respectively. The validated model is then applied to investigate the scour development beneath a submarine pipeline subjected to different upward hydraulic gradients. It is found that the

*This is a journal paper submitted to Coastal Engineering.

equilibrium scour width is increased with a large upward hydraulic gradient. The equilibrium scour depth stays in the range of 0.6 to 0.8 of the pipeline diameter for the live-bed cases. For the clear-water case, with a large upward hydraulic gradient, the equilibrium scour depth slightly decreases.

keywords: CFD; numerical model; submarine pipeline; seepage; scour

6.1.1 Introduction

Scour beneath a submarine pipeline has been investigated intensively by experiments, such as Mao (1986), Sumer and Fredsøe (1990) and Sumer and Fredsøe (1996), and numerical simulations such as Chao and Hennessy (1972), Chiew (1991), Brørs (1999), Liang et al. (2005), Fuhrman et al. (2014) and Larsen et al. (2016) in the previous studies. The effects of current, waves and combined waves and currents on the scour pattern beneath a pipeline have been thoroughly studied. In most of the numerical studies, the seabed is regarded as an impermeable wall (Brørs, 1999; Fuhrman et al., 2014; Larsen et al., 2016; Li and Cheng, 2000, 2001; Smith and Foster, 2005) and the effect of seepage flow in the seabed on the mobility of bed particles has been ignored. In fact, the seabed soil is a porous medium. Under the effect of waves or current, seepage forces can be induced in the seabed. In certain circumstances, an upward seepage force in the seabed can cause soil liquefaction and structural instability once it exceeds the initial effective stress that exists in the seabed. A number of studies have been performed to investigate the effect of wave-induced seepage forces on the liquefaction of the seabed beneath offshore foundations or subsea structures (Li et al., 2018; Luan et al., 2008; Ye et al., 2013; Zhang et al., 2015). However, very limited studies have been carried out to understand the effect of seepage in the soil on scour beneath offshore and subsea structures.

In the past decade, some studies have been carried out to investigate the change of flow structure and sediment stability in the presence of seepage in

the permeable sand bed. Lu et al. (2008) reviewed the experimental studies of seepage effects on the changes of the near-bed flow velocity profile, bed shear stress and bed particle stability. Cheng and Chiew (1999) derived equations for modifying the critical shear velocity of the sand bed particles in the presence of upward seepage. Lu and Chiew (2007) conducted experiments and proposed an empirical equation for the dune dimensions and repose angles of sand particles subjected to seepage. Dey and Singh (2007) did experiments on clear-water scour depth beneath a marine pipeline with different upward seepage velocities. Recently, Guo et al. (2019) did two-dimensional numerical studies on the sediment incipient motion around a free-spanning pipeline considering seepage flow in the seabed. However, the sediment transport and morphology of the seabed is not modelled in their study. So far, the scour development around subsea structures in the presence of seepage in the seabed has not been numerically modelled in any of the previous studies.

The seepage velocity inside the porous seabed is usually small compared to the free-stream velocity (Lu et al., 2008), so that it can have a minor effect on the free-stream velocity field. However, small seepage can cause a significant change to the hydrodynamic force on the bed surface. The bed friction velocity and the bed shear stress are changed. Meanwhile, upward seepage can also affect the stability of bed particles such that the threshold of incipient sediment motion, i.e., the critical Shields parameter, is also changed. Due to the decrease of the effective submerged weight of sand particles, the angle of repose is also reduced (Lu and Chiew, 2007). Therefore, the process of sediment transport, and the furthermore scour patterns can be largely affected. In the present study, a modified numerical model of scour around a submarine pipeline, considering upward seepage effects, is proposed. The present model is based on a fully-coupled hydrodynamic and morphologic model (Jacobsen, 2011; Jacobsen and Fredsoe, 2014; Jacobsen et al., 2014). The unsteady Reynolds-averaged Navier-Stokes (URANS) equations are solved together with the $k-\omega$ turbulence closure. The same (or very similar)

turbulence model has been successfully used to solve scour problems in Roulund et al. (2005), Fuhrman et al. (2014), Baykal et al. (2015) and Larsen et al. (2016). The following modifications are implemented in order to couple seepage effects with the scouring problem.

1. In the presence of upward seepage flow, the incoming flow structure near the seabed is changed. The bed friction velocity and the streamwise velocity distribution above the seabed are modified, as discussed later in Section 6.1.2.2. The bed shear stress is reduced due to the upward seepage effect. The present model utilizes separate one-dimensional vertical (1DV) simulations driven by the body force to generate the fully-developed velocity boundary layer flow without upward seepage and then two-dimensional (2D) simulations without morphology to develop the inlet flow with upward seepage velocities until reaching equilibrium. The velocity profiles subjected to upward seepage velocities are validated against the experiments of Cheng and Chiew (1998) and Dey and Nath (2009), respectively, in Section 6.1.3.1.

2. The critical Shields parameter of bed particles in the presence of upward seepage is modified. The critical Shields parameter describes the threshold condition of sediment movement. Due to additional upward seepage forces, the critical Shields parameter is decreased, as described in Section 6.1.2.3.

3. For solving the sediment transport, the present scour model uses the bed load transport model proposed by Roulund et al. (2005). The scour model is validated against the experiments of Mao (1986) in Section 6.1.3.2. In the presence of an additional upward seepage force, the bed load transport model in Roulund et al. (2005) is modified, as discussed in Section 6.1.2.4.

4. The presence of the upward seepage will also change the repose angle of the sediment. According to Lu and Chiew (2007), with upward seepage forces, the repose angle is reduced based on the ratio of the upward hydraulic gradient i to the critical hydraulic gradient under quick conditions i_c, as discussed in Section 6.1.2.5.

Based on the considerations above, new scour profiles due to the incoming flow and the effect of upward seepage will emerge. The equilibrium scour depth and scour width with upward seepage can be different from that without upward seepage. The present modified model is applied to investigate the scour pattern around a submarine pipeline in the presence of upward seepage forces. The strength of the seepage effect is described by i/i_c, i.e., the ratio of the upward hydraulic gradient i to the critical hydraulic gradient i_c. The critical hydraulic gradient i_c describes the critical condition of liquefaction/fluidization, under which the upward seepage force just balances the submerged weight of a sand particle. If the hydraulic gradient i exceeds the critical hydraulic gradient i_c, the effective stresses between the individual grains will vanish and the fluid-sediment mixture will behave like a viscous liquid. Sumer et al. (2006) conducted experiments to investigate the sequence of sediment behaviour during wave-induced liquefaction in the soil. They found that sand ripples started to emerge only after the liquefaction and compaction process. This implies that scour does not occur during the liquefaction process, since the liquefied fluid-sediment mixture does not have a repose angle. Therefore, the present theory does not cater to fully liquefied situations. Hydraulic gradient ratios i/i_c ranging from 0 to 0.9 are thus modelled in the present numerical investigations.

6.1.2 Mathematical Equations

6.1.2.1 The fully-coupled hydrodynamic and morphologic CFD model

The present numerical model incorporating upward seepage effects into scour prediction is developed based on the fully-coupled hydrodynamic and morphologic CFD model developed by Jacobsen (2011) and Jacobsen and Fredsoe (2014) in the OpenFOAM* framework. The hydrodynamic model was built by solving the incompressible unsteady Reynolds-averaged Navier-Stokes

*OpenFOAM is a registered trademark of OpenCFD Ltd.

(URANS) equations together with the $k-\omega$ turbulence closure (Wilcox, 2006, 2008). Detailed equations for the hydrodynamic model can be found in Jacobsen (2011), Jacobsen et al. (2014), and Fuhrman et al. (2014).

The sediment transport model consists of a bed load transport model and a suspended sediment model. The bed load transport model was first proposed by Engelund and Fredsøe (1976) and extended to 3D by Roulund et al. (2005). The suspended sediment model was proposed by Fredsøe and Deigaard (1992) and described in Jacobsen (2011) in which a turbulent-diffusion equation for the concentration is solved. A full description and numerical implementation of the sediment transport model can be found in Jacobsen (2011), Jacobsen et al. (2014) and Jacobsen and Fredsoe (2014).

The morphological model for predicting the bed deformation is based on the sediment continuity (Exner) equation:

$$\frac{\partial h_b}{\partial t} = \frac{1}{1-n}\left[-\frac{\partial q_{bi}}{\partial x_i} + D + E\right], i = 1,2 \tag{6.1}$$

where h_b is the bed elevation, n is the porosity which is taken as 0.4 in the present study, q_{bi} the bed load sediment transport rate in the ith direction, D is the deposition and E is the erosion calculated from the suspended sediment model. Further details of the computation of the bed load sediment transport rate, deposition and erosion terms are given in Jacobsen and Fredsoe (2014). To prevent the un-physical steepening of the scour hole, a sand slide model proposed by Roulund et al. (2005) is utilized in the present numerical model.

Based on the fully-coupled hydrodynamic and morphologic model as described above, the following modifications (Section 6.1.2.2 - 6.1.2.5) are implemented in order to couple seepage effects with the scouring problem.

6.1.2.2 Modified incoming flow velocity distribution subjected to upward seepage

For a two-dimensional flow over a horizontal impermeable rough bed without seepage, the vertical distribution of streamwise velocity can be expressed as:

$$\frac{u}{u_f} = \frac{1}{\kappa}\left(\ln\left(\frac{30y}{k_s}\right)\right) \tag{6.2}$$

where u is the streamwise flow velocity, $u_f = \sqrt{\tau_b/\rho}$ is the friction velocity, τ_b is the wall shear stress, ρ is the fluid density, $\kappa = 0.4$ is the von Karman constant, $k_s = 2.5d$ is Nikuradse's equivalent sand roughness, d is the median grain diameter.

When upward seepage is applied to an open-channel flow, the resulting velocity distribution over a flat bed is expressed with a modifed logarithmic law derived in Cheng and Chiew (1998):

$$\frac{u}{u_f} = \frac{1}{\kappa}\ln\left(\frac{30y}{k_s}\right) + \frac{v_s}{4u_f}\left(\frac{1}{\kappa}\ln\left(\frac{30y}{k_s}\right)\right)^2 \tag{6.3}$$

where v_s is the upward seepage flow velocity.

In the present numerical model, the friction velocity u_f is determined from the tangential velocity at the nearest cell center based on the modified logarithmic velocity distribution:

$$u_f = \frac{u_{y_c} - \frac{v_s}{4}\left(\frac{1}{\kappa}\ln\left(\frac{30y_c}{k_s}\right)\right)^2}{\frac{1}{\kappa}\ln\left(\frac{30y_c}{k_s}\right)} \tag{6.4}$$

where u_{y_c} is the streamwise velocity at the level of y_c without seepage, $y_c = \Delta y/2$ is the normal distance from the wall to the first cell center. The friction velocity is utilized based on standard wall functions for k and ω in the first

layer of the cells nearest to the wall (Wilcox, 2006, 2008).

$$k = \frac{(u_f)^2}{\sqrt{\beta^*}} \tag{6.5}$$

$$\omega = \frac{u_f}{\sqrt{\beta^*}\kappa\Delta y} \tag{6.6}$$

where $\beta^* = 0.09$ is the standard closure coefficient. Detailed equations for the present hydrodynamic model can be referred to Fuhrman et al. (2014). Equation 6.4 indicates that the friction velocity at the seabed with the upward seepage is reduced compared to the friction velocity at the seabed without the upward seepage. In the present work, the incoming flow velocity profile and the friction velocity subjected to upward seepage effects are computed via 1DV and 2D simulations and are validated in Section 6.1.3.1.

6.1.2.3 Modified incipient sediment motion equation subjected to upward seepage

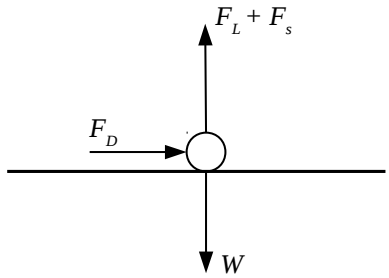

Figure 6.1 Two-dimensional force balance on a single moving particle on a flat bed.

Assuming the bed load particle as a sphere, the forces acting on the particle on a flat bed consist of the effective weight force W, the flow-induced drag force F_D, the flow-induced lift force F_L, and the upward seepage force F_S, as shown in Figure 6.1. The direction of the upward seepage flow is

assumed normal to the bed surface such that the seepage force acts in the same direction as the lift force. The equations of each force are expressed as follows:

$$W = \frac{1}{6}\pi(s-1)\rho g d^3 \tag{6.7}$$

$$F_D = C_D \frac{\pi d^2}{8}\rho u_r^2 \tag{6.8}$$

$$F_L = C_L \frac{\pi d^2}{8}\rho u_r^2 \tag{6.9}$$

where C_D and C_L are the drag and lift coefficients, s is the relative sediment density, ρ is the density of fluid, d is the mass median diameter of sediment particles, g is the gravitational acceleration, u_r is the velocity of the flow (at the particle position) relative to that of the particle. For a 2D case, the relative velocity u_r directly relates to the shear friction velocity u_f, according to Chiew and Parker (1994).

$$u_r = \frac{u_f}{\sqrt{f_*}} \tag{6.10}$$

where f_* is a form of friction factor.

The seepage force normal to the bed surface F_S is expressed as

$$F_S = \frac{i\rho g\pi d^3}{6(1-n)} \tag{6.11}$$

where n is the porosity. The seepage force acting on a porous medium per unit volume is expressed as $S = i\rho g$ (Bear, 2013). The number of sediment particles per unit volume is expressed as $N = \frac{1-n}{\pi d^3/6}$ (Cheng and Chiew, 1999). S/N yields the seepage force on a single particle in Eqn. 6.11.

On a flat bed with an upward seepage force, the force balance at incipient sediment motion can be written as

$$F_D - (W - F_L - F_S)\tan\phi_s = 0 \tag{6.12}$$

where ϕ_s is the repose angle of the sediment particles. $\tan\phi_s$ equals to the static friction velocity μ_s.

Substituting Eqns. 6.7, 6.8, 6.9, 6.10 and 6.11 into Eqn. 6.12, the critical friction velocity at incipient sediment motion can be expressed as

$$\frac{u_f^2}{f_*(s-1)gd} = \frac{\frac{4}{3}\left[1-\frac{i}{(s-1)(1-n)}\right]}{C_L + C_D/\tan\phi_s} = \frac{\frac{4}{3}\left(1-\frac{i}{ic}\right)}{C_L + C_D/\tan\Phi_s} \tag{6.13}$$

where $i_c = (s-1)(1-n)$ is the aforementioned critical hydraulic gradient which describes the critical condition of liquefaction/fluidization of the sand bed sediments.

The action of flow on the bed can be measured by a dimensionless form of the shear stress, which is so-called Shields parameter θ expressed as

$$\theta = \frac{u_f^2}{(s-1)gd} \tag{6.14}$$

The critical Shields parameter $\theta_{c0} = \frac{u_{fc}^2}{(s-1)gd}$ describes the threshold condition of incipient sediment motion on the flat bed.

Therefore, the critical Shields parameter on the horizontal flat bed without seepage is expressed as

$$\theta_{c0} = \frac{\frac{4}{3}\left(1-\frac{i}{ic}\right) f_*}{C_L + C_D/\tan\phi_s} \tag{6.15}$$

If we consider the incipient motion equation without seepage, i.e. $i = 0$, the equation for critical Shields parameter $\theta_{c0,i=0}$ is:

$$\theta_{c0,i=0} = \frac{\frac{4}{3} f_*}{C_L + C_D/\tan\phi_s} \tag{6.16}$$

Combining Eqn. 6.15 and Eqn. 6.16, the relation between the critical Shields parameters with and without the seepage force is

$$\frac{\theta_{c0}}{\theta_{c0,i=0}} = 1 - \frac{i}{i_c} \tag{6.17}$$

Now, we consider the force balance with upward seepage on a sloping bed, as shown in Figure 6.2. On a sloping bed of angle β, the force balance at

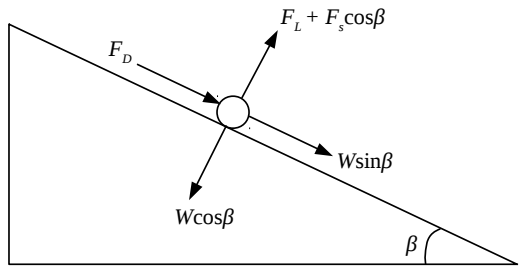

Figure 6.2 Two-dimensional force balance on a single moving particle on a sloping bed.

incipient sediment motion can be written as

$$W\sin\beta + F_D = (W\cos\beta - F_L - F_S\cos\beta)\tan\phi_s \tag{6.18}$$

where ϕ_s is the repose angle of the sediment particles. $\tan\phi_s$ again is equal to the static friction coefficient μ_s. Substituting Eqns. 6.7, 6.8, 6.9, 6.10 and 6.11 into Eqn. 6.18, the critical Shields parameter on a sloping bed with upward seepage force is expressed as

$$\theta_c = \frac{\frac{4}{3}\left[\cos\beta - \frac{\sin\beta}{\tan\phi_S} - \frac{i\cos\beta}{(s-1)(1-n)}\right] f_*}{C_L + C_D/\tan\phi_s} \tag{6.19}$$

Combining Eqn. 6.15 and Eqn. 6.19, the slope correction of the critical Shields parameter with upward seepage force is written as

$$\frac{\theta_c}{\theta_{c0}} = \cos\beta - \frac{\frac{\sin\beta}{\tan\phi_S}}{1-\frac{i}{i_c}} \tag{6.20}$$

6.1.2.4 Modified bed load transport model subjected to upward seepage

The present bed load transport model is based on Roulund et al. (2005) which is a generalized 3D extension of the transport formulation proposed by Engelund and Fredsøe (1976). The 3D force balance equations for the bed load transport is simplified to 2D in the present study. An additional upward seepage force is added in the force balance equations.

The forces acting on the particle consist of the agitating forces and the stabilizing forces (Fredsøe and Deigaard, 1992). The agitating forces include the gravity in the slope direction $W\sin\beta$ and the flow-induced drag and lift forces. In the model of Engelund and Fredsøe (1976), the drag and lift forces are considered as one force which is given by

$$F_{D,L} = \frac{1}{2}\rho c \frac{\pi}{4} d^2 u_r^2 \tag{6.21}$$

The empirical equation of the coefficient $c = C_D + \mu_d C_L$ is (Fredsøe and Deigaard, 1992)

$$c = \frac{4\mu_s}{3a^2(\theta_{c0}/2)} \tag{6.22}$$

where μ_d is the dynamic friction coefficient, here taken as 0.51, following Fredsøe and Deigaard (1992); a is an empirical constant taken as 10 according to Engelund and Fredsøe (1976) and Roulund et al. (2005).

The stabilizing force is the friction force that acts in the direction opposite to the particle motion, which was $\mu_d W\cos\beta$ in the original formulation in

Engelund and Fredsøe (1976). In the presence of the upward seepage force, the stabilizing force is modified to $\mu_d(W - F_s)\cos\beta$.

Therefore, the modified dynamic force balance equation on a sloping bed is written as

$$F_{D,L} + W sin\beta = \mu_d(W - F_s)\cos\beta \tag{6.23}$$

The relation between u_r and the bed load transport velocity u_b is given by

$$u_r = a \cdot u_f - u_b \tag{6.24}$$

According to Engelund and Fredsøe (1976), the bed load sediment transport rate q_b can be written as

$$q_b = \frac{\pi}{6} d^3 \frac{p_{EF}}{d^2} u_b \tag{6.25}$$

u_b is solved by Eqn. 6.23 and Eqn. 6.24. p_{EF} is the percentage of particles in motion in the surface layer of the bed, and is expressed by Engelund and Fredsøe (1976):

$$p_{EF} = \left[1 + \left(\frac{\frac{1}{6}\pi\mu_d}{\theta - \theta_c} \right)^4 \right]^{-1/4} \tag{6.26}$$

θ is the computed Shields parameter according to Eqn. 6.14. θ_c is the critical Shields parameter with the upward seepage and slope corrections, according to Eqn. 6.17 and Eqn. 6.20.

6.1.2.5 Angle of repose

Lu and Chiew (2007) inspected the influence of seepage on the critical slope of sediment. They found that the repose angle of the sediment is reduced with injection and is increased with suction. In the present work, the empirical equation derived by Lu and Chiew (2007) is used to predict the critical slope

(angle of repose) of the sediment subjected to upward seepage:

$$\frac{i}{i_c} = C_s \sin(\phi_{s0} - \phi_s) \tag{6.27}$$

where C_s is the coefficient related to the sediment properties, ϕ_{s0} and ϕ_s are the repose angle of the sediment without and with upward seepage. In the present simulations, $\phi_{s0} = 34^\circ$ and $C_s = 2.63$ are adopted based on the study of Lu and Chiew (2007).

6.1.3 Validations

6.1.3.1 Validation of boundary layer velocity profile with seepage

When upward seepage is applied to an open-channel flow, the resulting streamwise velocity profile in the boundary layer is changed. Cheng and Chiew (1998) and Dey and Nath (2009) conducted experiments of flow propagating over the immobile rough bed in wave tanks and measured the vertical velocity distributions subjected to the upward seepage velocities. Two of their experiments are reproduced using the present numerical model with the $k-\omega$ turbulence closure to validate the incoming flow simulation in the present work.

The experiment of Dey and Nath (2009) was conducted in a wave flume which is 0.6 m wide, 0.71 m deep and 12 m long. In their experiment, a seepage zone of 2 m long, 0.6 m wide was placed at 7.5 m downstream from the inlet. A uniform gravel layer was placed at the tank bottom and the seepage kit surface to achieve the same roughness. The gravel sediments had a median size of $d_{50} = 4.1$ mm and a relative density of $s = 2.65$. The velocity profile was measured at the location where flows traveled 1.2 m over the seepage zone. The measured depth-averaged streamwise velocity was 0.555 m/s and the flow depth was 0.15 m. The upward seepage velocity through the gravel-layer was 4 mm/s and was uniformly distributed within the gravel

layer. The roughness Reynolds number $k_s^+ = \frac{k_s u_f}{\nu}$ in their experiments was $k_s^+ = 338$ for $v_s = 0$ and $k_s^+ = 317$ for $v_s = 4$ mm/s. In the present numerical simulation, a 2D numerical wave tank is modelled. The top boundary of the tank is treated as a frictionless slip wall where the vertical velocity component is zero. First, a one-dimensional vertical (1DV) simulation driven by the body force is conducted to achieve a fully-developed velocity profile without the seepage effect. The body force is $F = \frac{u_f^2}{h}$, where u_f is the desired friction velocity without the seepage and h is the height of the numerical wave tank. In the simulations, the smallest cells near the tank bottom have a height of $0.3k_s$. Next, after the 1DV flow is fully-developed, the u, k and ω fields are applied as the boundary conditions for the inlet in the 2D simulation. The 2D wave tank is 2 m long and 0.71 m deep. An upward seepage velocity $v_s = 4$ mm/s is set at the tank bottom. The flows eventually reach a new equilibrium state, with a reduced friction velocity. The final vertical profile of the streamwise velocity in the 2D numerical wave tank with upward seepage is compared with the experimental data of Dey and Nath (2009) measured at the centerline of the flume (i.e. with equal horizontal distance to the two lateral sides of the tank). As seen in Figure 6.3a, a reasonable agreement is achieved between the present numerical simulation and the experimental measurements. The minor discrepancy may be because that in the experiment of Dey and Nath (2009), the flow was not fully-developed before reaching the seepage zone. The vertical profiles of streamwise velocity with and without seepage velocity produced by the present numerical simulations are compared in Figure 6.4. It is seen that with the upward seepage, the streamwise flow velocity close to the bed is reduced. The bed friction velocity decreases. Also, the velocity profile shifts up.

Cheng and Chiew (1998) have conducted a similar experiment in a 30 m long, 0.7 m wide and 0.6 m deep wave flume. In their experiment, the seepage zone was located 16 m from the inlet, to allow the incoming flow to be fully developed. The seepage zone was 2.0 m long. They conducted

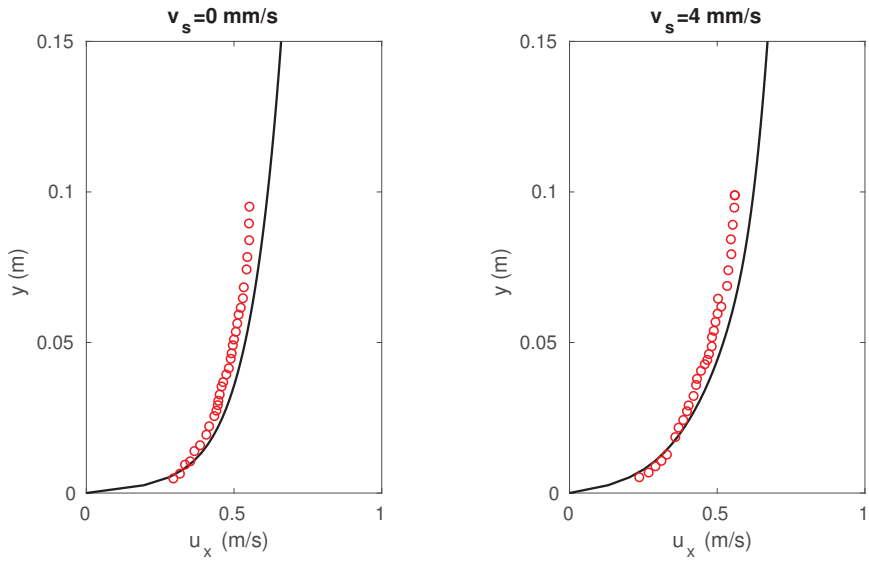

(a) (b)

Figure 6.3 Vertical profiles of streamwise velocity measured at the location where flows traveled 1.2 m over the seepage zone. The seepage zone was placed at 7.5 m downstream from the inlet. The flows in the experiments were not fully-developed, yielding a different u_f from that in the present numerical simulation where the flows are fully-developed. Therefore, the plots here are dimensional in stead of normalized by u_f.
– : Present numerical simulations; ○: Experiemental measurement by Dey and Nath (2009).

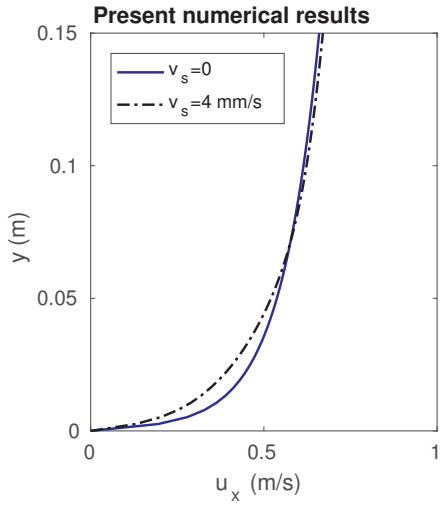

Figure 6.4 Comparison of vertical profiles of streamwise velocity without and with upward seepage (numerical reproduction of the experiment of Dey and Nath (2009)).

a series of experiments to validate the proposed empirical equation for the vertical profile of the streamwise velocity, as given in Eqn. 6.3. The present work reproduced one of their experiment with sediments of $d_{50} = 1.95$ mm and $s = 2.65$. The velocities are measured at 1 m upstream of the beginning of the the seepage zone. The depth-averaged streamwise velocity was 0.36 m/s and the flow depth was 0.148 m. The upward seepage velocity at the seepage zone surface is 2.35 mm/s. The roughness Reynolds number in their experiments was $k_s^+ = 120$ for $v_s = 0$ and $k_s^+ = 84$ for $v_s = 2.35$ mm/s. The non-dimensional plots of the vertical distributions of the streamwise velocity from the present numerical simulation and the experiment are compared in Figure 6.5. The present numerical result is in good agreement with the measurements reported by Cheng and Chiew (1998). A minor discrepancy is observed at the location further away from the bed. This may be because that in the experiment the limited width of the tank generated a secondary flow in the transverse direction near to the free surface. However, the secondary flow

effect does not exist in the numerical simulation since the numerical wave tank is 2D, assuming that there is no wall effect of the lateral sides.

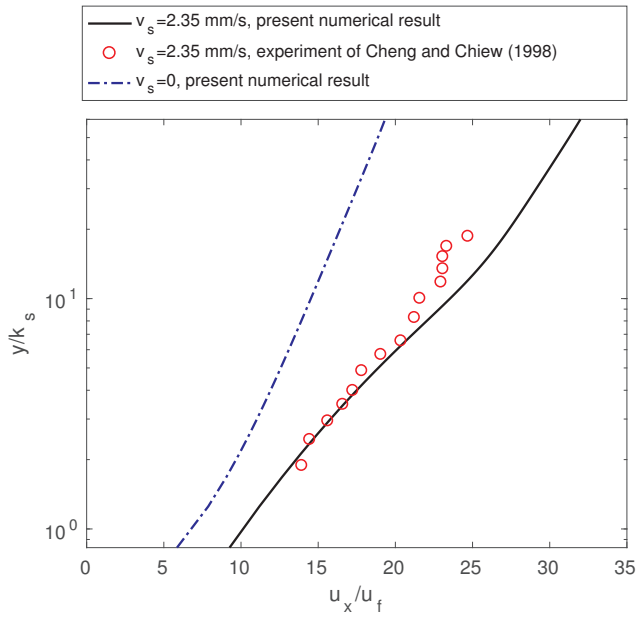

Figure 6.5 Vertical profiles of streamwise velocities u_x with and without seepage, normalized by their friction velocities at the bed u_f. The data are measured at the location where flows traveled 1 m over the seepage zone. The seepage zone was placed at 16 m downstream from the inlet.

6.1.3.2 Validation of the scour model

The present scour model is validated against the scour experiments beneath a submarine pipeline conducted by Mao (1986) in the clear-water regime and live-bed regime, respectively. The Shields parameter θ is 0.048 for the clear-water scour and 0.098 for the live-bed scour in the experiments of Mao (1986) and the present simulations. The critical Shields parameter θ_{c0} is set as 0.045 for the live-bed scour and 0.05 for the clear-water scour in the present numerical simulations. The present work utilizes the same 2D mesh

as in Fuhrman et al. (2014) for modeling scour beneath a submarine pipeline. An initial hole of $S_0/D = 0.15$ is specified in the numerical simulations. The pipeline diameter in the present simulations is 0.03 m, while in the experiments of Mao (1986) the pipeline diameter is 0.1 m. The grain size in Mao (1986) is $d = 0.36$ mm while in the present simulations $d = 0.19$ mm. Following the discussion in Larsen et al. (2016), it is comparable in terms of the non-dimensional scour developments between two different scales once the Shields parameter is kept the same. The comparison between the present numerical simulation and the experiment of Mao (1986) are performed in terms of S/D over the non-dimensional time t^* defined as

$$t^* = \frac{\sqrt{g(s-1)d^3}}{D^2}t \tag{6.28}$$

where t is the physical time. The far-field friction velocity u_f is calculated using Eqn. 6.14 and is equal to 0.012 m/s for the clear-water scour case and 0.017 m/s for the live-bed scour case in the present simulations. The specific gravity of the sediment grains is $s = 2.65$ for both the experiment (Mao, 1986) and the present simulation. The repose angle of the sediment is 34° in the present simulations.

The time series of the non-dimensional scour depth development and the scour profiles from the present numerical simulations and the experimental measurements of Mao (1986) are compared in Figure 6.6 and Figure 6.7. It is seen that the present numerical results are in good agreement with the experimental measurements in Mao (1986) for both the live-bed case and the clear-water case. Because of the initial hole in the numerical mesh, an approximation time $t_0 = \frac{S_0/D}{dS/dt}$ is added to the beginning of the time series for the development of the initial scour hole, in order to compare the scour development process with the experiments of Mao (1986).

It is shown in Figure 6.6a that the time series of scour depth development in the live-bed regime matches well with the experimental measurement of

Mao (1986). It is noted that the scour profile in Figure 6.6a is slightly different from that in Figure 5.2 in Chapter 5. It is because the mesh configuration is different and the repose angle in Figure 6.6a is set as 34° while in Figure 5.2 is set as 32°. In Figure 6.6b, the scour profiles at the upstream of the pipeline also match well with the experiment. The downstream shoulder predicted by the present simulation is slightly smaller than that measured by the experiment at $t^* = 0.24$ and is slightly larger than the experiment at $t^* = 4.86$. The comparison of scour in the clear-water regime is presented in Figure 6.7. The scour depth development predicted by the present numerical simulation at the initial time is slightly faster than that measured in the experiment. When reaching equilibrium, the present numerical simulation results are in good agreement with the experimental measurement in both the time series of scour depth (Figure 6.7a) and the scour profile (Figure 6.7b).

6.1.4 Scour beneath the pipeline with upward seepage

The present work investigates the effect of upward seepage on scour beneath a pipeline in the live-bed regime and clear-water regime, respectively. The investigations are performed based on the numerical cases of scour without the seepage effect, i.e., the live-bed scour case and the clear-water scour case of Mao (1986) in the validation study in Section 6.1.3.2. Nine levels of upward hydraulic gradients ($i/i_c = 0.1, 0.2, 0.3, ..., 0.9$) are applied to the live-bed scour case and the clear-water scour case, respectively.

The relationship between the upward hydraulic gradient i and the seepage velocity v_s can be derived by Darcy's law (Bear, 2013) when the seepage flow through the porous bed is linear, i.e., the seepage velocity v_s is proportional to the hydraulic gradient i:

$$v_s = Ki \tag{6.29}$$

where K is the permeability of the sand bed. However, it is noted that Darcy's law neglects the kinetic energy of the pore water. Therefore, it is feasible

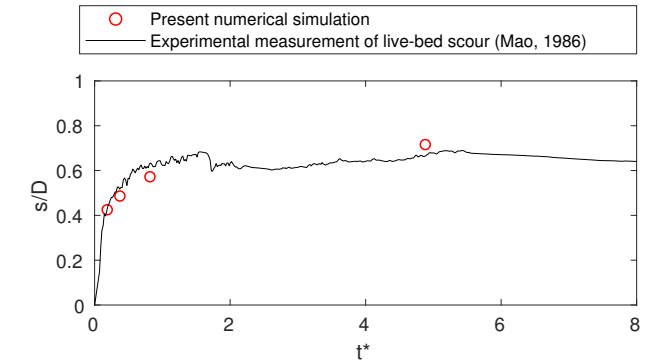

(a) Time series.

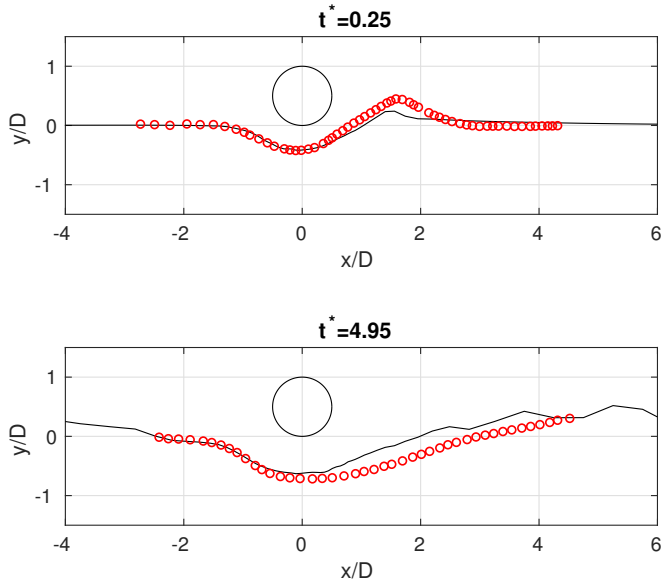

(b) Scour profiles.

Figure 6.6 Comparison of the present numerical results of scour depth development in the live-bed regime to the experimental data of Mao (1986), with $\theta = 0.098$ for both the experiment and the present simulation.

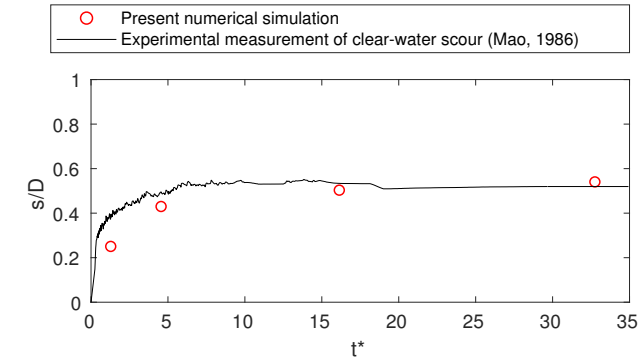

(a) Time series.

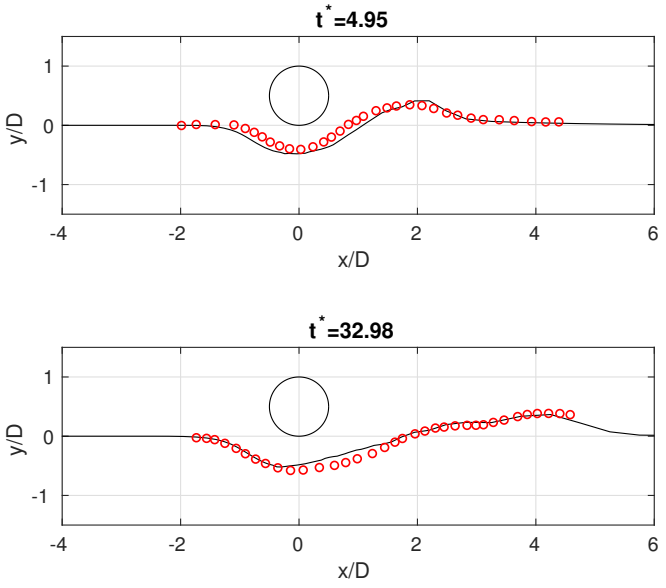

(b) Scour profiles.

Figure 6.7 Comparison of the present numerical results of scour depth development in the clear-water regime to the experimental data of Mao (1986), with $\theta = 0.048$ for both the experiment and the present simulation.

for the porous seabed consisting of fine sand where the kinetic energy of the seepage flow is insignificant and the seepage flow is within the laminar region (Cheng and Chiew, 1999). In the present study, fine sand with a grain size of 0.19 mm and a permeability K of 0.001 m/s is considered. Darcy's law is applied for the relationship between i and v_s.

Meanwhile, in the presence of various levels of i/i_c, the desired friction velocity at the bed (Eqn. 6.4), the critical Shields parameter (Eqn. 6.17) and the angle of repose (Eqn. 6.27) are changed when subjected to upward seepage. The parameters in the present numerical cases are presented in Table 6.1.

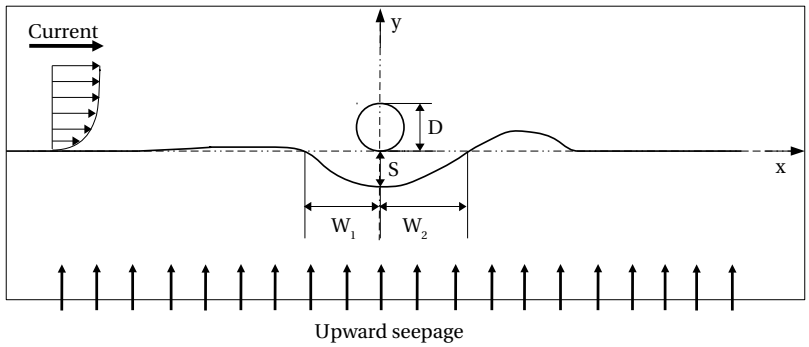

Figure 6.8 Layout of the present numerical simulations of scour beneath a pipeline in current and upward seepage.

According to Eqn. 6.17, with the upward seepage, the critical Shields parameter will be reduced. In certain circumstances, as the upward seepage increases, the initial clear-water condition may turn to a live-bed condition, such as clear-water cases with $i/i_c = 0.4$ to 0.9 in Table 6.1, i.e., the far-field Shields parameter exceeds the critical Shields parameter. The far-field θ and critical Shields parameter θ_{cr0} for live-bed cases and clear-water cases are plotted in Figure 6.9a and 6.9b, respectively. For the clear-water cases with $i/i_c = 0.2$ and 0.3, θ is just slightly higher than θ_{cr0}. These two cases are still

Table 6.1 Parameters in the present simulations for the live-bed scour and the clear-water scour with upward hydraulic gradients

i/i_c	0	0.1	0.2	0.3	0.4	0.5	0.6	0.7	0.8	0.9
$v_s = Ki$ cm/s	0	0.0099	0.0198	0.0297	0.0396	0.0495	0.0594	0.0693	0.0792	0.0891
Live-bed cases										
Desired u_f m/s	0.0174	0.0169	0.0165	0.016	0.0156	0.0151	0.0147	0.0142	0.0138	0.0133
Far-field θ	0.098	0.093	0.0881	0.0833	0.0787	0.0742	0.0698	0.0655	0.0614	0.0575
Repose angle ϕ_s	34	31.82	29.64	27.45	25.25	23.04	20.81	18.56	16.29	13.99
θ_{cr0}	0.045	0.0405	0.036	0.0315	0.027	0.0225	0.018	0.0135	0.009	0.0045
Clear-water cases										
Desired u_f m/s	0.0122	0.0117	0.0113	0.0108	0.0103	0.0099	0.0094	0.0090	0.0085	0.0081
Far-field θ	0.048	0.0445	0.0411	0.0379	0.0348	0.0318	0.0290	0.0263	0.0237	0.0212
Repose angle ϕ_s	34	31.82	29.64	27.45	25.25	23.04	20.81	18.56	16.29	13.99
θ_{cr0}	0.05	0.045	0.04	0.035	0.03	0.025	0.02	0.015	0.01	0.005

resembling clear-water cases. In the present work, although some of the clear-water cases subjected to large upward hydraulic gradients have transformed to the live-bed regime, they are discussed within the clear-water regime in the present study in order to compare with the initial condition without the seepage effect. This regime change is, in fact, a potentially important effect of seepage.

To simulate an accurate flow field in the parametric studies with different upward seepage velocities, first, the 1DV simulation driven by the body force is computed to generate a fully developed velocity boundary layer profile without seepage. Second, in the 2D simulations of scour beneath a submarine pipeline, a Dirichlet boundary is specified with time-varying u, k and ω, taken from the preliminary 1DV simulations. The morphology is switched off to run the pure flow for a duration of $t = 20L/u$ until the flow propagating in the whole domain reaches equilibrium. Here, L is the domain length and u is

the free stream velocity at the pipeline center. At the third step, the upward seepage velocity v_s is added at the bottom boundary to run the pure flow for another $t = 20L/u$. Finally, when the flow field is well-developed, the morphology is switched on and the scour hole begins to develop.

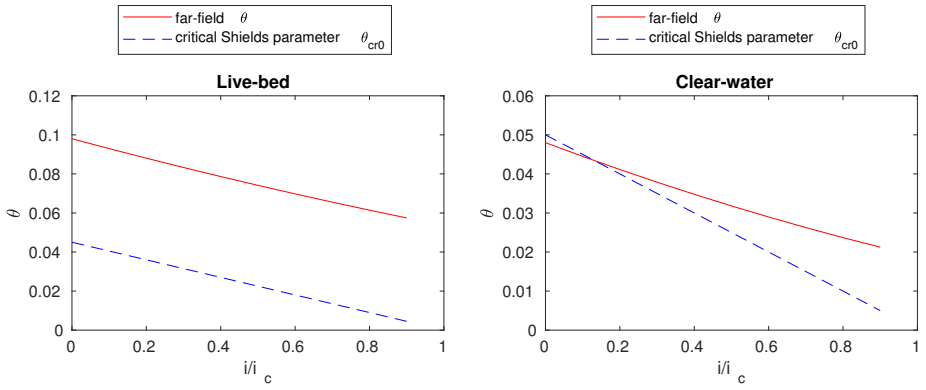

(a) (b)

Figure 6.9 Far-field θ and critical Shields parameter θ_{cr0}.

6.1.4.1 Live-bed scour with upward seepage

For live-bed cases with upward seepage, the time series of the non-dimensional scour depth S/D beneath the center of the pipeline and the scour profiles at the equilibrium stages are presented in Figure 6.10. It is seen in Figure 6.10a and Figure 6.10b that with small and medium upward hydraulic gradients, i.e., $i/i_c = 0.1 - 0.6$, the patterns of the time series curves S/D are very similar to that with $i/i_c = 0$. The time it takes to reach the equilibrium status is almost the same among the cases with $i/i_c = 0.1 - 0.6$. After reaching the equilibrium stage, the scour profiles with upward seepage have slightly larger depths below the center of the pipeline compared to those without upward seepage. Also, larger scour widths are observed both upstream and downstream of the pipeline. Figure 6.10c shows the time series and scour profiles with large upward hydraulic gradients, i.e., $i/i_c = 0.7 - 0.9$. It is seen in the left column

of Figure 6.10c that during the early stage of the scour development, the cases with a larger i/i_c have an obviously smaller S/D. However, after reaching equilibrium, the scour depths with $i/i_c = 0.7 – 0.9$ reach a similar value as with $i/i_c = 0$.

The equilibrium scour depth and scour width are calculated based on data of 180 s time duration in the equilibrium stage (non-dimensional time duration $t^* = 2.1$). The average upstream scour width W_1/D and the downstream scour width W_2/D are calculated and the total scour width is calculated as $W_e/D = \frac{W_1+W_2}{D}$. W_1 and W_2 are the horizontal distances from the center of the pipeline to the end of the scour hole, as shown in Figure 6.8. The equilibrium scour depths with i/i_c from 0 to 0.9 are shown in Figure 6.11a and the equilibrium scour widths are shown in Figure 6.11b. It is observed that with upward hydraulic gradients, the equilibrium scour depths in the live-bed regime are still distributed in the range of $S_e/D = 0.6$ to 0.8 (in the live-bed regime without the upward seepage, the empirical relation is $S_e/D = 0.6 \pm 0.2$ (Sumer and Fredsøe, 2002)). Figure 6.11b shows that with small and medium upward hydraulic gradients, i.e., $i/i_c = 0.1 – 0.6$, the total scour widths are similar and are only slightly larger than that with $i/i_c = 0$. As the upward hydraulic gradient increases from 0.7 to 0.9, the scour width increases dramatically. As also seen in the scour profile in Figure 6.10c, the final scour profile has a much wider and milder slope because of the decrease of the repose angle in a large upward hydraulic gradient. It is also observed in Figure 6.11b that, as i/i_c increases, the upstream scour width W_1/D generally increases. W_1/D is smaller than W_2/D with small i/i_c but is almost the same as W_2/D with large i/i_c.

6.1.4.2 Clear-water scour with upward seepage

For the clear-water cases with the upward seepage, the time series of S/D beneath the center of the pipeline and the scour profiles at the equilibrium stages are presented in Figure 6.12. It is shown that with a relatively small

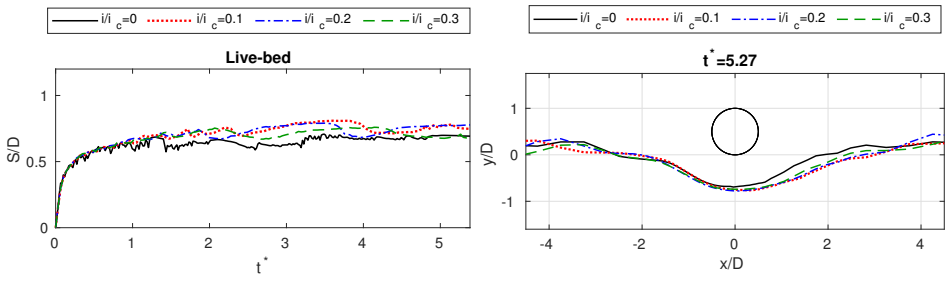

(a)

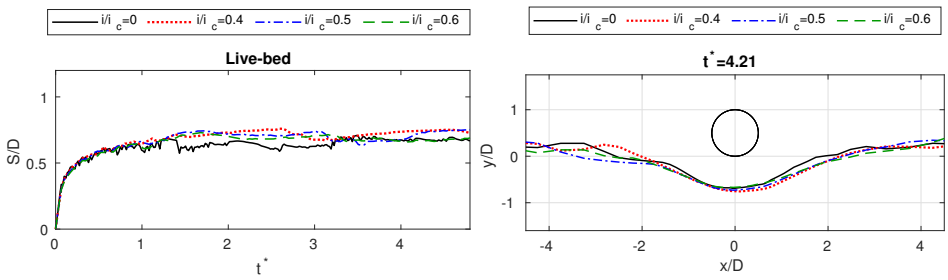

(b)

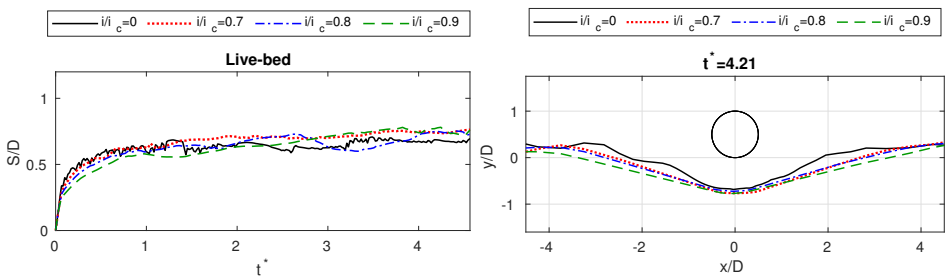

(c)

Figure 6.10 Numerical results of scour depth development and scour profiles for the live-bed scour with upward hydraulic gradients.

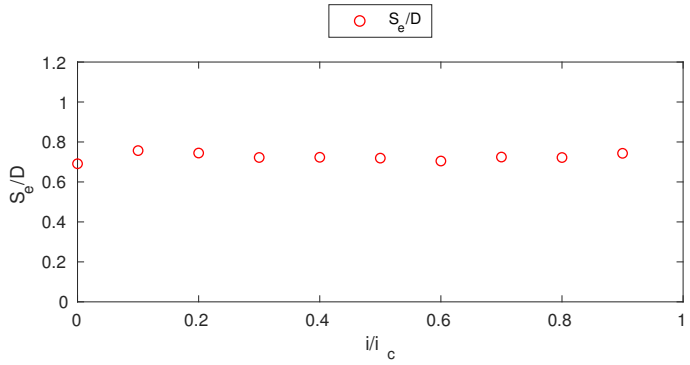

(a) Equilibrium scour depth with upward hydraulic gradients in the live-bed regime.

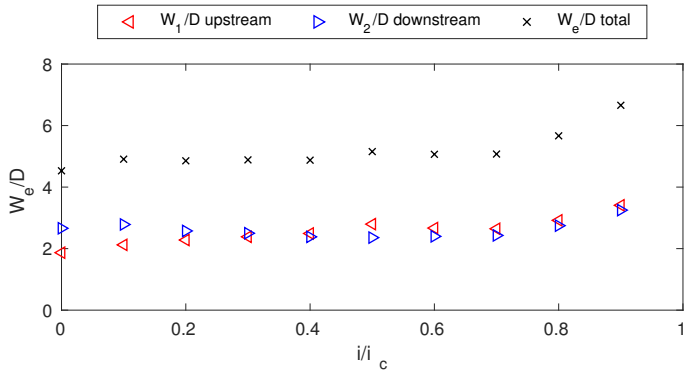

(b) Equilibrium scour width with upward hydraulic gradients in the live-bed regime. .

Figure 6.11 Equilibrium scour depth and width with upward hydraulic gradients in the live-bed regime.

i/i_c, i.e., $i/i_c = 0.1 - 0.4$, the S/D after reaching equilibrium is slightly larger than that with $i/i_c = 0$. However, with $i/i_c = 0.5 - 0.9$, the S/D after reaching equilibrium is smaller than that with $i/i_c = 0$. As i/i_c increases from 0.5 to 0.9, S/D decreases. It is observed in the scour profiles in Figure 6.12c that with $i/i_c = 0.7 - 0.9$, the location of maximum scour moves slightly upstream with larger upward hydraulic gradients. Figure 6.13a shows the equilibrium scour depth S_e/D beneath the center of the pipeline and also the maximum S_e/D beneath the pipeline. It appears that both S_e/D beneath the center of the pipeline and the maximum S_e/D decrease as i/i_c increases from 0.4 to 0.9. As i/i_c increases, the location of the maximum S_e/D moves more upstream so that the difference between the S_e/D beneath the center of the pipeline and the maximum S_e/D increases. This is because the far-field Shields parameter is small for the original clear-water case. With a large upward hydraulic gradient, the bed friction velocity becomes even smaller. Therefore, the downstream sediment cannot be washed away from the scour hole.

Figure 6.14 shows a comparison of the near-bed velocity field between the live-bed case and the clear-water case with $i/i_c = 0.9$. It is seen that at a relatively early stage of scour development ($t^* = 1.74$ for the live-bed case and $t^* = 3.74$ for the clear-water case), both the live-bed and the clear-water cases have a maximum scour depth slightly upstream of the pipeline center. This is due to the reduced repose angle with $i/i_c = 0.9$ so that sediments downstream slide down into the scour hole. However, since the live-bed case has a relatively high bed friction velocity, the downstream sediments are eventually washed away and the maximum scour depth moves to below the center of the pipeline. The vertical profiles of the horizontal velocity close to the seabed at $x/D = 2.67$ for the live-bed and the clear-water cases with $i/i_c = 0.9$ are compared in Figure 6.15. It is seen in both Figure 6.14b and Figure 6.15 that the bed-friction velocity for the clear-water case with $i/i_c = 0.9$ is so small compared to the live-bed case that it is not capable

of transporting sediments upward along the downstream slope out from the scour hole.

The equilibrium scour widths for the clear-water cases with upward hydraulic gradients are presented in Figure 6.13b. Similar to the live-bed cases, the scour widths for the clear-water cases with small and medium upward hydraulic gradients ($i/i_c = 0.1 - 0.6$) are similar with a slightly increasing trend. As the upward hydraulic gradient increases from 0.6 to 0.9, the scour width has an obvious increasing trend. The upstream scour width generally increases with i/i_c, while the downstream scour width remains almost the same.

6.1.5 Conclusions

The present study has proposed a numerical model of scour beneath subsea structures considering the upward seepage effect in the seabed. Subjected to upward seepage, the bed friction velocity and the bed shear stress are changed. Meanwhile, the threshold of incipient sediment motion, i.e., the critical Shields parameter and the angle of repose of the sand particles are both reduced. To validate the present numerical model, first, the boundary layer velocity profile subjected to upward seepage has been validated against the experiments of Cheng and Chiew (1998) and Dey and Nath (2009). Good agreement has been achieved. Then, the fully-coupled hydrodynamic and morphologic scour model has been validated against the live-bed scour and clear-water scour experiments of Mao (1986). The present scour model has provided reasonably accurate predictions to the scour depths and the scour profiles.

The validated numerical model has then been applied to investigate the scour beneath a submarine pipeline in the presence of upward seepage. The investigations have been based on the numerical cases of scour without seepage effects, i.e., the live-bed scour and the clear-water scour of Mao (1986). Nine levels of upward hydraulic gradients ($i/i_c = 0.1 - 0.9$) have been

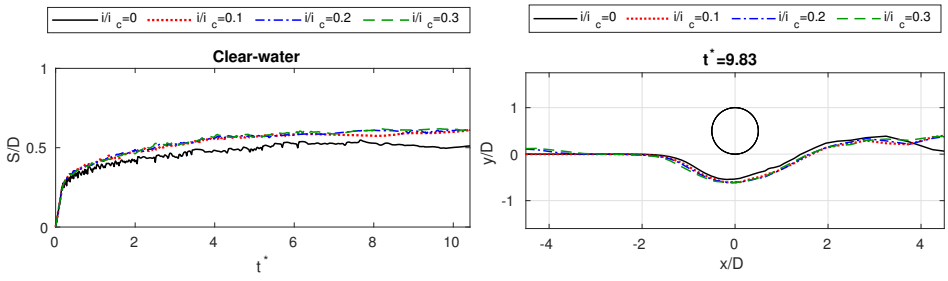

(a)

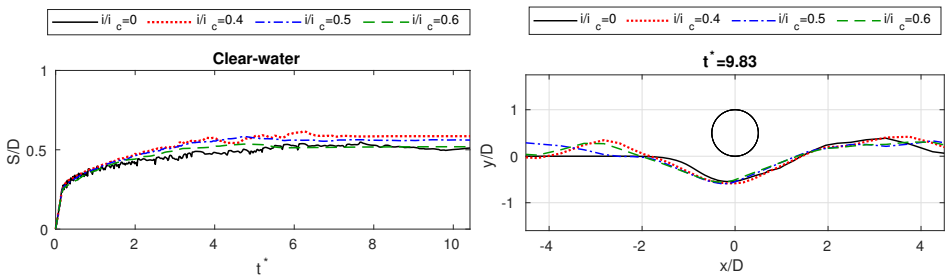

(b)

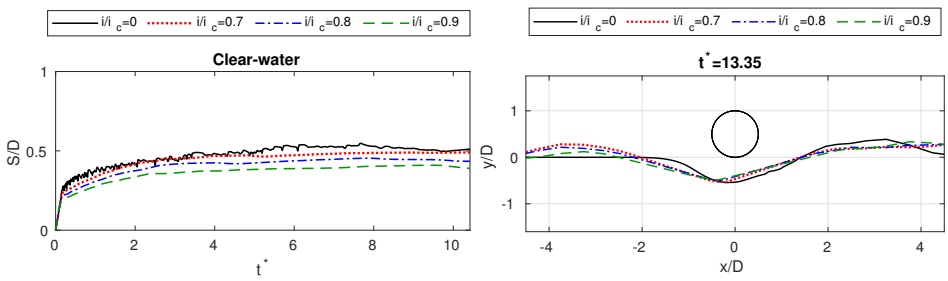

(c)

Figure 6.12 Numerical results of scour depth development and scour profiles for the clear-water scour with upward hydraulic gradients.

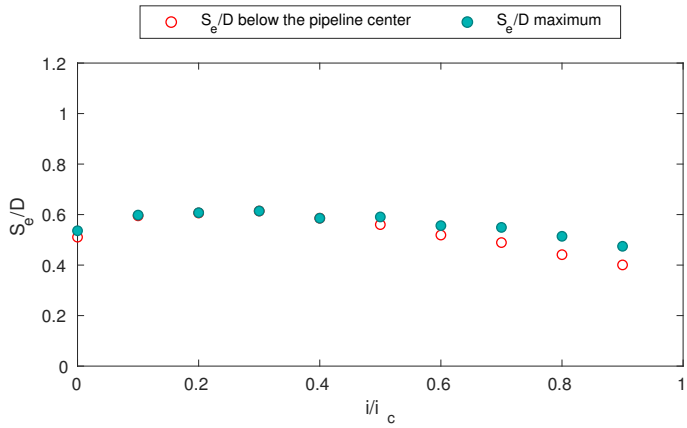

(a) Equilibrium scour depth with upward hydraulic gradients in the clear-water regime.

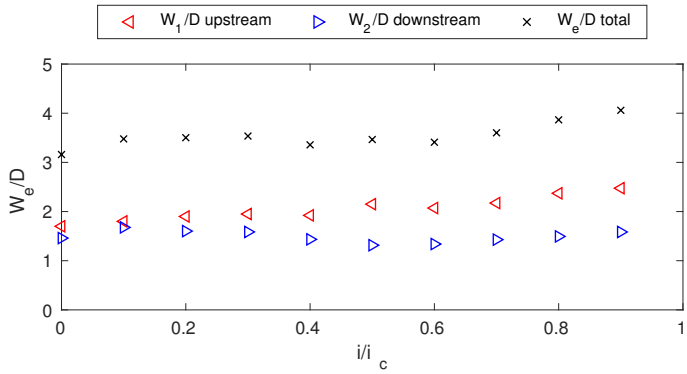

(b) Equilibrium scour width with upward hydraulic gradients in the clear-water regime.

Figure 6.13 Equilibrium scour depth and width with upward hydraulic gradients in the clear-water regime.

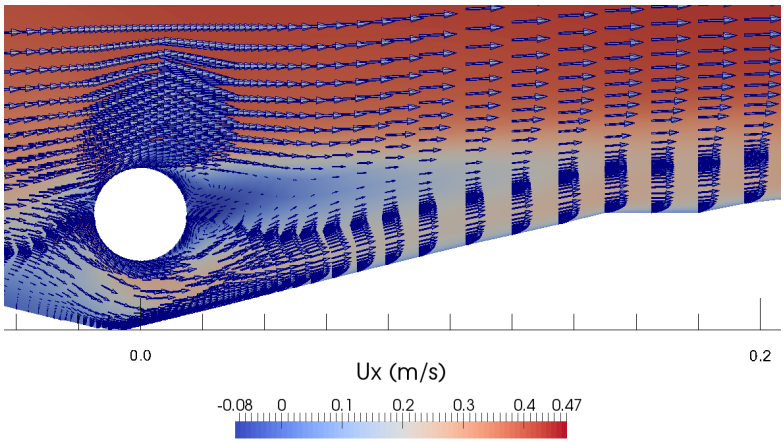

(a) Horizontal velocity field of the live-bed case with $i/i_c = 0.9$ ($t^* = 1.74$).

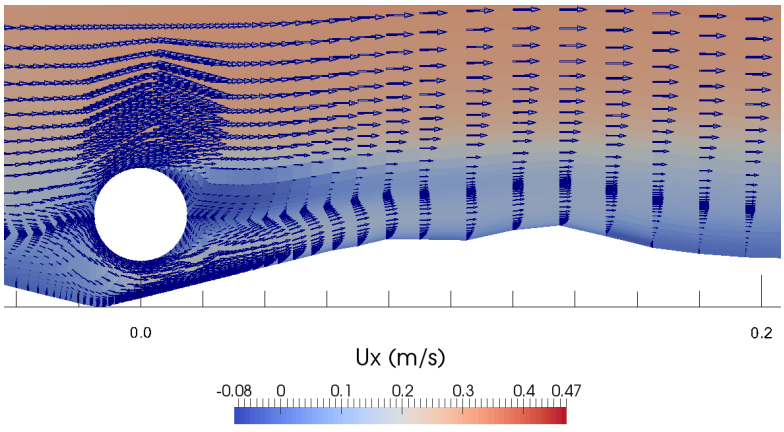

(b) Horizontal velocity field of the clear-water case with $i/i_c = 0.9$ ($t^* = 3.54$).

Figure 6.14 Horizontal velocity field of cases with $i/i_c = 0.9$.

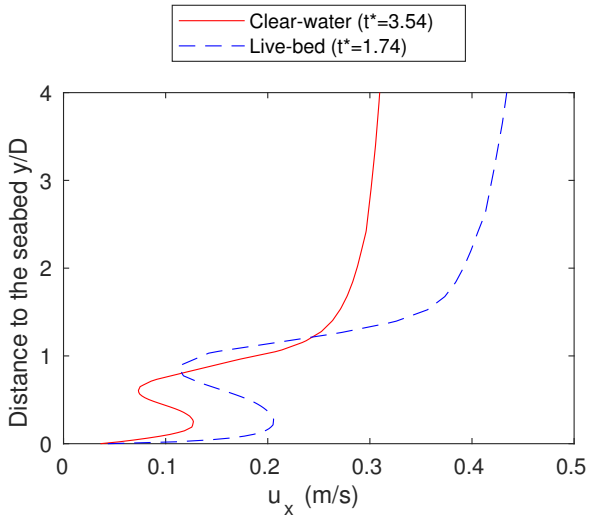

Figure 6.15 Vertical distributions of the horizontal velocity near the seabed with $i/i_c = 0.9$ at $x = 0.08$ m ($x/D = 2.67$).

applied to the live-bed scour case and the clear-water scour case, respectively. The following conclusions can be drawn from the present study:

1. For the live-bed case in the present work, with upward hydraulic gradients $i/i_c = 0.1 - 0.9$, it is observed that the equilibrium scour depths are in the range of $S/D = 0.6 - 0.8$. During the initial stage of scour development, the scour depths with large upward hydraulic gradients, i.e., $i/i_c = 0.7 - 0.9$, are smaller than that with $i/i_c = 0$. However, after reaching equilibrium, the scour depths with $i/i_c = 0.7 - 0.9$ reach similar values as with $i/i_c = 0$. For small and medium upward hydraulic gradients, i.e., $i/i_c = 0.1 - 0.6$, the scour widths are similar, and are only slightly larger than with $i/i_c = 0$. As the upward hydraulic gradient increases from 0.7 to 0.9, the scour width increases more dramatically.

2. For the clear-water case in the present work, as the upward hydraulic gradient increases, the initial clear-water condition may turn into a live-bed condition, i.e., the far-field Shields parameter exceeds the critical Shields parameter, such as clear-water cases with $i/i_c = 0.4$ to 0.9 in the present study.

It appears that the equilibrium scour depth decreases as i/i_c increases from 0.4 to 0.9. As i/i_c becomes higher, the location of the maximum S_e/D moves upstream of the pipeline center. For the clear-water cases with large upward hydraulic gradients, the equilibrium scour width increases with i/i_c. The upstream scour width increases with i/i_c, while the downstream scour width remains almost the same. Therefore, the total scour width W_e/D generally increases.

3. A general finding is that with upward seepage, the scour depth beneath the submarine pipeline may either increase or decrease, or remain similar in value. The scour width remains similar with small and medium hydraulic gradients and significantly increases with the existence of large upward hydraulic gradients.

It is noted that in the present parametric study, the relation between i and v_s is based on a linear assumption. Also, for sediment particles with different properties, the empirical coefficient C_s for predicting the angle of repose subjected to upward seepage may differ. Nevertheless, the present numerical model, in terms of modeling the incoming flow velocity profile subjected to upward seepage and modeling the hydrodynamic- and morphologic- coupled scour beneath a submarine pipeline, has been validated. Therefore, it seems capable of providing practical predictions for engineering problems based on reasonable assumptions and parameters.

Acknowledgment

This study was supported in part with computational resources provided by the Norwegian Metacenter for Computational Science (NOTUR), under Project No: NN9372K. The PhD project was financed by the Statoil Akademia program at the University of Stavanger.

Chapter 7

Conclusion and recommendations for further work

7.1 Conclusions

Momentary liquefaction and scour are two mechanisms that have been addressed in this PhD study. Both mechanisms are related to the interaction between water, structure and sediments. The mechanisms of momentary liquefaction is associated with the seepage induced by waves in the porous seabed. The mechanisms of scour is associated with sediment transport processes in the vicinity of marine structures in waves and current. Considering both the seepage in the seabed and the sediment transport at the bed surface, the present PhD study has proposed a numerical model to couple the scouring process with the continuous upward seepage in the seabed. The conclusions of this PhD work will be presented in a way of answering the research questions that have been raised in Section 2.3.

A1-Q1 For liquefaction analysis, an integrated model of wave-induced soil response around offshore foundations and coastal structures has been developed within the finite volume method (FVM) based OpenFOAM®

framework. The model consists of a consolidation analysis model, a WSSI analysis model, and a momentary liquefaction analysis module. First, the poro-elastic soil model in the quasi-static form developed by Tang et al. (2015) has been incorporated in the integrated WSSI model. The soil model has been validated in the present work against the experiment of standing waves induced pore pressure in the sand bed below a vertical wall (Tsai and Lee, 1995). Grid convergence study has also been performed to verify the numerical soil model. Recently, Qi and Gao (2014) performed a series of experiments to investigate the local scour and pore pressure in the seabed around a large-diameter monopile in the conditions of waves, current and combined waves and current. Their experimental data of wave-induced pore pressure in the soil around the monopile has been used in this PhD work to validate the wave-structure-seabed interaction model with a newly implemented partial-dynamic poro-elastic soil model ($u-p$ model). Good agreement has been obtained for both wave modeling and the soil response modeling around the structure.

A2-Q2 In fact, some of the previous studies of wave-induced soil response around monopiles did not perform a consolidation analysis. This is justifiable because monopile foundations are usually cylindrical hollow tubes which are driven into the seabed by stream or hydraulic powered hammers. Therefore, there is no much compression in soil volume under the bottom of the monopile since it is penetrate trough the soil instead of being laid on the seabed. However, the gravity-based structures are usually placed on the seabed surface with a large contact interface. Due to the presence of the gravity-based structure, the underneath soil will be compressed and experience the gradual dissipation of the excess pore pressure induced by the gravitational force from the structure. The initial state (i.e., initial effective stress and displacement) of the surrounding soil has been changed. Therefore, consolidation

analysis is essential in order to predict the liquefaction risk around gravity-based structures. In the present PhD study, the investigation of wave-induced soil response around gravity-based foundations began with the consolidation analysis, in order to check the initial vertical effective stress in the soil after the foundation is built on the seabed. Then, the WSSI analysis was performed to investigate the wave-induced seabed response around the structure. Finally, liquefaction assessment was performed based on the initial vertical effective stress from the consolidation analysis and the excess pore pressure / vertical effective stress from the WSSI analysis.

A3-Q3 The presence of the gravity-based foundations on the seabed leads to compression of the soil in the vicinity of the structure during the consolidation process. The initial vertical effective stress in the surrounding soil is increased. The slab geometry of the foundation affects the initial effective stress distribution. For the circular foundation, the initial vertical effective stress is evenly distributed in the surrounding soil. However, for the hexagonal foundation, the geometry triggers stress concentration in the soil around the corners. The compressive stress at the corners is much higher than that at the edges. For the circular foundation, the liquefaction depth is approximately distributed averagely around the circular foundation, except that the upstream side has a sightly higher liquefaction depth than the downstream side. For the hexagonal foundations, the distribution of the initial soil effective stress from the consolidation process affect the liquefaction zone distribution. The momentary liquefaction is less likely to happen around the hexagon corners due to high initial vertical effective stress. Wave direction also affects the pore pressure and the liquefaction distribution around the hexagonal foundation. Waves propagate towards the hexagon corner and towards the hexagon edge can trigger different liquefaction distribution. In the real ocean environment, the waves are nonuniform and

non-unidirectional, so that both the corners and edges of the hexagonal foundation can experience liquefaction and therefore need liquefaction protections.

A4-Q4 This PhD work has applied the finite volume wave-structure-seabed interaction toolbox to numerically investigate the wave-induced soil response and the liquefaction probability around rubble mound breakwaters with submerged berms. A parametric study has been carried out with various berm configurations (i.e. the berm height and the berm length). For all the tested configurations, the effects of the consolidation process on the wave-induced soil response, have been taken into account. Results indicate that the presence of submerged berms tends to mitigate the momentary liquefaction occurrences compared to the case of a straight sloped conventional breakwater without a berm. In addition, it appears that the momentary liquefaction phenomena are more influenced by changing the berm length rather than the berm height. The most effective momentary liquefaction attenuation is given by long berms with an intermediate height within the considered range.

A5-Q5 Three forms of the Biot's poro-elastic model were discussed in the previous work, in terms of the quasi-static form, the partial dynamic form (i.e., the $u-p$ formulation), and the fully dynamic form. The difference between the forms is based on the consideration of including inertial terms associated with the motion of fluids and solids. The partial-dynamic model considers the acceleration of the soil and neglects the pore fluid acceleration relative to the solid phase, in order to reduce the computational effort compared to the fully dynamic form and provide better accuracy than the quasi-static form. The present PhD study found that the predicted excess pore pressure by the $u-p$ model was relatively higher than that by the quasi-static model and matched better with the experimental results. The quasi-static form showed an underestimation of the wave-induced soil response around

structures. Therefore, it is recommend to use $u-p$ model for predicting the wave-induced soil response in a more accurate and efficient way for engineering problems. Two liquefaction criteria based on the effective stress and based on the excess pore pressure, respectively, have been implemented. For 1D quasi-static Biot's model, the criterion based on the excess pore pressure and that based on the vertical effective stress should lead to the same result (Sumer, 2014a), since the vertical effective stress $\sigma_z^{'}$ is theoretically the same as $p-p_b$ due to the force balance in the vertical direction. However, for 3D problems with considering the inertia force of the soil skeleton, the two criteria will lead to different assessment results. It has been observed in the present work that the criteria based on the excess pore pressure provides more conservative solutions for evaluating the liquefaction risk around 3D gravity-based offshore foundations.

A6-Q6 The present study has investigated the local scour beneath two pipelines in tandem in the wave-plus-current conditions. A fully-coupled hydrodynamic and morphologic numerical model based on unsteady Reynolds-averaged Navier-Stokes (URANS) equations with k-ω turbulence closure has been applied. The scour profiles, scour time series and the equilibrium scour depths have been studied for two pipelines in tandem, with horizontal gap ratios between the too pipelines ranging from 1 to 4, coupled with various Keuleagan–Carpenter number KC and relative current strengths m. It has been found that the effect of KC on the scour beneath two pipelines is dominant when the current strength is low ($m = 0$ and 0.25) and the horizontal gap ratio is high ($G/D \geq 3$). When KC is small, e.g. $KC = 5.6$, vortex shedding does not occur because the wave period is small and the flows change direction prior to vortices being shed. Therefore, the horizontal gap ratio has a less significant influence on the equilibrium scour depth. With the relative current strength is 0.5, KC has insignificant effect on the scour

depth and the results tend to be similar to those in the pure-current conditions. For the effect of the horizontal gap ratio, G/D, the present study has found that in pure-waves, when $G/D = 1$ the vortex shedding behind the upstream pipeline is suppressed, except for $KC = 5.6$, where vortex shedding does not occur. As the horizontal gap ratio increases, the two pipelines become more independent and essentially separate scour holes beneath each pipeline are formed.

A7-Q7 The seepage velocity inside the porous seabed is usually small compared to the free-stream velocity, so that it can have a minor effect to the free-stream velocity field. However, the small seepage can have a significant change to the hydrodynamic force on the bed surface. The bed friction velocity and the bed shear stress are changed. Meanwhile, upward seepage can also affect the stability of the sand particles on the seabed so that the threshold of incipient sediment motion, i.e., the critical Shields parameter, is also changed. Due to the decrease of submerged weight of the sand particles, the angle of repose of the sand particles is also reduced. Therefore, the process of sediment transport and the further scour pattern can be largely affected. The present PhD study has proposed a numerical model of scour beneath subsea structures with considering the upward seepage effect in the seabed. The present model is based on a fully-coupled hydrodynamic and morphologic model (Jacobsen, 2011; Jacobsen and Fredsoe, 2014). The following modifications have been implemented in order to couple the seepage effect with the scouring problem: 1) modification of the incoming flow structure near the seabed; 2) modification of the critical Shields parameter of sand particles on the seabed; 3) modification of the bed load transport model; 4) modification of the repose angle of the sediments. To validate the present numerical model, first, the boundary layer velocity profile subjected to upward seepage has been validated against the existing experiments. Then, the fully-coupled

hydrodynamic and morphologic scour model has been validated against existing experiments of the scour beneath a pipeline. Good agreement has been achieved.

A8-Q8 The validated numerical model has then been applied to investigate the scour beneath a submarine pipeline in the presence of upward seepage. It has been found that for the live-bed cases in the present work, the equilibrium scour depths with upward hydraulic gradients are in the range of $S/D = 0.6 – 0.8$. With small and medium upward hydraulic gradients, the scour widths are only slightly larger than that without seepage. At large upward hydraulic gradients, the scour width increases more dramatically. For the clear-water case in the present work, as the upward hydraulic gradient increases, the initial clear-water condition may turn into a live-bed condition, i.e., the far-field Shields parameter exceeds the critical Shields parameter. It has been observed that with a larger upward hydraulic gradient, the equilibrium scour depth decreases and the equilibrium scour width increases. A general finding was that with upward seepage, the scour depth beneath the submarine pipeline may either increase or decrease, or remain similar in value. The scour width remains similar with small and medium hydraulic gradients and significantly increases with the existence of large upward hydraulic gradients.

7.2 Original contributions

The originality and main contributions of the present PhD work are summarized as follows:

- Applications of the wave-induced seabed response model on momentary liquefaction prediction for gravity-based offshore foundations and coastal breakwaters.

- Development of the consolidation analysis model, the partial-dynamic poro-elastic soil model in the FVM OpenFOAM framework. Development of liquefaction analysis module with different liquefaction criteria for 3D engineering problems.
- Investigation of wave-plus-current induced scour beneath two submarine pipelines in tandem.
- Development, validation and application of a CFD model for predicting scour beneath marine structures including the effect of upward seepage in the seabed.

7.3 Recommendations for further work

- The soil models for wave-seabed interactions in existing works have been built based on the constitutive models developed for onshore geotechnical engineering. Most studies have been performed based on Biot's (1941) consolidation model. In fact, the seabed is under seawater and subjected to complicated environmental loads such as waves, current and seismic loadings. To date, an appropriate seabed constitutive model for marine geotechnical engineering is not yet available in the public literature. Whether the constitutive relations for onshore can be applied to offshore environment remains to be investigated.
- The present PhD work modeled the interaction of waves, structure and the seabed in a one-way coupling approach, by assuming the seabed soil is stiff enough to support the structure in place during the simulation. Most previous studies for wave-structure-seabed interaction have also been limited to uncoupled approach or semi-coupled approach, rather than a fully-coupled approach. In fact, as the seabed deformed under environmental loading, it will affect the wave field and environmental loading in return. Under circumstances such as complete liquefaction

failures and large deformations, the soil can no longer sustain the structure and the structure will move significantly. Therefore, a fully-coupled model with strong two-way interaction of wave-structure-soil system is necessary to be developed in future.

- For scouring problems, a gap still exists between research works and engineering practice. The existing laboratory experiments and numerical studies have been conducted with uniform, fine sediment and simplified environmental loads. However, in the real environment, the environmental impact is highly unsteady, non-uniform and from multiple directions. Therefore, transforming theoretical, numerical and experimental findings to a real environment is a major remaining problem.

- 2D scour around marine pipelines have been studied extensively in both exiting works and the present work. 2D experiments and modeling can provide good and reasonable predictions of scour pattern below the pipeline. However, the actual scour pattern contains 3D features. To date, very limited numerical studies have been carried on 3D scour along pipelines due to the complexity of flow pattern and numerical mesh handling in FEM or FVM frameworks. Numerical modeling and investigations of 3D development of scour around the pipeline can be carried out in future work.

- The present PhD work proposed the first numerical model for coupling scour and upward seepage in the seabed. However, the seepage in the present work has been simplified as uniform and unidirectional, while the wave-induced seepage flows in the seabed will have time-varying directions and magnitudes. Further work of considering wave-induced time-varying seepage effect in the seabed is recommended.

References

Alabart, J., Sanchez-Arcilla, A., and Van Vledder, G. P. (2014). Analysis of the performance of swash in harbour domains. In *Proceedings of the 3rd IAHR Europe congress, 1-10.(2014), Porto, Portugal*. IHAR.

Baykal, C., Sumer, B. M., Fuhrman, D. R., Jacobsen, N. G., and Fredsøe, J. (2015). Numerical investigation of flow and scour around a vertical circular cylinder. *Philosophical Transactions of the Royal Society A: Mathematical, Physical and Engineering Sciences*, 373(2033):20140104.

Bayraktar, D., Ahmad, J., Larsen, B. E., Carstensen, S., and Fuhrman, D. R. (2016). Experimental and numerical study of wave-induced backfilling beneath submarine pipelines. *Coastal Engineering*, 118:63–75.

Bear, J. (2013). *Dynamics of fluids in porous media*. Courier Corporation.

Berberović, E., van Hinsberg, N. P., Jakirlić, S., Roisman, I. V., and Tropea, C. (2009). Drop impact onto a liquid layer of finite thickness: Dynamics of the cavity evolution. *Physical Review E*, 79(3):036306.

Bernetti, R., Bruschi, R., Valentini, V., and Venturi, M. (1990). Pipelines placed on erodible seabeds. In *Proceedings of the 9th International Conference on Offshore Mechanical and Arctic Engineering (OMAE), New York*, page 155–164. American Society of Mechanical Engineers.

Biot, M. A. (1941). General theory of three-dimensional consolidation. *Journal of applied physics*, 12(2):155–164.

Biot, M. A. (1956). Theory of propagation of elastic waves in a fluid-saturated porous solid. ii. higher frequency range. *The Journal of the acoustical Society of america*, 28(2):179–191.

Brøker, I. H. (1985). Wave generated ripples and resulting sediment transport in waves. *Institute of Hydrodynamics and Hydraulic Engineering, Technical University of Denmark*, Series paper No. 36.

Brørs, B. (1999). Numerical modeling of flow and scour at pipelines. *Journal of hydraulic Engineering*, 125(5):511–523.

Cebeci, T. and Chang, K. (1978). Calculation of incompressible rough-wall boundary-layer flows. *AIAA Journal*, 16(7):730–735.

Celli, D., Li, Y., Ong, M. C., and Di Risio, M. (2019). The role of submerged berms on the momentary liquefaction around conventional rubble mound breakwaters. *Applied Ocean Research*, 85:1–11.

Celli, D., Pasquali, D., De Girolamo, P., and Di Risio, M. (2018). Effects of submerged berms on the stability of conventional rubble mound breakwaters. *Coastal Engineering*, 136:16 – 25.

Chang, K.-T. and Jeng, D.-S. (2014). Numerical study for wave-induced seabed response around offshore wind turbine foundation in donghai offshore wind farm, shanghai, china. *Ocean Engineering*, 85:32–43.

Chao, J. and Hennessy, P. (1972). Local scour under ocean outfall pipelines. *Journal (Water Pollution Control Federation)*, pages 1443–1447.

Chen, B. and Cheng, L. (2001). Three-dimensional modelling of flow around a free-spanned pipeline. In *Proceedings of the First Asian and Pacific Coastal Engineering Conference*, pages 721–730.

Chen, B. and Cheng, L. (2004). Numerical investigation of three-dimensional flow and bed shear stress distribution around the span shoulder of pipeline. *Journal of Hydrodynamics*, 16(6):687–694.

Chen, L., Zang, J., Hillis, A., Morgan, G., and Plummer, A. (2014). Numerical investigation of wave–structure interaction using openfoam. *Ocean Engineering*, 88:91–109.

Cheng, L., Yeow, K., Zang, Z., and Li, F. (2014). 3d scour below pipelines under waves and combined waves and currents. *Coastal engineering*, 83:137–149.

Cheng, L., Yeow, K., Zhang, Z., and Teng, B. (2009). Three-dimensional scour below offshore pipelines in steady currents. *Coastal Engineering*, 56(5-6):577–590.

Cheng, L. and Zhao, M. (2010). Numerical model for three-dimensional scour below a pipeline in steady currents. In *Proceedings 5th International*

Conference on Scour and Erosion (ICSE-5), November 7-10, 2010, San Francisco, USA, pages 482–490.

Cheng, N.-S. and Chiew, Y.-M. (1998). Modified logarithmic law for velocity distribution subjected to upward seepage. *Journal of Hydraulic Engineering*, 124(12):1235–1241.

Cheng, N.-S. and Chiew, Y.-M. (1999). Incipient sediment motion with upward seepage. *Journal of Hydraulic Research*, 37(5):665–681.

Chiew, Y.-M. (1990). Mechanics of local scour around submarine pipelines. *Journal of Hydraulic Engineering*, 116(4):515–529.

Chiew, Y.-M. (1991). Prediction of maximum scour depth at submarine pipelines. *Journal of Hydraulic Engineering*, 117(4):452–466.

Chiew, Y.-M. and Parker, G. (1994). Incipient sediment motion on non-horizontal slopes. *Journal of Hydraulic Research*, 32(5):649–660.

Chowdhury, B., Dasari, G., and Nogami, T. (2006). Laboratory study of liquefaction due to wave–seabed interaction. *Journal of geotechnical and geoenvironmental engineering*, 132(7):842–851.

Chung, S., Kim, S., Kang, Y., Im, J., and Nagendra Prasad, K. (2006). Failure of a breakwater founded on a thick normally consolidated clay layer. *Geotechnique*, 56(6):393–409.

CIRIA/CUR/CETMEF (2007). *The Rock Manual: The use of rock in hydraulic engineering*, volume 683. Ciria.

Dean, R. G. (1965). Stream function representation of nonlinear ocean waves. *Journal of Geophysical Research*, 70(18):4561–4572.

Demirdžić, I., Horman, I., and Martinović, D. (2000). Finite volume analysis of stress and deformation in hygro-thermo-elastic orthotropic body. *Computer methods in applied mechanics and engineering*, 190(8):1221–1232.

Demirdžić, I. and Martinović, D. (1993). Finite volume method for thermo-elasto-plastic stress analysis. *Computer Methods in Applied Mechanics and Engineering*, 109(3):331–349.

Demirdžić, I. and Muzaferija, S. (1994). Finite volume method for stress analysis in complex domains. *International Journal for Numerical Methods in Engineering*, 37(21):3751–3766.

Dey, S. and Nath, T. K. (2009). Turbulence characteristics in flows subjected to boundary injection and suction. *Journal of Engineering Mechanics*, 136(7):877–888.

Dey, S. and Singh, N. P. (2007). Clear-water scour depth below underwater pipelines. *Journal of Hydro-Environment Research*, 1(2):157–162.

Di Risio, M., Lisi, I., Beltrami, G., and De Girolamo, P. (2010). Physical modeling of the cross-shore short-term evolution of protected and unprotected beach nourishments. *Ocean Engineering*, 37(8):777 – 789.

Elsafti, H. and Oumeraci, H. (2016a). A numerical hydro-geotechnical model for marine gravity structures. *Computers and Geotechnics*, 79:105–129.

Elsafti, H. and Oumeraci, H. (2016b). A numerical hydro-geotechnical model for marine gravity structures. *Computers and Geotechnics*, 79:105 – 129.

Elsafti, H. and Oumeraci, H. (2017). Analysis and classification of stepwise failure of monolithic breakwaters. *Coastal Engineering*, 121:221 – 239.

Engelund, F. and Fredsøe, J. (1976). A sediment transport model for straight alluvial channels. *Hydrology Research*, 7(5):293–306.

Esteban, M., Couñago, B., López-Gutiérrez, J., Negro, V., and Vellisco, F. (2015). Gravity based support structures for offshore wind turbine generators: Review of the installation process. *Ocean Engineering*, 110:281–291.

Fenton, J. (1988). The numerical solution of steady water wave problems. *Computers & Geosciences*, 14(3):357–368.

Fenton, J. D. (1985). A fifth-order stokes theory for steady waves. *Journal of waterway, port, coastal, and ocean engineering*, 111(2):216–234.

Franco, L. (1994). Vertical breakwaters: the italian experience. *Coastal Engineering*, 22(1-2):31–55.

Fredsøe, J. (2016). Pipeline–seabed interaction. *Journal of Waterway, Port, Coastal, and Ocean Engineering*, 142(6).

Fredsøe, J. and Deigaard, R. (1992). *Mechanics of Coastal Sediment Transport*, volume 3. World scientific publishing company.

Fredsoe, J., Hansen, E., Mao, Y., and Sumer, B. M. (1988). Three-dimensional scour below pipelines. *Journal of offshore mechanics and arctic engineering*, 110(4):373–379.

Fredsøe, J. and Hansen, E. A. (1987). Lift forces on pipelines in steady flow. *Journal of Waterway, Port, Coastal, and Ocean Engineering*, 113(2):139–155.

Fredsøe, J., Sumer, B. M., Arnskov, M., et al. (1991). Time scale for wave/current scour below pipelines. In *Proceeding of the First International Offshore and Polar Engineering Conference*. International Society of Offshore and Polar Engineers.

Fuhrman, D. R., Baykal, C., Sumer, B. M., Jacobsen, N. G., and Fredsøe, J. (2014). Numerical simulation of wave-induced scour and backfilling processes beneath submarine pipelines. *Coastal Engineering*, 94:10–22.

Fuhrman, D. R., Schløer, S., and Sterner, J. (2013). RANS-based simulation of turbulent wave boundary layer and sheet-flow sediment transport processes. *Coastal Engineering*, 73:151–166.

Gao, F.-p. and Luo, C.-c. (2010). Flow-pipe-seepage coupling analysis of spanning initiation of a partially-embedded pipeline. *Journal of hydrodynamics*, 22(4):478–487.

Gatmiri, B. (1990). A simplified finite element analysis of wave-induced effective stresses and pore pressures in permeable sea beds. *Geotechnique*, 40(1):15–30.

Geremew, A. M. (2011). Pore-water pressure development caused by wave-induced cyclic loading in deep porous formation. *International Journal of Geomechanics*, 13(1):65–68.

Gravesen, H. and Fredsøe, J. (1983). Modelling of liquefaction, scour and natural backfilling process in relation to marine pipelines. In *Offshore oil and Gas Pipeline Technology, European Seminar*.

Grue, J. and Huseby, M. (2002). Higher-harmonic wave forces and ringing of vertical cylinders. *Applied ocean research*, 24(4):203–214.

Guo, Z., Jeng, D.-S., Zhao, H., Guo, W., and Wang, L. (2019). Effect of seepage flow on sediment incipient motion around a free spanning pipeline. *Coastal Engineering*, 143:50–62.

Hammar, L., Andersson, S., Rosenberg, R., and Dimming, A. (2010). *Adapting offshore wind power foundations to local environment*. Naturvårdsverket.

Hansen, E., Klomp, W., Smed, P., Chen, Z., Bijker, R., and Bryndum, M. (1995). Free span development and self-lowering of pipelines/cables. In *Proceedings of the 14th Offshore Mechanics and Arctic Engineering Conference, ASME, Copenhagen, Denmark*, volume 5, pages 409–417.

Hansen, E. A., Fredsoe, J., and Mao, Y. (1986). Two-dimensional scour below pipelines. In *Proceedings of the 5th International Conference on Offshore Mechanical and Arctic Engineering (OMAE), Vol. 3*, page 670–678. American Society of Mechanical Engineers.

Hansen, E. A., Staub, C., Fredsøe, J., and Sumer, B. M. (1991). Time-development of scour induced free spans of pipelines. In *Proceedings of the 10th Conf. on Offshore Mechanics and Arctic Engineering, Pipeline Technology*, volume 5, pages 25–31.

Higuera, P., Lara, J. L., and Losada, I. J. (2013). Realistic wave generation and active wave absorption for navier–stokes models: Application to openfoam®. *Coastal Engineering*, 71:102–118.

Hsu, J. and Jeng, D. (1994a). Wave-induced soil response in an unsaturated anisotropic seabed of finite thickness. *International Journal for Numerical and Analytical Methods in Geomechanics*, 18(11):785–807.

Hsu, J. R. C. and Jeng, D. S. (1994b). Wave-induced soil response in an unsaturated anisotropic seabed of finite thickness. *International Journal for Numerical and Analytical Methods in Geomechanics*, 18(11):785–807.

Hur, D.-S., Kim, C.-H., and Yoon, J.-S. (2010). Numerical study on the interaction among a nonlinear wave, composite breakwater and sandy seabed. *Coastal Engineering*, 57(10):917–930.

Jacobsen, N. G. (2011). *A full hydro-and morphodynamic description of breaker bar development*. PhD thesis, Technical University of Denmark.

Jacobsen, N. G. and Fredsoe, J. (2014). Formation and development of a breaker bar under regular waves. part 2: Sediment transport and morphology. *Coastal Engineering*, 88:55–68.

Jacobsen, N. G., Fredsoe, J., and Jensen, J. H. (2014). Formation and development of a breaker bar under regular waves. Part 1: Model description and hydrodynamics. *Coastal Engineering*, 88:182–193.

Jacobsen, N. G., Fuhrman, D. R., and Fredsøe, J. (2012). A wave generation toolbox for the open-source cfd library: Openfoam®. *International Journal for Numerical Methods in Fluids*, 70(9):1073–1088.

Jasak, H. and Weller, H. (2000). Application of the finite volume method and unstructured meshes to linear elasticity. *International journal for numerical methods in engineering*, 48(2):267–287.

Jeng, D. and Hsu, J. (1996). Wave-induced soil response in a nearly saturated sea-bed of finite thickness. *Geotechnique*, 46(3):427–440.

Jeng, D. and Seymour, B. (1997). Response in seabed of finite depth with variable permeability. *Journal of geotechnical and geoenvironmental engineering*, 123(10):902–911.

Jeng, D.-S. (1997a). Soil response in cross-anisotropic seabed due to standing waves. *Journal of geotechnical and geoenvironmental engineering*, 123(1):9–19.

Jeng, D.-S. (1997b). Soil response in cross-anisotropic seabed due to standing waves. *Journal of geotechnical and geoenvironmental engineering*, 123(1):9–19.

Jeng, D.-S. (1997c). Wave-induced seabed instability in front of a breakwater. *Ocean Engineering*, 24(10):887–917.

Jeng, D.-S. (1998). Wave-induced seabed response in a cross-anisotropic seabed in front of a breakwater: An analytical solution. *Ocean engineering*, 25(1):49–67.

Jeng, D.-S. (2012). Porous models for wave-seabed interactions. pages 13–17. Springer Science & Business Media.

Jeng, D.-S. and Cha, D. (2003). Effects of dynamic soil behavior and wave non-linearity on the wave-induced pore pressure and effective stresses in porous seabed. *Ocean Engineering*, 30(16):2065–2089.

Jeng, D.-S. and Lin, Y.-S. (2000). Poroelastic analysis of the wave–seabed interaction problem. *Computers and Geotechnics*, 26(1):43–64.

Jeng, D.-S. and Rahman, M. (2000). Effective stresses in a porous seabed of finite thickness: Inertia effects. *Canadian Geotechnical Journal*, 37(6):1383–1392.

Jeng, D.-S. and Rahman, M. (2001). Wave-induced oscillatory soil response: Difference between quasi-static and dynamic solutions. *Computer Methods and Advances in Geomechanics*, 2:1103–1106.

Jeng, D.-S. and Ye, J. (2012). Three-dimensional consolidation of a porous unsaturated seabed under rubble mound breakwater. *Ocean Engineering*, 53:48 – 59.

Jeng, D.-S., Ye, J.-H., Zhang, J.-S., and Liu, P.-F. (2013a). An integrated model for the wave-induced seabed response around marine structures: Model verifications and applications. *Coastal Engineering*, 72:1–19.

Jeng, D.-S., Ye, J.-H., Zhang, J.-S., and Liu, P.-F. (2013b). An integrated model for the wave-induced seabed response around marine structures: Model verifications and applications. *Coastal Engineering*, 72:1 – 19.

Jeppsson, J., Larsen, P. E., and Larsson, Å. (2008). Technical description lillgrund wind power plant. *Lillgrund Pilot Project. Vattenfall Vindkraft AB*.

Journée, J. and Massie, W. (2000). *Offshore hydromechanics*. TU Delft.

Kazeminezhad, H., Yeganeh-Bakhtiary, A., Etemad-Shahidi, A., and Baas, J. H. (2011). Two-phase simulation of wave-induced tunnel scour beneath marine pipelines. *Journal of Hydraulic Engineering*, 138(6):517–529.

Kirca, V. O., Sumer, B. M., and Fredsøe, J. (2013). Residual liquefaction of seabed under standing waves. *Journal of Waterway, Port, Coastal, and Ocean Engineering*, 139(6):489–501.

Kjekstad, O. and Lunne, T. (1981). Soil parameters used for design of gravity platforms in the north sea. *Applied Ocean Research*, 3(2):50–58.

Kudella, M., Oumeraci, H., De Groot, M., and Meijers, P. (2006a). Large-scale experiments on pore pressure generation underneath a caisson breakwater. *Journal of waterway, port, coastal, and ocean engineering*, 132(4):310–324.

Kudella, M., Oumeraci, H., de Groot, M. B., and Meijers, P. (2006b). Large-scale experiments on pore pressure generation underneath a caisson breakwater. *Journal of Waterway, Port, Coastal, and Ocean Engineering*, 132(4):310–324.

Lamberti, A., Archetti, R., Kramer, M., Paphitis, D., Mosso, C., and Di Risio, M. (2005). European experience of low crested structures for coastal management. *Coastal Engineering*, 52(10):841 – 866. Low Crested Structures and the Environment.

Larsen, B. E., Fuhrman, D. R., Baykal, C., and Sumer, B. M. (2017). Tsunami-induced scour around monopile foundations. *Coastal Engineering*, 129:36–49.

Larsen, B. E., Fuhrman, D. R., and Sumer, B. M. (2016). Simulation of wave-plus-current scour beneath submarine pipelines. *Journal of Waterway, Port, Coastal, and Ocean Engineering*, 142(5):04016003.

Le Mehaute, B. (2013). *An introduction to hydrodynamics and water waves*. Springer Science & Business Media.

Lee, C.-H., Low, Y. M., and Chiew, Y.-M. (2016). Multi-dimensional rheology-based two-phase model for sediment transport and applications to sheet flow and pipeline scour. *Physics of Fluids*, 28(5):053305.

Li, F. and Cheng, L. (1999). Numerical model for local scour under offshore pipelines. *Journal of Hydraulic Engineering*, 125(4):400–406.

Li, F. and Cheng, L. (2000). Numerical simulation of pipeline local scour with lee-wake effects. *International Journal of Offshore and Polar Engineering*, 10(03).

Li, F. and Cheng, L. (2001). Prediction of lee-wake scouring of pipelines in currents. *Journal of waterway, port, coastal, and ocean engineering*, 127(2):106–112.

Li, X.-J., Gao, F.-P., Yang, B., Zang, J., et al. (2011). Wave-induced pore pressure responses and soil liquefaction around pile foundation. *International Journal of Offshore and Polar Engineering*, 21(03).

Li, Y. (2016). Implementation of multiple time steps for the multi-physics solver based onchtmultiregionfoam. In *CFD with OpenSource Software, 2016, Edited by Nilsson. H.* Chalmers University of Technology.

Li, Y., Ong, M. C., and Tang, T. (2018). Numerical analysis of wave-induced poro-elastic seabed response around a hexagonal gravity-based offshore foundation. *Coastal Engineering*, 136:81–95.

Li, Y., Ong, M. C., and Tang, T. (2019). https://github.com/liyzpearl/elasticsoilsolvers.

Liang, D. and Cheng, L. (2005). Numerical model for wave-induced scour below a submarine pipeline. *Journal of waterway, port, coastal, and ocean engineering*, 131(5):193–202.

Liang, D., Cheng, L., and Li, F. (2005). Numerical modeling of flow and scour below a pipeline in currents: Part ii. scour simulation. *Coastal engineering*, 52(1):43–62.

Liao, C., Tong, D., and Chen, L. (2018a). Pore pressure distribution and momentary liquefaction in vicinity of impermeable slope-type breakwater head. *Applied Ocean Research*, 78:290 – 306.

Liao, C., Tong, D., Jeng, D.-S., and Zhao, H. (2018b). Numerical study for wave-induced oscillatory pore pressures and liquefaction around impermeable slope breakwater heads. *Ocean Engineering*, 157:364 – 375.

Lin, Y. and Jeng, D.-S. (1997). The effects of variable permeability on the wave-induced seabed response. *Ocean engineering*, 24(7):623–643.

Lin, Z., Pokrajac, D., Guo, Y., Jeng, D.-S., Tang, T., Rey, N., Zheng, J., and Zhang, J. (2017). Investigation of nonlinear wave-induced seabed response around mono-pile foundation. *Coastal Engineering*, 121:197–211.

Liu, X., García, M. H., Muscari, R., et al. (2007). Numerical investigation of seabed response under waves with free-surface water flow. *International Journal of Offshore and Polar Engineering*, 17(02).

Lu, Y. and Chiew, Y.-M. (2007). Seepage effects on dune dimensions. *Journal of Hydraulic Engineering*, 133(5):560–563.

Lu, Y., Chiew, Y.-M., and Cheng, N.-S. (2008). Review of seepage effects on turbulent open-channel flow and sediment entrainment. *Journal of Hydraulic Research*, 46(4):476–488.

Luan, M., Qu, P., Jeng, D.-S., Guo, Y., and Yang, Q. (2008). Dynamic response of a porous seabed–pipeline interaction under wave loading: soil–pipeline contact effects and inertial effects. *Computers and Geotechnics*, 35(2):173–186.

Maasland, M. (1957). Soil anisotropy and land drainage. In *Drainage of agricultural lands*, volume 7, pages 216–285. ASA Madison, Wis.

Madsen, O. S. (1978). Wave-induced pore pressures and effective stresses in a porous bed. *Géotechnique*, 28(4):377–393.

Mao, Y. (1986). The interaction between a pipeline and an erodible bed. *Institute of Hydrodynamics and Hydraulic Engineering, Technical University of Denmark*, PhD thesis.

Marieu, V., Bonneton, P., Foster, D., and Ardhuin, F. (2008). Modeling of vortex ripple morphodynamics. *Journal of Geophysical Research: Oceans*, 113(C9).

Marmoush, R. and Mulligan, R. (2016). Physical modelling and non-hydrostatic numerical modelling of wave propagation in a wave basin.

Mase, H., Sakai, T., and Sakamoto, M. (1994). Wave-induced porewater pressures and effective stresses around breakwater. *Ocean Engineering*, 21(4):361–379.

Mathieu, A., Nagel, T., Bonamy, C., Chauchat, J., Cheng, Z., Liu, X., and Hsu, T.-J. (2018). Application of a eulerian two-phase flow model to scour processes. In *E3S Web of Conferences*, volume 40, page 05015. EDP Sciences.

Menter, F. R. (1994). Two-equation eddy-viscosity turbulence models for engineering applications. *AIAA journal*, 32(8):1598–1605.

Nago, H., Maeno, S., Matsumoto, T., Hachiman, Y., et al. (1993). Liquefaction and densification of loosely deposited sand bed under water pressure variation. In *Proceedings of the Third International Offshore and Polar Engineering Conference*. International Society of Offshore and Polar Engineers.

Nataraja, M. and Gill, H. (1983). Ocean wave-induced liquefaction analysis. *Journal of Geotechnical Engineering*, 109(4):573–590.

Niemann, S., Fredsøe, J., and Jacobsen, N. G. (2010). Sand dunes in steady flow at low froude numbers: Dune height evolution and flow resistance. *Journal of Hydraulic Engineering*, 137(1):5–14.

Okusa, S. (1985). Wave-induced stresses in unsaturated submarine sediments. *Geotechnique*, 35(4):517–532.

Ong, M. C., Li, H., Leira, B. J., and Myrhaug, D. (2013). Dynamic analysis of offshore monopile wind turbine including the effects of wind-wave loading and soil properties. In *ASME 2013 32nd International Conference on Ocean, Offshore and Arctic Engineering*, pages V008T09A029–V008T09A029. American Society of Mechanical Engineers.

Ong, M. C., Trygsland, E., and Myrhaug, D. (2016). Numerical study of seabed boundary layer flow around monopile and gravity-based wind turbine foundations. In *Proceedings of the 35th International Conference on Ocean, Offshore and Arctic Engineering*, pages V002T08A011–V002T08A011. American Society of Mechanical Engineers.

Oumeraci, H. (1994). Review and analysis of vertical breakwater failures—lessons learned. *Coastal Engineering*, 22(1-2):3–29.

Pasquali, D., Di Risio, M., and De Girolamo, P. (2015). A simplified real time method to forecast semi-enclosed basins storm surge. *Estuarine, Coastal and Shelf Science*, 165:61 – 69.

Paulsen, B. T., Bredmose, H., Bingham, H. B., and Jacobsen, N. G. (2014). Forcing of a bottom-mounted circular cylinder by steep regular water waves at finite depth. *Journal of fluid mechanics*, 755:1–34.

Phillips, E. (1869). De l'equilibre des solides elastiques semblables. *CR Acad. Sci., Paris*, 68:75–79.

Qi, W.-G. (2018). Personal communication by email.

Qi, W.-G. and Gao, F.-P. (2014). Physical modeling of local scour development around a large-diameter monopile in combined waves and current. *Coastal Engineering*, 83:72–81.

Raman-Nair, W., Sabin, G. C. W., Biot, Mohr, and Coulomb (1991). Wave-induced failure of poroelastic seabed slopes: A boundary element study. *Proceedings of the Institution of Civil Engineers*, 91(4):771–794.

Rienecker, M. and Fenton, J. (1981). A fourier approximation method for steady water waves. *Journal of fluid mechanics*, 104:119–137.

Rijn, L. C. v. (1984). Sediment transport, part ii: suspended load transport. *Journal of hydraulic engineering*, 110(11):1613–1641.

Roulund, A., Sumer, B. M., Fredsøe, J., and Michelsen, J. (2005). Numerical and experimental investigation of flow and scour around a circular pile. *Journal of Fluid Mechanics*, 534:351–401.

Saponieri, A., Di Risio, M., Pasquali, D., Valentini, N., Aristodemo, F., Tripepi, G., Celli, D., Streicher, M., and Damiani, L. (2018a). Beach profile evolution in front of storm seawalls: a physical and numerical study. *Coastal Engineering Proceedings*, 1(36):70.

Saponieri, A., Valentini, N., Di Risio, M., Pasquali, D., and Damiani, L. (2018b). Laboratory investigation on the evolution of a sandy beach nourishment protected by a mixed soft–hard system. *Water*, 10(9).

Sassa, S. and Sekiguchi, H. (1999). Wave-induced liquefaction of beds of sand in a centrifuge. *Geotechnique*, 49(5):621–638.

Sassa, S. and Sekiguchi, H. (2001). Analysis of wave-induced liquefaction of sand beds. *Geotechnique*, 51(2):115–126.

Sekiguchi, H., Kita, K., and Okamoto, O. (1995). Response of poro-elastoplastic beds to standing waves. *Soils and Foundations*, 35(3):31–42.

Sekiguchi, H. and Phillips, R. (1991). Generation of water waves in a drum centrifuge. In *Proc of Int Conf Centrifuge*, pages 343–350.

Seng, S. (2012). Slamming and whipping analysis of ships.

Shabani, B. et al. (2008). Wave-associated seabed behaviour near submarine buried pipelines.

Smit, P., Zijlema, M., and Stelling, G. (2013). Depth-induced wave breaking in a non-hydrostatic, near-shore wave model. *Coastal Engineering*, 76:1–16.

Smith, H. D. and Foster, D. L. (2005). Modeling of flow around a cylinder over a scoured bed. *Journal of waterway, port, coastal, and ocean engineering*, 131(1):14–24.

Soulsby, R. (1995). Bed shear-stresses due to combined waves and currents. *Advances in Coastal Morphodynamics*, 1995.

Sui, T., Zhang, C., Guo, Y., Zheng, J., Jeng, D.-S., Zhang, J., and Zhang, W. (2016). Three-dimensional numerical model for wave-induced seabed response around mono-pile. *Ships and Offshore Structures*, 11(6):667–678.

Sui, T., Zhang, C., Jeng, D.-s., Guo, Y., Zheng, J., Zhang, W., and Shi, J. (2019). Wave-induced seabed residual response and liquefaction around a mono-pile foundation with various embedded depth. *Ocean Engineering*, 173:157–173.

Sui, T., Zhang, C., Zheng, J., Guo, Y., and Xie, M. (2018). Numerical study of standing wave-induced seabed residual response with the non-homogeneous soil property. *Journal of Coastal Research*, 85(sp1):921–925.

Sui, T., Zheng, J., Zhang, C., Jeng, D.-S., Zhang, J., Guo, Y., and He, R. (2017). Consolidation of unsaturated seabed around an inserted pile foundation and its effects on the wave-induced momentary liquefaction. *Ocean Engineering*, 131:308–321.

Sumer, B. M. (2007). Mathematical modelling of scour: A review. *J. Hydraulic Research*, 45(6):723–735.

Sumer, B. M. (2014a). *Liquefaction around marine structures*. World Scientific Publishing Company.

Sumer, B. M. (2014b). A review of recent advances in numerical modelling of local scour problems. In *Proceeding of the 7th International Conference on Scour and Erosion*, pages 61–70.

Sumer, B. M. and Fredsøe, J. (1990). Scour below pipelines in waves. *Journal of waterway, port, coastal, and ocean engineering*, 116(3):307–323.

Sumer, B. M. and Fredsøe, J. (1993). Self-burial of pipelines at span shoulders. In *Proceedings of the 3rd International Offshore and Polar Engineering Conference*. International Society of Offshore and Polar Engineers.

Sumer, B. M. and Fredsøe, J. (1996). Scour around pipelines in combined waves and current. In *Proceeding of the 15th Conference on Offshore Mechanics and Arctic Engineering, Florence, Italy*, pages 595–602. American Society of Mechanical Engineers.

Sumer, B. M. and Fredsøe, J. (2002). *The mechanics of scour in the marine environment*, volume 17. World Scientific Publishing Company.

Sumer, B. M. and Fredsøe, J. (2006). *Hydrodynamics around cylindrical strucures*, volume 26. World scientific.

Sumer, B. M., Fredsøe, J., Christensen, S., and Lind, M. (1999). Sinking/floatation of pipelines and other objects in liquefied soil under waves. *Coastal Engineering*, 38(2):53–90.

Sumer, B. M., Hatipoglu, F., and Fredsøe, J. (2007). Wave scour around a pile in sand, medium dense, and dense silt. *Journal of waterway, port, coastal, and ocean engineering*, 133(1):14–27.

Sumer, B. M., Hatipoglu, F., Fredsøe, J., and Sumer, S. K. (2006). The sequence of sediment behaviour during wave-induced liquefaction. *Sedimentology*, 53(3):611–629.

Sumer, B. M., Jensen, H. R., Mao, Y., and Fredsøe, J. (1988). Effect of lee-wake on scour below pipelines in current. *Journal of Waterway, Port, Coastal, and Ocean Engineering*, 114(5):599–614.

Sumer, B. M., Ozgur Kirca, V., Fredsøe, J., et al. (2012). Experimental validation of a mathematical model for seabed liquefaction under waves. *International Journal of Offshore and Polar Engineering*, 22(02).

Sumer, B. M., Truelsen, C., Sichmann, T., and Fredsøe, J. (2001). Onset of scour below pipelines and self-burial. *Coastal engineering*, 42(4):313–335.

Sumner, D. (2010). Two circular cylinders in cross-flow: a review. *Journal of Fluids and Structures*, 26(6):849–899.

Suzuki, T., Altomare, C., Veale, W., Verwaest, T., Trouw, K., Troch, P., and Zijlema, M. (2017). Efficient and robust wave overtopping estimation for impermeable coastal structures in shallow foreshores using swash. *Coastal Engineering*, 122:108–123.

Tang, T. (2014). *Modeling of soil-water-structure interaction: A Finite Volume Method (FVM) approach to fully coupled soil analysis and interactions between wave, seabed and offshore structure.* PhD thesis, Technical University of Denmarke.

Tang, T., Hededal, O., and Cardiff, P. (2015). On finite volume method implementation of poro-elasto-plasticity soil model. *International journal for numerical and analytical methods in geomechanics*, 39(13):1410–1430.

Tang, T., Johannesson, B., and Roenby, J. (2014). An integrated fvm simulation of wave-seabed-structure interaction using openfoam. In *Proceedings of the 9th OpenFOAM Workshop, 23-26 June 2014 in Zagreb, Croatia*.

Teh, T., Palmer, A., and Damgaard, J. (2003). Experimental study of marine pipelines on unstable and liquefied seabed. *Coastal Engineering*, 50(1-2):1–17.

Terzaghi, K. (1944). *Theoretical soil mechanics*. Chapman And Hali, Limited John Wiler And Sons, Inc; New York.

The SWASH team (2017). *SWASH user manual, version 4.01*.

Tsai, C. (1995). Wave-induced liquefaction potential in a porous seabed in front of a breakwater. *Ocean Engineering*, 22(1):1–18.

Tsai, C.-P. and Lee, T.-L. (1995). Standing wave induced pore pressures in a porous seabed. *Ocean engineering*, 22(6):505–517.

Ulker, M., Rahman, M., and Guddati, M. (2009a). Breaking wave-induced dynamic response of rubble mound and seabed under a caisson breakwater. In *Proceeding of the 28th International Conference on Ocean, Offshore and Arctic Engineering*, pages 141–150. American Society of Mechanical Engineers.

Ulker, M., Rahman, M., and Guddati, M. (2010). Wave-induced dynamic response and instability of seabed around caisson breakwater. *Ocean Engineering*, 37(17):1522–1545.

Ulker, M., Rahman, M., and Jeng, D.-S. (2009b). Wave-induced response of seabed: various formulations and their applicability. *Applied Ocean Research*, 31(1):12–24.

US Army Corps of Engineers (USACE) (2002). *Coastal engineering manual (CEM)*. USACE, Washington, DC.

Vafai, K. and Tien, C. (1981). Boundary and inertia effects on flow and heat transfer in porous media. *International Journal of Heat and Mass Transfer*, 24(2):195–203.

van den Bos, J., Verhagen, H. J., and Kuiper, C. (2015). Numerical modelling of wave reflection and transmission in vertical porous structures. In *Proceedings 7th Coastal Structures conference (ASCE-COPRI), Boston, USA 9-11 September 2015 (authors version)*. ASCE-COPRI.

van den Bos, J., Verhagen, H. J., Zijlema, M., and Mellink, B. (2014). Towards a practical application of numerical models to predict wave-structure interaction: an initial validation. *Coastal Engineering Proceedings*, 1(34):50.

Van Der Meer, J. W. (1988). Rock slopes and gravel beaches under wave attack.

Van Gent, M. R. (2013). Rock stability of rubble mound breakwaters with a berm. *Coastal Engineering*, 78:35–45.

Wang, H. F. (2017). Theory of linear poroelasticity with applications to geomechanics and hydrogeology. chapter 6, pages 124–128. Princeton University Press.

Whitehouse, R. (1998). *Scour at marine structures: A manual for practical applications*. Thomas Telford.

Wilcox, D. C. (2006). *Turbulence modeling for CFD, 3rd edition*, volume 2. DCW industries La Canada, CA.

Wilcox, D. C. (2008). Formulation of the $k-\omega$ turbulence model revisited. *AIAA journal*, 46(11):2823–2838.

Wu, Y. and Chiew, Y.-M. (2012). Three-dimensional scour at submarine pipelines. *Journal of hydraulic engineering*, 138(9):788–795.

Wu, Y. and Chiew, Y.-M. (2013). Mechanics of three-dimensional pipeline scour in unidirectional steady current. *Journal of Pipeline Systems Engineering and Practice*, 4(1):3–10.

Wu, Y. and Chiew, Y.-M. (2014). Mechanics of pipeline scour propagation in the spanwise direction. *Journal of Waterway, Port, Coastal, and Ocean Engineering*, 141(4):04014045.

Yamamoto, T. (1981). Wave-induced pore pressures and effective stresses in inhomogeneous seabed foundations. *Ocean Engineering*, 8(1):1–16.

Yamamoto, T., Koning, H., Sellmeijer, H., and Van Hijum, E. (1978). On the response of a poro-elastic bed to water waves. *Journal of Fluid Mechanics*, 87(01):193–206.

Ye, B., Lu, J., and Ye, G. (2015a). Pre-shear effect on liquefaction resistance of a fujian sand. *Soil Dynamics and Earthquake Engineering*, 77:15–23.

Ye, J. (2012a). 3D liquefaction criteria for seabed considering the cohesion and friction of soil. *Applied Ocean Research*, 37:111–119.

Ye, J. (2012b). *Numerical analysis of Wave-Seabed-Breakwater interactions.* PhD thesis, University of Dundee.

Ye, J., Jeng, D., Wang, R., and Zhu, C. (2015b). Numerical simulation of the wave-induced dynamic response of poro-elastoplastic seabed foundations and a composite breakwater. *Applied Mathematical Modelling*, 39(1):322–347.

Ye, J., Jeng, D., Wang, R., and Zhu, C. (2015c). Numerical simulation of the wave-induced dynamic response of poro-elastoplastic seabed foundations and a composite breakwater. *Applied Mathematical Modelling*, 39(1):322 – 347.

Ye, J., Jeng, D.-S., Chan, A., Wang, R., and Zhu, Q. (2016). 3D integrated numerical model for fluid–structures–seabed interaction (fssi): Elastic dense seabed foundation. *Ocean Engineering*, 115:107 – 122.

Ye, J., Jeng, D.-S., Liu, P.-F., Chan, A., Ren, W., and Changqi, Z. (2014). Breaking wave-induced response of composite breakwater and liquefaction in seabed foundation. *Coastal Engineering*, 85:72–86.

Ye, J., Jeng, D.-S., Wang, R., and Zhu, C. (2013). A 3-D semi-coupled numerical model for fluid–structures–seabed-interaction (FSSI-CAS 3D): Model and verification. *Journal of Fluids and Structures*, 40:148–162.

Ye, J. and Wang, G. (2016). Numerical simulation of the seismic liquefaction mechanism in an offshore loosely deposited seabed. *Bulletin of Engineering Geology and the Environment*, 75(3):1183–1197.

Zang, Z., Cheng, L., Zhao, M., Liang, D., and Teng, B. (2009). A numerical model for onset of scour below offshore pipelines. *Coastal Engineering*, 56(4):458–466.

Zen, K. and Yamazaki, H. (1990a). Mechanism of wave-induced liquefaction and densification in seabed. *Soils and Foundations*, 30(4):90–104.

Zen, K. and Yamazaki, H. (1990b). Oscillatory pore pressure and liquefaction in seabed induced by ocean waves. *Soils and Foundations*, 30(4):147–161.

Zhang, C., Sui, T., Zheng, J., Xie, M., and Nguyen, V. T. (2016). Modelling wave-induced 3d non-homogeneous seabed response. *Applied Ocean Research*, 61:101–114.

Zhang, C., Zhang, Q., Wu, Z., Zhang, J., Sui, T., and Wen, Y. (2015). Numerical study on effects of the embedded monopile foundation on local wave-induced porous seabed response. *Mathematical Problems in Engineering*, 2015.

Zhang, Q., Draper, S., Cheng, L., Zhao, M., and An, H. (2017). Experimental study of local scour beneath two tandem pipelines in steady current. *Coastal Engineering Journal*, 59(01):1750002.

Zhang, X., Jeng, D.-S., and Luan, M. (2011). Dynamic response of a porous seabed around pipeline under three-dimensional wave loading. *Soil Dynamics and Earthquake Engineering*, 31(5):785–791.

Zhao, H., Jeng, D.-S., Liao, C., and Zhu, J. (2017a). Three-dimensional modeling of wave-induced residual seabed response around a mono-pile foundation. *Coastal Engineering*, 128:1–21.

Zhao, H., Jeng, D.-S., Zhang, J., Liao, C., Zhang, H., and Zhu, J. (2017b). Numerical study on loosely deposited foundation behavior around a composite breakwater subject to ocean wave impact. *Engineering Geology*, 227:121 – 138. New Advances in Coastal Engineering Geology and Geotechnics.

Zhao, H., Liang, Z., Jeng, D.-S., Zhu, J., Guo, Z., and Chen, W. (2018). Numerical investigation of dynamic soil response around a submerged rubble mound breakwater. *Ocean Engineering*, 156:406 – 423.

Zhao, H.-Y. and Jeng, D.-S. (2015). Numerical study of wave-induced soil response in a sloping seabed in the vicinity of a breakwater. *Applied Ocean Research*, 51:204 – 221.

Zhao, M. and Cheng, L. (2008). Numerical modeling of local scour below a piggyback pipeline in currents. *Journal of Hydraulic Engineering*, 134(10):1452–1463.

Zhao, M., Cheng, L., and Zhou, T. (2009). Direct numerical simulation of three-dimensional flow past a yawed circular cylinder of infinite length. *Journal of Fluids and Structures*, 25(5):831–847.

Zhao, M., Vaidya, S., Zhang, Q., and Cheng, L. (2015). Local scour around two pipelines in tandem in steady current. *Coastal Engineering*, 98:1–15.

Zhou, Y. and Yiu, M. (2006). Flow structure, momentum and heat transport in a two-tandem-cylinder wake. *Journal of Fluid Mechanics*, 548:17–48.

Zhu, B., Ren, J., and Ye, G.-L. (2018). Wave-induced liquefaction of the seabed around a single pile considering pile–soil interaction. *Marine Georesources & Geotechnology*, 36(1):150–162.

Zienkiewicz, O., Chang, C., and Bettess, P. (1980). Drained, undrained, consolidating and dynamic behaviour assumptions in soils. *Geotechnique*, 30(4):385–395.

Zijlema, M. and Stelling, G. S. (2005). Further experiences with computing non-hydrostatic free-surface flows involving water waves. *International Journal for Numerical Methods in Fluids*, 48(2):169–197.

Zijlema, M. and Stelling, G. S. (2008). Efficient computation of surf zone waves using the nonlinear shallow water equations with non-hydrostatic pressure. *Coastal Engineering*, 55(10):780 – 790.

Zijlema, M., Stelling, G. S., and Smit, P. (2011). Swash: An operational public domain code for simulating wave fields and rapidly varied flows in coastal waters. *Coastal Engineering*, 58(10):992 – 1012.